NUI MAYNOOTH

Ollscoil na hÉireann Má Nuad

Analysis and Design of Wideband Voltage Controlled Oscillators using Self-Oscillating Active Inductors

by

Grzegorz Szczepkowski, B. E. Eng.

A thesis submitted in fulfillment
of the requirements for the degree of

Doctor of Philosophy

in
Department of Electronic Engineering
National University of Ireland, Maynooth
Co. Kildare
Ireland

29$^{\text{th}}$ October, 2010

Supervisor: Dr. Ronan Farrell

Head of Department: Dr. Seán Mcloone

To my wife Ela for saving my life every single day we are together.

To my sister Justyna for being the greatest sister one can have.

To my Mum Danuta and my Dad Józef for always being there for me.

Padać i wstawać,

padać i wstawać,

padać i wstawać,

padać i wstawać − i wstać!

"Przypowieść o ślepcach"

Jacek Kaczmarski

To be falling and rising,

falling and rising,

falling and rising,

falling and rising − and rise!*

"The Parable of the Blind"

Jacek Kaczmarski

* Translation, courtesy of Dr. Ewa Rajewska,

Adam Mickiewicz University, Poznań, Poland.

Abstract

Voltage controlled oscillators (VCOs) are essential components of RF circuits used in transmitters and receivers as sources of carrier waves with variable frequencies. This, together with a rapid development of microelectronic circuits, led to an extensive research on integrated implementations of the oscillator circuits. One of the known approaches to oscillator design employs resonators with active inductors – electronic circuits simulating the behavior of passive inductors using only transistors and capacitors. Such resonators occupy only a fraction of the silicon area necessary for a passive inductor, and thus allow to use chip area more effectively. The downsides of the active inductor approach include: power consumption and noise introduced by transistors.

This thesis presents a new approach to active inductor oscillator design using self-oscillating active inductor circuits. The instability necessary to start oscillations is provided by the use of a passive RC network rather than a power consuming external circuit employed in the standard oscillator approach. As a result, total power consumption of the oscillator is improved. Although, some of the active inductors with RC circuits has been reported in the literature, there has been no attempt to utilise this technique in wideband voltage controlled oscillator design. For this reason, the dissertation presents a thorough investigation of self-oscillating active inductor circuits, providing a new set of design rules and related trade-offs. This includes: a complete small signal model of the oscillator, sensitivity analysis, large signal behavior of the circuit and phase noise model. The presented theory is confirmed by extensive simulations of wideband CMOS VCO circuit for various temperatures and process variations. The

obtained results prove that active inductor oscillator performance is obtained without the use of standard active compensation circuits. Finally, the concept of self-oscillating active inductor has been employed to simple and fast OOK (On-Off Keying) transmitter showing energy efficiency comparable to the state of the art implementations reported in the literature.

Acknowledgements

Although this dissertation is my own work it would not be possible to complete it without the help of other people. Let this paragraph be my own way to thank those who contributed or supported me along the way. So there it is.

All you can see here would not be possible without Dr. Ronan Farrell, the project supervisor. He gave me a chance to work at NUI Maynooth and was both supportive and motivating. I do not recall exactly how many times he convinced me to continue, and he was right - it was all worth it. Numerous times he provided me with constructive criticism and acted as the main editor of this dissertation. I would like to thank him for making this project happen.

Next person I would like to thank is Dr. Matthieu Fillaud. Few years ago he convinced me to use LaTeX and Emacs to produce high quality publications (if anybody has ever done it there is really no way back to any WYSIWYG type of text editor). Thanks to him I started to use M4 Circuit Macros to produce circuit schematics presented in this work. He showed me tons of various tips and tricks in Linux. We had lots of crucial discussions on CMOS design and layout, active inductors and VCOs, as Matthieu has also mastered these areas. Matthieu, I want to thank you for everything you did to help me with the project.

Special thanks to Michael Soudan, "Zee German" who was my MATLAB guru, helped me on countless occasions with calculation problems (although knowing Michael, as modest person as he is, he probably will deny most of his contribution). Being my "brother in arms" on the postgraduate front, he helped me a lot to cope with the stress

of PhD studies. On many occasions, he dropped whatever he was doing just to help me. Michael, I want to thank you for your unconditional support over these few years we worked together.

Without Matthieu and Michael coffee and lunch breaks are not the same.

This work would not be possible without my two high school teachers who I met years ago. Mr. Dariusz Charzyński who taught electronic circuits (yes, I graduated technical secondary school), did it so well, that during my studies at university in Poland I could easily solve many of the exam problems. Thank you very much for that. The second person is the late Mr Wiesław Dobosz who was my mathematics teacher. He was the first teacher to prove to me the importance of homework and self study. This, I believe, helped me to become one of the best students in my class and subsequently led me to the doctoral degree. Thank you very much for all you did back then.

For all these years, all of my friends supported me along the way. I would like to thank Agnieszka Kasprzyk for being there for me in 1999 when I really needed it. I will never forget that. I know since she moved to England and became a mum we do not have many occasions to meet and talk in person. But whatever happens I know there is at least one person willing to talk to me - and this is Agnieszka. Thank you for that. Kamil Czajka, who become a philosopher and mathematician long before he actually graduated both (sic!), was always ready to listen when I needed to talk. Although I have known Kamil for years, he has not changed a bit, always being honest and supportive. Thank you for everything.

I would like to thank the people that helped my in various ways. In my first days in Maynooth, Barbara Walsh and Livia Ruiz helped me adapting to a new environment. Before I could buy a car, for almost 6 months I was carpooling every day with Magda Sanchez for free. Ger Baldwin convinced me to write my first paper. Dr. Ludovic Barrandon, Dr. Aidan Keady (who also answered tons of CMOS related questions), Diarmuid Collins, Prakash Srinivasan, and Joanna O'Grady (who helped me a lot with registration process every year). All of you and the others from the Callan Institute - it was a true honour to work with you all.

List of published contributions

- G. Szczepkowski, J. Dooley and R. Farrell, "The Concept of CMOS OOK transmitter using low voltage self-oscillating active inductor", IEEE International Conference on Signals and Electronic Systems, ICSES 2010, Gliwice, Poland.

- G. Szczepkowski and R. Farrell, "Analysis and design of oscillators based on low-voltage self-oscillating active inductors", IET Irish Signal and Systems Conference, ISSC 2010, Cork, Ireland.

- G. Szczepkowski and R. Farrell, "Noise and dynamic range of CMOS degenerated active inductor resonators", IEEE European Conference on Circuit Theory and Design, ECCTD 2009, Antalya, Turkey.

- G. Szczepkowski and R. Farrell, "Negative resistance generation in degenerated gyrator", RIA Colloquium on Emerging Trends in Wireless Communications 2008, Dublin, Ireland.

- G. Szczepkowski, G. Baldwin and R. Farrell, "Wideband 0.18 μm CMOS VCO Using Active Inductor with Negative Resistance", IEEE European Conference on Circuit Theory and Design, ECCTD 2007, Seville, Spain.

Contents

Contents

Contents

Contents

Contents

List of Figures

List of Figures

List of Figures

List of Tables

List of Symbols

β_{half} half bandwidth of LC resonator

γ CMOS process dependent noise parameter

$\Im\{\cdot\}$ real-valued imaginary part of complex function

$\mathcal{L}(\omega_m)$ normalised theoretical one-sided spectrum of oscillator signal

ω_0 resonant frequency, carrier frequency

ω_m offset frequency

ω_{0ai} resonant frequency of ideal standard active inductor

ω_{0dg} resonant frequency of ideal degenerated gyrator

ω_{0ndg} resonant frequency of non-ideal degenerated gyrator

ω_{RC} cut-off frequency of RC phase shifter

ϕ phase shift

$\phi_n(t)$ zero-mean phase fluctuations of noise voltage

ϕ_{RC} phase shift of RC network

$\Re\{\cdot\}$ real-valued real part of complex function

A_{DC} DC gain of CMOS transistor

$A_{n...}(j\omega), Z_{n...}(j\omega)$ noise transfer functions

List of Symbols

C	generic capacitance
C_g	gyration capacitance
C_i	input capacitance of non-ideal degenerated gyrator
C_M	Miller capacitance
C_o	output capacitance of non-ideal degenerated gyrator
C_p	parallel capacitance
C_s	series capacitance
C_T	total tank capacitance including parasitics
C_t	tank capacitance
C_{ex1}, C_{ex2}	capacitances connected to single MOS negative resistor
C_{gd}	gate to drain capacitance
C_{gs}	gate to source capacitance
C_{max}	maximum varactor capacitance
C_{min}	minimum varactor capacitance
C_{o1}, C_{o2}	total capacitances of gyrator ports
C_{ox}	oxide capacitance
C_{sim}	simulated capacitance
D_{rate}	data rate
E_C	critical electric field causing electron drift velocity saturation in MOS device
f_t	frequency of CMOS unit current gain

List of Symbols

FBW	fractional bandwidth
FOM_{OOK}	OOK figure of merit
$FOMT$	VCO figure of merit including tuning range
$FOMTP$	VCO figure of merit including tuning range and RF power
g_1, g_2	gyration conductances
G_i	input conductance of non-ideal degenerated gyrator
G_o	output conductance of non-ideal degenerated gyrator
g_{ds}	drain to source conductance
G_{o1}, G_{o2}	total conductances of gyrator ports
G_{pdg}	equivalent parallel conductance of degenerated gyrator
Gm	large signal transconductance
gm	transconductance
gm_1, gm_2	gyrator transconductances
$h(\tau)$	impulse response
$H_n\{x(t)\}$	n^{th}-order Volterra operator
HD_2, HD_3	second and third order distortion
I_B	bias current
I_D	DC drain current
i_D	total drain current consisting on DC and AC components
i_d	AC drain current
$i_l(t)$	instantaneous inductor current

List of Symbols

i_{in}	AC input current
$i_{NL...}$	non-linear probing current sources
$ISF, \Gamma(x)$	impulse sensitivity function
k	Boltzmann's constant
$K_n(\omega_1, \ldots, \omega_n)$	frequency domain representation of nth-order Volterra kernel
$k_n(\tau_1, \tau_2, \ldots, \tau_n)$	n^{th}-order Volterra kernel
K_{VCO}	oscillator gain, tuning constant
L	generic inductance
L_p	parallel inductance
L_s	series inductance
L_{npdg}	equivalent parallel inductance of non-ideal degenerated gyrator
L_{nsdg}	series simulated inductance of non-ideal degenerated gyrator
L_{pai}	parallel equivalent inductance of standard active inductor
L_{pdg}	equivalent parallel inductance of degenerated gyrator
L_{sim}	simulated inductance of gyrator
P_{mWcore}	maximum DC power consumption of VCO core
P_{RF}	RF power
PN	phase noise level
Q	quality factor
$q(t)$	instantaneous charge
Q_0	unloaded quality factor

List of Symbols

Q_c quality factor of capacitor

Q_L loaded quality factor

Q_l quality factor of passive inductor

Q_{0tot} total unloaded quality factor of non-ideal resonator

q_{max} maximum charge stored in a tank capacitor

Q_{nsdg} quality factor of non-ideal degenerated gyrator

Q_{sdg} quality factor of degenerated gyrator

R generic resistance

r_g gate resistance

R_p parallel resistance

R_s series resistance

R_T total resistance of loaded tank

R_{act} active resistance generated by negative impedance converter

r_{cp} parallel equivalent resistance of capacitor

r_{cs} series resistance of capacitor

r_{ds} drain to source resistance

R_{eff} effective resonator resistance

R_{in}, C_{in} resistance and capacitance of input phase shifter

R_{load} load resistance

r_{lp} parallel equivalent resistance of passive inductor

r_{ls} series resistance of passive inductor

List of Symbols

R_{npdg}	equivalent parallel resistance of non-ideal degenerated gyrator
$R_{ns-loss}$	series resistance representing losses of non-ideal degenerated gyrator
$R_{ns_n eg}$	series negative resistance of non-ideal degenerated gyrator
R_{out}, C_{out}	resistance and capacitance of output phase shifter
R_{pai}	total parallel equivalent resistance of standard active inductor
R_{pdg}	equivalent parallel resistance of degenerated gyrator
S_x^y	classical sensitivity function
$S_{\phi_n}(\omega)$	power spectrum of phase modulating noise
T	temperature
THD	total harmonic distortion
V_0	voltage amplitude
$v_c(t)$	instantaneous capacitor voltage
$v_n(t)$	zero-mean amplitude fluctuations of noise voltage
$v_r(t)$	instantaneous resistor voltage
V_{DS}	drain to source voltage
v_{gs}	AC gate to source voltage
v_{inMAX}, v_{outMAX}	maximum voltage swing on gyrator ports
v_{in}	AC input voltage
$v_{out}(t)$	output voltage
V_{OV}	overdrive voltage
V_{th}	threshold voltage

List of Symbols

V_{tune}	oscillator tuning voltage
VDD	positive supply voltage of CMOS circuit
W, L	MOS drawn width and length
$Y(j\omega)$	small signal conductance
y_{xy}	small signal admittance matrix element
$Z(j\omega)$	small signal impedance
$\overline{i^2}/\Delta f$	noise current power spectral density
$\overline{v^2}/\Delta f$	noise voltage power spectral density

Chapter 1

Introduction

1.1 Motivation

Communication between people is one of the foundations of civilisation. The modern society we live in nowadays is communications hungry, demanding faster and more reliable ways to provide an information flow. Most of the communication today is mobile - you can make a call from any given place on the globe (providing you can afford a satellite phone call from South Pole for example). We want to download music, videos, make a call on the move, in a car, train or an aeroplane. To be portable, these mobile communication systems have to be relatively small, light and power efficient.

Over the last century, a huge effort has been made to utilise radio waves to transmit various communication signals over long distances. To allow the transmission, the signal (a sound or digital bit stream, also known as baseband signal) has to be up-converted in frequency. This process is known as *frequency conversion* or *modulation*. This is achieved by multiplying it with a high frequency signal known as the *carrier*. The result represents a radio frequency signal containing the information in a band of frequencies around the carrier that, after some additional conditioning, is ready for radio transmission. On the receiving end, this information can be extracted only if the same carrier frequency is available. In most RF systems this is a sinusoidal signal and to ensure a high-performance transmission, this signal has to be as close to the ideal
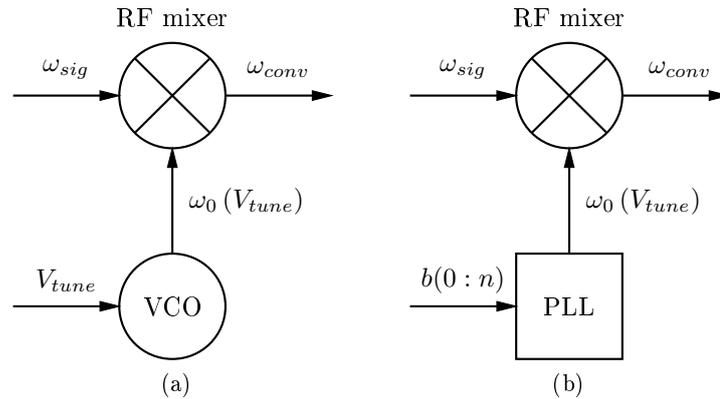
Figure 1.1: Frequency conversion using VCO: (a) directly (V_{tune} is a voltage controlling oscillator), (b) using PLL ($b(0:n)$ is a binary signal controlling PLL).

as possible. Unlike DC currents and voltages, high frequency sinusoidal signals are not readily available and have to be generated using special circuits known as *harmonic oscillators*.

Figure 1.1 shows two methods of the frequency conversion. In the first case, the oscillator (VCO) is connected directly to an RF mixer that multiplies the generated carrier frequency, $\omega_0(V_{tune})$ with the incoming signal ω_{sig}. The main advantage of this direct approach is simplicity of the conversion circuit. The main disadvantage however is an unwanted frequency drift due to frequency changes of the oscillator caused by noise or temperature. In the second case, the oscillator is a part of a control system known as a *phase lock loop* (PLL) that can, to a certain extent, track and compensate frequency drifts.

Figure 1.2 presents a standard concept of a PLL. The reference oscillator is typically a low frequency, high performance oscillator (e.g. crystal) whose frequency is compared with the divided frequency of the RF oscillator on the output of the loop. If both signals differ in phase or frequency, the digital phase and frequency detector (PFD) generates a train of electrical pulses. These pulses drive the charge pump that together with the loop filter produce a voltage proportional to the direction and magnitude of the required phase or frequency change. The last stage is voltage controlled oscillator (VCO) which frequency can be set proportionally to tuning voltage V_{tune}. By changing the division

2

ratio (nowadays fractional divisions are often used), the VCO frequency can be adjusted to the required value. Thus, a VCO is a critical component of radio-frequency circuits.

Over the past decade, integrated CMOS circuits have become the technology of choice for RF circuits. Very large scale of integration allows one to build high frequency circuits using lumped components rather than distributed structures. Due to the popularity of CMOS technology, there is a huge demand on miniaturisation of the circuits for one simple, but fundamental reason - production cost. The cost of integrated system decreases if on the same silicon area more circuits can be produced. Leaving reliability problems aside, the main obstacle in the circuit integration is the problem of different scalability of various components on the same chip. In existing processes, the minimum size of analog circuits is still larger than that of digital circuits. Currently, the largest analog circuit component is a passive inductor, and for a proper operation of a sinusoidal VCO, this component must not be omitted. For this reason, a harmonic oscillator occupies significant chip area.

The issue of silicon area required for the LC oscillator can be resolved by the use of active inductors. These circuits simulate inductive impedance using transistors and capacitors, significantly reducing the chip area. This solution has problems: transistors generate high levels of noise, are non-linear, consume DC power and are potentially unstable due to parasitic components. The last issue raises following questions:
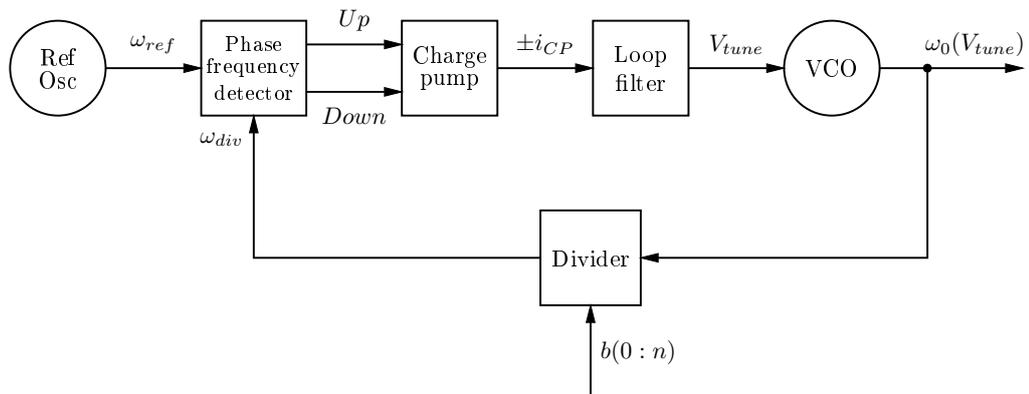
Figure 1.2: Standard phase lock loop.

- Can this inherent instability be utilised to obtain a harmonic oscillator?

- Can the oscillator architecture be simplified only to a LC tank and save DC power?

- Can such an oscillator operate over wide bandwidth and what is its performance?

- How would one design such a VCO?

This thesis presents a thorough analysis and complete design procedure of self-oscillating active resonator answering the above questions.

1.2 Structure of thesis

This dissertation is divided into the following parts:

- Chapter 2 presents the fundamentals of harmonic oscillators. Standard VCO models and design methods are presented together with short characterisation of each component of the integrated oscillator. Oscillator phase noise and the other main VCO performance parameters are presented. A noise analysis of passive resonators is presented, allowing comparison with active inductor solutions.

- Chapter 3 introduces the concept of gyrators and active inductors, focusing on their application in oscillators. The noise and quality factor issues of active inductor resonators are discussed. The phase noise of a standard active inductor oscillator is also analysed. The last part describes the parasitic effects of non-ideal gyrators and its proposed application in VCO design based on a new concept of *degenerated gyrator*.

- Chapter 4 describes a new small signal model of the self-oscillating active inductor. The sensitivity of the circuit is explored and mathematical formulae for oscillation criteria, tuning range and resonant frequency are derived. In this chapter a new noise model of the proposed circuit is also presented and compared to a standard gyrator approach from Chapter 3.

- Chapter 5 answers the question of what happens with the proposed degenerated active inductor VCO under large signal operation. Using the Volterra kernel technique, a new non-linear model of the proposed oscillator circuit is derived and used to predict amplitudes and frequencies of the oscillator signal.

- Chapter 6 delivers a new linear time invariant model of phase noise of self-oscillating active inductor, allowing the analysis of how the oscillator phase noise depends on various circuit parameters.

- Chapter 7 presents the practical design and simulation of two experimental circuits confirming the theory presented in the previous chapters. The first circuit is a 434 MHz wideband oscillator whilst the second circuit is a novel, energy efficient OOK (On-Off Keying) transmitter for ISM (Industrial, Scientific and Medical) applications.

- Chapter 8 concludes the dissertation and presents avenues for future work.

1.3   Main contributions

The general focus throughout this dissertation is on the complete analysis of a self-oscillating active inductor, able to generate a wide range of RF frequencies with low power consumption and minimising a silicon area. The initial discussion on parasitic effects in practical active inductors evolves into the concept of the degenerated gyrator oscillator. Prior to this thesis, no mathematical description of such circuits was found. Without such an analysis, it is impossible to draw any conclusions on a practical design of VCO using a self-oscillating gyrator. Therefore, it is essential to develop a new set of circuit models able to analyse the behavior of the proposed oscillator. First, this thesis focuses on a small signal model, allowing one to define the oscillation criteria, the sensitivity to various circuit parameters and noise performance of the non-ideal circuit. Secondly, as the oscillator is a large signal device, the dissertation covers the important topic of non-linear effects using a new large signal model of the degenerated gyrator.

1.3 Main contributions

The mathematical description of the oscillator circuit is then concluded by a new phase noise model. All of these theoretical insights are proven through design and simulation of a practical CMOS circuit. The design procedure is presented in a clear, step by step manner and the reader can use it as a reference to the design of any negative resistance oscillator. Thanks to its simplicity, the proposed VCO circuit allows one to use it as a new, fast fully integrated OOK transmitter, being an attractive alternative to the existing solutions.

Chapter 2

Voltage controlled oscillators

2.1 Introduction

Oscillators have been known long before electronic systems were discovered. The most fundamental example can be a weight suspended from the spring as presented on Figure 2.1. When a weight is first pulled down and then released, an extended spring attempts to move it back to the equilibrium point. Because a moving mass has a momentum, it easily passes through the equilibrium point, compressing the spring. At a certain point, kinetic energy decreases to zero, spring expands again, moving the mass in the opposite direction. If this system was lossless i.e. no drag nor friction were present, once pulled, the weight would oscillate indefinitely around the system equilibrium point. In reality, oscillations decay due to energy dissipation over time with the speed depending on the amount of losses present in the system. If these losses were fully compensated by injecting additional energy into the system, a sustained movement of the weight would be achieved.

2.2 Electronic oscillator

The harmonic behavior of the mechanical pendulum can be translated into an electronic system. Capacitors and inductors store energy using electric and magnetic fields, re-
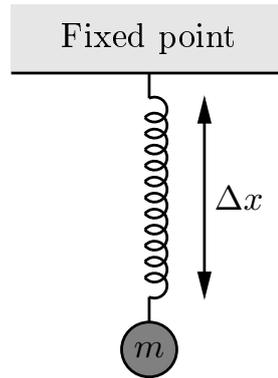
Figure 2.1: Mechanical harmonic oscillator.

spectively. Instead of a moving weight and spring, the energy moves electrons in the system, resulting in periodic changes of currents and voltages. Following the mechanical example presented earlier, energy stored in the inductor can represent a kinetic energy of the moving weight. Similarly, energy stored in the electric field by the capacitor can be considered as an analog to a mechanical energy stored by the spring. To allow energy transfer between components this electronic equivalent of a pendulum has to be a closed loop circuit, as illustrated on Figure 2.2
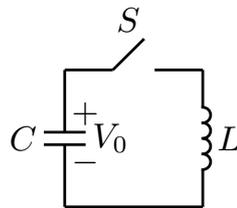
Figure 2.2: Ideal sinusoidal oscillator.

2.2.1 Ideal circuit

According to Kirchhoff's laws, for any time instant, a total voltage drop around a closed loop has to be equal zero. Also, at any given time, currents flowing through an inductor and capacitor have to be equal. Assume that C is initially charged to voltage V_o. When switch S is closed, current starts to flow from the capacitor because the inductor has to produce voltage to satisfy the voltage condition around closed loop.

At a certain stage, the inductor becomes fully charged and its voltage drop reaches zero. However the inductor current reaches its maximum now, and to fulfill Kirchhoff's second law, the same current has to flow through the capacitor as well, charging it again. Thus, the energy transfers forth and back between magnetic and electric field and periodic changes of voltages and currents are observed. Solving Kirchhoff's laws in the time domain reveals that these periodic variations have a sinusoidal character. If the voltage around the loop is calculated, the oscillator is described by a second order, ordinary differential equation related to instantaneous charge $q(t)$ transported between components. Since the initial conditions are: $q(0) = V_0 \cdot C$ and $q'(0) = 0$, equation

$$L\frac{\delta i_l(t)}{\delta t^2} + v_c(t) = \frac{\delta^2 q(t)}{\delta t} + \frac{q(t)}{LC} = 0 \qquad (2.1)$$

has a particular solution of

$$q(t) = V_0 C \cos\left(\frac{t}{\sqrt{LC}}\right) \qquad (2.2)$$

and capacitor voltage is equal to

$$v_c(t) = \frac{q(t)}{C} = V_0 \cos(\omega_0 t) \qquad (2.3)$$

where $\omega_0 = 1/\sqrt{LC}$ is known as *resonant frequency* because circuit responds only for that particular rate of change of current. For this reason, presented architecture is known as *resonator* or *resonant tank*, after it's ability to store energy.

2.2.2 Non-ideal circuit

The circuit from Figure 2.2, although simple, is not practical. The energy stored in the resonator can't be taken out without disturbing the stable operation of the oscillator. Also, real reactive components are lossy and a portion of energy is dissipated as a heat in each cycle. Thus, even if nothing else is connected to the tank, oscillations cease over time, exactly as in the case of the mechanical spring pendulum suspended in air.

Figure 2.3 depicts a modified circuit, where all of the resonator losses are represented by a single resistor R. Therefore, (2.1) changes to

$$L\frac{\delta i_l(t)}{\delta t} + v_R(t) + v_c(t) = \frac{\delta^2 q(t)}{\delta t^2} + \frac{\delta q(t)}{\delta t}\frac{R}{L} + \frac{q(t)}{LC} = 0 \qquad (2.4)$$
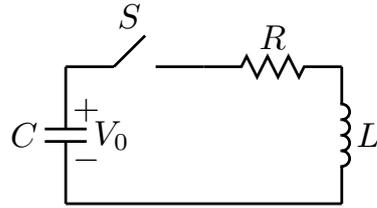
Figure 2.3: Lossy resonator.

Assuming that R dissipates only a small fraction of energy in each cycle, and initial conditions are the same as before, the capacitor voltage $v_c(t)$ is now given

$$v_c(t) = V_0 \cdot e^{-\frac{R}{2L}t} \cdot \cos\left(\sqrt{\omega_0^2 - \left(\frac{R}{2L}\right)^2} \cdot t\right) \qquad (2.5)$$

which shows that the amplitude of the oscillations decays exponentially with time and a speed proportional to R. The losses can't be removed physically from the circuit, instead each time when energy is dissipated, the same amount must be supplied from additional external circuitry. As a result, the oscillator reaches its energetic equilibrium and behaves as if $R = 0$.

Depending on the type of the output signal sampled from the oscillator (either current or voltage), series and parallel resonator configurations can be found, Figure 2.4. Resistors R_s and R_p represent circuit losses and load effects caused by external circuits connected to the resonators. At resonance, both reactances cancel each other, making $Z_{ser}(j\omega)$ and $Y_{par}(j\omega)$ real valued functions. From circuit analysis perspective it is
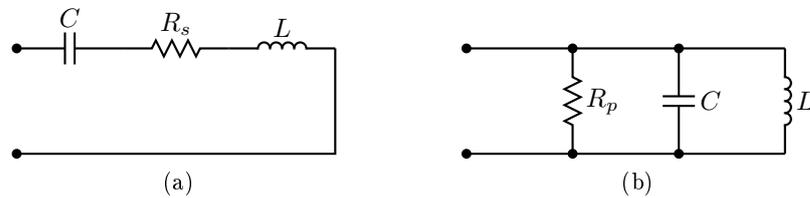
Figure 2.4: LC resonators: (a) series and (b) parallel configuration.

more convenient to describe series resonator using total impedance $Z_{ser}(j\omega)$, whereas equivalent admittance $Y_{par}(j\omega)$ is more suitable for a parallel tank. Both functions are

given by

$$Z_{ser}(j\omega) = R_s + j\omega \left(L - \frac{1}{\omega^2 C} \right) \tag{2.6}$$

$$Y_{par}(j\omega) = \frac{1}{R_p} + j\omega \left(C - \frac{1}{\omega^2 L} \right) \tag{2.7}$$

2.3 Oscillator design methodologies

To start and sustain oscillations, electrical energy has to be supplied to the resonator from a DC source. From this perspective, DC power is transformed into an AC signal in a similar fashion as in amplifiers. The main difference is that the oscillator is autonomous, and apart of bias, does not require any additional excitation to produce an output signal. The way that energy is supplied to the circuit is determined by the resonator architecture. In general, integrated resonators can be considered either a two port or one port network, leading to a corresponding methodologies of oscillator design: *feedback* and *negative resistance* methods. In the feedback approach, the oscillator has a form of a closed loop circuit consisting of two port networks. Therefore, feedback theory can be used directly to analyse its behavior. On the other hand, the negative resistance method employs the concept of a one port, energy restoring circuit that imposes one port description of the resonator.

2.3.1 Feedback oscillator

Figure 2.5 presents a generic model of a feedback system consisting of a two port networks. The gain of the direct and feedback paths is given by $A(j\omega)$ and $\beta(j\omega)$ respectively and the transfer function is given by

$$\frac{Y_{out}(j\omega)}{X_{in}(j\omega)} = \frac{A(j\omega)}{1 - \beta(j\omega)A(j\omega)} \tag{2.8}$$

When the input signal $X_{in}(j\omega)$ is disconnected from the system, a non-zero output $Y(j\omega)$ is obtained only if $1 - \beta(j\omega)A(j\omega) = 0$ which corresponds to

$$|\beta(j\omega)A(j\omega)| = 1 \tag{2.9}$$

Figure 2.5: Feedback oscillatory system.

that is the system has unity open loop gain $(\beta(j\omega)A(j\omega))$, and

$$\angle\beta(j\omega) + \angle A(j\omega) = 2k\pi \quad \text{for} \quad k = 0, 1, 2, \ldots \quad (2.10)$$

the total phase shift of open loop equals zero (or multiple of 2π). Conditions (2.9) and (2.10) are known respectively as *Barkhausen's amplitude and phase criteria*. For a given frequency, such defined feedback system may oscillate, however does not always have to. The assumption that both criteria automatically specify boundary of stability of the circuit is a common mistake and some additional requirements are necessary to transform a potentially unstable system into an electronic oscillator [1]. Lesurf [2] proves, that in the feedback system from Figure 2.5 oscillations can build up at a certain frequency if:

- Phase condition is fulfilled. Signal at the input of $A(j\omega)$ is in phase with the output signal (ideal positive feedback).

- Amplitude condition is $|\beta(j\omega)A(j\omega)| \geq 1$. For open loop gain larger than 1, amplitude of oscillations increases exponentially with each cycle.

- Circuit is initially excited by a fluctuation at the same frequency.

This leads to a generic feedback oscillator architecture from Figure 2.6. First two requirements described above are achieved using amplifier, that controls an open loop gain, and phase shift network to establish a positive feedback. Signal fluctuations originate either from a power supply transients or thermal noise sources of amplifier. These are a relatively short perturbations that occupy a wide frequency spectrum and provide
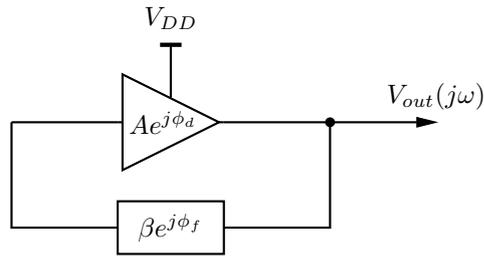
Figure 2.6: Feedback oscillator using amplifier and phase shifter.
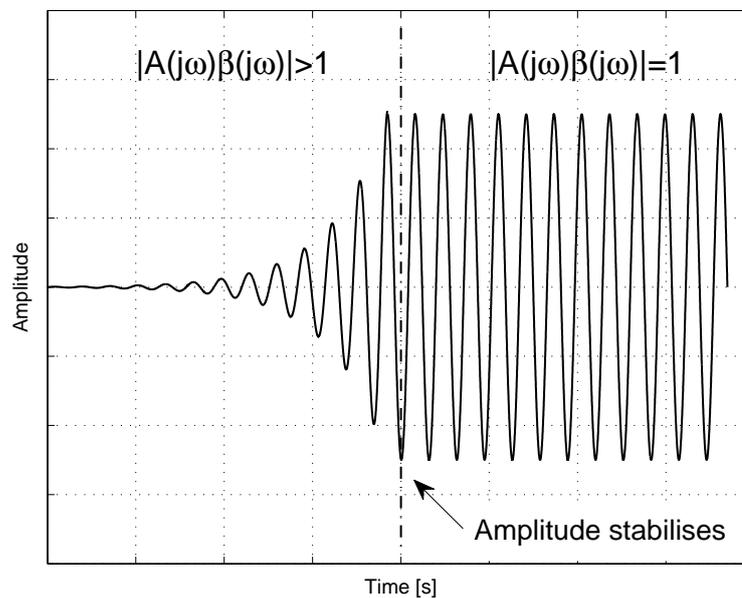
Figure 2.7: Signal build-up in feedback oscillator.

an initial energy at the wanted frequency. Figure 2.7 illustrates how a small fluctuation, injected to the described system, grows over time. The dashed line represents the moment when the amplitude stabilises i.e. when the open loop gain reaches unity. This is possible because increasing signal amplitude, drives the amplifier into saturation region, reducing apparent gain. The oscillator reaches steady state when all losses are compensated by a periodic energy injections from the active circuit. Note that the Barkhausen criteria can't predict the amplitude of oscillations as they are derived under linear, small signal conditions.

Figure 2.8 illustrates a practical example of an integrated feedback oscillator, named the *Colpitts oscillator* after its inventor E. H. Colpitts [3]. In the presented configuration, an inverting NMOS transconductance amplifier is used. A π-network LC resonator provides the 180° phase shift necessary to complete a positive feedback loop.
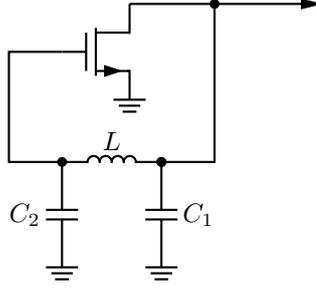
Figure 2.8: Colpitts oscillator (bias not shown).

2.3.2 Negative resistance oscillator

In some oscillators feedback loop can't be clearly identified (for example resonators made of distributed components). In this approach, an oscillator can be represented as a circuit consisting only of one port components, rather than a feedback loop system presented before. Figure 2.9 illustrates equivalent oscillator circuits designed using the one port approach.
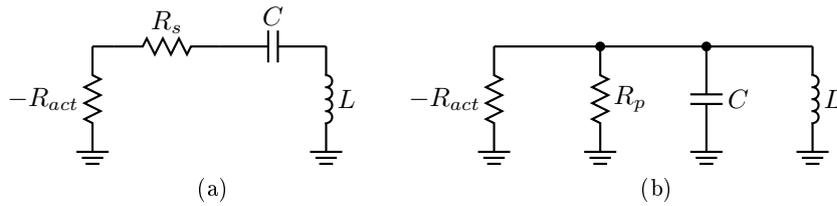
Figure 2.9: Negative resistance oscillator using: (a) series and (b) parallel LC resonator.

In both cases, lossy resonators are connected to an additional component characterised by a negative resistance $-R_{act}$. The total resistance of each resonator is equal to

$$R_{totS} = R_s - R_{act} = \left.\right|_{R_{act} \equiv R_s} = 0 \qquad (2.11)$$
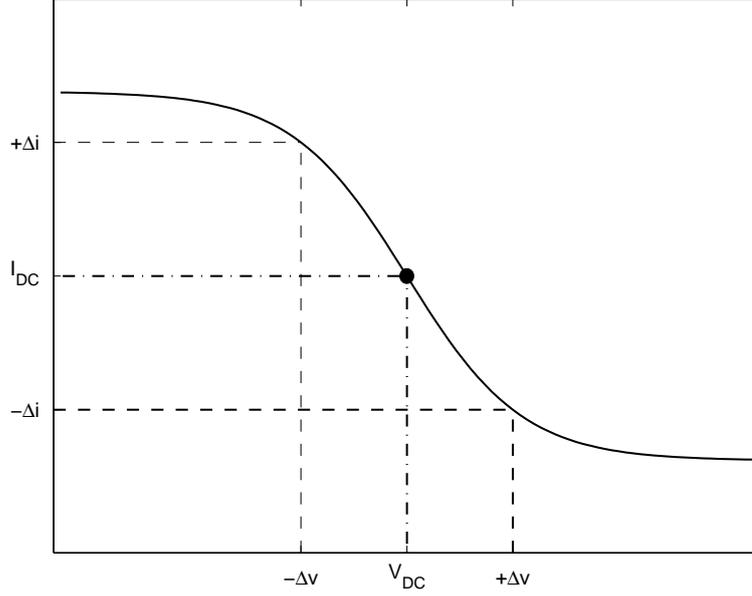
Figure 2.10: I-V curve of component experiencing negative dynamic resistance.

$$R_{totP} = \frac{-R_p R_{act}}{R_p - R_{act}} = \left.\vphantom{\frac{1}{1}}\right|_{R_{act} \equiv R_p} = \infty \qquad (2.12)$$

Just enough magnitude of $-R_{act}$ and the resonator starts to behave as an ideal circuit from Figure 2.2.

There are no passive CMOS negative resistors available. In general, such component violates Ohm's law because, to produce $-R_{act}$, a current changes have to be inversely proportional to voltage variations. For this reason, it is not possible to construct this device using passive resistors only. Also, the power dissipation $P_{act} = -R_{act} I_{act}^2$ is negative, which implies that the negative resistor supplies energy to the resonator instead of dissipating it. Figure 2.10 presents a generic I-V curve of such component. To understand how negative resistance is obtained in practice, it is important to understand the difference between static and dynamic circuit parameters. If the device is biased as shown, its static resistance is positive because $R_{stat} = V_{DC}/I_{DC}$ fulfills Ohm's law. However, if AC voltage with the amplitude of Δv is applied, it moves the bias point forth and back along the curve, causing corresponding variations of the current. As the

slope around the static bias point is negative i.e.

$$\frac{\partial i}{\partial v} < 0; \quad \frac{\partial v}{\partial i} < 0 \tag{2.13}$$

the changes of current are inversely proportional to the driving voltage. Thus, in the presence of an AC signal the device behaves as a dynamic negative resistor, even though its static resistance is always positive. Historically, the best known example of a component showing negative dynamic resistance is a Gunn diode [4]. It consists of three layers of N-type semiconductor, and when biased properly, the conductance through the device drops with increasing voltage amplitude. Another example is the Eski diode widely known as a tunnel diode that uses quantum effects of semiconductor materials to transport low energy particles through high energy gaps. As a result, a dynamic negative resistance is observed. Both devices are extensively used in microwave oscillators at high-GHz frequencies, and despite limited research on CMOS implementations [5, 6], they are not available in a standard commercial processes as yet.

Negative resistance can also be obtained using amplifiers and passive components. To achieve it, a circuit has to introduce a 180° phase shift between voltage and current of the same port. This requirement can be satisfied if inductors and capacitors (each introducing own phase shift of 90°), are combined with at least one controlled voltage or current source [7]. As an example, consider a generic circuit presented on Figure 2.11a. Using KVL, the small signal input impedance of the circuit is equal to

$$Z_{in}(j\omega) = \frac{v_{out}}{i_{in}} = gmZ_1Z_2e^{j(\phi_1+\phi_2)} + Z_1e^{j\phi_1} + Z_2e^{j\phi_2} \tag{2.14}$$
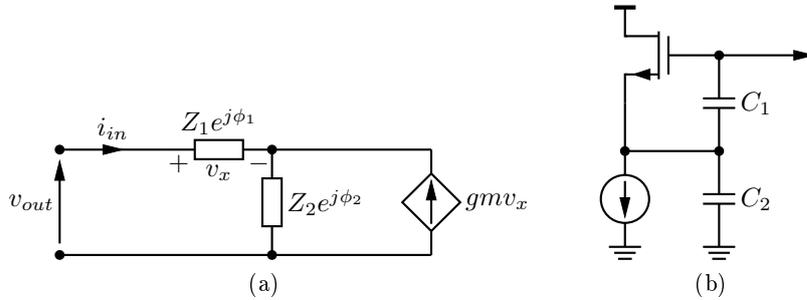
Figure 2.11: One port negative resistor: (a) concept, (b) practical implementation.

The last two terms represent parasitics that have to be included in a resonator circuit. If both impedances Z_1 and Z_2 are of the same type and imaginary, then the first term from (2.14) becomes real with phase shift of $\phi_1 + \phi_2 = \pm 180°$ because

$$gmZ_1Z_2e^{j\pm\pi} = gmZ_1Z_2\left(\cos\pm\pi + j\sin\pm\pi\right) = -gmZ_1Z_2 \tag{2.15}$$

Figure 2.11b depicts a single ended CMOS implementation of negative resistance, where common drain amplifier serves as a voltage controlled current source with capacitive Z_1 and Z_2.
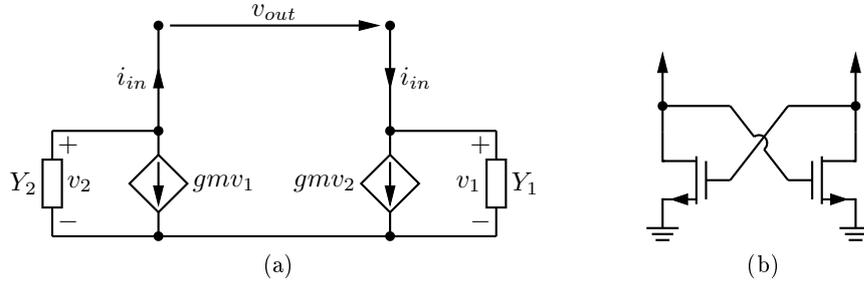
Figure 2.12: Differential negative resistor: (a) concept, (b) practical implementation.

Negative resistor can also be obtained without the use of dedicated reactive components. Figure 2.12a presents a differential circuit composed of two voltage controlled current sources. Admittances Y_1 and Y_2 produce the required control voltages and can be resistive. If both admittances Y and sources are the same, input admittance is equal to

$$Y_{in}(j\omega) = \frac{i_{in}}{v_{out}} = \frac{-gm}{2} + \frac{Y}{2} \tag{2.16}$$

In practice, this circuit is obtained using the well known MOS cross-coupled pair, depicted in Figure 2.12b. Admittances Y_1 and Y_2 equal to $g_{ds} + j\omega C_{gs}$ represent transistor parasitics, and typically have capacitive character at RF frequencies.

Figure 2.13 illustrates a typical implementation of a differential NMOS oscillator using a cross-coupled negative resistor and connected to an LC tank. The main advantages of this circuit include: a natural ability to generate output voltages shifted by 180° at each output, ease of integration and good noise performance. For this rea-
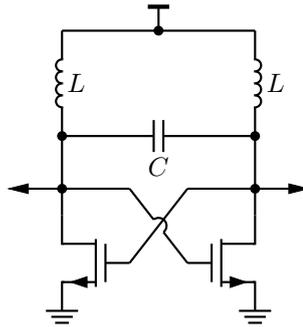
Figure 2.13: Differential NMOS integrated oscillator.

son, cross-coupled oscillators have been the focus of extensive research over the past decade [8–20].

Even though a negative resistance oscillator is not described using Barkhausen criteria directly, the circuit behavior has to be the same as in the case of feedback approach. These criteria can be transformed into a negative resistance domain, analysing either a total impedance Z_{tot} or admittance Y_{tot} of a complete oscillator circuit. A system starts to oscillate when an open loop gain of feedback circuit is greater than one. This translates to the situation where magnitude of a negative resistance is larger than all losses of the resonator. In this case, more power is supplied to the resonator than dissipated. Due to the non-linearity of an amplifier, increasing circuit amplitude reduces the amount of negative resistance generated in the circuit. At a certain signal level $-R_{act} \equiv R_{loss}$ and oscillations reach stable amplitude. The resonant frequency of the circuit is a frequency for which a total reactance of the resonator becomes zero. Therefore, the Barkhausen criteria for negative resistance oscillators translate to

$$\Re\{Z_{tot}, Y_{tot}\} \leq 0 : \text{ amplitude condition} \tag{2.17}$$

$$\Im\{Z_{tot}, Y_{tot}\} = 0 : \text{ phase condition} \tag{2.18}$$

To start oscillations, an initial signal fluctuation at the resonant frequency is required, as in the case of a feedback circuit.

2.4 Voltage controlled oscillators

As shown previously, regardless which design methodology is used, the resonant frequency of the oscillator is always controlled by the Barkhausen phase criterion. If reactances of the oscillator can be varied, the frequency of oscillation will change accordingly. As a result, a single oscillator is now able to deliver signals at variable frequencies in a controllable fashion.

Historically, to obtain frequency tuning, mechanical variable capacitors were used but due to the size it is impossible to integrate them on a chip. The exemption from this are MEMS (micro electro-mechanical systems) resonators, consisting of nano-scale, three dimensional structures. MEMS resonators are tuned by a mechanical displacement of one or more parts of the structure using electrical field. Integration of these devices in standard CMOS requires additional post processing and their size is still typically larger than those of passive inductors and capacitors. More details on MEMS applications in oscillators, can be found in recent publications [21–24].

The most common method of tuning integrated oscillators employs varactors - semiconductor devices whose capacitance is voltage dependent. An example is a reverse-biased P-N junction, where the width of the depletion region varies with reverse voltage [25]. The depletion region can be considered as an insulator controlling the effective capacitance of the junction, and thus resonant frequency is tuned electronically. The main advantage of varactors is good on-chip scale of integration. The downsides include non-linear behavior limiting the dynamic range of resonators.

The use of voltage tuned reactances leads to a concept of *voltage controlled oscillator* (VCO) architecture. In CMOS technology, two subtypes of VCOs are commonly used: LC and ring oscillators.

2.4.1 LC oscillator

An LC VCO consists of amplifier and resonator with varactors, inductors and capacitors. A more detailed description of a resonator structure can be found in Section 2.5

in this chapter. Examples of LC VCO include Colpitts architecture from Figure 2.8 and cross-coupled oscillator from Figure 2.13 presented previously. During the design stage a LC resonator has to be characterised such that its parasitic components (stray capacitances, conductor resistivity, inductance of wires etc.) are known. This ensures that the Barkhausen criteria are defined correctly for a given resonant frequency.

In most cases, an LC VCO integrated in CMOS can be designed either by feedback or negative resistance methods. For example, Razavi [26] shows that Colpitts oscillator normally designed using feedback theory may be also successfully derived using the one port approach, depending on convenience and resonator configuration. The example of this duality is illustrated on Figure 2.14. It can be seen that the negative resistor is obtained through a capacitive feedback loop of MOS amplifier.
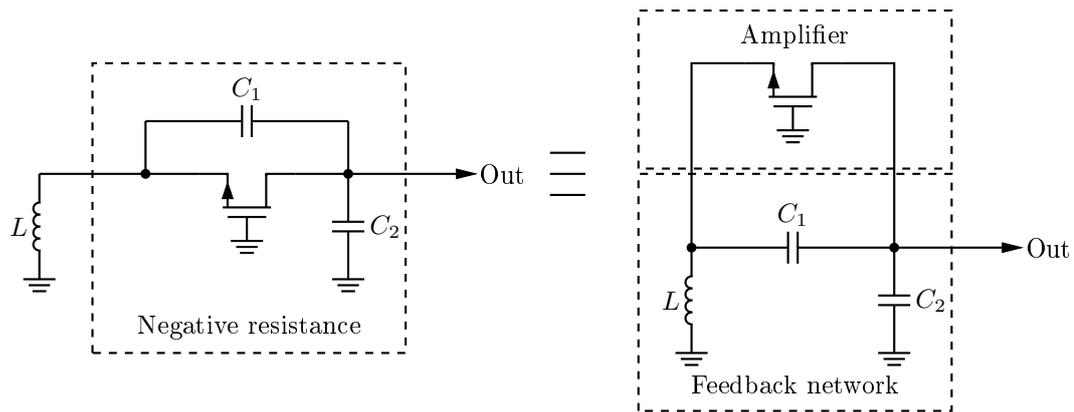
Figure 2.14: One port and feedback representations of Colpitts oscillator.

LC voltage controlled oscillators are widely used in RF circuits due to a good noise performance, low harmonic distortion and wide tuning ranges. These types of VCO are also covered in this dissertation.

2.4.2 Ring oscillator

The feedback oscillator model does not explicitly require an LC network for proper operation. Any two port network able to provide a positive feedback can satisfy the Barkhausen conditions. Therefore, a combination of capacitive and resistive circuits

can be used instead of an LC tank. As the phase relationship between input current and output voltage of any RC circuit changes with frequency between $0 \leq \phi_{RC} \leq \pi/2$, the required phase difference can be designed by proper choice of R and C. Due to a lack of inductance, the circuits from this group are known as *resonatorless* oscillators.

The ring VCO is an example of a resonatorless oscillator. It consists of a cascade of amplifiers where the output signal is fed back to the first stage. Figure 2.15 depicts an example of a ring oscillator using five inverters. Each stage shifts a signal from the previous block by 180° and also delays it due to its own RC parasitics. The circuit oscillates at a frequency for which the combined phase shift equals an integer multiple of 2π. Ring oscillators operate in switching fashion generating square wave signals.
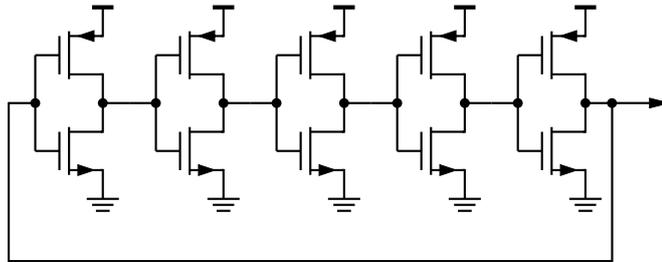
Figure 2.15: Five stage CMOS ring oscillator

The simplest form of ring VCO tuning is known as the *current starving* technique where each amplifier is biased through a separate current mirror [27]. When the amplifier is on, its bias current charges parasitic capacitances of the stage. The larger the current, the faster the charging and reduced propagation delay. This in turn changes the phase shift of the stage and signal frequency changes. The reference current for the mirrors is usually supplied through a transconductor, allowing voltage control over the frequency.

Despite high signal distortion and noise, these oscillators are used in many high speed digital circuits due to an ease of integration, small chip area, high oscillation frequencies and wide tuning ranges.

2.4.3 Parameters of voltage controlled oscillators

The performance of any voltage controlled oscillators is typically described by the following (set of) parameters.

2.4.3.1 Oscillation frequency and tuning range

Oscillation frequency and tuning range of VCO are determined by the assigned frequency spectrum a circuit operates in. The most challenging VCO designs require high frequencies and wide tuning ranges available from a single oscillator. To compare tuning capabilities of various designs, *fractional bandwidth* (FBW) can be used. It is expressed as a percentage of tuning range to a frequency in the centre of the bandwidth. Typically, wideband oscillators have relative tuning ranges of at least 20% - 25% (whereas narrowband structures have usually FBW of 5% or less), however there is no defined limit between narrow and wideband VCOs.

2.4.3.2 Tuning constant

This parameter defines the tuning sensitivity of an oscillator and is commonly denoted as K_{VCO}. It represents a magnitude of oscillation frequency changes due to control voltage. Typical values of K_{VCO} for RF circuits are in the range of tens to hundreds of MHz/V. The tuning constant is derived by calculating a slope of a tuning curves where the negative value indicates an inverse proportionality between frequency and control voltage. Small values of K_{VCO} reduces AM-PM noise conversion because the oscillator sensitivity to noise from the control path decreases. On the other hand, large tuning constant allows one to obtain wide tuning ranges for a limited control voltage, valuable in sub-micron technologies.

2.4.3.3 Output power

This represents amount of AC power that can be delivered to the load. Typically, integrated circuits are low-voltage and hence available powers are in the range up to

1 mW (0 dBm). In order to prevent excessive energy losses in the resonator, the oscillator signal is transmitted to the load using buffer amplifiers with large input impedance. The design of the buffer becomes crucial in the case of wideband VCOs since the oscillator signal power varies with frequency as a result of complex parasitic structure of the circuit.

2.4.3.4   Harmonic distortion

The quality of the output signal is also important from a frequency conversion perspective. Although differential architectures typically minimise even harmonics, total harmonic distortion of the output signal should be kept as small as possible. Typically harmonic suppression should be more than 15 dB for high performance harmonic oscillators.

2.4.3.5   Supply pushing

This is a measure how much a resonant frequency changes due to variations of DC supply. As parasitics of active devices depend also on bias conditions, changes in the bias voltage may cause shifts of oscillation frequency. This is especially important if the VCO is in close proximity to power stages that can feed energy through supply connections [28].

2.4.3.6   Load pulling

Any reactive load at the oscillator output contributes to total impedance of a tank, pulling resonant frequency down. The buffer amplifier primarily used to deliver the oscillator signal to the load also minimises the described effect. Due to a high input impedance (that has to be characterised during design of oscillator circuit), the buffer provides an effective isolation between the load and the resonator. Load pulling is also observed in a presence of extracted layout parasitics.

2.4.3.7 Power consumption

This is a crucial parameter for a low-power designs as battery operated devices, as oscillators convert DC power into AC signal. The less power consumed for given performance, the more efficient the oscillator.

2.5 Passive resonators for LC voltage controlled oscillators

This section describes the most common CMOS implementations of LC resonant tanks, with special emphasis on a wideband operation.

2.5.1 MIS varactor

In modern CMOS processes MIS (metal-insulator-semiconductor) devices are used. Figure 2.16 presents a cross-section of a varactor, built in N-well in the same was as PMOS transistor but without the drain and source implants. Capacitance is tuned by fixing the voltage on one lead and varying the voltage on the other lead. The maximum capacitance of the device depends on W to L ratio of the device and is increased by increasing number of gates (effective size) and $N+$ implants.
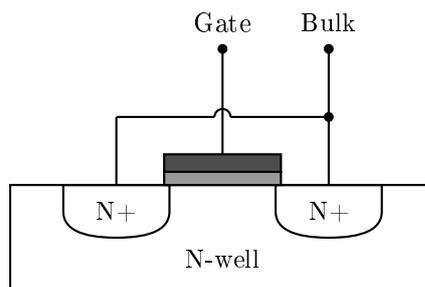
Figure 2.16: MIS varactor structure.

Figure 2.17 shows an example of the C-V curve for a MIS varactor in a 180 nm process, together with a resonant frequency of tank utilising this device. Plots illustrate a typical tuning performance of integrated varactor with a maximum to minimum ca-

pacitance ratio in the range of 3. The typical value of capacitance per area of unbiased MIS varactor in the presented 180 nm process is approximately 3 fF/µm^2.
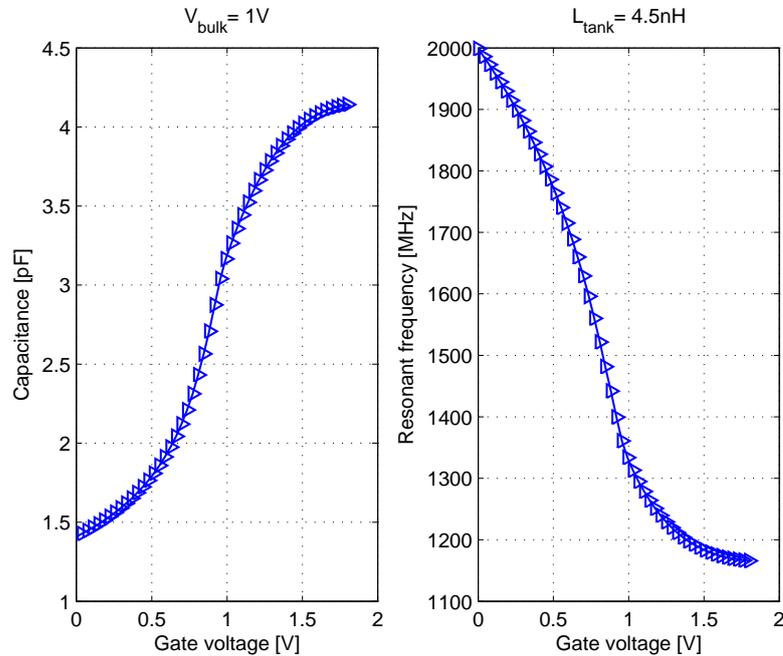
Figure 2.17: C-V curve of gate voltage tuned MIS varactor and resulting oscillator tuning curve.

Using a single varactor to tune the oscillator introduces some negative effects. To cover a wide band of frequencies, a single varactor requires a high C_{max}/C_{min} ratio. This makes a circuit vulnerable to noise present in the tuning path, because K_{VCO} is high and noise translates into parasitic FM modulation. This phenomenon is known as AM-PM noise conversion and can be minimised if the capacitance ratio of varactor is left low. As the ratio can't be freely chosen, the most common solution is back-to-back connection of two varactors that also improves the harmonic distortion over that of a single device [29–31].

2.5.2 Switched capacitor array

The low capacitance ratio used to minimise AM-PM conversion of noise decreases the tuning range. This trade-off can be relaxed if a *switched capacitance array* (SCA) from

Figure 2.18 is implemented. The array consists of a parallel connection of fixed capacitors and MOS transistors acting as switches. In each consecutive line the capacitance and transistor width are doubled to keep constant time delay through the branch.
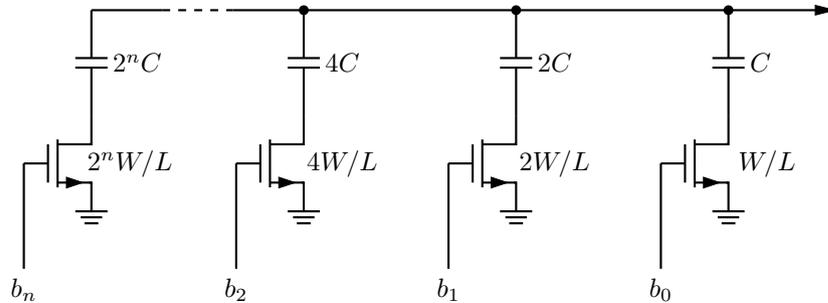
Figure 2.18: Binary switched capacitor array.

When the SCA is connected to the varactor, the total capacitance of the resonator is now also controlled by array switching. As a result, low capacitance ratio varactors can be used to tune small frequency variations (fine tuning) around a frequency determined by the array (coarse tuning) as illustrated on Figure 2.19. The tuning range is increased with more linear response and improved noise conversion. The disadvantages are larger chip area (due to a number of capacitors and switching transistors) and additional digital circuitry to control the switching.

2.5.3   MIM capacitor

Metal-insulator-metal capacitors provide fixed capacitance to the resonator. These devices are built using an additional conductive layer (known as MMC, metal-metal-capacitor) between existing metal layers of a chip. The capacitance is proportional to the area of the MMC, and may be increased by multiple connection of smaller devices (multi rectangle capacitor). In modern sub-micron CMOS processes, a typical capacitance per area values between 1 fF/µm^2 and 2 fF/µm^2 can be achieved.
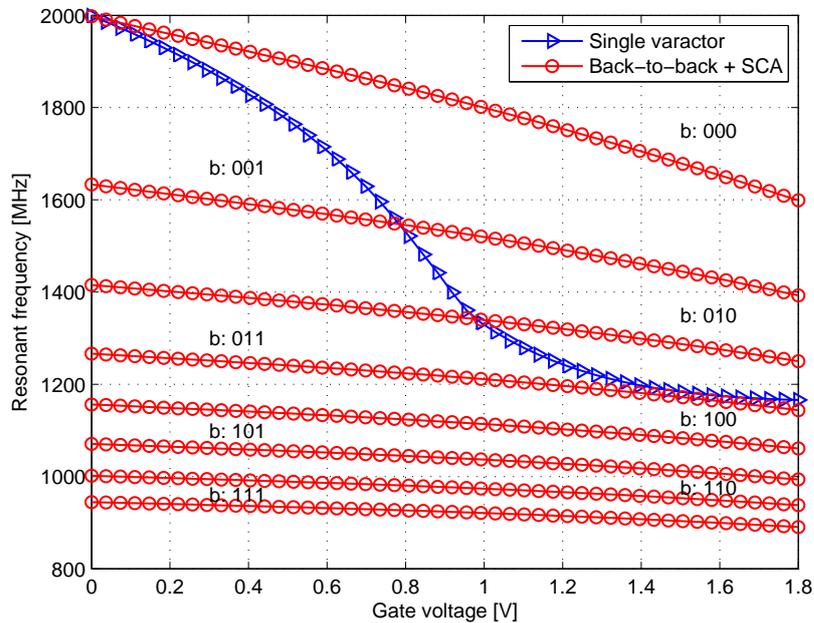
Figure 2.19: Tuning range improvement with SCA and low capacitance ratio varactor. Symbol *b* represents a 3-bit word controlling SCA switches.

2.5.4 Inductors

Monolithic inductors are typically designed on the top metal layer in the form of a spiral. Figures 2.20a and 2.20b show a top view of two most popular architectures, however hexagonal, octagonal and square shapes are also widely used [32]. The inductance value is proportional to the physical dimensions of the spiral i.e. conductor width, diameter and number of turns. Typically, CMOS inductors occupy the largest chip area among other passive components and extensive research has been conducted to find various ways of miniaturisation [32–36]. As an example, consider the inductor available in UMC 180 nm process with 5.5 turns and maximum inductance of 14 nH. The complete inductor (including diffusion dummy around it) occupies an area of at least 400 µm per 400 µm. The problem of inductor size becomes more pronounced for lower resonant frequencies where large capacitors have to be also used and therefore increasing total area of a LC tank.

In addition, integrated inductors suffer from following parasitics [32]:

- Series resistance: The conductor is relatively long and narrow, and therefore the finite conductivity of metal contributes to the resistive losses. At higher frequencies, the skin effect decreases effective cross-section experienced by a passing current, increasing total resistance.

- Inductor to ground plane capacitance: A relatively small distance between the inductor coil and the ground plane (approximately 10 µm for modern sub-micron processes) results in parasitic capacitance which reduces the maximum operational frequency of the inductor.

- There is at least one crossover through the lower metal layer providing connection to one of the inputs, causing capacitive coupling and lowers effective inductance.

- As the inductor is suspended over a conductive ground plane, magnetic fields from the spiral induces eddy currents in this metal layer. According to Lenz's law

(a)   (b)

(c)
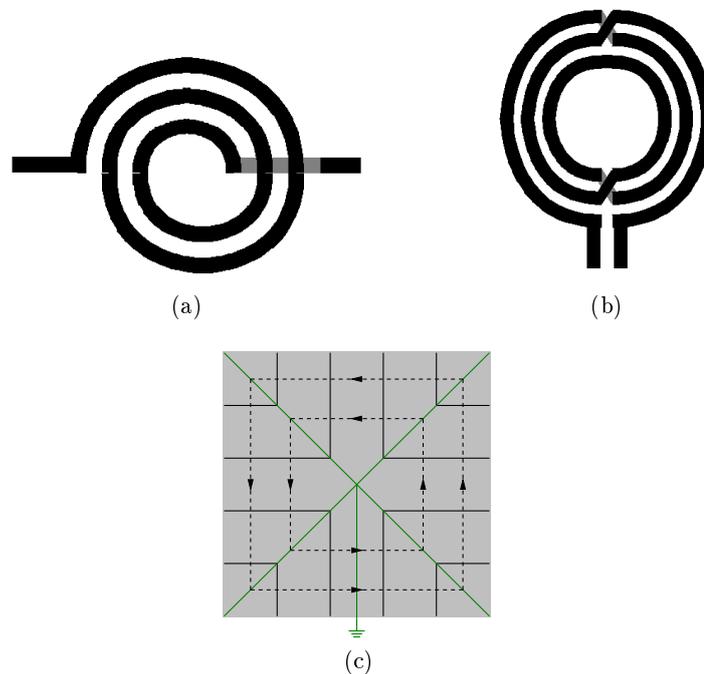
Figure 2.20: Monolithic spiral inductors: (a) single ended and (b) differential. Illustration (c) presents a patterned ground shield to minimise parasitic induction in substrate [33]. The copper layer (light gray) is connected to ground (green) and is grooved (black) to brake the flow of induced eddy currents (dashed arrows).

these currents create a magnetic field opposing one form the spiral, decreasing effective inductance. This may be minimised if instead of solid, a patterned ground shield (PGS) is used, effectively breaking induced current flow, as presented on Figure 2.20c [33].

The aforementioned negative effects of integrated inductors manifest itself in a form of increased circuit losses. As a result, integrated oscillator performance is always inferior to the one built of a discrete off-chip components [28].

Another type of integrated inductor in a form of bondwires can be found [34–36]. This is a relatively long, low resistance wire, suspended in a large distance from conductive planes and hence minimise parasitic coupling. Due to the large wire diameter, conductivity is also improved resulting in small resistive losses. The cost however is low reliability and a relatively poor process tolerance.

There is no direct way of tuning passive inductance value using electrical signals. Few circuits attempting electronic control over passive inductors were published [10, 37, 38]. In these methods, spiral inductor is connected in series with a transistor controlling amount of current passing through it. As a result, the tank experiences variable inductance, however the transistor contributes significantly to the resonator losses and injects noise directly to the tank.

2.5.5   Quality factor of resonator

The performance of resonator can be characterised by *quality factor Q*, a unitless function indicating how much energy is dissipated in each cycle in relation to the amount of energy stored in a resonator [39]. In general, quality factor can be described using different definitions. The common misconception is to consider all definitions the same, but different assumptions were made in each case thus these are not always compatible. The simplest form of Q is given by

$$Q = 2\pi \frac{\text{Energy stored in resonator}}{\text{Energy dissipated in one cycle}} \tag{2.19}$$

Q gives an immediate information how lossy a system is and hence how much energy has to be used to compensate it. If the circuit is not able to store the energy, the quality factor is zero. Also, if energy dissipated in each cycle is much greater than the stored one, Q is much less than 1. On the other hand if only small portion of energy is dissipated, quality factor is relatively large (as a rule of thumb one can assume a good value of Q at least in the range > 20). Finally, if there is no dissipation, Q becomes infinite for lossless circuits. This parameter can be applied any resonant structures including non-ideal inductors and capacitors.

2.5.5.1 Peak energy definition

This is suitable to systems working at frequencies much less than the resonant frequency and is defined as

$$Q = \frac{\left|\Im\{Z_{ser}(j\omega)\}\right|}{\Re\{Z_{ser}(j\omega)\}} = \frac{\left|\Im\{Y_{par}(j\omega)\}\right|}{\Re\{Y_{par}(j\omega)\}} \tag{2.20}$$

In this formula, a difference between peak magnetic and electrical energies is considered [33]. For example, consider the case of a non-ideal inductor, where magnetic energy is lost not only through a resistive dissipation but also due to a parasitic capacitive coupling. Thus, effective energy stored in inductor decreases with frequency. Similarly, in the case of capacitor, electrical energy is decreased due to parasitic inductances. For this reason, (2.20) applies only to inductors or capacitors far from self-resonance frequency. The same applies to LC resonator. At resonance, total impedance or admittance of a resonator becomes zero, and according to (2.20), corresponding Q factor should be zero as well. In this case no energy would be stored during resonance which is a wrong assumption. During resonance, energy constantly changes between magnetic and electric fields, and its total amount in each consecutive oscillation cycle is affected by resistive dissipation taking place in the circuit(providing reactive components are still far from self-resonance).

2.5.5.2 Average energy definition

Yue and Wong [33] show that at resonance quality factor of a tank depends on sum of average magnetic and electric energy stored in the tank. Also, at certain instants of a single oscillation cycle, one of the reactive components stores maximum energy. Thus quality factor is given by

$$
\begin{aligned}
Q &= 2\pi \frac{\text{Average magnetic energy} + \text{average electric energy}}{\text{Energy dissipated in one cycle}} = \\
&= 2\pi \frac{\text{Peak magnetic energy}}{\text{Energy dissipated in one cycle}} = \\
&= 2\pi \frac{\text{Peak electric energy}}{\text{Energy dissipated in one cycle}}
\end{aligned}
$$

$$(2.21)$$

For lossy series and parallel resonators from Figure 2.4 in Section 2.2.2 this corresponds to

$$
Q_{ser} = \frac{\omega_0 L}{R_s} = \frac{1}{\omega_0 C R_s} = \frac{\sqrt{L/C}}{R_s} \quad : \text{series RLC} \tag{2.22}
$$

$$
Q_{par} = \frac{R_p}{\omega_0 L} = \omega_0 C R_p = \frac{R_p}{\sqrt{L/C}} \quad : \text{parallel RLC} \tag{2.23}
$$

Thus, although at resonance the reactances of the tank cancel each other, the Q factor is non-zero as long as energy is stored in the circuit. Also, if there are no losses i.e. $R_s = 0$, $R_P = \infty$ the quality factor becomes infinite and resonator behaves as ideal oscillator.

2.5.5.3 Phase definition

Quality factor definition calculated from (2.22) and (2.23) assumes inductances and capacitances remain constant over frequency. This is generally true for low frequencies however is not necessarily valid at GHz frequencies. Close to the resonance quality factor can be determined measuring total impedance or admittance of the tank (it crosses through zero at resonance) and finding a derivative of phase from [7]

$$
Q = \frac{\omega_0}{2} \left. \frac{\partial \phi}{\partial \omega} \right|_{\omega = \omega_0} \tag{2.24}
$$

2.5.6 Unloaded and loaded Q

Quality factor derived for the resonator in relation to its internal losses is known as the *unloaded quality factor*, Q_0. In practice, energy is sampled from the oscillator through buffer amplifier that is modelled as additional resistive loss. As a result, the apparent Q of the resonator changes. A quality factor that includes load effects is known as *loaded quality factor*, Q_L. If resonator is not compensated by a negative resistance, Q_L is always smaller than the unloaded one. However, if all losses are compensated, the resulting loaded Q becomes infinite and a circuit oscillates. Note that even when a resonator is fully compensated, its unloaded quality factor is still finite.

2.5.7 Total Q of integrated resonator

Due to own parasitic reactances, varactors, capacitors and spiral inductors are self-resonant structures. Thus, total unloaded Q factor of integrated resonator is limited by quality factors of all components of the tank. To characterise the total unloaded Q of resonator it is important to recognise that an LC tank never represents a simple parallel or series circuit. Typically, a capacitor and inductor losses are modeled as resistors connected in series. Parasitic inductances and capacitances due to metal paths and substrate leakage are usually characterised as parallel components. These complex structures can be significantly simplified using series to parallel transformations technique [32]. The transformation is narrow band in a sense that is only valid in close vicinity to the resonant frequency of a tank.

For example, consider a simple parallel tank consisting of a lossy spiral inductor and capacitor. Components C_p, L_p and R_p represent parallel equivalents at particular resonant frequency and are given by

$$r_{lp} = r_{ls}\left(Q_l^2 + 1\right) \approx r_{ls}Q_l^2 \Big|_{Q_l \gg 1}$$
$$r_{cp} = r_{cs}\left(Q_c^2 + 1\right) \approx r_{cs}Q_c^2 \Big|_{Q_c \gg 1}$$
$$R_p = \frac{r_{lp}r_{cp}}{r_{lp} + r_{cp}} \tag{2.25}$$
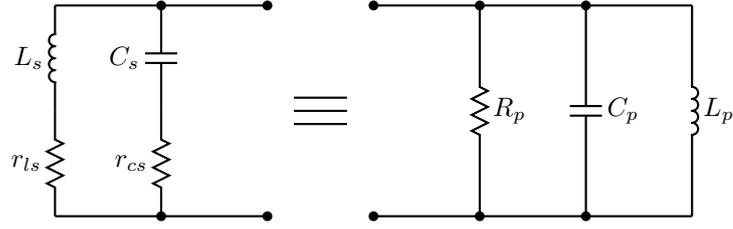
Figure 2.21: Concept of RLC transformation.

and

$$L_p = L_s \left(\frac{Q_l^2 + 1}{Q_l^2} \right) \approx L_s \Big|_{Q_l \gg 1}$$

$$C_p = C_s \left(\frac{Q_c^2}{Q_c^2 + 1} \right) \approx C_s \Big|_{Q_c \gg 1} \qquad (2.26)$$

where Q_l and Q_c are quality factors of inductor and capacitor respectively.

$$Q_l = \frac{\omega_0 L_s}{r_{ls}} = \frac{r_{lp}}{\omega_0 L_p}$$

$$Q_c = \frac{1}{\omega_0 C_s r_{cs}} = \omega_0 C_p r_{lp} \qquad (2.27)$$

Thus, although a non-ideal inductor and capacitor are used, the circuit can be transformed into a pure parallel tank to which (2.7) applies.

Using (2.25), (2.27) and (2.23), a total unloaded quality factor of the tank at resonant frequency can be found

$$Q_{0tot} = \frac{R_p}{\sqrt{L/C}} = \frac{\dfrac{r_{pl} r_{pc}}{r_{pl} + r_{pc}}}{\sqrt{L/C}} = \frac{Q_l Q_c}{Q_l + Q_c} \approx Q_l \Big|_{Q_l \ll Q_c} \qquad (2.28)$$

Lee [32] reports Q factors in the range of 10 for on-chip spiral inductors and 50 for bondwires. The quality factors of MIS varactors and MIM capacitors are substantially higher, typically more than 70. Thus, the quality factor of spiral inductor Q_l limits unloaded Q_{0tot} of the resonator to $Q_{0tot} \leq 10$ for most applications. In the case of discrete off-chip inductors, the quality factor values are much higher. For example a 3.9 nH inductor from Coilcraft (symbol CT-3N9X_LU) achieves Q in the range of 90 at 1.7 GHz [40], the value far beyond that of an integrated spiral inductor.

2.6 Oscillator phase noise

As oscillators use lossy resonators and active circuits, noise introduced by these circuits has a direct influence on oscillator performance. To understand how noise affects the oscillator assume that a output voltage of non-ideal oscillator is given by

$$v_{out}(t) = \left[V_0 + v_n(t)\right]\cos\left[\omega_0 t + \phi_n(t)\right] \approx V_0 \cos\left[\omega_0 t + \phi_n(t)\right] \qquad (2.29)$$

where $v_n(t)$ and $\phi_n(t)$ represent zero-mean noise fluctuations of amplitude and phase of the signal. Typically, amplitude perturbations can be significantly lowered because oscillator has intrinsic mechanism of keeping constant amplitude. Unfortunately phase fluctuations are not tracked by any means in free running oscillators, and hence accumulate [41]. The output described by (2.29) represents, in fact a phase modulated (PM) wave where the noise acts as a modulating signal. Perrot [42] shows that if the noise RMS is much smaller than the signal amplitude, (2.29) can be approximated with

$$v_{out}(t) \approx V_0 \cos\left(\omega_0 t\right) - V_0 \sin\left(\omega_0 t\right)\phi_n(t) \qquad (2.30)$$

where the first term corresponds to the ideal oscillator signal. The modulating noise component is bandpass limited by LC resonator (however noise floor of the system is not affected) and the power spectrum density of the output signal (2.30) is given by

$$S_{out}(\omega) = S_{ideal}(\omega) + S_{ideal}(\omega) * S_{\phi_n}(\omega) \qquad (2.31)$$

where $S_{\phi_n}(\omega)$ represents the power spectrum of phase modulating noise [42]. As an ideal signal is sinusoidal, its Fourier transform is given by a Dirac delta function at ω_0. As the signal is also convolved with noise, its spectrum contains additional side skirts at frequencies close to the carrier frequency. Thus, the output signal of a noisy oscillator occupies a certain bandwidth instead of a single frequency. The measure of phase noise is the power of side skirt within 1 Hz bandwidth around a single frequency $\omega_m \neq \omega_0$, compared to the power of carrier signal at ω_0. The phase noise is therefore a relative quantity expressed in dBc/Hz.

The main negative effects of a noisy oscillator are: spurious emission and reciprocal mixing. The first effect is experienced in RF transmitter where a signal is upconverted to the carrier frequency using noisy oscillator. As a result, some energy is radiated to the frequency band occupied by a different system. In extreme cases the spurious emission can swamp a weak signal in an adjacent channels completely, as illustrated on Figure 2.22
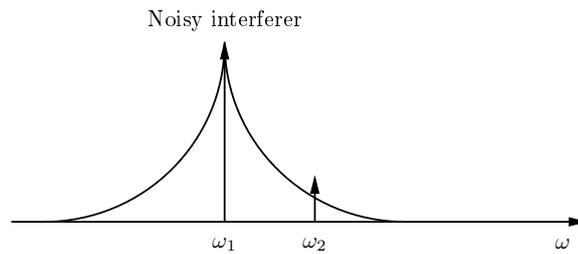
Figure 2.22: Noisy high power interferer causing spurious emission [26].

The second negative effect affects a frequency conversion in a receiver. When two signals are received, one being a large amplitude interferer close to the wanted signal, both are translated by a mixer to new frequency band. After conversion, the large interferer can superimpose upon the wanted signal and proper signal detection is no longer impossible (Figure 2.23). Thus, from a wireless system perspective it is important to keep phase noise as small as possible and to achieve this a phase noise modelling becomes one of the main aspects of RF oscillator design.

2.6.1 Typical phase noise performance

Figure 2.24 presents range of phase noise performance for various types of oscillators published by Gardner [41]. To allow fair comparison between circuits, phase noise levels were normalised to the resonant frequency of each oscillator. Among presented circuits, the lowest phase noise can be obtained using crystal resonators (XTAL) that use mechanical resonance of piezoelectric materials to stabilise oscillation frequency. Dielectric resonator oscillators (DRO) use ceramic materials also provide good noise performance. These two approaches require devices that are not available in standard
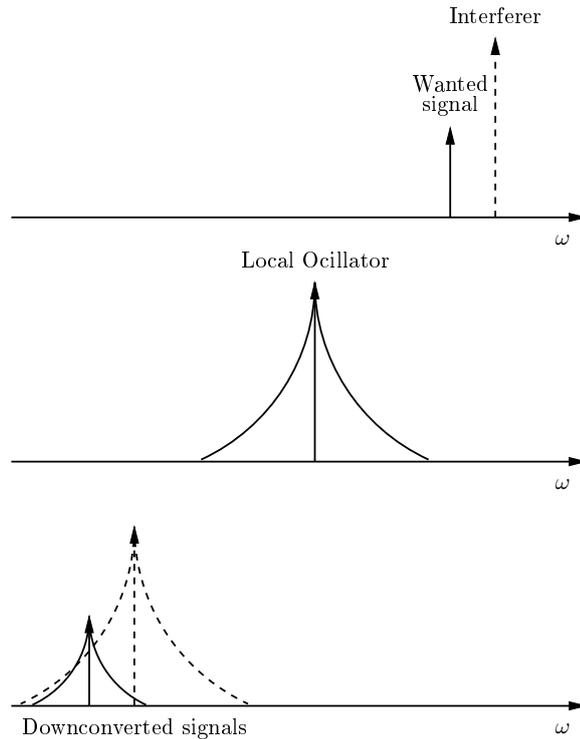
Figure 2.23: Reciprocal mixing in receiver during down-conversion [26].

CMOS process. LC oscillators generate substantially higher phase noise and are readily available in CMOS at RF frequencies up to 10-20 GHz. The cost is a significant chip area occupied by a spiral inductor. Finally, ring oscillators that largely reduce silicon area, generate highest phase noise due to the number of active devices.

Figure 2.24 also shows the apparent dependence of phase noise performance on the quality factor of resonators. Piezoelectric and DRO tanks have typically very high Q_0 in the range of 10000. The Q_0 of integrated CMOS LC tanks in the range of 10 can be found, whereas ring oscillators rely on RC phase shifters with even lower quality factor (about 1).

2.6.1.1 Noise of integrated LC resonator

As phase noise depends mostly on noise generated in an oscillator, it is important to show how noise is produced in the resonator and active circuit. Consider an example of
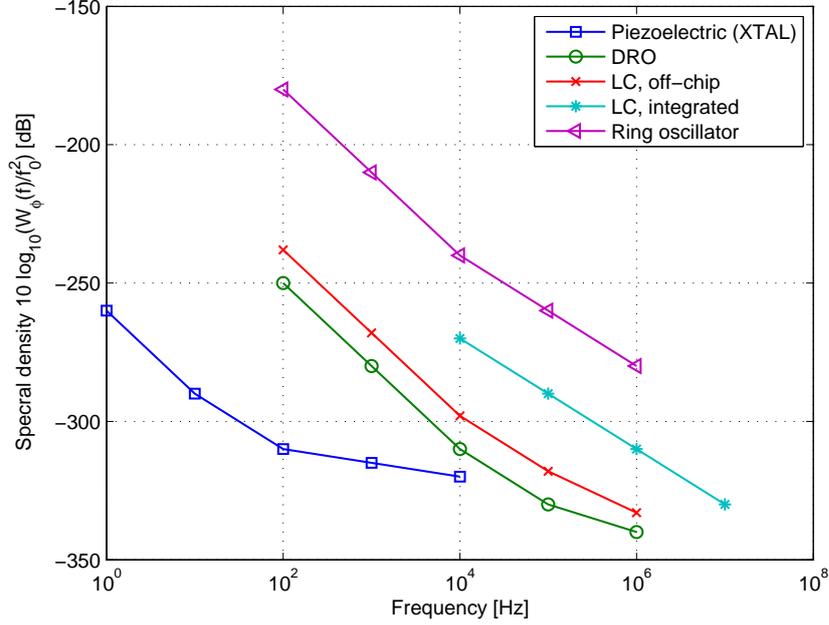
Figure 2.24: Comparison of typical phase noise performance of various oscillators [41].

a lossy parallel resonator from Figure 2.21. If the tank is unloaded and high-Q capacitor is used, the only noise source present in the circuit is a thermal noise originating from an inductor because its resistive losses dominate. Thus, even if no external signal is applied to the circuit, the resonator generates output voltage by itself. Thus, a single thermal noise generator of an equivalent tank resistance R_p is sufficient enough to describe the noise behavior of the parallel resonator. As noise of any resistor is represented by the power spectrum density (PSD) function, in the case of R_p equal to

$$\frac{\overline{i_{nR_p}^2}}{\Delta f} = \frac{4kT}{R_p} \approx \frac{4kT}{r_{sl}Q_0^2} \tag{2.32}$$

where k is a Boltzmann's constant and T is a temperature in Kelvins [26]. Output noise PSD is shaped in accordance to the resonator noise transfer function that is found from the equivalent model depicted on Figure 2.25.

The noise transfer function is equal to

$$Z_n\left(j\omega\right) = \frac{j\omega L_p R_p}{j\omega L_p + R_p\left(1 - \omega^2 C_p L_p\right)} \tag{2.33}$$
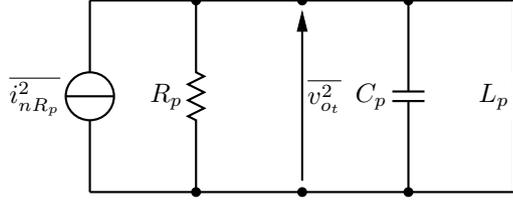
Figure 2.25: Noise model of passive parallel resonator.

and the output noise PSD can be found

$$\frac{\overline{v_{o_t}^2}}{\Delta f} = \frac{\overline{i_{nR_p}^2}}{\Delta f} \left| Z_n(j\omega) \right|^2 = \frac{4kTR_p\omega^2 L_p^2}{\omega^2 L_p^2 + R_p^2 \left(1 - \omega^2 C_p L_p\right)^2} = \left. 4kTR_p \right|_{\omega=\omega_0} \qquad (2.34)$$

Equation (2.34) allows one to calculate a spot noise at any frequency of interest and indicates that white noise injected into the parallel LC resonator is in fact band-pass filtered. To describe the resonator noise in more depth, it is also important to calculate the total noise power over a given frequency band. The total noise power for any circuit where noise sources are uncorrelated is found from

$$\overline{v_{ntot}^2}, \overline{i_{ntot}^2} = \frac{1}{2\pi} \sum_{k=1}^{N} \left(\frac{\overline{v_k^2}}{\Delta f}, \frac{\overline{i_k^2}}{\Delta f} \right) \int_0^\infty \left| T_{nk}(j\omega) \right|^2 \, d\omega \qquad (2.35)$$

where $\overline{v_{ntot}^2}$, $\overline{i_{ntot}^2}$ are either a voltage or current referred total output noise power; $\overline{v_k^2}$, $\overline{i_k^2}$ are uncorrelated noise voltage or current generators, and $T_{nk}(j\omega)$ is a noise transfer function corresponding to each source.

In the case of passive resonator, the total output noise is equal to

$$\frac{\overline{i_{nR_p}^2}}{\Delta \omega} = \frac{1}{2\pi} \frac{\overline{i_{nR_p}^2}}{\Delta f}$$

$$\overline{v_{o_t}^2} = \frac{\overline{i_{nR_p}^2}}{\Delta \omega} \int_0^\infty \left| Z_n(j\omega) \right|^2 \, d\omega = \frac{4kT}{2\pi R_p} \frac{\pi}{2} \frac{R_p}{C_p} = \frac{kT}{C_p} \qquad (2.36)$$

The results are illustrated on Figure 2.26 using an example of a 434 MHz integrated resonator. The output noise voltage spectrum density of has been modeled for two different unloaded Q_0 values, 100 and 30 respectively. Third curve represents the noise of the resonator where capacitance has been doubled. It can be seen that for a fixed
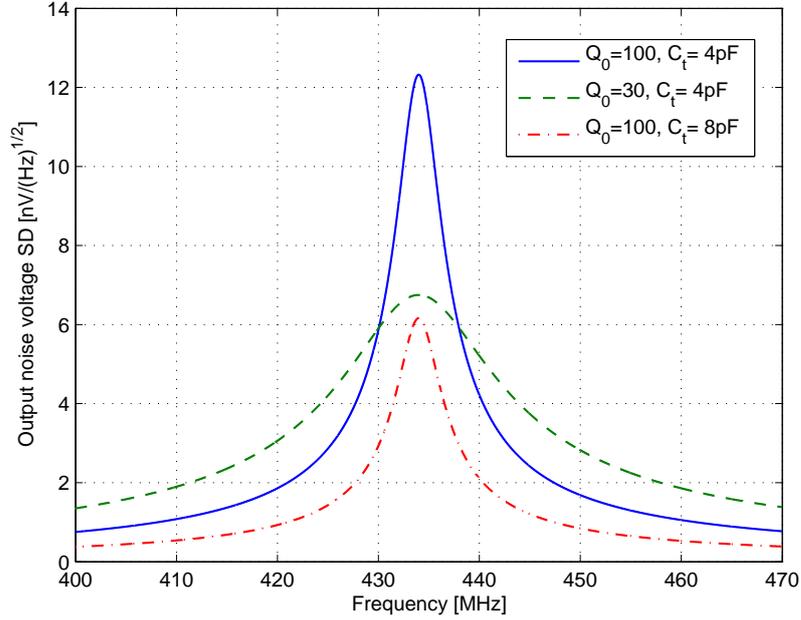
Figure 2.26: Noise spectral density of parallel passive resonator.

capacitance, the spot noise at resonance increases proportionally to Q_0 and depends only on R_p, as indicated by (2.33). In accordance with (2.36), the area under the first two curves is independent of Q_0 hence the total RMS output noise is constant with changing R_p. In the third case (dash-dot curve), for a fixed quality factor, an increasing C_p causes both the spot noise (due to adjusted R_p value to keep Q_0 constant) and the total RMS output noise to be reduced.

2.6.1.2 Noise of negative resistors

The noise delivered by the negative resistor is proportional to the amount of energy necessary to compensate circuit losses, however its magnitude mostly depends on a converter architecture. It has been proved that for certain configurations, a negative resistor noise can be lower than of a passive resistor with the same absolute resistance value [7].

Figure 2.27 depicts the equivalent noise model of a single MOS capacitively degenerated negative resistor from Section 2.3.2. To simplify the analysis it is assumed that
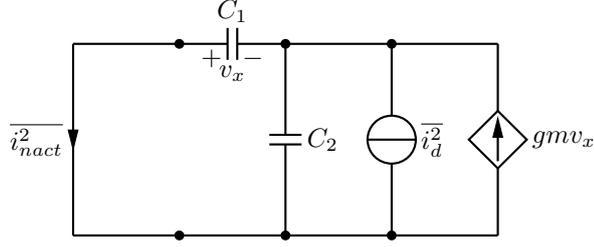
Figure 2.27: Equivalent noise model of capacitively degenerated negative resistor.

the single transistor is characterised by thermal noise only given by [43, 44]

$$\frac{\overline{i_d^2}}{\Delta f} = 4kT\gamma gm \tag{2.37}$$

where γ is a process dependent constant and its typical values reported in literature vary between 2 to 5 for a short channel MOS transistors [44]. Thus the short circuit current noise PSD of single ended negative resistor from Figure 2.27 is equal to

$$\frac{\overline{i_{nact}^2}}{\Delta f} = \frac{\overline{i_d^2}}{\Delta f}\frac{\omega^2 C_1^2}{\omega^2\left(C_1 + C_2\right)^2 + gm^2} = 4kT\gamma\frac{C_1}{C_2}\left|\frac{1}{R_{act}}\right| \tag{2.38}$$

where R_{act} is a parallel equivalent of negative resistor equal to

$$R_{act} = -\frac{gm^2 + \omega^2(C_1 + C_2)^2}{\omega^2 C_1 C_2 gm} \tag{2.39}$$

Equation (2.38) reveals that the noise current injected to the resonator may be reduced if $C_2 > C_1$ [7, 32]. If the presented single MOS converter is used in oscillator, the actual capacitance ratio used can't usually be made arbitrarily small. Typical ratios suggested by Lee [32] vary between 3:1 and 4:1, yielding the least phase noise level as a result of the optimal oscillation amplitude in proportion to a resonator noise level. These properties makes a single MOS negative resistor a practical solution for a high frequency oscillators, especially when Q_0 factor of a resonator is high and thus a relatively small DC power consumption of the circuit.

Noise PSD of a cross-coupled negative resistor from Section 2.3.2 is derived using method presented by Hajimiri [45] (Figure 2.28).
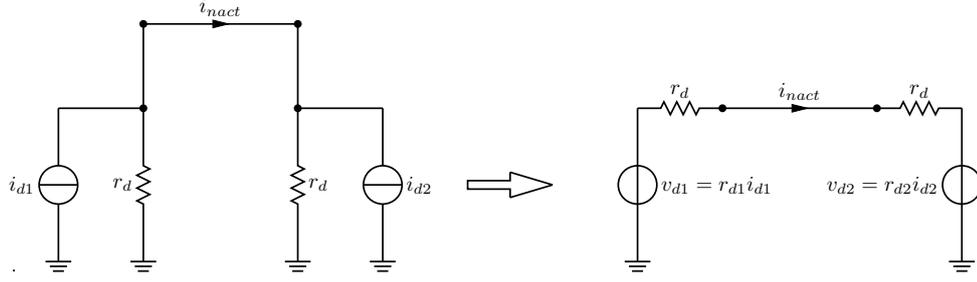
Figure 2.28: Calculation of equivalent short circuit noise current in cross-coupled MOS negative resistor.

Using KVL, an equivalent short circuit noise current is found

$$i_{nact} = \frac{v_{d1} + v_{d2}}{2r_d} = \frac{i_{d1} + i_{d2}}{2}$$

$$\frac{\overline{i_{nact}^2}}{\Delta f} = \frac{\frac{\overline{i_{d1}^2}}{\Delta f} + \frac{\overline{i_{d2}^2}}{\Delta f}}{4} = 2kT\gamma gm = 4kT\gamma \left| \frac{1}{R_{act_{diff}}} \right| \tag{2.40}$$

Assuming that r_d is much greater than the total differential resonator input resistance, it can be neglected in further analysis. By shortening the differential input, any correlation between transistors is cancelled and, as (2.40) indicates that a cross-coupled negative resistor achieves noise properties comparable to its single ended counterpart.

2.6.1.3 Q requirements for low noise of passive LC resonators

The above derivations show, that for a low phase noise design, a high Q_0 passive resonator is necessary. Firstly, a high quality factor minimises spot noise generated by resonator, decreasing its relative power at frequencies $\omega_m \neq \omega_0$. Also, high Q corresponds to a small losses and hence less amount negative resistance is required for resonator compensation. According to (2.38) and (2.40) this minimises noise originating from active circuits and can lead to improved phase noise performance.

2.7 Chapter summary

In this chapter the basic voltage controlled oscillator theory has been presented. It is shown that LC resonators produce oscillations, however to sustain them an active

device is required to compensate for dissipated energy. The magnitude of dissipation is controlled by resonator quality factor that also determines noise performance of the oscillator. It was shown that to improve noise generated in LC oscillator, Q in integrated resonators has to be maximised. Even if the low Q factor of spiral inductors can be enough to deliver acceptable phase noise levels, the cost of silicon area consumed is disproportionally large in comparison with other oscillator components. This problem becomes more pronounced at lower RF frequencies where inductances in the range of tens of nH can be required, forcing a circuit designer to choose off-chip (discrete) inductors.

Historically, the concept of *active inductor* became a possible alternative to passive inductors. In this approach, an inductance is simulated using transistors and capacitors only. Thus, LC resonator can be integrated on much smaller area than in the case of a spiral inductors. The next chapter deals with fundamentals of VCO design using active inductors with special emphasis on circuit noise, large signal behavior and tuning range.

Chapter 3

Active inductor oscillators

3.1 Introduction

This chapter delivers a comprehensive review of published active inductor circuits and its application to voltage controlled oscillators. First, a basic circuit description is presented, providing useful design insights for further VCO design. The most important parameters of active inductors then are considered to allow a fair comparison to the passive LC tank approach from Chapter 2. To achieve this a corresponding linear analysis of small signal models is conducted.

A step by step analysis of noise, reveals the main noise generation mechanisms in active inductor oscillator. The study of noise confirms why active inductor circuits can not be assumed equivalents of their passive counterparts - a common misconception propagated through the literature. The noise analysis presented in this chapter extends previously published results of Abidi [46] and Kaunisto [7] by considering total noise of active inductor resonator compensated with negative resistor. In addition, a phase noise model of an active inductor VCO is presented [47], showing expected phase noise performance of gyrator-based oscillators.

Finally, a parasitic effect taking place in active inductors at high frequencies is discussed. The results of this study lead to the main concept of self-oscillating active inductor resonator presented in this dissertation.

3.2   Active inductors

When passive inductors are biased with a sinusoidal current, the resulting voltage phase is shifted by 90°. This behavior is conveyed by impedance and admittance functions, that characterise electronic circuits in the frequency domain. If one is able to design a circuit using non-inductive components connected such that the resulting impedance preserves the described 90° phase shift, the circuit simulates the behavior of the inductor. This section shows that transistors and capacitors are sufficient to design such a circuit, allowing a significant reduction of silicon area due to the compact size of these devices.

3.2.1   Gyrator fundamentals

The phase relationship between the voltage and current of a capacitor is inverse of that of an inductor. For this reason, the circuit simulating inductance by means of capacitors has to invert a capacitive impedance to provide the required phase relationship. This inversion is obtained using a two port network known as a *gyrator*, presented by Tellegen [48]. A gyrator consists of two voltage controlled current sources (VCCS) connected as illustrated on Figure 3.1.
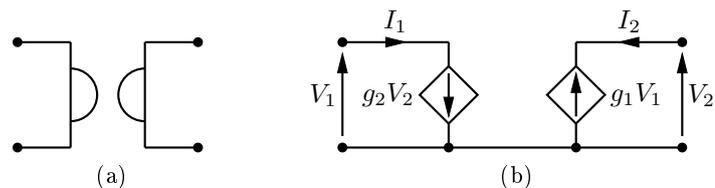
Figure 3.1: Gyrator: (a) symbol, (b) schematic.

The first observation is that Tellegen's circuit violates the network reciprocity rule. According to the theorem, when an electromagnetic force E is connected in one branch of a reciprocal network it produces current I in another branch. If E is moved from the first to the second branch, it will cause the same current in the original branch, where E has been replaced by a short circuit [49]. If the circuit from Figure 3.1b was reciprocal

the currents on both outputs would be the same, which corresponds to the impossible requirement of $g_2 \equiv -g_1$ for non-zero g_1 and g_2.

The most convenient method of gyrator description has a form of an admittance matrix given by

$$[I] = [Y][V]$$

$$\begin{bmatrix} I_1 \\ I_2 \end{bmatrix} = \begin{bmatrix} y_{11} & y_{12} \\ y_{21} & y_{22} \end{bmatrix} \cdot \begin{bmatrix} V_1 \\ V_2 \end{bmatrix} = \begin{bmatrix} 0 & g_2 \\ -g_1 & 0 \end{bmatrix} \cdot \begin{bmatrix} V_1 \\ V_2 \end{bmatrix} \tag{3.1}$$

where g_1 and g_2 are real and known as *gyration conductances* [50]. If one of the ports is loaded by generic admittance $Y_{load}(j\omega)$ such that $I_2 = Y_{load}(j\omega) \cdot V_2$ then the input admittance $Y_{in}(j\omega)$ and impedance $Z_{in}(j\omega)$ of the gyrator are equal to

$$Y_{in}(j\omega) = \frac{I_1}{V_1} = y_{11} - \frac{y_{12}y_{21}}{Y_{load}(j\omega) + y_{22}} = \frac{g_1 g_2}{Y_{load}(j\omega)} \tag{3.2}$$

and

$$Z_{in}(j\omega) = \frac{1}{Y_{in}(j\omega)} = \frac{Y_{load}(j\omega)}{g_1 g_2} \tag{3.3}$$

Active inductors are in fact a particular case of a more general gyrator concept. If a gyrator is loaded using a capacitor then the generic $Y_{load}(j\omega)$ becomes $j\omega C$ and the input impedance according to (3.3) is now equal to

$$Z_{in}(j\omega) = j\omega \frac{C}{g_1 g_2} \equiv j\omega L \tag{3.4}$$

Equation (3.4) proves mathematically that a gyrator can mimic an inductive impedance using a single capacitor and two voltage controlled current sources. From a design perspective both VCCS are always implemented using transconductance amplifiers and require a DC bias to operate. Thus, in contrary to the passive approach from Chapter 2, any resonator consisting of active inductance dissipates power.

3.2.2 Types of active inductors

In general, various types of active inductors can be distinguished:

- Single ended or differential: Single ended circuits have only one port where inductive impedance is experienced. These circuits have typically simple architectures. Differential active inductors use differential transconductors for improved rejection of common mode signals, however require twice the number of components as single ended implementations.

- Grounded or floating: Grounded inductors have one lead connected either to ground or VDD [51] i.e. simulate parallel inductance. Floating active inductors have two ports with inductive impedance in series between them and are suitable for applications requiring series inductance.

- Single or multistage transconductance amplifiers: Single stage amplifiers use one transistor to provide gyration conductance. Multistage amplifiers provide larger gains and can minimise some of parasitic effects. The cost is larger power consumption and required number of components.

In practice, combinations of the above are used. Typically, a single ended architecture leads to a grounded inductor circuit, whereas the differential arrangement is more suitable for a floating gyrator. In all cases, multistage amplifiers can be employed if necessary. Figure 3.2 depicts some examples of grounded inductors that over the years served as a base for further improvements reported in numerous papers [52–54]. In all cases one of the ports is always loaded by capacitance (some authors use transistor parasitics only), whereas the opposite port produces inductive impedance. It is important to indicate that practical circuits are seldom symmetrical and for this reason one of the ports is usually preferred as an input. The grounded gyrators from Figure 3.2a and 3.2b represent the simplest architectures: single ended using single stage transconductors. The advantages are straightforward design and smallest number of devices used. The cost of simplicity is relatively large circuit losses due to transistor parasitics. The third gyrator from Figure 3.2c uses a two stage amplifier to increase input impedance of the active inductor. In comparison with the former architectures, an extra transistor introduces additional noise and non-linearity to the circuit.
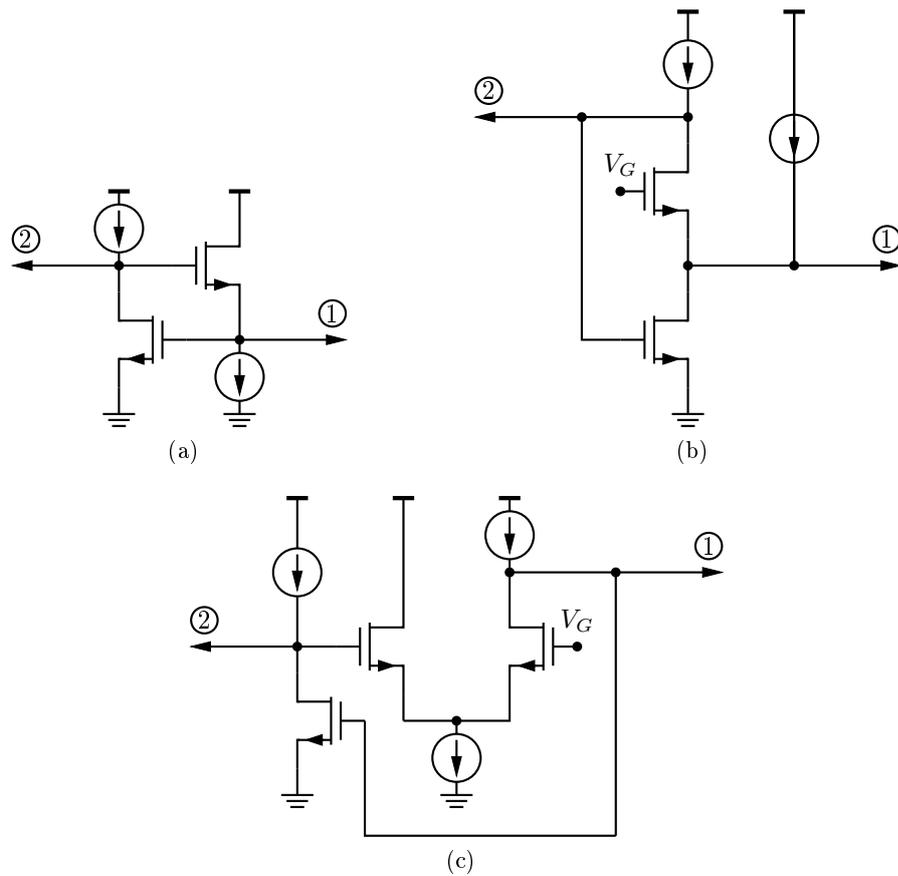
Figure 3.2: Most common CMOS grounded gyrator implementations: (a) common source - common drain [52], (b) common source - common gate [53], (c) common source - two stage amplifier [54].

3.2.3 Active inductor applications

Over the years various circuits using gyrators in place of passive inductors were designed. The typical applications include: RF filters, low noise amplifiers, power splitters, phase shifters and oscillators, to name a few. Table 3.1 presents some of the recently published integrated circuits using CMOS active inductors.

Table 3.1: State of the art of active inductor circuits [51].

Reference	Year	Node	Application	Frequency*
Thanachayanont [55]	2000	0.8µm	LC VCO	0.45-1.2 GHz
Lin [56]	2000	0.35µm	LC VCO	1.1-2.1 GHz
Sackinger [57]	2000	0.25µm	Limiting amp.	3 GHz
Wu et al. [53]	2001	0.35µm	LC VCO	0.1-0.9 GHz
Grozing et al. [58]	2001	0.30µm	LC VCO	0.4-4 GHz
Wu et al. [59, 60]	2001	0.35µm	RF bandpass	0.4-1.1 GHz
Thanachayanont [61]	2002	0.35µm	RF bandpass	2.4-2.6 GHz
Xiao [62]	2002	0.18µm	RF lowpass	4.57 GHz
Xiao et al. [54]	2004	0.18µm	RF bandpass	3.5-5.7 GHz
Lu et al. [63]	2005	0.18µm	RF power divider	4.5 GHz
Liang et al. [64]	2005	0.18µm	RF bandpass	3.45-3.6 GHz
Gao et al. [65–67]	2005	0.25µm	RF bandpass	2.05-2.45 GHz
Chen et al. [68]	2005	0.35µm	Limiting amp.	2.3 GHz
Lu et al. [69]	2005	0.18µm	RF phase shifter	360°
Mahmoudi [70]	2005	0.18µm	QVCO	8 GHz
Jiang et al. [71]	2005	0.18µm	Gbps Tx.	10 Gbps
Yuan [72, 72]	2006	0.18µm	Ring VCO	1.7-2.7 GHz
Lu et al. [73]	2006	0.18µm	LC VCO	0.5-3.0 GHz
Xiao et al. [74]	2007	0.18µm	RF bandpass	3.34-5.72 GHz
Weng [75]	2007	0.18µm	RF bandpass	2-2.9 GHz
Tang et al. [76]	2007	0.18µm	RF modulators	1.6 GHz
Tang et al. [77]	2007	0.18µm	VCOs	1.6 GHz

∗ - For bandpass filters, the frequency range is the center frequency range,
for VCOs, the frequency range is the oscillation frequency range,
for limiting amplifiers, the frequency is the bandwidth of the amplifiers.

3.3 Basic operation, noise properties and dynamic range of active inductors

As mentioned, in the simplest case, an active inductor is obtained using two single stage transconductance amplifiers connected back to back and loaded by a capacitor, as illustrated on Figure 3.3a. A closer examination of (3.1) reveals that for proper operation, one VCCS has always a form of an inverting amplifier. At this stage it is assumed that both transconductors are ideal i.e. have an infinite input impedance and ideal current sources at the output. In this case the value of the simulated inductance

(a)

(b)

(c)

Figure 3.3: Generic model of active inductor:(a) ideal circuit, (b) lossy circuit, (c) equivalent model of lossy circuit

calculated from (3.4) is given by

$$L_{sim} = \frac{C_g}{gm_1 gm_2} \tag{3.5}$$

The chief advantage of an active inductance over a passive counterpart is its inherent tuning ability through a bias dependent amplifier transconductance gm. Therefore, by varying the quiescent point of the transconductors, the resonant frequency of a resonator can be changed and no varactors are required for oscillator tuning. Due to non-idealities of the transconductance amplifiers integrated gyrators are always lossy. First, amplifiers

have finite input and output impedances, effectively changing a capacitive load into an RC network. Secondly, transconductors contain complex parasitic networks, that cause additional performance degradation at higher frequencies. These are described in more detail at the end of this chapter.

To analyse in detail how circuit parasitics influence the behavior of gyrators, one can consider a generic model of a lossy grounded active inductor circuit, illustrated in Figure 3.3b. Components $G_{o1,o2}$ represent total conductances at given nodes and consists of resistive losses of transconductors as well as real part of input/output admittances depending on amplifier configurations. Similarly, $C_{o1,o2}$ represent the total node capacitances due to intrinsic transistor parasitics and architecture dependent reactances like Miller capacitance, for example. As a result, the gyrator circuit no longer simulates ideal inductance, but a more complex resonant structure. Note that transconductance $gm_{1,2}$ is considered real. The input admittance is now equal to

$$Y_{in}(j\omega) = G_{o2} + j\omega C_{o2} + \frac{gm_1 gm_2}{j\omega \left(C_g + C_{o2}\right) + G_{o1}} \tag{3.6}$$

and the corresponding equivalent circuit is depicted in Figure 3.3c. As a result inductance is now simulated with series resistor proportional to the losses on the gyrator output which, together with G_{o2}, deteriorate the quality factor of the circuit. In addition, input capacitance limits a maximum frequency at which active inductor can operate before reaching self-resonance.

3.3.1   Quality factor of non-ideal active inductor

Using (2.20), the quality factor of lossy active inductor is found [51] as

$$Q = \frac{\omega L_s}{R_s} \cdot \frac{R_{po2}}{R_{po2} + R_s \left(1 + \dfrac{\omega^2 L_s^2}{R_s^2}\right)} \cdot \left(1 - \frac{R_s^2 C_p}{L_s} - \omega^2 L_s C_p\right) \tag{3.7}$$

where

$$R_{po2} = \frac{1}{G_{o2}}$$

$$C_p = C_{o2}$$

$$R_s = \frac{G_{o1}}{gm_1 gm_2}$$

$$L_s = \frac{C_g + C_{o1}}{gm_1 gm_2} \tag{3.8}$$

Far from the self-resonance frequency, the quality factor of the active inductor is primarily controlled by R_s only. Thus, to minimise losses, G_{o1} should be as small as possible. Typically, this conductance corresponds to the output conductances of the MOS transistors used in amplifiers and its value can not be decoupled from the transconductance without the use of multistage amplifiers. This problem becomes important in sub-micron devices where drain to source resistance is lower than for long channel transistors.

The quality factor from (3.7) can be used to transform the active inductor model from Figure 3.3c into a parallel equivalent. Recalling the transformation technique presented in Chapter 2 for spiral inductor tanks, and assuming a signal frequency much less than self-resonance, this leads to the following model

$$R_{pai} = \frac{1}{G_{o2}} + \frac{G_{o1}}{gm_1 gm_2}\left(1 + Q^2\right) \approx \frac{1}{G_{o2}} + \frac{G_{o1}}{gm_1 gm_2}\left[1 + \left(\frac{\omega(C_g + C_{o1})}{G_{o1}}\right)^2\right] \tag{3.9}$$

$$L_{pai} = \frac{C_g + C_{o1}}{gm_1 gm_2}\left(\frac{Q^2 + 1}{Q^2}\right) \approx \frac{C_g + C_{o1}}{gm_1 gm_2}\left[1 + \left(\frac{G_{o1}}{\omega(C_g + C_{o1})}\right)^2\right] \tag{3.10}$$

Equations (3.7), (3.9) and (3.10) prove that for a successful resonator design, the active inductor circuit requires more thorough modeling than a passive inductor. Transistors have more complex parasitic networks that in general tend to be dispersive. In addition, the presented formulas represent small signal approximations of non-linear amplifier parameters, hence they become less accurate with increasing signal amplitude. This is an essential observation for oscillator design, commonly omitted in existing literature.

3.3.2 Noise of active inductor resonators

As presented in the previous chapter, the noise properties of a resonator have direct impact on oscillator performance. For this reason, a noise analysis of active inductors is essential to establish a proper base for the solutions presented in this dissertation. To simplify calculations, it is assumed that output conductance G_{o1} is negligible and therefore has no influence on resonator noise. Even though the accuracy of such an assumption is somehow lower (as in practice G_{o1} is not negligible and contributes to noise transfer functions), it allows one to pin-point the main sources of gyrator noise.

The main misconception widely propagated in the literature is the assumption that the parallel equivalent circuit of an active inductor represents the same behavior as its passive counterpart. This is true from a small signal model point of view, however as shown in this and in following chapters, this is never the case for noise and large signal behavior. Thus all of the conclusions based on an analysis of passive resonators do not apply to active inductors. Abidi [46] was the first who reported this behavior and presented a closed form solution for total RMS noise voltage produced by an active inductor resonator. This solution has been later confirmed by Kaunisto [7] who delivers the most thorough analysis published previously.

The noise analysis presented in this chapter consists of two parts. First, the noise of an uncompensated active inductor is presented using the same methodology as Kaunisto [7], however for calculation convenience, the parallel conductance is substituted by a resistance. The second part shows a noise analysis of an active inductor resonator compensated using a negative resistor. This closed form solution, not found in previously published literature, represents a more practical noise model for an active inductor resonator.

3.3.2.1 Uncompensated active inductor resonator

Figure 3.4 depicts the equivalent noise model of an active inductor resonator. The capacitor C_T represents total tank capacitance and includes input parasitic capacitance from

52
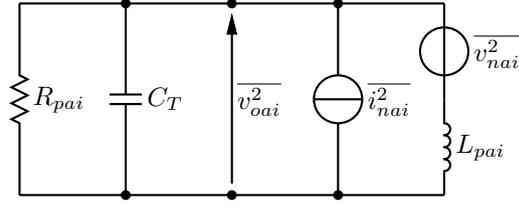
Figure 3.4: Noise model of active inductor resonator.
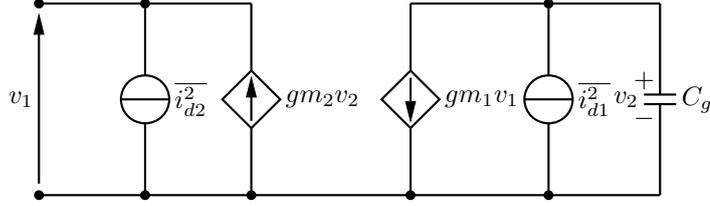
Figure 3.5: Noise sources of active inductor.

transconductors. The noise performance of this resonator is calculated using the same approach as presented in Chapter 2, Section 2.6.1.1. First, to compare performance of active and passive resonators, a noise analysis of an uncompensated and unloaded tank is performed. The circuit is characterised by an unloaded quality factor Q_0. By using a parallel tank transformation from Chapter 2, Section 2.5.7 an equivalent resistance R_{pai} is introduced in place of R_p from the passive resonator from Figure 2.25. This parallel resistor can be considered noiseless because most of the noise originates from both transconductance amplifiers (node conductances of gyrator are not dissipating power in general). As indicated in Section 3.3.1, R_{pai} depends on the circuit configuration and the transconductors used, with the effect that Q_0 can not be freely adjusted to a specified value.

In contrast to the passive tank, there are now two noise sources present, each corresponding to a single amplifier. In the most elementary case, single MOS amplifiers are used and, for a simplicity of calculations, only the thermal noise of a transistor is considered [26]. Figure 3.5 depicts this resulting equivalent noise model of a gyrator. A detailed analysis reveals that the corresponding noise sources are equal to [78]

$$\frac{\overline{i_{nai}^2}}{\Delta f} = \frac{\overline{i_{d2}^2}}{\Delta f} = 4kT\gamma gm_2 \tag{3.11}$$

53

$$\frac{\overline{v_{nai}^2}}{\Delta f} = \frac{1}{gm_1^2} \frac{\overline{i_{d1}^2}}{\Delta f} = \frac{4kT\gamma}{gm_1} \tag{3.12}$$

The solution is valid only for single MOS amplifiers. If multistage transconductors are used, the noise generators have to be derived separately.

Equations (3.11) and (3.12) indicate that the noise of both transconductors can be decreased if gm_1 and gm_2 values are maximised and minimized respectively. However for a maximum input signal amplitude, both transconductors have the same gain. This is especially crucial for a VCO design because phase noise level is inversely proportional to the signal power delivered by an oscillator. For this reason, an active inductor resonator noise can't be minimised by setting gm_2 to be much less than gm_1. A thorough circuit analysis is necessary to indicate other means for controlling tank noise.

As in the case of the passive resonator, the transfer function of a noise current generator $\overline{i_{nai}^2}$ is equal to the total impedance of the circuit and is calculated from (2.33), substituting L_{pai} in place of L_p. Using the methodology from [7, 46], the transfer function of the equivalent input noise voltage source $\overline{v_{nai}^2}$ is found from Figure 3.4

$$A_{nai}(j\omega) = \frac{R_{pai}}{j\omega L_{pai} + R_{pai}(1 - \omega^2 C_T L_{pai})} \tag{3.13}$$

Using (2.33) and (3.11)-(3.13), the output noise PSD of a gyrator-based resonator is derived as

$$\frac{\overline{v_{oai}^2}}{\Delta f} = \frac{\overline{i_{nai}^2}}{\Delta f} |Z_{nai}(j\omega)|^2 + \frac{\overline{v_{nai}^2}}{\Delta f} |A_{nai}(j\omega)|^2 =$$

$$= \frac{4kT\gamma R_{pai}^2}{\omega^2 L_{pai}^2 + R_{pai}^2(1 - \omega^2 C_T L_{pai})^2} \left(\omega^2 L_{pai}^2 \, gm_2 + \frac{1}{gm_1} \right) =$$

$$= 8\gamma Q_0^2 \frac{kT}{gm} \Bigg|_{\substack{\omega=\omega_0 \\ gm_1=gm_2=gm \\ C_T=C_g \\ Q_0=R_{pai}/\omega_0 L_{pai}}} \tag{3.14}$$

and the total output noise power of the tank is now equal to

$$\overline{v_{oai}^2} = \frac{1}{2\pi} \frac{\overline{i_{nai}^2}}{\Delta f} \int\limits_0^\infty |Z_{nai}(j\omega)|^2 \, d\omega + \frac{1}{2\pi} \frac{\overline{v_{nai}^2}}{\Delta f} \int\limits_0^\infty |A_{nai}(j\omega)|^2 \, d\omega =$$

$$= \frac{kT\gamma R_{pai}}{C_T} \left(gm_2 + \frac{1}{gm_1} \frac{C_T}{L_{pai}} \right) =$$
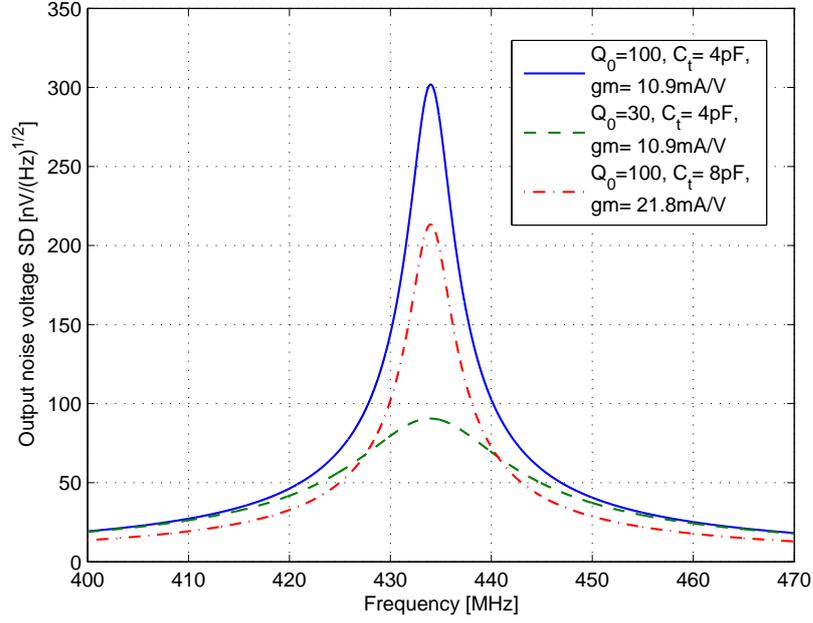
Figure 3.6: Noise voltage spectral density of active inductor resonator.

$$= \frac{kT\gamma}{C_T} R_{pai} \omega_0 C_T \left(\frac{gm_2}{\omega_0 C_T} + \frac{\omega_0 C_T}{gm_1} \right) = 2\gamma Q_0 \frac{kT}{C_T} \Bigg|_{\substack{gm_1=gm_2=gm \\ C_T=C_g \\ Q_0=\omega_0 C_T R_{pai}}} \tag{3.15}$$

Equation (3.15) indicates that not only is the total output noise power substantially larger than that of the passive tank but it is also proportional to the unloaded quality factor of the active inductor. As a result, the high Q_0 values cause a serious limitation of dynamic range and phase noise in filters and oscillators, respectively. This fact is commonly omitted in publications in this area, where active inductor resonators with high quality factors are presented without any indication of its impact on the total resonator noise. The spot noise at resonance calculated from (3.14) is inversely proportional to the transconductance of both amplifiers, proving that active inductor noise can be minimised at the cost of increased power consumption.

As in Chapter 2, Section 2.6.1.1 the noise of an example resonant tank is simulated using MATLAB. Figure 3.6 depicts output voltage noise spectral density (SD) functions of an uncompensated resonator designed for 434 MHz and three different cases. The
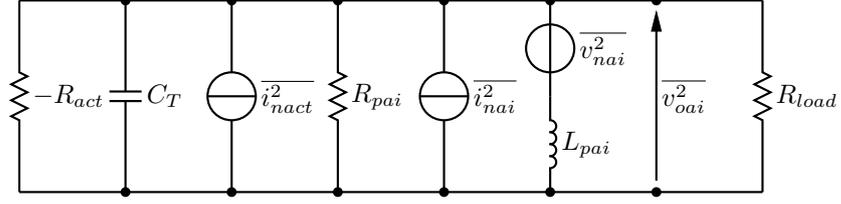
Figure 3.7: Noise model of active inductor resonator with negative resistance compensation.

first two curves represent the resonator with a quality factor equal to 100 and 30, respectively. The tank capacitance is again set to 4 pF and the gyrator is symmetrical (i.e. $gm_1 = gm_2$), with a transconductance equal to 10.9 mA/V. In the third case the capacitance value has been doubled and to keep the resonant frequency constant the transconductance has been doubled as well. As shown by (3.15), in contrast to the passive resonator, the area under each curve is now directly proportional to Q_0.

3.3.2.2 Compensated active inductor resonator

As the quality factor of an uncompensated active inductor resonator can't usually be freely adjusted, the typical approach employs a negative resistance circuit to compensate tank losses in controllable fashion. Thus, apart of the noise sources of the transconductors, the resonant tank also suffers from the noise introduced by the negative resistor. For this reason, a noise analysis of a compensated gyrator-based resonator is necessary.

Figure 3.7 depicts the equivalent noise model of a gyrator-based resonator with negative resistor. It is assumed that all of the gyrator parameters remain the same as in the case of uncompensated active tank.

A negative resistor can, to a certain extent, produce any value of parallel resistance, allowing total compensation of resonator losses, thus boosting its loaded quality factor to infinity. If the resonator is used in a filter, to prevent instability, an additional resistance R_{load} is connected, bounding effectively a value of Q_L. In the case of an oscillator tank, R_{load} represents the real part of the input impedance of the following

stage, usually a buffer amplifier. As the majority of noise in an active inductor resonator comes from the transconductors and a negative resistor, it can be assumed that R_{load} does not add a substantial amount of noise to the resonator. If the contribution of R_{load} is important, the following analysis allows for its inclusion. In this case a noise current generator representing the load resistor adds in parallel to the current noise generator of the active inductor.

To characterize the resonator behaviour in a presence of R_{load}, the loaded quality factor Q_L is used. If the same resonator is used in a sinusoidal oscillator, it is evident that the negative resistor is designed to cancel all the circuit losses, including those originating from subsequent stages, otherwise oscillations would be attenuated. This implies Q_L is infinite but for the purpose of this section, Q_L of the tank is assumed to be finite.

The noise transfer functions from Section 3.3.2.1 have to be modified accordingly as R_{load} and $-R_{act}$ are now connected to the resonator. If R_T is the total resistance of the tank, then it is equal to

$$R_T = \cfrac{1}{\cfrac{1}{R_{load}} + \cfrac{1}{R_{pai}} - \cfrac{1}{R_{act}}} = R_{load}\bigg|_{R_{act}=R_{pai}} \tag{3.16}$$

Hence, the modified transfer functions are now

$$Z_{naiQ}(j\omega) = \frac{j\omega L_{pai} R_T}{j\omega L_{pai} + R_T\left(1 - \omega^2 C_T L_{pai}\right)}$$
$$A_{naiQ}(j\omega) = \frac{R_T}{j\omega L_{pai} + R_T\left(1 - \omega^2 C_T L_{pai}\right)} \tag{3.17}$$

The result of a noise analysis of a typical Q-enhancing circuit from Chapter 2 shows that the impact of negative resistor noise can't be neglected. Yet by a proper design of negative resistor, this effect can be usually minimised. Hence, by combining results from Section 2.6.1.2 with (3.15), the proposed total output noise of a Q-enhanced resonator

is equal to

$$
\overline{v_{oaiQ}^2} = \frac{1}{2\pi} \left(\overline{\frac{i_{nai}^2}{\Delta f}} + \overline{\frac{i_{nact}^2}{\Delta f}} \right) \int\limits_0^\infty |Z_{naiQ}(j\omega)|^2 \, d\omega + \frac{1}{2\pi} \overline{\frac{v_{nai}^2}{\Delta f}} \int\limits_0^\infty |A_{naiQ}(j\omega)|^2 \, d\omega =
$$

$$
= \frac{kT\gamma R_T}{C_T} \left(gm_2 + \frac{C_{ex1}}{C_{ex2}} \left| \frac{1}{R_{act}} \right| + \frac{1}{gm_1} \frac{C_T}{L_{pai}} \right) =
$$

$$
= \frac{kT\gamma}{C_T} Q_L \left(2 + \frac{1}{gm} \frac{C_{ex1}}{C_{ex2}} \left| \frac{1}{R_{act}} \right| \right) \Bigg|_{\substack{gm_1=gm_2=gm \\ C_T=C_g \\ Q_L=\omega_0 C_T R_T}} \qquad \text{:single MOS} \quad (3.18)
$$

$$
= \frac{kT\gamma}{C_{T_{diff}}} Q_{L_{diff}} \left(2 + \frac{1}{gm \left| R_{act_{diff}} \right|} \right) \Bigg|_{\substack{gm_1=gm_2=gm \\ C_{T_{diff}}=C_{g_{diff}} \\ Q_{L_{diff}}=\omega_0 C_{T_{diff}} R_{tot_{diff}}}} \qquad \text{:differential} \quad (3.19)
$$

The total output noise is higher in relation to the uncompensated tank because the negative resistor inevitably increases the total output noise power. Equations (3.18) and (3.19) prove that in the case of active inductors with a low unloaded Q_0, this contribution can not be simply neglected (low Q_0 requires more power for compensation and therefore more noise can be injected to the resonator). Analysing (3.18) and (3.19) one may also conclude that the term describing the noise contribution of the negative resistor (i.e. containing R_{act}) is always inversely proportional to the gyrator transconductance gm and can be minimised this way. Usually however, resonator losses have a certain proportionality to gm, increasing together with it. This, in turn, causes a proportionally higher transconductance for the negative resistor required for compensation. In the case of the low Q_0 active inductor, we found the noise contribution from an impedance converter is constant with changing gm.

The presented noise analysis suggests few possible solutions to improve noise performance of gyrator-based resonators. The simplest method, efficient for both passive and active resonators is to increase the tank capacitance. However, for a constant resonance frequency, a gyrator transconductance has to increase as well, causing either a larger static power consumption or larger transconductor dimensions Abidi [46]. Another method utilises a relatively low quality factor gyrator, restricting applications to low selectivity resonators. A third method involves lowering the transconductor noise by using either long MOS devices or, if a resonator is driven by a low source impedance (up

to few kΩ), bipolar transistors may be a more practical solution [43]. This results in a trade-off between power consumption, chip area, resonator quality factor and generated noise.

3.3.3 Linearity and dynamic range

Active inductors are non-linear by definition. As a result, the input impedance of an active resonator changes with signal amplitude. Thus, an active resonator holds its designed function only until a critical signal magnitude is reached. On the other hand, increased noise decreases input signal to noise ratio and effectively limits the dynamic range of the active tank. Wang and Abidi [78] suggest that for gyrator based resonators, the dynamic range is proportional to

$$DR \propto VDD\sqrt{\frac{C_T}{kT}} \frac{1}{\sqrt{Q_0}} \tag{3.20}$$

confirming that for a high dynamic range, gyrators with low unloaded Q_0 factor, large tank capacitors C_T and high VDD technology have to be used.

The linearity issue manifests itself in a form of harmonic distortion. As oscillators operate in large signal regime using non-linear amplifiers, the negative effects of harmonics on the behavior of the active inductor resonator have to be thoroughly analysed. This problem is addressed later in this thesis in Chapter 5. As a rule of thumb for both passive and active resonators, total harmonic distortion can be minimised if the tank capacitance C_T is large, effectively shorting the high frequencies to ground but providing infinite impedance at the resonant frequency [30].

3.4 Active inductor VCO

An active inductor oscillator can be designed using either feedback or negative resistance approach from Chapter 2 using the same oscillation criteria. The latter approach is more convenient if a one port equivalent circuit of the resonator is available and it is especially suitable for grounded active inductors. Such a VCO consists of a tank

capacitor (or switched capacitance array) and electronically tunable inductance. The resonant frequency of the oscillator is proportional to

$$\omega_0 \propto \sqrt{gm_1 gm_2} = gm \mid_{gm_1=gm_2=gm} \tag{3.21}$$

The unloaded quality factor of the resonator is determined by the Q_0 of the active inductor. Comparing (3.21) with (3.7), Q changes with tuned transconductance and therefore with ω_0. This results in a more complex dependence between noise, oscillation amplitude and tuning range than in the case of passive resonators.

3.4.1   Oscillator tuning range

In general, the available tuning range using a single active inductor is larger than the one provided by a single varactor because inductance is inversely proportional to the product of gm_1 and gm_2. In theory, as long as power consumption is not a concern, gm can be varied freely shifting the resonant frequency of an oscillator. However, due to parasitics, the tuning range of real active resonators is always restricted.

Recall the lossy inductor model from Figure 3.3b and 3.3c where the impedance of series resistor R_s and simulated inductance L_s is equal to $Z_s = R_s + j\omega L_s$. At low frequencies, $Z_s \approx R_s$ because the active inductance becomes superimposed by gyrator losses. Thus a lower limit of tuning range is found from

$$R_s = \omega_{low} L_s \rightarrow \omega_{low} = \frac{R_s}{L_s} = \frac{G_{o1}}{C_g + C_{o1}} \tag{3.22}$$

At high frequencies $Z_s \approx j\omega L_s$ because inductive impedance is now much larger than R_s. Due to the input capacitance of the gyrator, the circuit reaches its self-resonance frequency given by

$$\omega_{self} = \sqrt{\frac{1}{L_s C_{o2}}} = \sqrt{\frac{gm_1 gm_2}{(C_g + C_{o1}) C_{o2}}} \tag{3.23}$$

Thus, an active inductor can be tuned between frequencies calculated from (3.22) and (3.23) which confirms results presented previously in [51]. Note, that the self-resonant frequency depends on the transconductance and allows one to increase the tuning range

at the cost of power. This also corresponds to a higher tuning constant of the oscillator that in general is not straight forward to minimise. Lu et al. [79] attempted to use varactors for fine tuning around the carrier frequency. The carrier frequency was controlled through active inductance (adjusted using MOS devices in triode region). In theory, this should result in a reduced sensitivity of active inductor inductance on tuning voltage and reduced AM-PM noise conversion, however no further explanation is given.

3.4.2   Maximising amplitude of oscillations

At a given frequency the amplitude of the signal generated by a gyrator-based oscillator can be controlled through transconductance and capacitance values. The transconductances gm_1 and gm_2 can be tuned separately, keeping in mind that for a given resonant frequency their product has to be held constant. Assuming that transconductance losses are negligible in this case, the amplitude of the voltage at active inductor output is approximately equal to

$$|v_{out}| \approx \frac{|gm_1 v_{in}|}{\omega C_g} \tag{3.24}$$

Similarly, the input signal amplitude is approximated by

$$|v_{in}| \approx \frac{|gm_2 v_{out}|}{\omega C_T} \tag{3.25}$$

where C_T is a tank capacitance. If the maximum signal amplitude at the input of the active inductor is reached, for example the maximum allowable voltage for a given technology, it also can not be exceeded at the output of an active inductor. For this reason

$$\left| \frac{v_{inMAX}}{v_{outMAX}} \right| = 1 \equiv \frac{gm_1}{C_g} = \frac{gm_2}{C_T} \tag{3.26}$$

From the noise perspective it would be beneficial to decrease gm_2 and increase gm_1. In this case however the required C_g has to be larger than the tank capacitance C_T already maximised for small noise. Therefore (3.26) represents an original mathematical proof

confirming the observations done by Cranickx and Steyaert [47] that for a maximum amplitude in standard active inductor resonators $C_T = C_g$ and $gm_1 = gm_2$ should be used.

3.4.3 Phase noise

During preparation of this thesis no non-linear phase noise model of a gyrator based oscillator has been found. Since active inductor structures can't effectively compete with a phase noise performance of passive LC circuits, there is currently no real demand for such models. As far as linear phase noise analysis go, there is only a limited number of papers briefly describing it [79, 80]. The most informative among available sources is that of Craninckx and Steyaert [47], presenting a simple linear and time invariant model for an active inductor tank and compensated with a generic amplifier, illustrated in Figure 3.8.
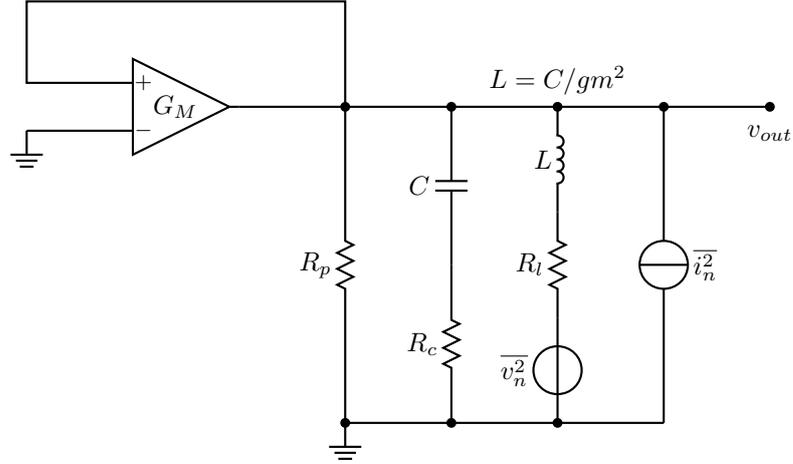
Figure 3.8: Oscillator model with noisy active inductor [47].

Craninckx derives a simple expression for a noise PSD of an oscillator at frequency offsets ω_m from the carrier assuming $\omega_m \ll \omega_0$. If the gyrator is symmetrical i.e. both transconductances and port capacitances are the same, the noise PSD at offset frequency is equal to

$$S_{out}(\omega_m) = kTR_{eff}\left(1 + A + 2Q\right)\frac{\omega_0^2}{\omega_m^2} \qquad (3.27)$$

where R_{eff} is an effective resonator resistance determining a quality factor of the resonator Q

$$R_{eff} = R_l + R_c + \frac{1}{R_p \left(\omega_0 C\right)^2} \tag{3.28}$$

$$Q_0 = \frac{1}{R_{eff}\omega_0 C} \tag{3.29}$$

Parameter A represents the noise factor of a non-ideal amplifier, C is a tank capacitance and L is a gyrator inductance. Note that (3.27) yields total noise (i.e. both phase and amplitude noise) at offset frequency and not only phase fluctuations. In practical circuits, some of the noise is removed due to inherent amplitude stabilisation mechanisms in oscillators [26, 41], however in a worst-case analysis it can be assumed that noise calculated from (3.27) represents the phase fluctuations of the oscillator [47].

Formula (3.27) shows a proportionality between noise PSD at ω_m to a quality factor of a resonator. This behavior is expected because the total noise of any active inductor resonator increases with quality factor as presented in Section 3.3.2. Therefore, to decrease noise at offset frequency from the carrier, a small Q_0 gyrator has to be used, proving that the noise analyses of passive LC tanks do not apply to active inductor circuits. In turn, as Q_0 factor has to be low, a substantial amount of power from the amplifier is required to compensate losses.

Once the noise PSD for a particular ω_m is found from (3.27), phase noise is then calculated using the formula for $\mathcal{L}$, a normalised theoretical one-sided spectrum of oscillator signal [41]

$$\mathcal{L}\left(\omega_m\right) = \frac{S_{out}(\omega_m)}{V_{out}^2/2} \tag{3.30}$$

where V_{out} is an amplitude of oscillator signal. For the circuit discussed in this section (3.30) translates into

$$\mathcal{L}\left(\omega_m\right) = \frac{kTR_{eff}\left(1 + A + 2Q\right)}{V^2/2}\frac{\omega_0^2}{\omega_m^2} \tag{3.31}$$

If Q_0 is much larger than one, (3.31) can be simplified to

$$\mathcal{L}(\omega_m) \approx \frac{1}{V^2}\frac{4kT}{\omega_0 C}\frac{\omega_0^2}{\omega_m^2} \tag{3.32}$$

Craninckx and Steyaert [47] deduct that phase noise of an oscillator with a standard active inductor resonator can be decreased if:

- Amplitude of the signal is large: Craninckx and Steyaert do not specify any possible drawbacks of an excessive signal amplitudes driving active inductor. This large signal problem is described in detail in Chapter 5. Due to the a non-linear nature of active inductors, an increase of signal amplitude causes larger harmonic distortion, that inevitably increases phase noise due to a frequency conversion of noise sources around signal harmonics. Therefore, for excessive amplitudes phase noise will be also large, however the linear phase noise model can't predict it.

- Tank capacitance C is increased: Craninckx and Steyaert explain that the power consumption of the amplifier increases to compensate for lower Q_0. Their observations are true but not well clarified. To keep the oscillation frequency constant, the inductance of the resonator has to decrease to keep the product of $L \cdot C$ constant. Assuming that both gyrator transconductances are the same, every time the C increases an n times, the gm of each transconductor has to increase n times as well. As $gm \propto \sqrt{I_D}$ this requires n^2 increase of the bias current for each amplifier. For the constant supply voltage this increases the DC power consumption of a gyrator by n^2 at least. Thus, the use of large tank capacitance C has to be used carefully.

3.4.4 Reported LC oscillators using active inductors

Due to an inferior noise performance in comparison with passive LC tank oscillators, only a limited number of publications on active inductor LC VCO can be found. Yuan [51] provides references to some of the important works in the field, presented in Table 3.2. The typical phase noise performance of harmonic VCO using gyrators is close to that of ring oscillators from Figure 2.24. Note that the phase noise level is proportional to the tuning range due to the relatively high K_{VCO} of active inductor based resonators.

A common feature of all the presented oscillators from Table 3.2 is that they are compensated using a negative resistor. As shown in this section for a low phase noise, low unloaded Q_0 factor inductors have to be employed. This imposes a large tank capacitance and dramatically increases power consumption of the oscillator due to gyrator losses. The following section describes an useful parasitic effect found in gyrators that, at least in theory, allows to minimise the described trade-off.

Table 3.2: Reported active inductor oscillators [51]

Reference	Year	Node	Type*	f_0 [GHz]	Phase noise [dBc/Hz]
Lin et al. [56]	2000	0.35μm	VCO	2.5	-88 @0.6 MHz
Wu et al. [53]	2001	0.35μm	VCO	0.1-0.9	-95 @0.5 MHz
Xiao et al. [81]	2002	0.20μm	VCO	4.95	-81 @0.5 MHz
Lu et al. [73]	2006	0.18μm	VCO	0.5-3.0	-101– -118 @1 MHz
Tang et al. [76]	2007	0.18μm	TVCO-A	1.6	-108 @1 MHz
Tang et al.[77]	2007	0.18μm	TVCO-AB	1.6	-125 @1 MHz
Tang et al. [82]	2007	0.18μm	QVCO	1.6	-115 @1 MHz
∗ - TVCO is using active transformer; A, AB amplifier class, QVCO - quadrature VCO					

3.5 Negative resistance in active inductors

3.5.1 Effects of non-ideal transconductors

In general, there are two mechanisms responsible for circuit losses in active inductors. Apart from node conductances, reactive networks inside the transconductors can deteriorate a circuit performance. This problem had been addressed in the past by Moulding [83, 84], who observed that at high frequencies, non-ideal transconductors introduce a negative real admittance component into an active inductor resonator. Figure 3.9 illustrates such a gyrator-based tank, where an amplifier parasitics manifest itself in a form of arbitrary phase lag of $\phi/2$ radians of each transconductor. This is a result of a finite resistive losses and parasitic capacitances of MOS devices and its biasing network. It is assumed that the phase shift, although not negligible, is small enough to satisfy the condition of $\sin(\phi) \approx \phi$.

Figure 3.9: Active inductor resonator with non-ideal transconductors [84].

The input admittance is then approximately equal to

$$y_{in}(j\omega) = G_{o2} + j\omega C_T + \frac{gm_1 gm_2}{G_{o1} + j\omega C_g} e^{-j\phi} =$$

$$= G_{o2} + j\omega C_T + \frac{gm_1 gm_2}{G_{o1} + j\omega C_g} \left(\cos\phi - j\sin\phi \right) \approx$$

$$\approx G_{o2} + j\omega C_T + \frac{gm_1 gm_2}{G_{o1} + j\omega C_g} - \phi \frac{gm_1 gm_2}{\omega C_g} \Bigg|_{\substack{\phi \le \pi/10 \\ G_{o1} \ll gm_1, gm_2}} =$$

$$= G_{o2} + j\omega C_T + \frac{1}{R_s + j\omega L_s} - \frac{\phi}{\omega L_s} \tag{3.33}$$

where

$$R_s = \frac{G_{o1}}{gm_1 gm_2}$$

$$L_s = \frac{C_g}{gm_1 gm_2} \tag{3.34}$$

An additional parallel negative resistor of $-\phi gm_1 gm_2 / \omega C_g$ is now present in the circuit. If not sufficiently suppressed, it causes resonator peaking at higher frequencies, in extreme cases leading to instability [78, 83, 84].

By approaching the problem from a different perspective, the effect of unwanted phase shift inside transconductors causes partial or even total compensation of gyrator losses, theoretically improving a selectivity of the tank or, in an extreme case, producing oscillations without an extra power consumption. As transistor parasitics are generally

hard to control, this compensation method can't fully rely on amplifier non-idealities. Instead, it is possible to generate the required phase shift by the means of RC components whose behavior is much more predictable. Due to the additional components used, the resonator represents a *degenerated* version of an ideal active inductor circuit. Hereinafter this term is used to describe the behavior of an active inductor with intentionally added phase lag components.

3.5.2 Practical active inductor circuits with negative resistance

Over the years, only a few active inductors with negative resistance have been published. In the most cases either GaAs-MESFET [85–87] or GaAs-HBT [88] devices are used, usually due to a high frequency of operation. This section presents the state of the art designs found in literature, showing that before this thesis, little has been done to explore the fundamental properties of these circuits.

3.5.2.1 Hara-Hayashi MMIC active inductors

Figure 3.10 illustrates four widely known circuit architectures, presented in the series of articles by Hara et al [85, 86] and later modified by Hayashi et al [89] using MMIC (Monolithic Microwave Integrated Circuits) technology. MMIC circuits use gallium arsenide (GaAs) instead of silicon which results in much higher frequency of operation in the range of hundreds of GHz. However the manufacturing cost of such circuits is substantially higher than using CMOS due to a smaller number of devices per wafer in MMIC. All of the circuits utilise a non-inverting cascode transconductor stage and various feedback amplifier topologies. The resulting input admittance/impedance functions are approximately equal to

$$y_{in}(j\omega) \approx gm_3 \left(1 - \frac{C_{gs2}gm_1}{C_{gs1}gm_2} \right) + \frac{1}{j\omega \frac{C_{gs1}}{gm_1gm_2}} \qquad \text{:type A} \qquad (3.35)$$

$$z_{in}(j\omega) \approx -\frac{1}{gm_2} + j\omega \frac{C_{gs1}}{gm_1} \left(\frac{1}{gm_2} + \frac{1}{gm_3} \right) \qquad \text{:modified type A} \quad (3.36)$$

$$y_{in}(j\omega) \approx \frac{1}{R_s} - gm \frac{C_{gs3,4}}{C_{gs1,2}} + \frac{1}{j\omega \frac{C_{gs1,2}}{gmgm_{3,4}}} \qquad \text{:type B} \qquad (3.37)$$

(a) Type A active inductor   (b) Type A modification

(c) Type B active inductor   (d) Type B modification
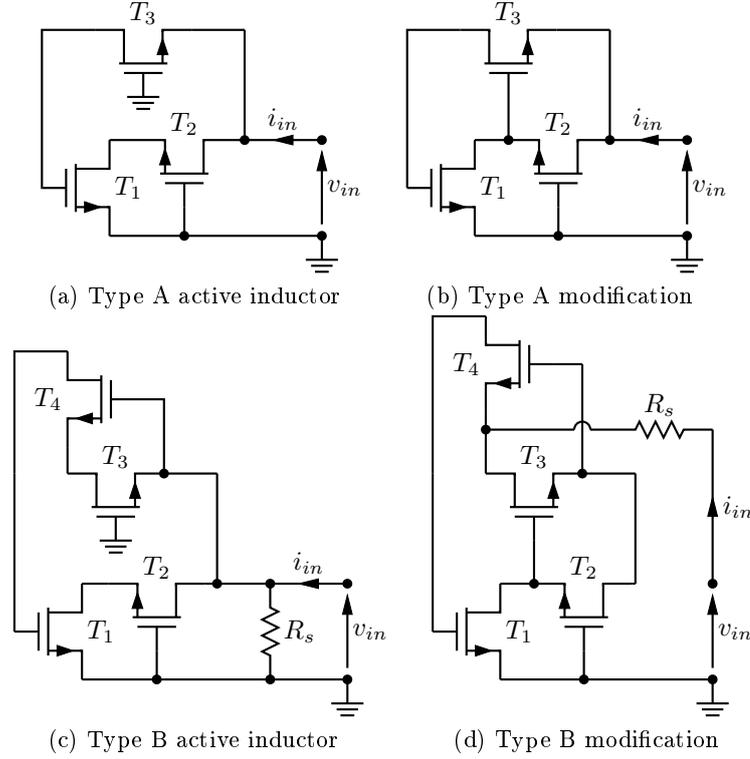
Figure 3.10: MMIC negative resistance gyrators: (a) and (c) present original Hara et al. gyrators [85, 86]; (b) and (d) depict Hayashi et al. respective modifications [89, 90].

$$z_{in}(j\omega) \approx R_s - \left(\frac{1}{gm_2} + \frac{1}{gm_3} \right) + j\omega \frac{C_{gs1}}{gm_1} \left(\frac{1}{gm_3} + \frac{1}{gm_4} \right) \quad :\text{modified type B} \quad (3.38)$$

In every case, all of the FET devices were described by simple small-signal models consisting only of a transconductance gm and gate to source capacitance C_{gs}. Thus all of the small-signal parameters are designed around a limited set of transistor parasitics. Resistors R_s have been added to improve stability and input matching without any further explanation.

The main advantages of the Hara-Hayashi circuits are wide operational bandwidth and a relatively high output power of 0 dBm. Hara and Hayashi do not include any noise or a non-linear analysis and no design rules are given. A relatively large DC power consumption between 50 mW to 80 mW has also been reported.

3.5.2.2   Wei passively compensated gyrator

Next circuit, depicted in Figure 3.11, was published in a brief letter by Wei et al. [91]. This active inductor is a further modification of Hayashi gyrator from Figure 3.10b. The active phase shifter is created by connecting an additional RC network between gate of transistor T_2 and AC ground. The authors report that the circuit generates a constant negative resistance roughly over a decade bandwidth with a power consumption of 30 mW, reaching quality factor values in the range of 1000. As previously, no noise and non-linear analysis in the presence of RC shifter is included nor an explanation of a chosen shifter configuration.

Nair et al. [92], have used the same approach in a cascode feedback active inductor for an ultra wide band (UWB) 180 nm CMOS LNA. For a small power consumption of 7 mW and 1 V supply voltage, typical performance of a gyrator-based circuits is reported, yet no further design insight into a complex RC network used has been given.
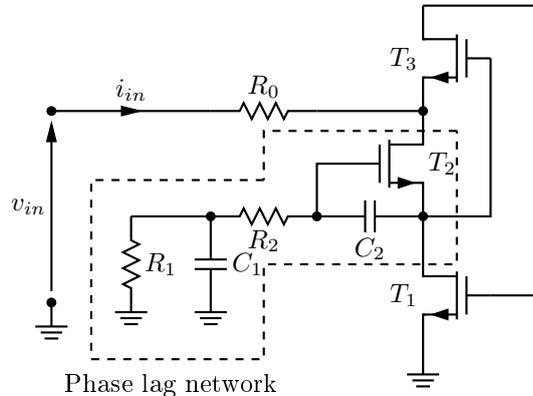
Figure 3.11: Feedback network compensated active inductor [91].

3.5.2.3   Kaunisto circuits

Another significant circuit, from Figure 3.12 was presented by Kaunisto [7, 88]. It achieves a potentially better power consumption than Hara active feedback circuits and its modifications. First, single transistor transconductors are used, possibly minimising
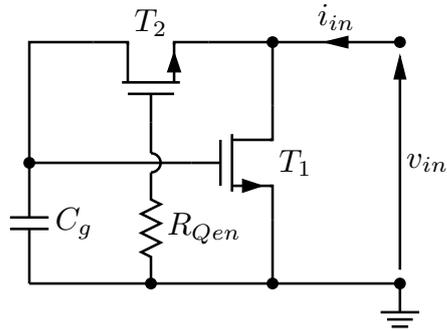
Figure 3.12: Kaunisto Q-enhanced active inductor [7].

DC power consumption. A phase lag network has been implemented using both lumped components and transistor in the linear regime. No analytical formulas regarding input admittance were enclosed, however several HBT [88] and Bi-CMOS [93] circuits based on this concept were built and measured. DC power consumption in the range of 25 mW has been reported, achieving noise voltage spectrum density of 18 nV/$\sqrt{\text{Hz}}$ at the resonant frequency of 3 GHz [7]. In addition, Kaunisto presents significant insights into stability of integrated resonators in the presence of a negative resistance generated by phase shifters as well as an influence of circuit parasitics on performance of active inductors.

3.5.2.4 Known CMOS architectures

One of the few CMOS circuits utilising a self-generated negative resistance is a double feedback active inductor by Yodoprasit and Ngarmnil [94]. In this approach the non-inverting transconductor is achieved using a long-tail pair, where the inverting output is fed back to the gyrator input node. This creates a positive feedback and negative resistance of $-2/gm$ is generated. The circuit was simulated in a 0.6 µm process and achieved Q_0 factor values of 12000, consuming 20 mW from a 3.3 V power supply. The evident decrease of linear operation due to increased complexity is shown by the reduced third order intercept point (IIP3) of only -25 dBm that was reported.

3.6 Chapter summary

This chapter presented a comprehensive overview of active inductor circuits, its basic parameters and performance limitations. It was shown that due to the use of active circuits, noise and dynamic range is reduced in comparison with standard spiral inductor resonators. However, the presented mathematical formulas prove that active inductors provide straightforward and wide band tuning of a resonant frequency. When designing a gyrator-based oscillator, the noise generated by the circuit should be as small as possible. To achieve this, the proposed formula for noise of active resonator compensated with negative resistor suggest a low-Q factor inductor and large tank capacitor have to be used. The obvious cost is increased power consumption required for the compensation. These novel results comply with more generic observations provided by Abidi [95] and Kaunisto [7] for the uncompensated active inductors.

It was also shown that negative resistance can be generated using passive phase shifters inside the gyrator leading to concept of degenerated gyrator. In theory, this allows the reduction in the power necessary for compensation due to an absence of any external negative resistance circuit. Although a very limited number of circuits in this area has been published in the past, to the Author's knowledge there was no reported attempt to employ it in integrated CMOS oscillator. This chapter revealed also that to date many important questions regarding degenerated gyrator performance have not yet been answered or even addressed. This include:

- The number of phase shifters necessary to provide negative resistance. The dependence on a small signal behavior of a resonator in a presence of different number of phase shifters and their relative location in the circuit is not clear.

- There is no defined sensitivity of small signal parameters on phase shifter components. This is important information, knowing that often integrated components have worse tolerances than discrete ones.

- The resonant frequency, tuning range and Barkhausen criteria for self-oscillating

active inductors remain unknown. This analysis is essential because circuit losses determine a tuning range and amount of negative resistance required for oscillations.

- The amplitude limiting mechanism for these group of oscillators is not clear. Nonlinear effects of a large swing in the oscillator signal have to be studied in depth.

- An analysis of how a phase shifter influences the noise of a resonator. It is important to evaluate phase noise performance of the oscillator as well.

This dissertation address and answers all of the above issues, providing a valuable contribution to the field of self-oscillating CMOS active inductors. Chapter 4 presents the proposed concept of an RF oscillator dealing with the most important small signal parameters and related design trade-offs.

Chapter 4

Concept of degenerated gyrator oscillator

4.1 Introduction

This chapter presents the novel concept of a CMOS oscillator utilising a self-oscillating active inductor. The circuit behavior is thoroughly studied using a small signal model of the oscillator. As a result important parameters such as resonant frequency or tuning range are clearly defined and a design methodology offered. Mathematical analysis employed in this chapter include:

- Immitance functions: For every considered circuit in this chapter an input impedance or admittance function is studied. As a result, closed form expressions for negative resistance and active inductance can be derived and used later for the design of a practical circuit. Immitance functions also allow the observation of the resonator response for AC signals at various frequencies and to calculate a Barkhausen criteria for the new oscillator.

- Sensitivity functions: These functions show the dependence of small signal parameters of the circuit on changes in different design variables. In general, this topic is commonly omitted in the literature on any active inductor circuits, hence

73

the sensitivity analysis conducted here represents a valuable contribution.

- Noise power spectral density functions. Using the methodology explained in Chapters 2 and 3, a new model of noise degenerated active inductor is proposed.

The above represent a well established design methodology of oscillators, however the results obtained by the use of these tools are novel. Prior to this thesis, there were no reported attempts to define a minimum number of phase shifters sufficient for oscillations. This problem is addressed in Section 4.2 explaining in detail the related design trade-offs.

Section 4.3 presents an ideal model of the proposed circuit that is used to study sensitivity of a circuit. The results allow to calculate how resonant frequency, negative resistance or inductance change when design parameters differ from its nominal values. The ideal circuit model from Section 4.3 is also used to deliver, for a first time, the oscillation criteria for the proposed circuit. A formula for a resonant frequency is given as well. Finally, the ideal model allows analysing a sensitivity of the proposed circuit on finite tolerances of the real components. The results of this analysis are presented in Section 4.4.

Next, Section 4.5 describes how parasitic components of active circuit affect the oscillator, especially if integrated using sub-micron CMOS process. A negative resistance and inductance in a presence of the losses are discussed and new corresponding formulas are derived. Barkhausen criteria and resonant frequency for a non-ideal oscillator are calculated. Limitations on the tuning range of the oscillator are also discussed.

Finally, Section 4.6 presents the analysis of noise in the proposed circuit. This section explains how RC phase shifting circuit affects the noise properties of the circuit with all related advantages and disadvantages. Novel expressions for power spectrum density, spot noise and total RMS noise of the proposed resonator are derived and compared to the standard active inductor tank from Chapter 3.

4.2 Generic model of degenerated gyrator resonator

4.2.1 Required number of phase shifters to generate negative resistance

At the end of Chapter 3, Section 3.5.2 some active inductor circuits using RC phase shifters to decrease resonator losses were presented. In these publications [85, 86, 89–92, 94] no explanation on the chosen number of phase shifters and their configuration is given. Kaunisto [7] is the only author specifying that for a proper operation of his filters, two identical phase shifting circuits have to be used. This conclusion is important for filters because the amount of negative resistance eventually produced by RC circuit must not lead to instability and for this reason have to be precisely controlled.

In the proposed degenerated gyrator the amount of negative resistance has to be sufficient to start oscillations, but its value does not have to be as precise as in the case of filters. Thus, one can conclude that a single RC phase shifter can be adequate for the oscillator application. However before this hypothesis can be confirmed, it is important to observe how the circuit behaves in the presence of multiple phase shifters first. This way any possible advantages and disadvantages of this approach will not be overlooked.

4.2.1.1 Two RC phase lag networks

Figure 4.1 depicts the proposed model of active inductor degenerated using two RC networks. This circuit is a transformed version of a generic model of the resonator given by Moulding [83] and presented previously in Chapter 3, Section 3.5. The intrinsic losses of the amplifiers are now substituted by the phase shifters connected at the input of each transconductor. It is assumed that the circuit operates at frequencies where the transconductor parasitics do not contribute significantly to the overall phase shift experienced by the resonator. Load capacitance C_g is connected at the output port as in the case of a standard gyrator, however this time its voltage does not drive the feedback amplifier directly. Instead, the output voltages of the phase shifters $R_{in}C_{in}$ and $R_{out}C_{out}$ are now controlling the corresponding transconductors.

4.2 Generic model of degenerated gyrator resonator

At this stage, for simplicity of calculations, it is assumed there are no additional resistive losses present at the input/output ports. These will be re-introduced later. Also, it will be assumed that both amplifiers are not drawing any current from the phase shifters. This assumption usually holds for practical circuits because input stage parasitics can be incorporated into corresponding phase lag networks.
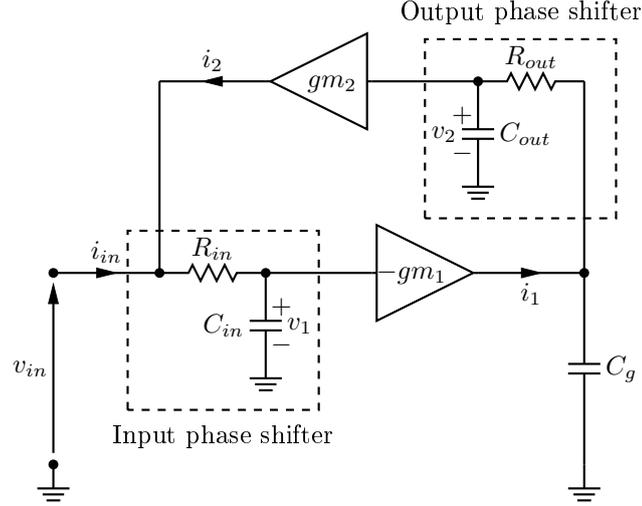
Figure 4.1: Proposed generic model of degenerated active inductor to study effects of two RC phase shifters.

As mentioned in the introduction to this chapter, immitance functions allow us to study the circuit response for AC signals. As the gyrator model from Figure 4.1 can be transformed to a parallel resonant structure, input admittance is a more convenient function to describe it. When the circuit is driven by the test current i_{in}, the resulting voltage v_{in} can be found by solving KVL equations for the input port. The input admittance is then found from

$$y_{in}(j\omega) = \frac{i_{in}}{v_{in}} = \frac{1}{z_1(j\omega)} + \frac{1}{z_2(j\omega) + z_3(j\omega) + z_4(j\omega)} \tag{4.1}$$

where

$$z_1(j\omega) = R_{in} + \frac{1}{j\omega C_{in}}$$

$$z_2(j\omega) = \frac{1}{j\omega} \frac{1}{\dfrac{gm_1 gm_2}{\omega^4 C_g C_{in} C_{out} R_{in} R_{out}}} = \frac{1}{j\omega C_{sim}}$$

76

$$z_3(j\omega) = j\omega \frac{C_g + C_{out}}{gm_1 gm_2} = j\omega L_{sim}$$
$$z_4(j\omega) = -\omega^2 \frac{(C_g + C_{out})\,C_{in}R_{in} + C_g C_{out}R_{out}}{gm_1 gm_2} = -R_{sim} \qquad (4.2)$$

The input admittance consists of two reactive networks connected in parallel. The first term, $1/z_1(j\omega)$ is equal to the total admittance of the input phase shifter. The second network is a series resonant circuit, consisting of three impedances: the parasitic capacitor $z_2(j\omega)$, the simulated inductance $z_3(j\omega)$ and the negative resistance $z_4(j\omega)$. Equation (4.1) differs from the generic model of Moulding [83] given by (3.33) because both RC networks draw current due to their finite admittances, nevertheless a negative resistance is successfully generated.

A brief mathematical analysis of (4.1) reveals that the circuit suffers from a low-frequency parasitic self-resonance caused by a parasitic capacitor C_{sim} described by $z_2(j\omega)$. As C_{sim} is inversely proportional to ω^4, it can be much larger than any other capacitance present in the circuit. Another shortcoming of this approach comes from the fact that two RC circuits introduce two thermal noise generators that contribute to the total noise of the resonator.

4.2.1.2   Single phase shifter

The circuit from Figure 4.1 can be modified if one of the phase lag networks is removed permanently. This results in two possible circuit arrangements. In the first case (Figure 4.2a), $R_{in}C_{in}$ is connected to the input of the inverting amplifier, whereas the second amplifier is connected directly to C_g. In the second case (Figure 4.2b), $R_{out}C_{out}$ phase shifter is switched on, and input of the inverting amplifier is connected directly to the input of the active inductor. When one of RC circuits is removed, one of the noise sources is automatically eliminated. The parasitic capacitor C_{sim} from (4.1) is also suppressed as it is the result of two phase shifters being present in the circuit. As a result, both circuits from Figure 4.2 can operate at higher frequencies.

To compare the behavior of the circuits with a single phase shifter, the corresponding
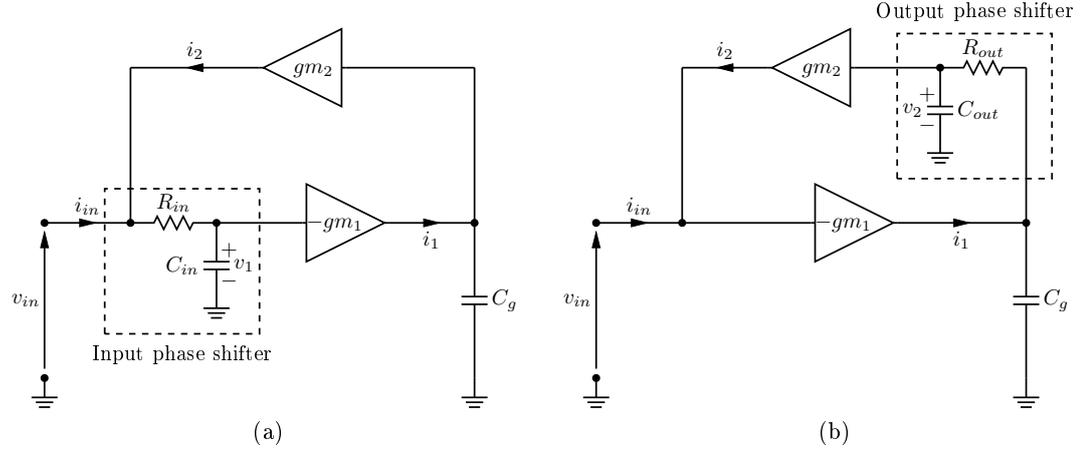
Figure 4.2: Degenerated active inductor with single phase shifter: (a) at the input, (b) at the output.

input admittance functions are analysed. When the $R_{in}C_{in}$ network is present, the input admittance is equal to

$$y_{in}(j\omega) = \cfrac{1}{R_{in} + \cfrac{1}{j\omega C_{in}}} + \cfrac{1}{j\omega \cfrac{C_g}{gm_1 gm_2} - \omega^2 \cfrac{C_g C_{in} R_{in}}{gm_1 gm_2}} \tag{4.3}$$

In this case, (4.3) represents a sum of two reactive networks. The admittance of the first term is equal to the total admittance of the phase shifter. As a result, the circuit from Figure 4.2a has an additional input capacitance, resulting in self-resonance. However, in comparison to the circuit with two shifters, the self-resonance frequency is much higher (as mentioned the capacitor C_{sim} from 4.1 is no longer present). The second term of (4.3) corresponds to a series connection of the inductance and the negative resistor. Thus, even though only a single phase shifter is used, negative resistance $(-\omega^2 C_g C_{in} R_{in}/gm_1 gm_2)$ is generated.

In the second case, the $R_{out}C_{out}$ phase shifter is used. The corresponding input admittance becomes now

$$y_{in}(j\omega) = \cfrac{1}{j\omega \cfrac{(C_g + C_{out})}{gm_1 gm_2} - \omega^2 \cfrac{C_g C_{out} R_{out}}{gm_1 gm_2}} \tag{4.4}$$

4.2 Generic model of degenerated gyrator resonator

This time the total admittance represents a series combination of a simulated inductance $(C_g/gm_1gm_2 + C_{out}/gm_1gm_2)$ and negative resistance $(-\omega^2 C_g C_{out} R_{out}/gm_1gm_2)$. No additional capacitance is present at the input and therefore there is no self-resonance. This statement is valid only for the ideal circuit considered here. Function (4.4) also proves that in this case a single RC phase shifter is sufficient to generate negative resistance. In comparison with the circuit with input RC network, the simulated inductance is larger by capacitance C_{out} whereas the negative resistance has the same character and frequency dependence.

To compare the AC performance of both circuits, (4.3) and (4.4) were implemented in MATLAB and simulated over a decade bandwidth from 100 MHz to 1000 MHz. An integrated resonator design for this particular bandwidth is interesting for few reasons. First of all, integrated passive inductors available in typical commercial CMOS process occupy a large chip area at these frequencies. Secondly, many different radio-communication systems are supported in these frequency ranges (TETRA, ISM, TV broadcasting, to name a few). Finally, a decade bandwidth is large enough to experiment with a various concepts of a wide-band resonators.

Table 4.1: Simulation parameters chosen to compare active inductors with single RC shifter.

Value	Model parameters						
	gm	R_{in}	R_{out}	C_{in}	C_{out}	C_g	Frequency
	mA/V	kΩ		pF			MHz
low	5	0.15		0.4			100
high	25	1.5					1000

The proposed mathematical models were simulated using the set of parameters given in Table 4.1. Terms *low* and *high* qualitatively describe the magnitude of each corresponding parameter. It is assumed that both amplifiers have the same transconductance gm which corresponds to the most common practical design choice in any active inductor circuit [47]. It is also assumed that capacitance C_{in} is small enough to avoid self-resonance of the gyrator with the input shifter within the considered frequency range. For the purpose of fair comparison $C_{in} = C_{out} = C_g$ which allows us

to observe the behavior of the circuits for the same RC network connected at different points. In addition, the phase shifter capacitance should have the same magnitude as the gyration capacitance to have any effect on the active inductor. Finally, because the input admittances (4.3) and (4.4) are complex, the real and imaginary parts were analysed separately.

Figures 4.3 and 4.4 present plots of the input conductance and equivalent parallel inductance functions for a low transconductance of amplifiers equal to 5 mA/V. The first diagram represents a situation where both R_{in} and R_{out} are also small, corresponding to a calculated phase lag less than 0.1π rad at 1000 MHz. The circuit with the output shifter from Figure 4.2b is less sensitive to frequency changes while at the same time generating a substantially lower negative conductance. The main advantage however, is the doubled inductance value which in turn requires a proportionally smaller on-chip capacitor (less chip area) to design LC tank at given frequency.

If both R_{in} and R_{out} are increased to 1.5 kΩ, the corresponding phase lag also increases, reaching 0.38π rad at the maximum signal frequency. In this case, illustrated on Figure 4.4, the input conductance of the gyrator with the input shifter from Figure 4.2a decreases much faster, yet in both inductors the magnitude of the negative component is larger than from Figure 4.3. The self-resonance of the circuit with the $R_{in}C_{in}$ network is lowered, which is manifested by a rapid inductance increase at higher frequencies. Thus, the bandwidth over which inductance is available is inevitably lower than in the case of the circuit with the output RC shifter. This behavior was expected, because as (4.4) suggests, the latter does not have an additional capacitor at its input.

The same type of behavior is observed for a relatively high transconductance of both amplifiers, set to 25 mA/V and chosen for the purpose of theoretical discussion only. Although the magnitude of the input admittance parameters has now changed, the frequency behavior remains the same, as illustrated on Figures 4.5 and 4.6. Note, that for the considered frequency band, the available inductance values are now impractically small. To compensate, either a larger R_{in}, R_{out} and C_g can be used, however this adjustment has to be carefully administrated since it may cause an unwanted change
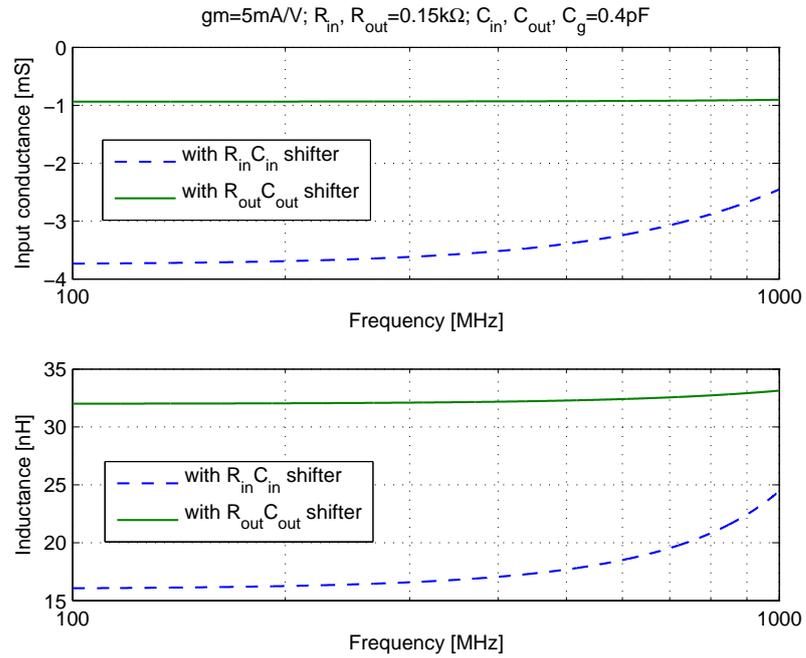
Figure 4.3: Input conductance and inductance of degenerated gyrator with a single RC phase shifter and low gm, R_{in} and R_{out}.
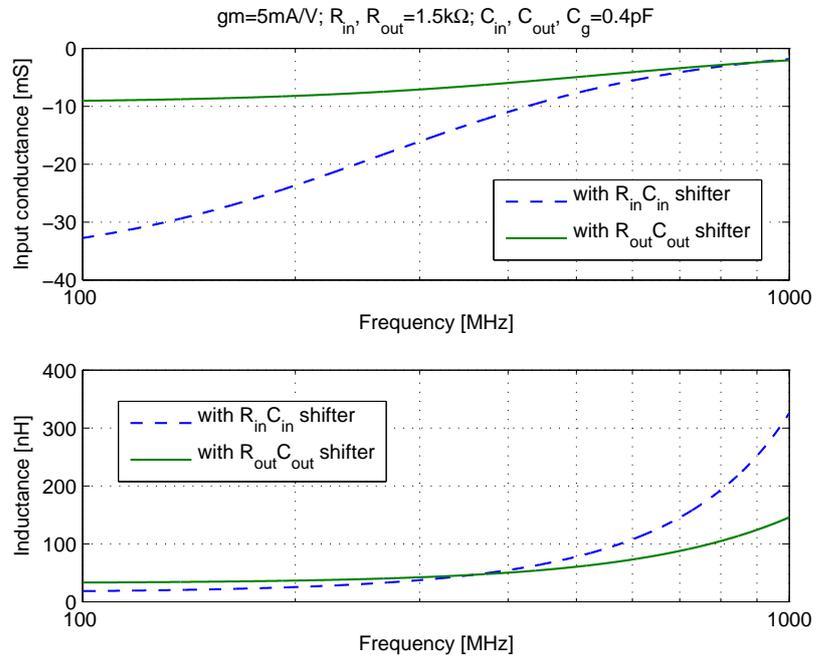
Figure 4.4: Input conductance and inductance of degenerated gyrator with a single RC phase shifter and low gm for high R_{in} and R_{out}.
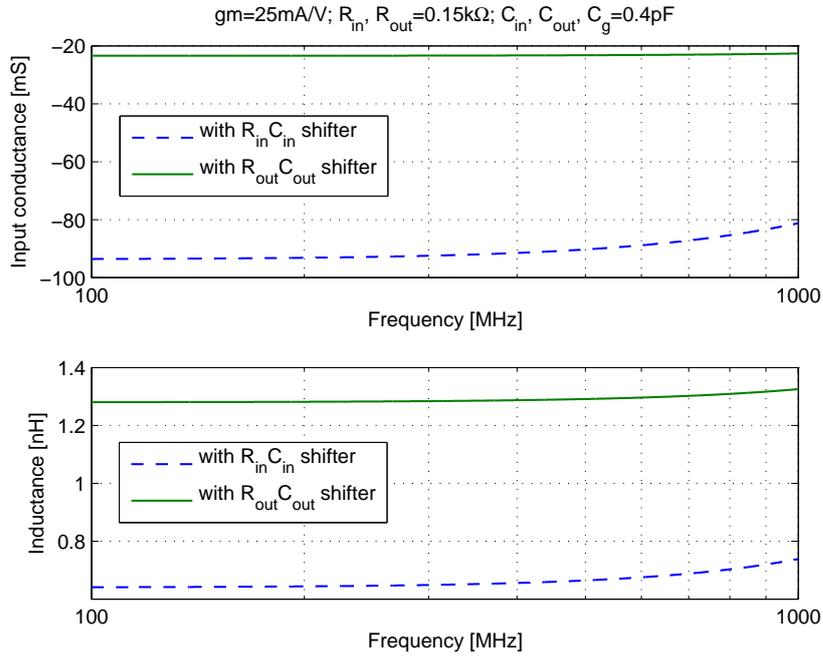
Figure 4.5: Input conductance and inductance of degenerated gyrator with a single RC phase shifter and high gm for low R_{in} and R_{out}.
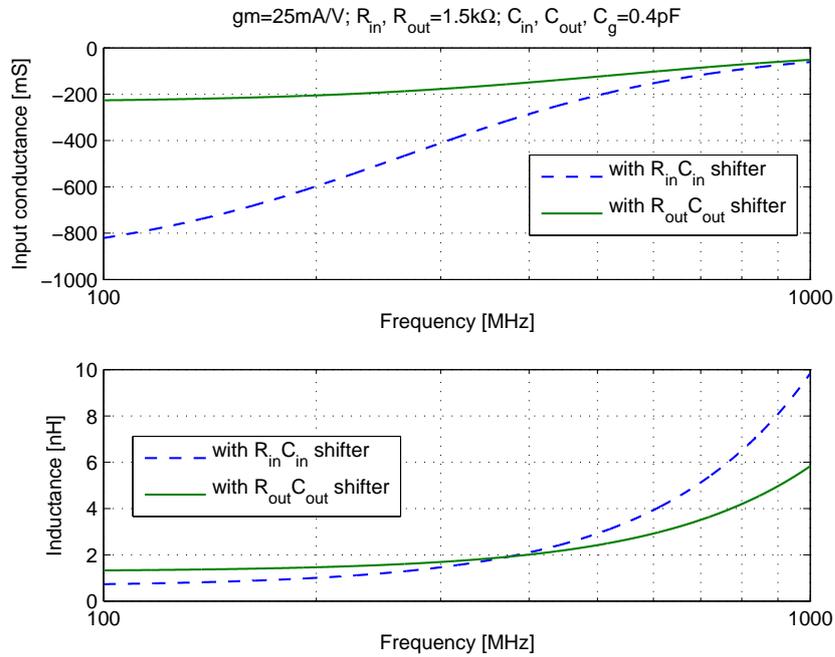
Figure 4.6: Input conductance and inductance of degenerated gyrator with a single RC phase shifter and high gm, R_{in} and R_{out}.

of the negative real admittance term and, as presented later in this dissertation, also affects the noise and large signal behavior of the resonator.

Based on the MATLAB simulation results illustrated in Figures 4.3-4.6 one can conclude that, in comparison to the other circuit, the gyrator with the output phase shifter $R_{out}C_{out}$ achieves:

- Negative conductance that is less sensitive to frequency changes.

- Larger inductance, for a given resonant frequency, allowing the use of an integrated tank capacitor with smaller dimensions.

- Simulated inductance occupying a broader frequency band due to a lack of input capacitor C_{in}. As a result, the resonator can operate over a wider frequency range.

For these reasons, the output phase lag network has been chosen as a chief mechanism of loss compensation method in a degenerated gyrator.

4.3   Ideal model of degenerated gyrator resonator

It was shown in Chapter 3 that for convenience of circuit analysis it is useful to transform an active inductor circuit into its parallel equivalent. As this transformation is only valid in a vicinity of a resonant frequency, any parallel equivalent is therefore a frequency dependent circuit, even if an original parameters before transformation are not. In the case of the degenerated gyrator, this effect is even more complex because the series negative resistance generated by a phase lag network is already a function of a signal frequency as indicated by (4.4).

Figure 4.7 depicts an ideal resonator based on the proposed degenerated gyrator circuit analysed in the previous section. Components C_T and R_T represent the total resonator capacitance and resistance, respectively. As before, to find a parallel equivalent, first the quality factor has to be found. Because of negative resistance, the quality factor is also negative, which means that power is added to the resonator instead of being dissipated. Although uncommon, a negative Q still yields proper results because
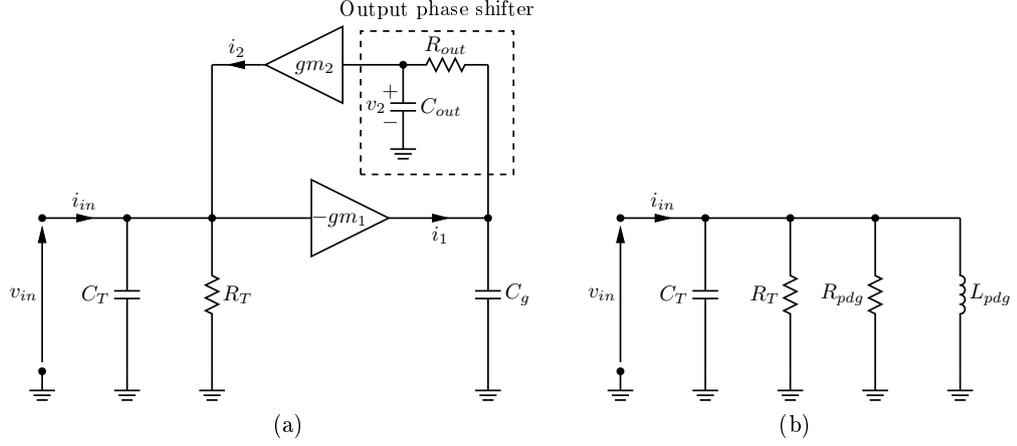
Figure 4.7: Ideal degenerated active inductor resonator: (a) circuit, (b) parallel equivalent model.

it is squared during transformation. Its magnitude and not sign determines the values of the parallel equivalents.

Using (4.4) a quality factor of the proposed degenerated gyrator circuit is found using the standard definition from Chapter 2, $Q(\omega) \stackrel{def}{=} \omega L_s / R_s$. Introducing the auxiliary variables

$$C_S = \frac{C_g C_{out}}{C_g + C_{out}} \qquad C_P = C_g + C_{out} \tag{4.5}$$

and

$$\omega_z = \frac{1}{R_{out} C_S} \tag{4.6}$$

a quality factor necessary for a narrow band transformation is calculated

$$Q_{sdg}(\omega) = \frac{\omega \left(C_g + C_{out} \right)}{-\omega^2 C_g C_{out} R_{out}} = \frac{1}{-\omega R_{out}} \frac{1}{\dfrac{C_g C_{out}}{C_g + C_{out}}} = \frac{-\omega_z}{\omega} \tag{4.7}$$

Thus using (4.5) and (4.6), the equivalent parallel resistance is equal to

$$R_{pdg}(\omega) = -\frac{\omega^2 C_g C_{out} R_{out}}{gm_1 gm_2} \left(Q_{sdg}(\omega)^2 + 1 \right) = -\frac{\omega^2 C_g C_{out} R_{out}}{gm_1 gm_2} \left(\frac{\omega_z^2}{\omega^2} + 1 \right) =$$
$$= -\frac{\omega_z C_P}{gm_1 gm_2} \left(1 + \frac{\omega^2}{\omega_z^2} \right) \tag{4.8}$$

4.3 Ideal model of degenerated gyrator resonator

Using the same procedure, the equivalent parallel inductance is found

$$L_{pdg}(\omega) = \frac{C_g + C_{out}}{gm_1 gm_2} \left(\frac{Q_{sdg}(\omega)^2 + 1}{Q_{sdg}(\omega)^2} \right) = \frac{C_P}{gm_1 gm_2} \left(1 + \frac{\omega^2}{\omega_z^2} \right) \tag{4.9}$$

It can be seen that both negative resistance and inductance are directly proportional to each other, similarly to Moulding generic model of lossy gyrator from Figure 3.9. For an ideal degenerated gyrator with the output RC phase lag network, the following relationship is true

$$R_{pdg}(\omega) = -\omega_z L_{pdg}(\omega) \longleftrightarrow L_{pdg}(\omega) = \frac{|R_{pdg}(\omega)|}{\omega_z} \tag{4.10}$$

Finally, the total input admittance of the resonator from Figure 4.7b is equal to

$$y_{in}(j\omega) = \frac{1}{R_T} - \frac{gm_1 gm_2}{\omega_z C_P \left(1 + \dfrac{\omega^2}{\omega_z^2} \right)} + j \left(\omega C_T - \frac{gm_1 gm_2}{\omega C_P \left(1 + \dfrac{\omega^2}{\omega_z^2} \right)} \right) \tag{4.11}$$

At resonant frequency both reactive admittances cancel each other. In order to find this frequency, the imaginary part of (4.11) has to be equal to 0 i.e. $\Im y_{in}(j\omega) = 0$. Recalling (4.9), it can be seen that the parallel equivalent inductance is frequency dependent. This imposes an additional level of complexity on the calculation, as the resonant frequency is now given by

$$\omega_0 = \frac{1}{\sqrt{L_{pdg}(\omega_0) C_T}} \tag{4.12}$$

which is a 4th order equation with real parameters. The Symbolic Math Toolbox in MATLAB was employed to derive the result, yielding 4 possible solutions. The calculation process involves *Maple* kernel, a computer algebra system that allows to conduct various mathematical calculations in a symbolic form as oppose to a numerical computing environment [96]. Among the obtained solutions there is the only one that is both real and positive. Thus, the resonant frequency of the proposed degenerated gyrator with output RC phase shifter is equal to

$$\omega_{0dg} = \frac{\sqrt{2}}{2} \omega_z \sqrt{\sqrt{1 + 4 \frac{gm_1 gm_2}{\omega_z^2 C_P C_T}} - 1} \tag{4.13}$$

Note that if the phase shifter is removed, ω_z becomes infinite and (4.13) approaches the limit equal to the resonant frequency of a standard gyrator-based resonator [51]

$$\omega_{0ai} = \sqrt{gm_1 gm_2 / C_g C_T} \qquad (4.14)$$

This confirms that the solution given by (4.13) is consistent with the published models.

4.3.1 Barkhausen criteria for ideal degenerated gyrator oscillator

An analysis of the new degenerated active inductor suggests that the negative resistance originating in the resonator can, at a given frequency, be equal to or larger than all the circuit losses. Therefore a controlled oscillator in the form of a self oscillating gyrator can be obtained. As indicated by (4.13), the resonant frequency of such an oscillator is directly controlled by the transconductance amplifiers (through gm), tank capacitance and the phase shifter (through C_P, $\omega_z \leftrightarrow R_{out}$, C_S). To estimate possible performance limitations of this oscillator, first conditions for a signal build-up across resonator have to be derived.

Recalling the Barkhausen criteria for a generic feedback system from Chapter 2, any oscillatory circuit has to meet both amplitude and phase condition at the same time for all frequencies of interest. As a degenerated gyrator produces negative resistance, it is more practical to translate the Barkhausen feedback theorem into its negative resistance equivalent. As explained in Chapter 2, the amplitude condition (2.17) corresponds to the situation when all of the tank losses are cancelled by the negative resistor. The phase condition (2.18) imposes that both resonator reactances have to have equal magnitudes and be out of phase, cancelling each other at a resonant frequency only. In the case of an ideal degenerated active inductor, both conditions are derived directly from (4.11)

$$\frac{1}{R_T} - \frac{gm_1 gm_2}{\omega_z C_P \left(1 + \dfrac{\omega^2}{\omega_z^2}\right)} = 0 \qquad \text{:amplitude condition} \qquad (4.15)$$

$$\omega C_T - \frac{gm_1 gm_2}{\omega C_P \left(1 + \dfrac{\omega^2}{\omega_z^2}\right)} = 0 \qquad \text{:phase condition} \qquad (4.16)$$

In the considered ideal case, the amplitude condition is met as long as resonator losses are smaller than the contribution from the compensating negative resistor. In practice R_T from Figure 4.7b decreases with frequency because it represents a parallel transformation of tank capacitance losses ($Q_{C_t} = 1/\omega r_{loss} C_t$). In CMOS integrated circuits, typically tank capacitance consists of MIM (metal-insulator-metal) capacitors together with an RF output buffer amplifier extracting the signal from an oscillator and preventing load pulling of the resonance frequency. Typically, due to its high Q factor, a MIM capacitor does not load the resonator significantly. The input impedance of a buffer amplifier, usually in the form of a common source follower stage, may be represented by gate resistance r_g and gate to drain capacitance C_{gd} connected in series. For signal frequencies much less than f_t of the device (frequency at which MOS gate current equals drain current), a quality factor of the input network of a buffer also reaches high values. Therefore, for typical values of gm in the range up to 20 mA/V, gyrator capacitances of few hundreds of fF and resistance R_{out} up to few kΩ, an ideal degenerated gyrator produces sufficient levels of negative resistance to sustain oscillations over a wide frequency band.

The phase condition determines the resonant frequency of the oscillator. In the case of the ideal resonator considered here, the only factor limiting upper oscillation frequency is the static power necessary to provide proportional magnitude of gm. The lower limit of tuning is restricted by a physical size of an integrated capacitor used. Thus as long as available power and silicon area are within predetermined values, the ideal degenerated gyrator does not limit the bandwidth of the oscillator.

It should be stated that the above conclusions are valid only if there are no losses present in the circuit and therefore are entirely theoretical. As all practical implementation of a CMOS resonator will suffer from various additional parasitic effects, the Barkhausen criteria have to be reviewed in the presence of these imperfections. To fully

describe an oscillator behavior, it is important to include all of the most significant circuit parasitics in the model. The issue of resonator losses is addressed later in this chapter.

4.4   Sensitivity of ideal degenerated gyrator resonator

Before the non-ideal degenerated active inductor circuit is discussed, it is also worth analysing how the circuit performance is affected by finite parameter tolerances. A standard analysis tool known as the *classical sensitivity functions* are usually sufficient to indicate the relative changes of small signal parameters with varying component values. Such functions are defined as [97]

$$S_x^y = \frac{\delta y}{\delta x} \frac{x}{y} \tag{4.17}$$

where y denotes analysed parameter and x represents the value of a single circuit component. When x differs from its predetermined designed value (either as a result of process tolerances or intentional change) it causes a respective change of y with a magnitude and direction determined by (4.17). In fact, this is a linear approximation of a parameter deviation around its static state exactly as a small signal approximation applied to a nonlinear circuit at a given DC bias point. Although for a large perturbation the relative error of this method increases, it still indicates the correct direction of a parameter change. The result of sensitivity function calculation is interpreted as the per-unit variation of y due to a given per-unit change of x [97]. For example, the sensitivity function of a resonant frequency of any passive LC tank to the variations of tank capacitance equals -0.5. Therefore for every 1% increase of the capacitance, the resonant frequency will drop by 0.5%, providing the tank inductance remains constant.

The sensitivity of an active inductor resonator differs from that of its passive counterpart. The active inductance depends on amplifiers and requires power supply while the passive one does not. Typically, the sensitivity of the inductance of a standard gyrator to power supply variations is given by sensitivity functions of a transconductance of respective amplifiers. Although parasitic capacitances of amplifiers also change

with supply voltage (influencing total inductance), the main contribution to total deviation comes from the gm of the transistors. In this case, the sensitivity function is approximately equal to [51]

$$S_{V_{DD}}^{L} = \frac{\delta L}{\delta VDD} \frac{VDD}{L} \approx -\left(S_{VDD}^{gm_1} + S_{VDD}^{gm_2}\right)\Bigg|_{L=\frac{Cg}{gm_1 gm_2}} \tag{4.18}$$

where $S_{VDD}^{gm_1}$ and $S_{VDD}^{gm_2}$ are the transconductance sensitivity functions of amplifiers on VDD variations. In general, these functions vary between different CMOS processes and also depend on the architecture of a transconductor. Usually a numerical simulation is sufficient to estimate it.

Since an active inductor tank is the main point of interest of this thesis, it is more convenient to extend Yuan's formula (4.18) to show how the resonant frequency changes with V_{DD}. Using (4.17) this function is found to be

$$S_{VDD}^{\omega_0} \approx \frac{\delta\omega_0}{\delta VDD} \frac{VDD}{\omega_0} = \frac{1}{\sqrt{C_T}} \frac{-1}{2\sqrt{L^3}} \frac{\delta L}{\delta VDD} \frac{VDD}{\omega_0} = -\frac{1}{2} S_{VDD}^{L} = \frac{1}{2}\left(S_{VDD}^{gm_1} + S_{VDD}^{gm_2}\right)$$
$$\tag{4.19}$$

As expected, any active inductor resonator is prone to power supply variations and therefore special care has to be taken to minimise this effect. The sensitivity function (4.19) can be treated as a normalised form of a frequency pushing of the resonator, that typically is expressed in Hz/V. In the case of the proposed degenerated gyrator tank, (4.19) holds as long as no active devices are used in place of R_{out} because these introduce additional degree of $\omega_0(VDD)$ dependence, not included in the analysis.

Other sensitivity functions can also be derived using the same approach. Table 4.2 consists of the most significant ones for a standard and the proposed degenerated gyrator circuit. All variables used in expressions correspond to a small signal model from Section 4.3. The first part includes an equivalent parallel inductance sensitivity, followed by a resonant frequency and an equivalent parallel negative resistance functions, respectively. Please note, as a standard active inductor lacks a phase shifter, no negative resistance is generated and some of the sensitivity functions do not apply. In addition, the results for a degenerated active inductor are functions rather than fixed

Table 4.2: Sensitivity comparison between active inductor resonators

Sensitivity function S_x^y	Active inductor resonator type		
	Standard	Degenerated	
	Value	Expression	Value
$S_{gm_1}^{L_p}$	-1	n/a	-1
$S_{gm_2}^{L_p}$			
$S_{C_g}^{L_p}$	1	$\dfrac{C_g}{C_P}\dfrac{1+\omega^2/\omega_z^2(1+2C_{out}/C_g)}{1+\omega^2/\omega_z^2}$	0.5-1.5
$S_{C_{out}}^{L_p}$	n/a	$\dfrac{C_{out}}{C_P}\dfrac{1+\omega^2/\omega_z^2(1+2C_g/C_{out})}{1+\omega^2/\omega_z^2}$	
$S_{R_{out}}^{L_p}$		$\dfrac{2\omega^2}{\omega_z^2+\omega^2}$	0.5-2
$S_{gm_1}^{\omega_0}$	0.5	$\dfrac{gm_1 gm_2}{\omega_z^2 C_P C_T+4gm_1gm_2-\sqrt{\omega_z^2 C_P C_T}\sqrt{\omega_z^2 C_P C_T+4gm_1 gm_2}}$	0.25-0.5
$S_{gm_2}^{\omega_0}$			
$S_{C_T}^{\omega_0}$	-0.5	$-S_{gm_{1,2}}^{\omega_0}$	
$S_{C_g}^{\omega_0}$		$\left(2-3\dfrac{C_g}{C_P}\right)S_{gm_{1,2}}^{\omega_0}-\dfrac{C_{out}}{C_P}$	-0.3- -0.5
$S_{C_{out}}^{\omega_0}$	n/a	$\left(2-3\dfrac{C_{out}}{C_P}\right)S_{gm_{1,2}}^{\omega_0}-\dfrac{C_g}{C_P}$	
$S_{R_{out}}^{\omega_0}$		$-1+2S_{gm_{1,2}}^{\omega_0}$	-0.5-0
$S_{gm_1}^{R_{pdg}}$		n/a	-1
$S_{gm_2}^{R_{pdg}}$			
$S_{C_g}^{R_{pdg}}$	n/a	$\dfrac{\omega^2}{\omega_z^2+\omega_2}\left(1+\dfrac{C_g^2-C_{out}^2}{C_P^2}\right)$	0-1
$S_{C_{out}}^{R_{pdg}}$		$\dfrac{\omega^2}{\omega_z^2+\omega_2}\left(1+\dfrac{C_{out}^2-C_g^2}{C_P^2}\right)$	
$S_{R_{out}}^{R_{pdg}}$		$\dfrac{\omega^2-\omega_z^2}{\omega_z^2+\omega_2}$	-1-1

values (excluding $S_{gm}^{L_p}$ and $S_{gm}^{R_{pdg}}$) and were evaluated for a set of parameters presented in Table 4.3. The magnitudes of these parameters is estimated assuming sub-GHz frequency of operation and reduced power consumption.

Table 4.3: Simulation parameters chosen to evaluate sensitivity of the proposed degenerated gyrator.

Value	Model parameters						
	gm_1	gm_2	R_{out}	C_{out}	C_g	C_T	Frequency
	mA/V		kΩ	pF			MHz
minimum	5		0.5	0.5		1	100
maximum	15		5	1.5		3	1000

As the presented results show, a degenerated active inductor resonator is more sensitive to component variations than a standard gyrator circuit. Although most of the common parameters are approximately the same, a degenerated resonator has two more components controlling its small signal parameters. Resistance R_{out} may be either realised as an active circuit or a passive component. The first solution, potentially allows us to set resistance to the wanted level, but in a presence of a large amplitudes, it introduces new non-linearities and is power supply sensitive. On the other hand, a passive resistor in a commercial sub-micron CMOS process typically has a tolerance of up to ±30%. In the worst case, such a large variation causes almost ±60% variation in inductance (Table 4.2, $S_{R_{out}}^{L_p} = 2$). Therefore one may conclude that using a passive phase shifter is rather impractical. However, as indicated by Table 4.2, the actual resonant frequency deviation in the worst case is only ∓15%. Due to a proportionality between the parallel equivalent inductance and the signal frequency from (4.9), when the resonant frequency is shifted down it also decreases inductance, partially compensating for any R_{out} variations. In addition, the transconductance of both amplifiers can be adjusted to tune the tank back to the nominal frequency. As gm is proportional to a bias current of transistor, some additional power consumption should be expected and therefore included early at a circuit design stage. Thus, passive resistors can be used to implement R_{out}, improving both the sensitivity on power supply changes and the linearity of the degenerated gyrator resonator.

4.5 Non-ideal model of degenerated active inductor resonator

In practice, all electronic circuits suffer from parasitics. From a gyrator-based resonator perspective, three types of non-idealities become especially important:

- Intrinsic RC phase shifting networks of transconductors. These include capacitances present at each node due to a geometry of MOSFET devices and resistance of transistor gate. As a result, parasitic phase shift components are generated, affecting the proposed negative resistance generation mechanism.

- Finite channel conductance of transistors: This is manifested as additional resistive losses that have to be compensated in order to start and sustain oscillations. As these losses depend on bias of active devices, their influence on a degenerated gyrator circuit is complex and require a separate, thorough analysis.

- Finite input resistance of a resonator: These contribute to total resistive losses of the resonator. Since an active inductor is in fact a feedback system, the resulting impedance seen at the input of a complete circuit is different than that of each separate block [43, 97]. Thus, the input impedance of degenerated gyrator depends not only on a limited conductance of MOS devices but also changes with a circuit configuration of transconductance amplifiers.

To study how parasitics affect a performance of degenerated gyrator resonator, a new circuit model is presented, illustrated in Figure 4.8. It depicts a resonant tank with a non-ideal transconductors and the output RC phase shifter. The model is a combination of the proposed ideal degenerated gyrator tank from Section 4.3 and a lossy standard active inductor resonator from Chapter 3, Section 3.5.

Typically, the largest parasitic capacitances originate from the DC bias current mirrors, that for the purposes of noise and current matching, are designed with larger channel lengths than the minimum achievable by a technology. These capacitors together

4.5 Non-ideal model of degenerated active inductor resonator
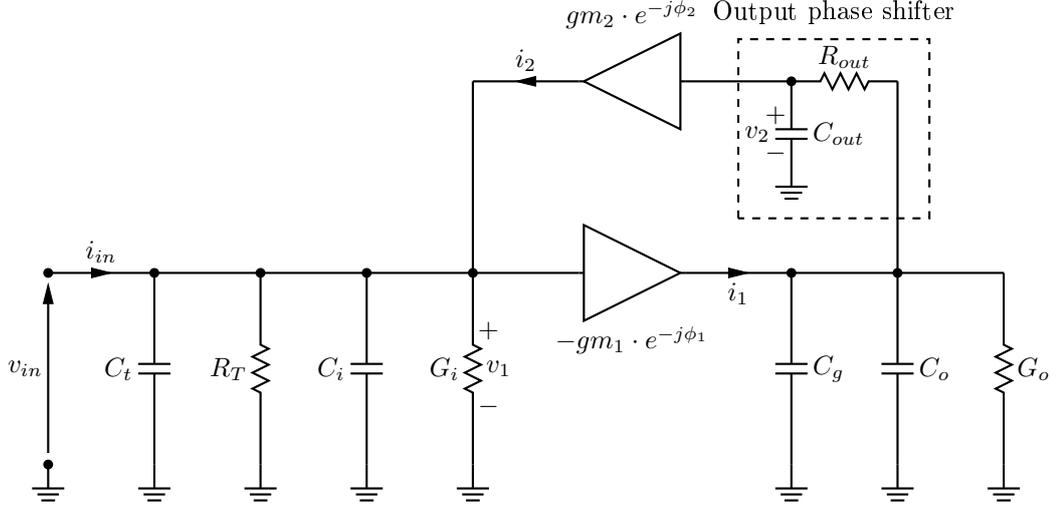
Figure 4.8: Non-ideal degenerated active inductor resonator.

with a finite output resistance of MOS transistors, introduce additional parasitic poles to the circuit. In the simplest situation, it is assumed that single MOS transconductors are employed and their phase lag is negligible due to proper device sizing and layout. This corresponds to $e^{-j\phi_{1,2}} \approx 1$ (Figure 4.8) and only the output phase shifter contributes to the compensation mechanism. Using KVL, an equivalent input admittance of degenerated gyrator is now

$$y_{in}(j\omega) = j\omega C_T + \frac{1}{R_T} + G_i + \frac{1}{R_{ns-loss} + R_{ns-neg} + j\omega L_{nsdg}} \tag{4.20}$$

where

$$C_T = C_t + C_i \tag{4.21}$$

$$R_{ns-loss} = \frac{G_o}{gm_1 gm_2} \tag{4.22}$$

$$R_{ns-neg} = -\frac{\omega^2 \left(C_g + C_o\right) C_{out} R_{out}}{gm_1 gm_2} \tag{4.23}$$

$$L_{nsdg} = \frac{C_g + C_o + C_{out} \left(1 + R_{out} G_o\right)}{gm_1 gm_2} \tag{4.24}$$

The first terms of (4.20) represent a total input capacitance and conductance. The third term consists of positive and negative resistors connected in series with an inductance. In contrast to a standard gyrator with losses, an inductance is now increased due to an output conductance G_o.

93

4.5 Non-ideal model of degenerated active inductor resonator

As in the case of an ideal degenerated resonator, it is more convenient to explore the parallel equivalent circuit. Note, that because there are now two resistors connected in series with an inductor, the real component after transformation consists of two resistors connected in series. To simplify the quality factor derivation, some auxiliary variables are used

$$C_G = C_g + C_o + C_{out}(1 + R_{out}G_o) \tag{4.25}$$

and

$$\omega_{z1} = \frac{G_o}{C_G} \tag{4.26}$$

$$\omega_{z2} = \frac{C_G}{(C_g + C_o)\,C_{out}R_{out}} \tag{4.27}$$

Substituting (4.25)-(4.27) into a standard definition of Q, the quality factor of a series RL circuit is found

$$Q_{nsdg}(\omega) = \frac{\omega L_{nsdg}}{R_{ns-loss} + R_{ns-neg}} = \frac{\omega C_G}{G_o - \omega^2\,(C_g + C_o)\,C_{out}R_{out}} = \frac{\omega\omega_{z2}}{\omega_{z1}\omega_{z2} - \omega^2} \tag{4.28}$$

The parallel equivalent resistance of non-ideal degenerated gyrator consists of two components in series and is equal to

$$R_{npdg}(\omega) = \frac{G_o - \omega^2\,(C_g + C_o)\,C_{out}R_{out}}{gm_1 gm_2}\left(1 + \frac{\omega^2\omega_{z2}^2}{(\omega_{z1}\omega_{z2} - \omega^2)^2}\right) =$$

$$= \frac{C_G}{gm_1 gm_2}\left(\omega_{z1} - \frac{\omega^2}{\omega_{z2}}\right)\left(1 + \frac{\omega^2\omega_{z2}^2}{(\omega_{z1}\omega_{z2} - \omega^2)^2}\right) \tag{4.29}$$

The narrow band inductance transformation yields

$$L_{npdg}(\omega) = L_{nsdg}\left(\frac{Q_{nsdg}^2 + 1}{Q_{nsdg}^2}\right) = \frac{C_G}{gm_1 gm_2}\left(1 + \frac{\left(\omega_{z1}\omega_{z2} - \omega^2\right)^2}{\omega^2\omega_{z2}^2}\right) \tag{4.30}$$

As in the case of the ideal circuit, there is also a direct proportionality between R_{npdg} and L_{npdg}, however the relationship is more complex in comparison with (4.10)

$$R_{npdg}(\omega) = \frac{\omega^2\omega_{z2}}{\omega_{z1}\omega_{z2} - \omega^2}L_{npdg}(\omega) \tag{4.31}$$

4.5 Non-ideal model of degenerated active inductor resonator

Finally, the input admittance of a resonator from (4.20) may be presented in a final form

$$y_{in}(j\omega) = \frac{1}{R_T} + G_i + \frac{gm_1 gm_2}{C_G \left(\omega_{z1} - \frac{\omega^2}{\omega_{z2}}\right)\left(1 + \frac{\omega^2 \omega_{z2}^2}{(\omega_{z1}\omega_{z2} - \omega^2)^2}\right)} +$$
$$+ j\left(\omega C_T - \frac{gm_1 gm_2}{\omega C_G \left(1 + \frac{\left(\omega_{z1}\omega_{z2} - \omega^2\right)^2}{\omega^2 \omega_{z2}^2}\right)}\right) \quad (4.32)$$

As before, by equalising the reactances of the parallel model, a resonant frequency can be found. Again, a 4$^{\text{th}}$ order equation has to be solved, and only one solution is real and positive. Thus, the resonant frequency of a non-ideal degenerated resonator is equal to

$$\omega_{0ndg} = \frac{\sqrt{2}}{2}\omega_{z2}\sqrt{\sqrt{1 - 4\frac{\omega_{z1}}{\omega_{z2}} + 4\frac{gm_1 gm_2}{\omega_{z2}^2 C_G C_T} + 2\frac{\omega_{z1}}{\omega_{z2}} - 1}} \quad (4.33)$$

If there are no losses in the circuit ($\omega_{z1} = 0$), the resonant frequency equals that of the ideal degenerated gyrator from (4.13) (providing that all of the other components are the same). Note, that the resonance is controlled not only by capacitors and transconductance but also depends on G_o through C_G, ω_{z1} and ω_{z2}.

The effective value of R_{npdg} no longer monotonically changes with frequency as in the case of ideal circuit. A finite G_o connected in series with the negative component modifies the total resistance experienced by the resonator. At low frequencies G_o becomes dominant and negative resistance is diminished. On the contrary, at high frequencies, the negative term becomes larger. Thus, the range of frequencies for which a negative resistance is available is inversely proportional to the circuit losses. To illustrate this behavior, the inverse of (4.31) was simulated using MATLAB and results are presented on Figure 4.9. The inverse of R_{npdg} is studied because at a certain frequency, given by

$$\omega = \sqrt{\omega_{z1}\omega_{z2}} \quad (4.34)$$

G_o cancels the negative term and the parallel resistance approaches infinity. Thus, it is more convenient to analyse and plot the total tank conductance instead.
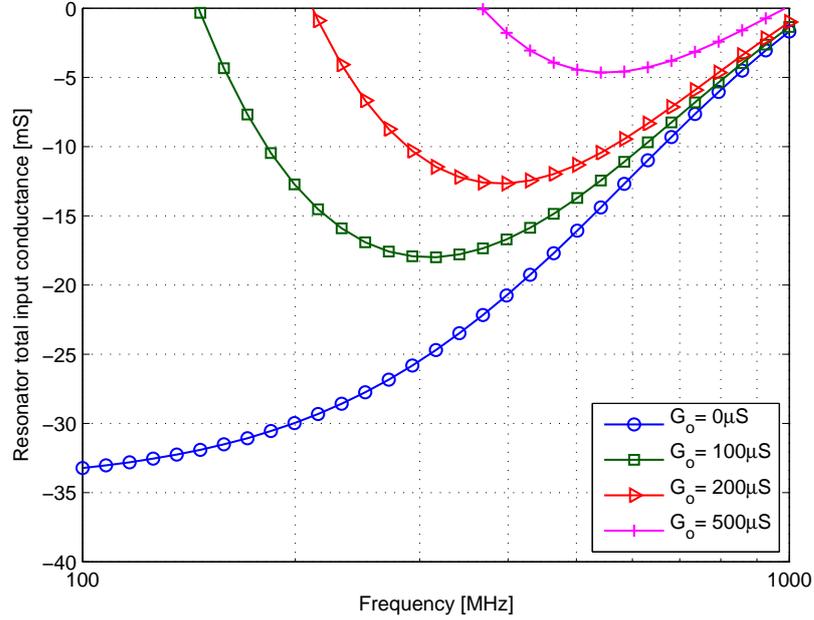
Figure 4.9: Total input conductance of lossy degenerated resonator as function of the finite output conductance.

Table 4.4: Simulation parameters chosen to evaluate influence of G_o on generated negative conductance.

Parameters									
gm_1	gm_2	R_{out}	C_{out}	C_g	C_o	C_i	C_t	R_T	G_i
mA/V		kΩ	pF					kΩ	mS
10		2	0.2				4	5	10

Table 4.4 contains a set of parameters used to simulate circuit behavior from 100 MHz to 1000 MHz. The input losses of the gyrator, represented by G_i are characterised with a relatively high value of 5 mS to simulate the behavior of low-Q active inductor. More details behind this particular choice are given later in this section. The first curve represents an ideal case with no losses i.e. $G_o = 0$, whereas the last three represent a situation where losses increase in relation to an amplifier transconductance. Interestingly, the behavior of all curves correspond to the results from [7], where Kaunisto studied thoroughly an influence of input losses of a standard active inductor on a quality factor of the RF filters he proposed. Thus, although the analysis presented in this

thesis is original and differs from the one of Kaunisto, both share similar results, giving confidence that the behavior of the proposed circuit in the presence of resistive losses is correct.

As explained before, an increased G_o shifts the boundary of negative resistance availability range into higher frequencies. In the worst of the presented cases, this range has been decreased by 370 MHz in comparison to the ideal one, showing the significant impact of G_o on the tuning range of a non-ideal resonator. For this reason it is important to give more insight on the origin of parasitic components in CMOS gyrators and possible ways of minimising their effect on circuit performance.

4.5.1   Intrinsic phase lag of transconductors

In general, transconductor parasitics depend on two factors. Available technology and related device fabrication process are the first one. In the case of a standard commercial CMOS process, UMC 18MM for example, all of the available transistor models are supplied by the manufacturer. Together with appropriate circuit simulations, these process libraries allow the extraction of the major parasitics. The second factor is related to a transconductance amplifier configuration. Depending on the required gyrator performance and power consumption, transconductance amplifiers may be obtained using either a single transistor or more elaborate, multistage circuits. For the purpose of this section, only the former is analysed. This choice can be explained as follows. As suggested in Chapter 3, Section 3.3.2, the noise of a gyrator resonator is proportional to its quality factor. Therefore low Q active inductors architectures using single transistor amplifiers [52, 53, 60] can be considered as a possible solution for decreased noise.

When single transistor transconductors are used, the analysis of how their parasitics influence the degenerated gyrator circuit is relatively simple. As an example, one can consider the input parasitic phase lag networks of three single MOS transconductance amplifiers, illustrated in Figure 4.10. Among the presented configurations, a common source circuit (CS) suffers the largest phase lag due to the Miller effect, where a relatively small gate-to-drain capacitance C_{gs} is multiplied by a device gain. Since the common
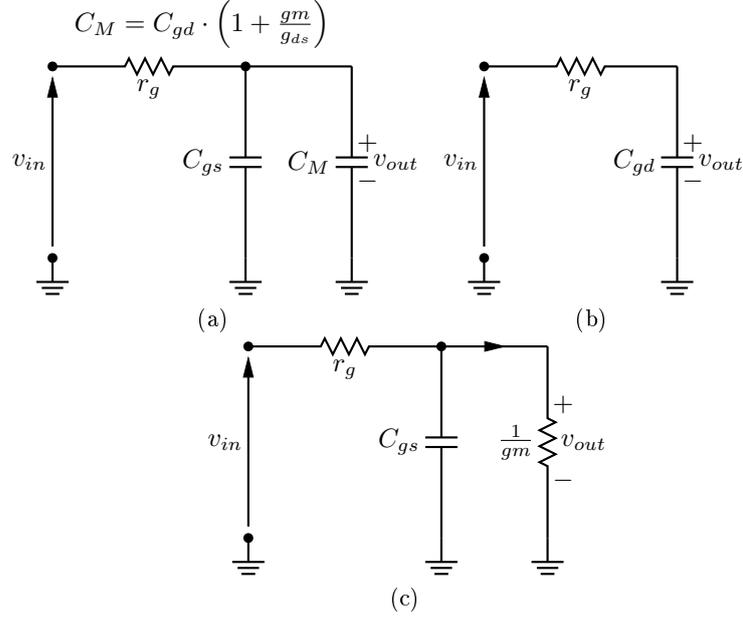
Figure 4.10: Input parasitic phase lag networks of basic CMOS transconductors: (a) common source with Miller capacitance, (b) common drain and (c) common gate.

drain (CD) and the common gate (CG), do not suffer from this effect, their respective phase shifts never exceed that of a CS amplifier. Practically, a CS transconductor is always present in the degenerated gyrator, as it provides the negative gain necessary to simulate inductance. Thus, care has to be taken to minimise intrinsic MOS phase lag where possible.

The corresponding parasitic phase shifts for each of the described transconductors are

$$\phi_{CS} = -\arctan \omega \left(C_{gs} + C_M \right) r_g \qquad (4.35)$$

$$\phi_{CD} = -\arctan \omega C_{gd} r_g \qquad (4.36)$$

$$\phi_{CG} = -\arctan \frac{\omega C_{gs} r_g}{1 + r_g gm} \qquad (4.37)$$

For all of the circuits form Figure 4.10, to ensure that the parasitic pole is negligibly small, the gate resistance r_g should be minimised. The common practice is either to use contacts on both ends of the transistor gate, a transistor folding or both. These techniques allow us to minimise r_g by up to a factor 4 [26]. Once r_g can be neglected,

the remaining capacitors can be directly incorporated into the output phase shifter or, in the case of a input transconductor, to the remaining components of the resonator.

To illustrate the importance of device characterisation and the corresponding magnitude of parasitics, typical submicron CMOS process parameters can be applied to (4.35)-(4.37). Table 4.5 presents the parameters and the calculation results for each type of a single transistor transconductance amplifier considered here. Assuming the highest signal frequency of 1000 MHz, approximate phase shifts are respectively: $\phi_{CS} \approx 0.023\pi$ rad for CS, ϕ_{CD}, $\phi_{CG} \approx 0.002\pi$ rad for CD and CG amplifiers. Although these values can be neglected for the frequencies up to 1000 MHz, the large input capacitance of the CS amplifier (C_{in} in the range of 0.2 pF-1 pF for 180 nm transistor) has to be included in the resonator tank. One can therefore conclude that the smallest available transistor size should be used, however this approach usually does not yield the optimal noise performance or circuit linearity.

Table 4.5: Calculated parasitic phase shift for a single transistor transconductance amplifier at 1 GHz

Transistor parameters			Amplifier	Phase shift	
				rad	deg
W	µm	72	CG		
L		0.25		0.002π	0.36
I_d	mA	1.3	CD		
gm	mA/V	10			
g_{ds}	µS	300	CS	0.023π	4.14
C_{gs}	fF	100			
C_{gd}		30			
r_g	Ω	<10			

4.5.2 Output resistance of MOS transistors

The main mechanism responsible for this parasitic component comes from the channel length modulation (CML) effect. At the boundary of the saturation, a MOS conductive channel is pinched-off at the drain, and the drain to source voltage V_{DS} ideally does not change channel current any more. However in practice, further increases in V_{DS} cause a

depletion region being formed between an actual pinch-off point and the drain contact. As a result, the effective channel length is decreased from its drawn (physical layout) dimension and transistor current increases proportionally to the difference between V_{DS} and saturation voltage. This behavior is represented as a finite differential resistance r_{ds} between drain and source. This becomes more significant when the MOS transistor drawn gate length becomes relatively small i.e. if minimum size devices are used. To compare various devices in terms of their output resistance, the *DC gain* can be defined

$$A_{DC} = gm \cdot r_{ds} = \frac{gm}{g_{ds}} \tag{4.38}$$

and for a sub-micron CMOS devices typical values in the range of 10-40 are observed. Although simple, (4.38) shows the important relationship between the transconductance and the output resistance of MOS devices. Large A_{DC} values indicate that for a given gm, the transistor introduces small output losses and its behavior is closer to that of the ideal current source. On the other hand, when the DC gain is small, g_{ds} represents a significant parasitic load of the transconductor.

As shown at the end of Section 4.5, from a degenerated active inductor resonator perspective, performance is bounded by the available DC gain of MOS transistors used. Both G_i and G_o increase positive losses, diminishing the effect of the negative resistance generated by the phase shifter. Thus to minimise this, a proper sized device has to be used to ensure sufficient levels of A_{DC}. Figures 4.11 and 4.12 illustrate the dependence of DC gain on different channel lengths and on drain current values for NMOS devices in UMC18MM process.

The negative impact of CML on MOS devices becomes more significant for short transistors, indicating an inevitable trade-off between size and performance of a degenerated resonator. For a constant device size, an increasing drain current also reduces gain. Thus, as gm is proportional to the drain current, the DC gain will be reduced for the maximum transconductance value used in the design. Therefore, care has to be taken to ensure that when the highest gm is set, the output resistance of the MOS transistor is still high enough.
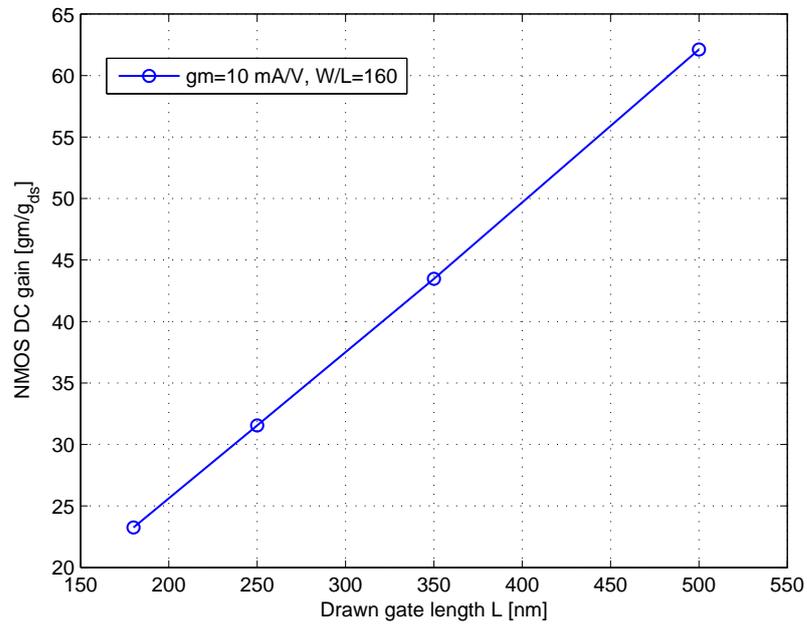
Figure 4.11: Sub-micron MOS transistor DC gain as a function of drawn gate length L for constant drain current.
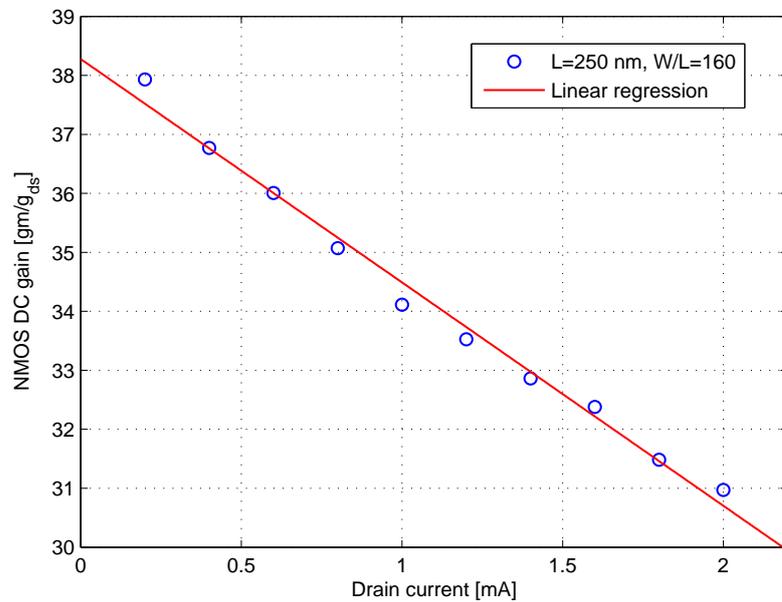
Figure 4.12: Sub-micron MOS transistor DC gain as a function of drain current for constant L.

A common trend in microelectronic design is to use the smallest devices available. As in this case the DC gain of devices becomes smaller, from a degenerated gyrator perspective this leads to increased G_o. This reduces negative conductance generated by the circuit. On the other hand, if the available chip area is severely limited and minimum size devices have to be used, the performance of the active resonator may not be optimal.

The problem of finite output resistance may be partially solved by the help of cascoding, the method previously applied to a standard gyrator by various researchers [55, 64, 75, 98, 99]. A cascoding increases output resistance and boosts A_{DC}, however it may impair circuit linearity and reduces available voltage headroom [51]. Thus, this is not a general solution for the problem of a finite g_{ds}, especially when signal swings are relatively large as in the case of an oscillator.

4.5.3   Input resistance of gyrator

This parasitic component is connected directly to the tank resistance R_T. Typically, a resonator is loaded by a buffer and G_i is larger than $1/R_T$, therefore dominating the total losses of the resonator. In general G_i consists of two terms. The first term, as shown in Chapter 3, comes from the finite drain-source resistance of MOS transistors. For this reason larger DC gain values are always preferable. The second term is related directly to a gyrator configuration. As an active inductor is a feedback circuit, this term is not equivalent to the resistance of the input transconductor but depends on the transfer functions of both amplifiers. In the case of a simple, two transistor architecture, the gyrator consists of a CS amplifier as an inverting stage and either a CD buffer [52] or a CG device [53] as the feedback non-inverting transconductor. Regardless of which port is chosen, the resistive part of the input admittance or impedance equals gm or $1/gm$ of one of the amplifiers, respectively. For high A_{DC}, this term dominates the total input resistance. As an example, to achieve resonant frequencies up to 1000 MHz using a standard gyrator, a typical value of a MIM capacitor employed can be in the range of 2 pF-4 pF. This corresponds to a transconductance values around 10 mA/V and a

parallel resistance of 100 Ω. If not compensated, this resistance reduces the quality factor of a resonator below any practical value.

To overcome this problem multistage amplifiers can be used. Karsilayan et al. [100] proposed a two stage non-inverting transconductor in CD-CG configuration. Uyanik et al. [101] presented a RF filter with also a non-inverting amplifier using a cascade of PMOS and NMOS inverters. Thanachayanont et al. [55] used cascode and regulated cascode in place of the inverting stage. For each of these methods, the input resistance is increased roughly by the factor of A_{DC}. The costs are an increased number of non-linear devices and possibly higher harmonic content in the presence of a large signal of the oscillator. On the other hand, if a simple transconductor are used, the obvious drawback is a large input conductance and power necessary to compensate it by an external circuit. If the proposed degeneration technique is used instead of an external negative resistor, then the total power consumption of an oscillator can be minimised because a passive RC phase shifter does not require any DC power to operate.

4.5.4 Barkhausen criteria for non-ideal degenerated gyrator oscillator

As in the case of an ideal resonator, the Barkhausen criteria can be derived from the expression for the input admittance (4.32). Both conditions are equal to

$$\frac{1}{R_T} + G_i + \frac{gm_1 gm_2}{C_G \left(\omega_{z1} - \dfrac{\omega^2}{\omega_{z2}} \right) \left(1 + \dfrac{\omega^2 \omega_{z2}^2}{(\omega_{z1}\omega_{z2} - \omega^2)^2} \right)} = 0 \quad \text{:amplitude condition} \quad (4.39)$$

$$\omega C_T - \frac{gm_1 gm_2}{\omega C_G \left(1 + \dfrac{(\omega_{z1}\omega_{z2} - \omega^2)^2}{\omega^2 \omega_{z2}^2} \right)} = 0 \quad \text{:phase condition} \quad (4.40)$$

Solving the phase condition yields a resonant frequency from (4.33). The amplitude condition can be simplified, assuming that a buffer amplifier is used and hence the resonator losses at the output are approximately $G_i + 1/R_T \approx G_i$. If both amplifiers have the same transconductance and the DC gain is large enough that $G_i \approx gm$, the

amplitude condition becomes

$$gm + C_G \left(\omega_{z1} - \frac{\omega^2}{\omega_{z2}} \right) \left(1 + \frac{\omega^2 \omega_{z2}^2}{(\omega_{z1}\omega_{z2} - \omega^2)^2} \right) = 0 \qquad (4.41)$$

This expression indicates the limits of the negative resistance range of a lossy degenerated resonator. Solving for ω yields two positive frequencies ω_{Rneg_L} and ω_{Rneg_H} for which the amplitude condition is fulfilled

$$\omega_{Rneg_{L,H}} = \sqrt{ \frac{\omega_{z2}}{2C_G} \left(gm + C_G(2\omega_{z1} - \omega_{z2}) \mp \sqrt{(gm - C_G\omega_{z2})^2 - 4C_G\omega_{z1}\omega_{z2}} \right) } \quad (4.42)$$

There is a critical gm for which both frequencies are equal, however because C_G, ω_{z1} and ω_{z2} depend on transconductance through G_o, there is no simple formula to calculate its value. Based on MATLAB simulations of (4.42) this value is found to be more than 50 mA/V at frequencies up to 1000 MHz, far more than typical sub-micron devices can reach without an excessive size and power consumption. Thus, as long as the resonant frequency is set between the points calculated from (4.42), the Barkhausen requirements for the oscillations build-up are fulfilled. Figure 4.13 depicts the total input negative conductance and susceptance of a degenerated gyrator resonator with gm depended losses. All of the circuit parameters are presented in Table 4.6.

Table 4.6: Parameters used to simulate total input admittance of degenerated gyrator as a function of gm.

Parameters						
R_{out}	C_{out}	C_g	C_o	C_i	C_T	A_{DC}
kΩ	pF					$-$
3	0.3	0.2	0.1	0.25	4.25	30

By varying the transconductance of both amplifiers simultaneously, the resonant frequency is changed whereas all the circuit losses sufficiently compensated. For a transconductance less than 5 mA/V, positive losses dominate and the circuit is stable. The upper boundary of tuning range is restricted by the power consumption, however the negative resistance is still generated for gm in the range of 25 mA/V.

Figure 4.14 shows a comparison of a tuning range between a standard active inductor tank, described by (4.14) and the circuit from the previous simulation. Both resonators
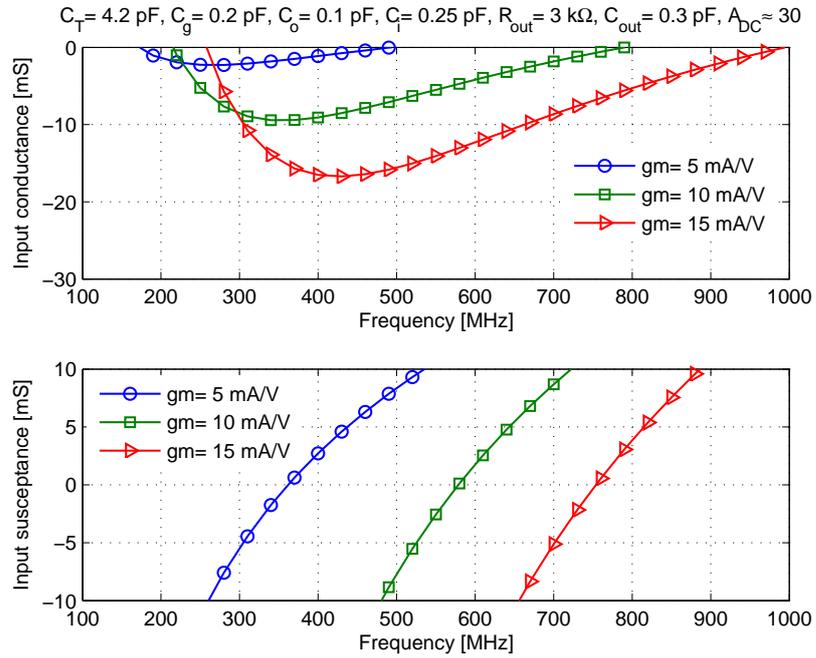
Figure 4.13: MATLAB simulation of real and imaginary parts of input admittance of the prototype tank
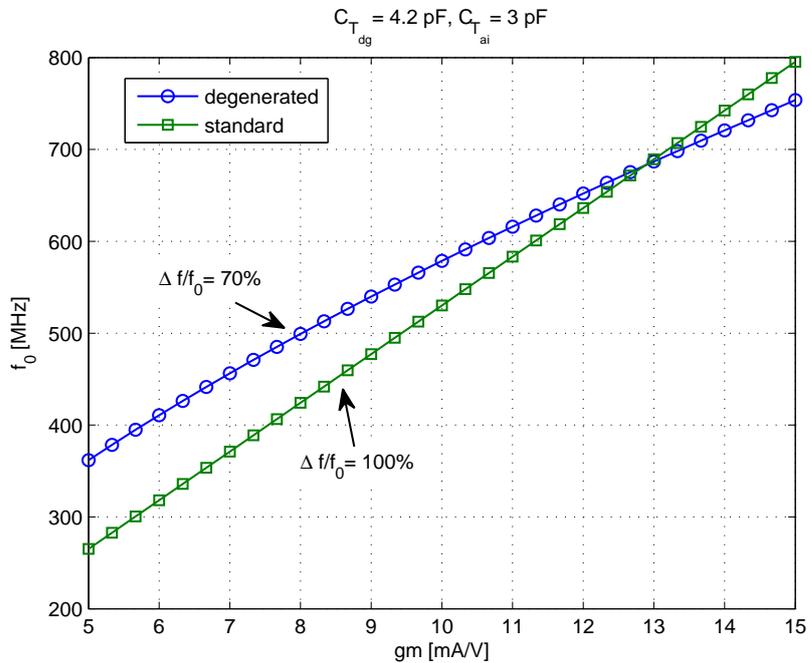
Figure 4.14: Tuning curves

105

are non-ideal and have the same parasitic components. Tank capacitance of the standard circuit has been decreased to place both resonators around the same center frequency. It can be seen that a fractional bandwidth of the degenerated tank is 30% less because the phase shifter introduces an additional pole. This pole modifies the relationship between gm and ω_0, effectively decreasing the tuning sensitivity. On the other hand, a standard gyrator requires more power to compensate the higher losses as long as G_i is not reduced by using multistage amplifiers. Although the tuning range of the degenerated active inductor is restricted, a theoretical tuning range of 70% still proves its capability for wide band operation.

4.6 Noise analysis of degenerated gyrator resonator

As degenerated gyrator resonators do not utilise an external impedance converter but instead use an additional RC circuit, a new noise analysis has to be carried out. The expected noise behaviour should be similar to that of a standard active inductor resonator as both tanks share the same inductance simulation mechanism. Therefore, the output noise should also be proportional to the loaded quality factor of the resonator. Secondly, due to a resistor presence, the noise level will also be higher than that of an uncompensated active inductor. Thus to study noise of a degenerated active inductor resonator, the new noise model has to be derived first.

4.6.1 Proposed noise model

Figure 4.15 depicts the equivalent noise model of a degenerated gyrator resonator, similar to the one from Figure 3.7, however this time the negative resistance is supplied by the gyrator instead. In order to simplify analysis it is assumed that L_{pdg} and R_{pdg} do not change much in a vicinity of the resonant frequency. As explained in Chapter 3, Section 3.3.2.2, R_{load} is used to limit the loaded quality factor, preventing oscillations. Both noise transfer functions from (3.17) are still the same, however due to the correlation between $\overline{v_{ndg}^2}$ and $\overline{i_{ndg}^2}$, they can't be used to calculate output noise directly. The

Figure 4.15: The proposed noise model of degenerated active inductor resonator.
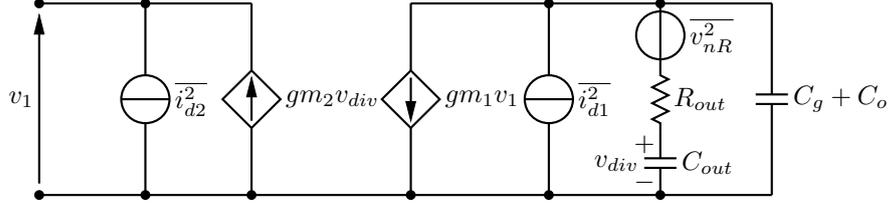
Figure 4.16: Noise sources of degenerated active inductor.

noise analysis begins with the equivalent noise circuit model of a degenerated active inductor illustrated on Figure 4.16. The equivalent input referred noise sources $\overline{v_{ndg}^2}$ and $\overline{i_{ndg}^2}$ are respectively equal to

$$\frac{\overline{i_{ndg}^2}}{\Delta f} = \frac{\overline{i_{d2}^2}}{\Delta f} + \frac{\overline{v_{nR}^2}}{\Delta f} \frac{gm_2^2}{\omega^2 C_{out}^2 R_{out}^2 + 1} = 4kT\gamma gm_2 + 4kT \frac{R_{out}gm_2^2}{\omega^2 C_{out}^2 R_{out}^2 + 1} \qquad (4.43)$$

and

$$\frac{\overline{v_{ndg}^2}}{\Delta f} = \frac{1}{gm_1^2}\left(\frac{\overline{i_{d1}^2}}{\Delta f} + \frac{\overline{v_{nR}^2}}{\Delta f} \frac{\omega^2 C_{out}^2}{\omega^2 C_{out}^2 R_{out}^2 + 1}\right) = \frac{4kT\gamma}{gm_1} + 4kT\frac{R_{out}}{gm_1^2}\frac{\omega^2 C_{out}^2}{\omega^2 C_{out}^2 R_{out}^2 + 1}$$

$$(4.44)$$

In the case of the equivalent current noise source $\overline{i_{ndg}^2}$, the higher the frequency the less noise contribution of R_{out} is. This is a result of the low-pass properties of the $R_{out}C_{out}$ voltage transfer function. Figure 4.17 illustrates the noise PSD of an arbitrary RC circuit in reference to the noise of its resistor. The area under the dashed curve is inversely proportional to the capacitance value as in the case of a passive resonator from Section 2.6.1.1. By contrast, the noise power density of an equivalent input voltage generator $\overline{v_{ndg}^2}$ is proportional to frequency, because the current of the $R_{out}C_{out}$ phase shifter, due to the thermal noise of R_{out}, increases with frequency. In this case the resistor noise is high-pass filtered, yet by analysing (4.43) and (4.44), this transfer function has a

107
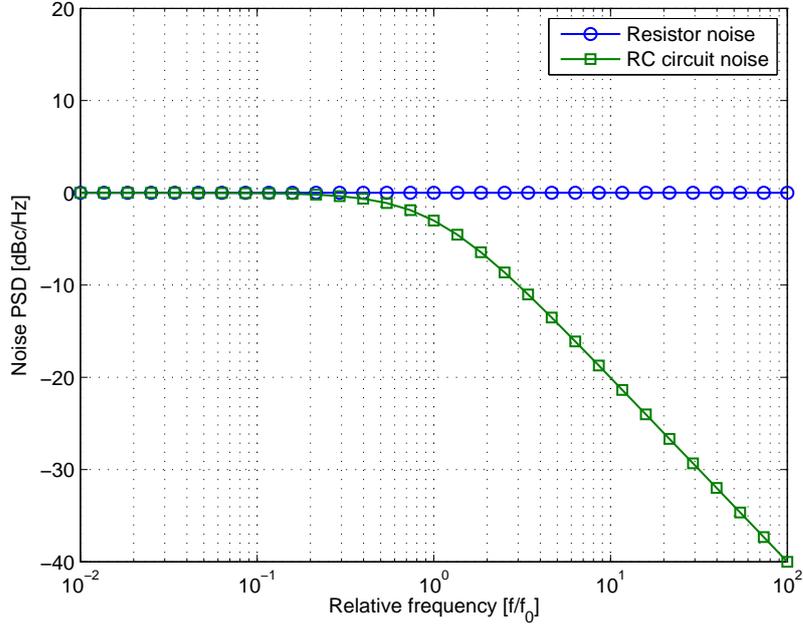
Figure 4.17: Noise power spectral density of RC low-pass filter.

substantially lower magnitude comparing to a low-pass part. Both generators are now correlated through R_{out} and to calculate a total output noise power from (2.35), the respective noise transfer function for the resistor has to be derived. Using KVL, these noise transfer functions of degenerated gyrator from Figure 4.15 are found

$$Z_{ndgQ}(j\omega) = \frac{j\omega L_{pdg} R_T}{j\omega L_{pdg} + R_T \left(1 - \omega^2 C_T L_{pdg}\right)} \tag{4.45}$$

$$A_{ndgQ}(j\omega) = \frac{R_T}{j\omega L_{pdg} + R_T \left(1 - \omega^2 C_T L_{pdg}\right)} \tag{4.46}$$

where R_T is now equal to

$$R_T = \frac{1}{\dfrac{1}{R_{load}} + G_i - \dfrac{1}{R_{pdg}}} = R_{load} \Bigg|_{1/G_i = R_{pdg}} \tag{4.47}$$

Using (4.45) together with (4.43), and grouping terms, the output noise voltage v_{odg} across the resonator is equal to

$$v_{odgQ} = i_{ndg} Z_{ndgQ}(j\omega) + v_{ndg} A_{ndgQ}(j\omega) =$$

108

$$= \left(i_{d2} + v_{nR} \frac{gm_2}{j\omega C_{out} R_{out} + 1} \right) \frac{j\omega L_{pdg} R_T}{j\omega L_{pdg} + R_T \left(1 - \omega^2 C_T L_{pdg} \right)} +$$

$$+ \frac{1}{gm_1} \left(i_{d1} + v_{nR} \frac{j\omega C_{out}}{j\omega C_{out} R_{out} + 1} \right) \frac{R_T}{j\omega L_{pdg} + R_T \left(1 - \omega^2 C_T L_{pdg} \right)} =$$

$$= \left(i_{d2} j\omega L_{pdg} + \frac{i_{d1}}{gm_1} \right) \frac{R_T}{j\omega L_{pdg} + R_T \left(1 - \omega^2 C_T L_{pdg} \right)} +$$

$$+ \frac{v_{nR}}{gm_1} \frac{R_T}{j\omega C_{out} R_{out} + 1} \frac{j\omega \left(C_{out} + gm_1 gm_2 L_{pdg} \right)}{j\omega L_{pdg} + R_T \left(1 - \omega^2 C_T L_{pdg} \right)} \tag{4.48}$$

The first two terms of (4.48) represent the noise behavior of a standard gyrator. The last component corresponds to the noise transfer function of R_{out}, shown below

$$A_{nRQ}(j\omega) = \frac{1}{gm_1} \underbrace{\frac{1}{j\omega C_{out} R_{out} + 1}}_{low-pass} \underbrace{\frac{R_T j\omega \left(C_{out} + gm_1 gm_2 L_{pdg} \right)}{j\omega L_{pdg} + R_T \left(1 - \omega^2 C_T L_{pdg} \right)}}_{band-pass} \tag{4.49}$$

This transfer function consists of a pass-band part associated with the resonator and also incorporating a transmittance zero of $R_{out} C_{out}$ admittance. The second part is a low-pass function related to a voltage gain of $R_{out} C_{out}$ described earlier.

As illustrated on Figure 4.17, this inherent low-pass property can be used to control the amount of resistor noise injected to the resonator. If the cutoff frequency of the RC shifter

$$\omega_{RC} = 1/C_{out} R_{out} \tag{4.50}$$

is set to be lower than the tank resonant frequency $\omega_0 = 1/\sqrt{C_T L_{pdg}}$ then the noise contribution from R_{out} is lowered. This leads to the conclusion that in when the ω_0 is set to 0 (or very close to it), the noise of the resistor can be fully attenuated. This is true, however in this case, the effect of RC phase shifter on the gyrator circuit is cancelled and the negative resistance will not be generated. Therefore, there is an important design trade-off between the amount of noise injected by R_{out} and the magnitude of the negative resistance generated by the resonator.

As an example, Figure 4.18 presents how a low-pass operation of the RC phase shifter affects the noise of a degenerated active inductor resonator. The plot shows an output noise PSD of the resonant tank, caused by the R_{out}, calculated in MATLAB using the last term of (4.48). Table 4.7 presents the corresponding parameters. In each
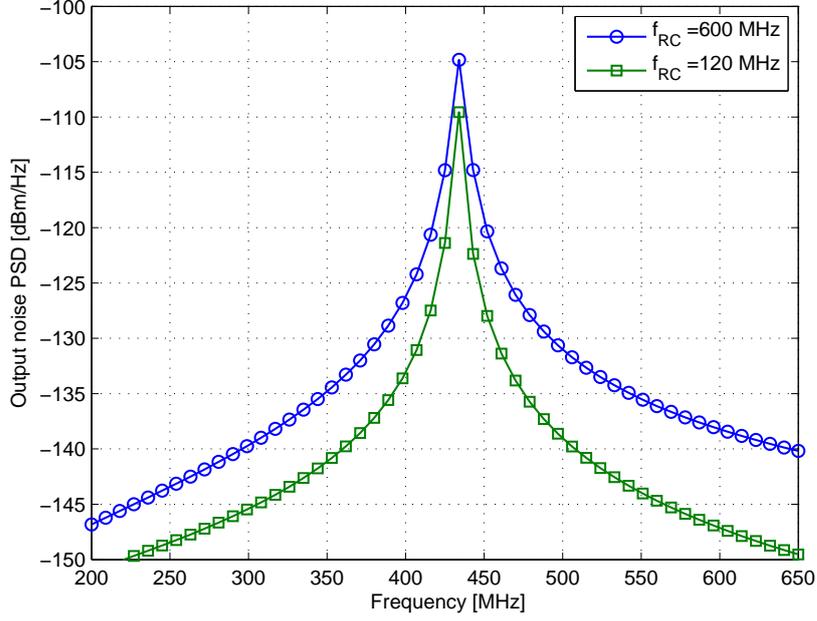
Figure 4.18: Output noise PSD of 434 MHz degenerated gyrator due to R_{out} and for a different RC pole frequencies.

Table 4.7: Simulation parameters used to analyse influence of RC shifter cutoff frequency on output noise of degenerated gyrator resonator

Degenerated gyrator resonator tuned to $f_0 = 434$ MHz							
f_{RC}	gm_1	gm_2	C_{out}	R_{out}	R_T	$C_g + C_o$	C_T
MHZ	mA/V		fF	kΩ		pF	
120	8.8		331	4	5	0.3	4.2
600	4.45		66.3				

case, R_{out} is constant and the cutoff frequency of the shifter is controlled through C_{out} only. When this capacitor is varied, the simulated inductance also changes, affecting the resonant frequency. Thus to keep f_0 constant, gm value is tuned according to (4.13). The curve with the circle marker represents the situation where the $R_{out}C_{out}$ bandwidth spans over a resonant frequency of the tank. The second graph corresponds to the case where a resonator noise has been decreased through a low-pass term from (4.49).

4.6.2 Total noise of degenerated gyrator resonator

Recalling (4.48) it can be seen that all of the noise sources are uncorrelated and the total output noise PSD of the degenerated gyrator is therefore equal to

$$\frac{\overline{v_{odgQ}^2}}{\Delta f} = \frac{\overline{i_{d2}^2}}{\Delta f} |Z_{ndgQ}(j\omega)|^2 + \frac{\overline{i_{d1}^2}}{\Delta f} \frac{1}{gm_1^2} |A_{ndgQ}(j\omega)|^2 + \frac{\overline{v_{nR}^2}}{\Delta f} |A_{nRQ}(j\omega)|^2 =$$

$$= \frac{4kT\gamma R_T^2 \left[\omega^2 L_{pdg}^2 \, gm_2 + \dfrac{1}{gm_1} + \dfrac{R_{out}}{\gamma gm_1^2} \dfrac{\omega^2 \left(C_{out} + gm_1 gm_2 L_{pdg} \right)^2}{\omega^2 C_{out}^2 R_{out}^2 + 1} \right]}{\omega^2 L_{pdg}^2 + R_{pdg}^2 \left(1 - \omega^2 C_T L_{pdg} \right)^2} \tag{4.51}$$

Using (4.51), the spot noise of the degenerated gyrator at the resonant frequency is approximately equal to

$$\frac{\overline{v_{odgQ}^2}}{\Delta f} \approx 4\gamma Q_L^2 \frac{kT}{gm} \left[2 + \frac{1}{\gamma gm R_{out}} \left(1 + \frac{C_T}{C_{out}} \right)^2 \right] \Bigg|_{\substack{\omega=\omega_0 \\ gm_1=gm_2=gm \\ C_T/gm^2 \equiv L_{pdg} \\ Q_L=R_T/\omega_0 L_{pdg} \\ \omega_0^2 C_{out}^2 R_{out}^2 \gg 1}} \tag{4.52}$$

Using (2.35) and the corresponding transfer functions, the total output noise power of the resonator from Figure 4.15 can be calculated.

$$\overline{v_{odgQ}^2} = \frac{1}{2\pi} \frac{\overline{i_{d2}^2}}{\Delta f} \int\limits_0^\infty |Z_{ndgQ}(j\omega)|^2 \, d\omega + \frac{1}{2\pi} \frac{\overline{i_{d1}^2}}{\Delta f} \frac{1}{gm_1^2} \int\limits_0^\infty |A_{ndgQ}(j\omega)|^2 \, d\omega +$$

$$+ \frac{1}{2\pi} \frac{\overline{v_{nR}^2}}{\Delta f} \int\limits_0^\infty |A_{nRQ}(j\omega)|^2 \, d\omega \tag{4.53}$$

Although the integrals related to the noise sources of the transconductors give the same result as in (3.15), the third function related to R_{out}, does not have a simple explicit solution. However, one can assume that the cutoff frequency of $R_{out}C_{out}$ is lower than the tank bandwidth and the resonant frequency. In this case, the noise from R_{out} is low-pass filtered by the RC phase shifter, as discussed in Section 4.6.1. As a result, the noise transfer function (4.49) becomes

$$A_{nRQ}(j\omega) \approx \frac{1}{gm_1} \frac{1}{j\omega C_{out} R_{out}} \frac{R_T j\omega \left(C_{out} + gm_1 gm_2 L_{pdg} \right)}{j\omega L_{pdg} + R_T \left(1 - \omega^2 C_T L_{pdg} \right)} =$$

$$= \frac{R_T(C_{out} + gm_1 gm_2 L_{pdg})}{gm_1 C_{out} R_{out}} \frac{1}{j\omega L_{pdg} + R_T \left(1 - \omega^2 C_T L_{pdg} \right)} \tag{4.54}$$

simplifying integration. The total output noise power from (4.53) is found as

$$
\overline{v_{odgQ}^2} \approx \frac{kT\gamma R_T}{C_T} \left[gm_2 + \frac{C_T}{gm_1 L_{pdg}} \left(1 + \frac{(C_{out} + gm_1 gm_2 L_{pdg})^2}{\gamma C_{out}^2 R_{out}} \right) \right] =
$$
$$
= \frac{kT\gamma}{C_T} Q_L \left[2 + \frac{1}{\gamma R_{out} gm} \left(1 + \frac{C_T}{C_{out}} \right)^2 \right] \Bigg|_{\substack{\omega = \omega_0 \\ gm_1 = gm_2 = gm \\ C_T/gm^2 \equiv L_{pdg} \\ Q_L = R_T/\omega_0 L_{pdg}}} \tag{4.55}
$$

The first conclusion is that the total output noise power of a degenerated gyrator resonator is similar to that of an active inductor tank with external negative resistance (3.18). In both cases the noise is proportional to the loaded quality factor of the resonator. In addition, (4.55) indicates that the intrinsic Q-enhancing mechanism contributes to the output noise through R_{out}. In this case, the noise of the RC phase shifter is directly related to the unloaded tank quality factor Q_0. If the resonator losses are mainly determined by the gyrator transconductance gm (which is the case when a single MOS transconductance amplifiers are used), the unloaded quality factor Q_0 is very low. To compensate for the high losses, larger values of R_{out} are necessary, which in turn causes a stronger low-pass filtration of the resistor noise around the resonant frequency. This explains the $1/R_{out}$ term in (4.55). When the same low quality factor gyrator is used together with an external negative resistor (instead of the RC phase shifter), then according to (3.18), the amount of noise injected to the resonator will increase. This is caused by gm_{ex} value approaching that of gm of the transconductors. Therefore, for simple active inductors, the proposed passive compensation method delivers less noise than the standard approach.

On the contrary, if a gyrator input losses are weakly dependent on gm, the resulting unloaded quality factor is substantially higher and therefore a small transconductance of an external negative resistor is sufficient for compensation. In the case of degenerated gyrator however, smaller R_{out} shifts $R_{out}C_{out}$ pole into higher frequencies. Most of the resistor noise is injected to the tank and even a relatively small R_{out} may still introduce more noise than the external negative resistor. It has to be indicated that (4.55) does not model noise behavior properly for extremely small resistances because if $R_{out} \to 0$

then the noise would be infinite. In this case, total output noise would be

$$\overline{v_{odgQ}^2} \approx \frac{kT\gamma}{C_T} Q_L \left[2 + \frac{R_{out}\omega_0^2 \left(C_T + C_{out}\right)^2}{\gamma gm} \right] \Bigg|_{\substack{\omega=\omega_0 \\ gm_1=gm_2=gm \\ C_T/gm^2 \equiv L_{pdg} \\ Q_L=R_T/\omega_0 L_{pdg} \\ \omega_0 < 1/R_{out}C_{out}}} \qquad (4.56)$$

Due to the evident dependency between amount of noise produced by an active inductor resonator and its unloaded quality factor Q_0, it is worth illustrating the described limitations of the proposed compensation technique in comparison with a standard active inductor tank compensated with an external negative resistor.

As an example, Figure 4.19 shows RMS noise voltage of two active inductor resonators as a function of different Q_0 values, simulated for the signal frequency of 434 MHz. Both tanks are modelled using the same gm and C_T values as well as loaded quality factor Q_L of 30. The noise parameter $\gamma = 2$ is typical for short-channel MOS transistors. Q_0 is adjusted by changing a ratio between the input losses represented by G_i and a gyrator transconductance. In practice, it can not be freely achieved as G_i is set by the active inductor architecture, however for the sake of the presented analysis it is assumed that any value of Q_0 can be chosen. As all of the points from Figure 4.19 represent noise of a fully compensated gyrator-based tank (i.e. $R_T = R_{load}$), the negative resistance has to be adjusted accordingly every time Q_0 is changed. It is accomplished by finding the corresponding gm_{ex}, R_{out} and C_{out} values for each resonator respectively, using (2.15) from Chapter 2 and (4.8) from this chapter.

Figure 4.19 illustrates, that for a low Q_0 resonator, the RMS noise voltage of a degenerated gyrator is comparable to the one of a standard active inductor tank with external negative resistor. When Q_0 increases, the RMS noise voltage the degenerated gyrator becomes larger than of the standard active inductor with the additional energy restorer. Thus, from a noise perspective, a practical application of the degenerated gyrator resonator is limited to the circuits with a relatively high input losses (directly proportional to gm) and low Q_0 (in the range of 1) [102].

In the case of low Q_0, the active inductor resonator with external negative resistor consumes more static power than the RC compensated gyrator, operating at the same
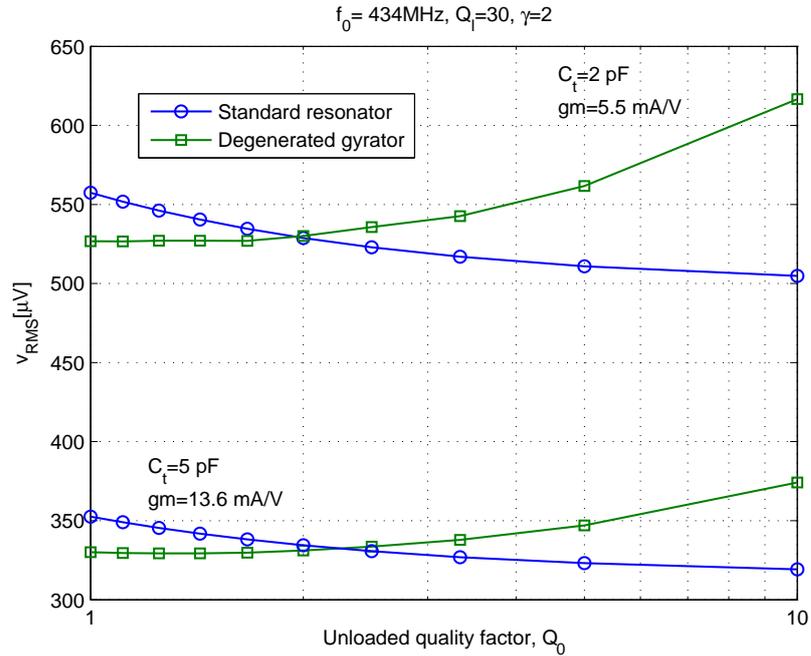
Figure 4.19: Output RMS noise voltage of active inductor resonators as a function of unloaded quality factor for $f_0 = 434$ MHz.

frequency, as shown by Szczepkowski et al. [102]. The difference can be used to increase the transconductance of the degenerated gyrator and therefore decrease the noise. In this case, the power consumption of both (a standard and degenerated active inductor) is equal.

4.7 Chapter summary

This chapter presented the novel concept of a degenerated gyrator using a single passive RC phase shifter to obtain a wideband negative resistance oscillator. First, the problem of the required number of phase shifters for proper operation was addressed and various scenarios thoroughly analysed. For the first time, it is shown that a single RC phase shifter is sufficient to provide negative resistance, even in the presence of relatively high circuit losses. The next section covered the topic of circuit sensitivity. Using the established technique of classic sensitivity functions, it was shown how various small

signal parameters of the proposed circuit change when the design variables differ from their nominal values. It was indicated that although passive resistors in CMOS process have low tolerances, the resulting change in the resonant frequency can be compensated by proper tuning of the gm of the amplifiers.

Next the issue of circuit parasitics and their influence on the operation of a degenerated gyrator was covered. The presented analysis indicated that lossy MOS devices are the main cause of the tuning range reduction of the proposed oscillator. Section 4.5.2 showed that minimum length transistors in sub-micron CMOS process have poor g_{ds} and therefore are not optimal for the proposed circuit. In addition, the problem of intrinsic RC parasitic networks originating in transconductors was studied. Despite the fact that these networks have limited influence on negative resistance generation at sub-GHz frequencies, their presence in the circuit can't be neglected and have to be characterised.

This chapter, for the first time, presented the Barkhausen criteria for oscillations both for ideal and non-ideal degenerated gyrator oscillators. It was demonstrated that, although a simple RC circuit is used to obtain a negative resistance, a relatively wide tuning range of such oscillator can be achieved.

Finally, a thorough noise analysis of the proposed resonator circuit has been presented using the new circuit model. The three main sources of noise were considered, including the one originating from RC phase shifter. Due to the low-pass character of this RC network, when its cutoff frequency is lower than the resonant frequency, less noise is injected to the resonator, decreasing the total RMS noise voltage. It was shown that the proposed technique can improve the noise performance of low-Q inductors, whereas a standard active inductor compensated by a negative resistor may be suitable for resonators with smaller losses. The importance of the proposed noise model comes from the fact that from the oscillator design perspective, phase noise is determined by two factors: the amplitude of a generated signal and noise of the circuit. Thus, some of the solutions presented here will be used later in Chapter 6 to estimate phase noise of a degenerated active inductor oscillator.

4.7 Chapter summary

This chapter covered the most important aspects of small signal modelling of degenerated gyrator. As any oscillator operate in a large signal regime, it is important to understand the effects of non-linearities of transconductors on the behavior of the circuit. Chapter 5 presents a thorough analysis of these effects with special emphasis on harmonic distortion and available level of amplitudes generated by the proposed circuit.

Chapter 5

Large signal behavior of degenerated gyrator

5.1 Introduction

This section presents a simplified non-linear, large signal analysis of the proposed degenerated gyrator. The importance of this study comes from the following factors:

- In principle, any oscillator operates under large signal conditions. If only a small signal model is considered, the circuit response will always scale proportionally with a magnitude of excitation without any limits, because small signal models are linear. In practice however, an oscillator circuit is built of active components that are non-linear. The increasing amplitude of oscillations drives the circuit into the region where a small signal model is no longer valid. As the proposed circuit is a harmonic oscillator it is therefore essential to recognise large signal effects and its influence on its performance.

- A practical degenerated gyrator, as such, is a non-linear circuit generating harmonics. As they affect a negative resistance and simulated inductance, a thorough study of how the proposed circuit behaves in the presence of harmonic signals is crucial.

117

- As shown in Chapter 2, Section 2.6, the phase noise of an oscillator depends on the circuit noise and RF signal power. Thus, to calculate the phase noise, the amplitude of the output signal has to be estimated. Linear models do not provide any information about amplitude settling mechanisms in a degenerated active inductor oscillator, making the presented large signal analysis important.

- Finally, the topic of the large signal behavior of an active inductor circuit is commonly omitted in the literature, being usually reduced to a vague report on a dynamic range of presented resonators. Typically, there is no indication on how the circuit behavior diverges from a small signal to a large signal regime and what are the implications for resonant frequency and circuit losses. To date, the only comprehensive large signal analysis of a standard active inductor was published by Kaunisto [7]. Therefore, the non-linear analysis presented in this chapter becomes an important part of understanding how active inductor oscillators work in practice.

Section 5.1 presents a short introduction to non-linear circuits with special emphasis on its characterisation using Taylor polynomials. The main issues related to a large signal excitation of a single transistor MOS transconductor are shown. In addition, the strengths and weaknesses of a circuit description using polynomials.

Section 5.3 contains the fundamentals of Volterra kernels technique, a mathematical tool used to describe a behavior of a non-linear circuit with memory (i.e. reactive components). Step by step, the methodology of kernel analysis is presented together with comments on its accuracy and limitations. Based on the previously published results of Kaunisto [7], the application of this technique to characterise the large signal operation of a standard active inductor resonator is discussed.

The main contribution of this chapter is presented in Sections 5.4-5.6. Using Volterra kernels, the non-linear model of a degenerated gyrator resonant tank is derived for the first time. It is then used to explain the mechanism behind amplitude limiting in the proposed oscillator circuit. In addition, the important problem of harmonic distortion

in the proposed circuit is studied.

5.2 Non-linear circuits

By definition a circuit is considered non-linear if it violates the principle of superposition, resulting in

$$f(a_1 x_1 + \ldots a_k x_k) \neq a_1 f(x_1) + \ldots + a_k f(x_k) \tag{5.1}$$

In other words, the linear combination of input signals x_k does not result in a linear combination of output responses $f(x_k)$ and different methods of circuit analysis have to be used to predict the behavior of the circuit. As an example, consider a single transistor transconductance amplifier driven by an ideal sinusoidal voltage at a single frequency. For a long channel MOS device in saturation, biased with an overdrive voltage of $V_{OV} = V_{GS} - V_{th}$, a large signal dependence between total drain current i_D and driving voltage v_{GS} is quadratic

$$i_D(t) = \frac{\mu_0 C_{ox}}{2} \frac{W}{L} v_{GS}(t)^2 = \frac{\mu_0 C_{ox}}{2} \frac{W}{L} \left(V_{OV} + v_{gs}(t) \right)^2 = I_D + i_d(t) \tag{5.2}$$

where

$$I_D = \frac{\mu_0 C_{ox}}{2} \frac{W}{L} V_{OV}^2 \tag{5.3}$$

$$i_d(t) = \frac{\mu_0 C_{ox}}{2} \frac{W}{L} \left(2 V_{OV} v_{gs}(t) + v_{gs}(t)^2 \right) = g m v_{gs}(t) + \frac{\mu_0 C_{ox}}{2} \frac{W}{L} v_{gs}(t)^2 \tag{5.4}$$

Assuming $v_{gs}(t) = A \sin(\omega_0 t)$, the AC response of the transistor is explained as follows. For small amplitude variations of $v_{gs}(t)$ the quadratic term in (5.4) can be considered to be negligible, a linear approximation is sufficient to describe the response of the amplifier. The linear approximation typically yields 10% of error for signal amplitudes in the range of 20% of V_{OV} [43]. As a result, single frequency excitation results in a single frequency response proportional to a device transconductance, well predicted by the superposition principle. Now, consider the case where the amplitude of the input signal increases. The contribution of the quadratic term of $i_d(t)$ becomes larger.

(a) v_{in}=1 mV

(b) v_{in}=50 mV

(c) v_{in}=150 mV

(d) v_{in}=200 mV
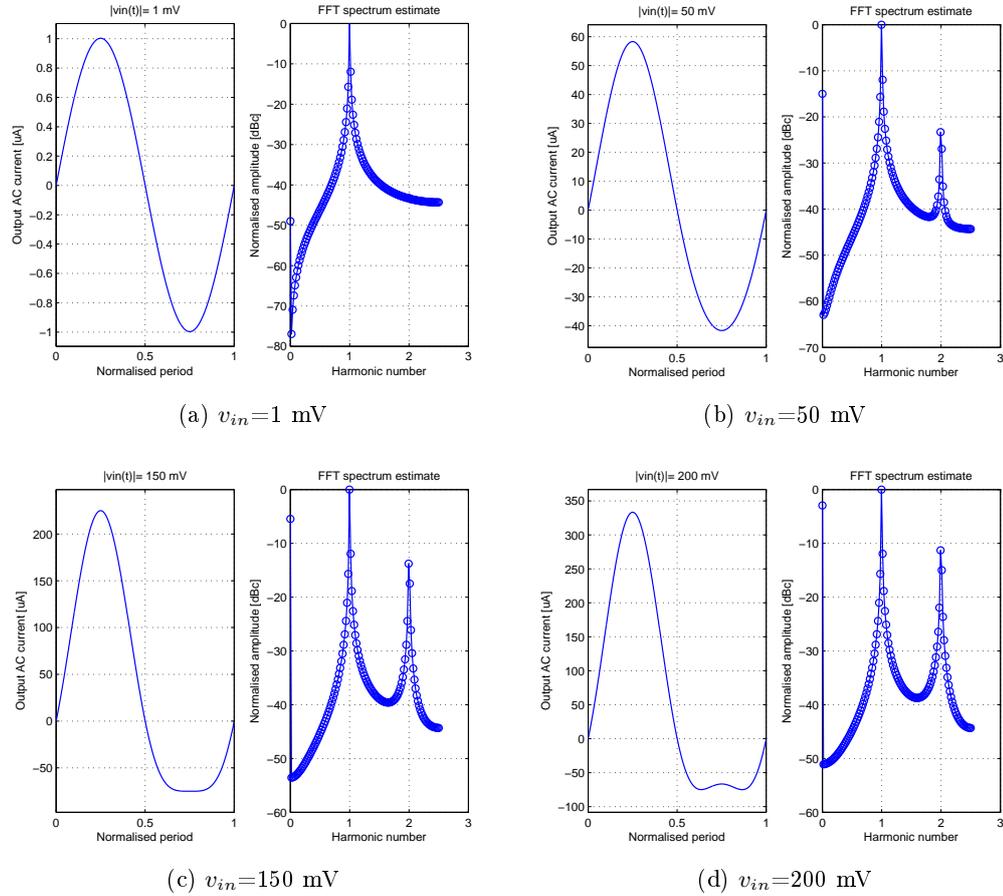
Figure 5.1: Evolution of an output current in a non-linear MOS transconductor with increasing input amplitude.

Since $A^2 \sin^2(\omega_0 t) = A^2/2 - A^2/2 \cos(2\omega_0 t)$, (5.4) has additional products at frequencies of 0 and $2\omega_0$, respectively. Therefore, the superposition condition is violated and the transconductor acts as a non-linear device under a large signal drive. Figure 5.1 illustrates simulation results obtained by implementing (5.2) in MATLAB.

In the case of active inductor resonators, problems related to a large signal swing are inevitably more severe than in the case of a passive counterpart. Two factors are dominant here. Firstly, both transconductance amplifiers experience harmonic distortion. As a gyrator is essentially a feedback system, the distorted output signal of first transconductor drives a feedback amplifier. This produces even more distortion due to the intermodulation products emerging from a harmonic-rich signal. Secondly, since

the resonator impedance is controlled directly by a small signal parameters of gyrator, the large excursions from a static bias point of both amplifiers change the effective inductance of the tank - depending on a signal amplitude. Therefore, even if a relatively simple quadratic approximation is used to describe MOS non-linearities, the large signal behavior is not straightforward to predict.

5.2.1 Power series representation of non-linear circuits

According to Taylor's theorem, any function $f(x)$ that has an infinite number of continuous derivatives at given point x_0 of its domain, can be expressed in the form of a power series of x and $f(x)$ derivatives, within a certain range in close vicinity to x_0. The actual distance from x_0 where this representation holds with given error is controlled by the reminder function $r_n(x)$. If $f(x)$ can be described as

$$f(x) = f(x_0) + \frac{(x-x_0)}{1!} \frac{\partial f(x_0)}{\partial x} + \frac{(x-x_0)^2}{2!} \frac{\partial^2 f(x_0)}{\partial x^2} + \frac{(x-x_0)^3}{3!} \frac{\partial^3 f(x_0)}{\partial x^3} +$$
$$+ \ldots + \frac{(x-x_0)^n}{n!} \frac{\partial^n f(x_0)}{\partial x^n} + r_n(x_0) \tag{5.5}$$

the function is known as *analytical*. From a circuit analysis perspective, if only a non-linear function of interest is analytical around a given bias point, then the corresponding polynomial can be found from Taylor's theorem (5.5). Even if an explicit formula describing $f(x)$ is not known but can only be measured, the results are then applied to approximate the corresponding power series. Note that in actual electronic components, non-linearities are usually multidimensional (through various parasitic effects) that $y = f(x_1, x_2, \ldots, x_n)$, which dramatically increases a complexity of polynomial calculation [103]

As an example of a practical application of the described method, consider a transfer curve $I_D = f(V_{GS})$ of a short-channel 180 nm NMOS transistor, presented on Figure 5.2. In contrast to a long-channel device, the drain current no longer has a quadratic dependence on input voltage but instead falls between a 2nd-order (for low
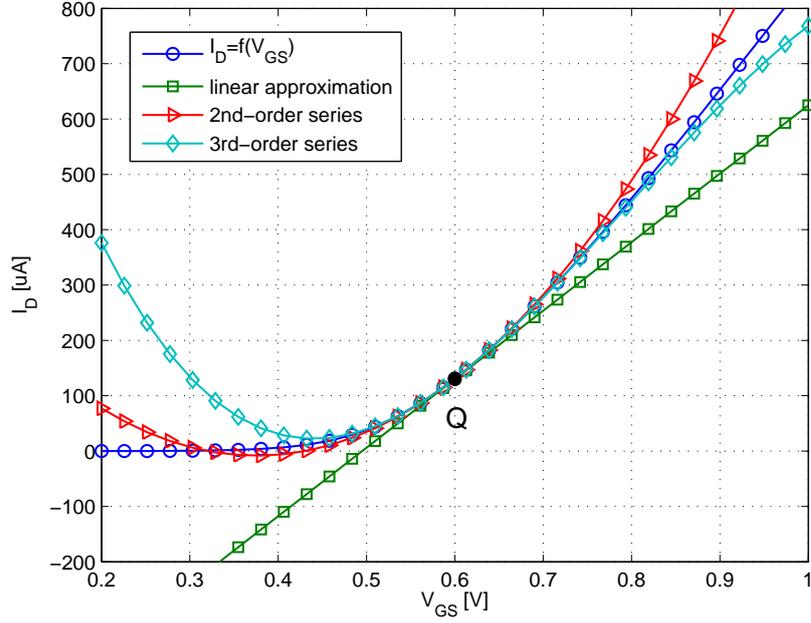
Figure 5.2: Approximations of a short-channel NMOS transfer curve.

V_{OV}) and a linear function (for higher V_{OV}) [43]

$$I_D \approx \frac{\mu_0 C_{ox}}{2} \frac{W}{L} V_{OV}^2 \frac{1}{1 + \dfrac{V_{OV}}{E_C L}} \tag{5.6}$$

where E_C is the critical electric field for which electron drift velocity saturates. If a linear approximation is used, the error becomes larger than 10% for variations of bias point Q_B larger than ±50 mV. In the case of 2nd and 3rd-order polynomials, the bias point is tracked from V_{th} to 870 mV and 1 V, respectively. Note that the approximations do not give proper results for the transistor in cut-off, demonstrating that indeed the Taylor series only represents the function of interest for a certain range of variable values.

5.2.2   Shortcomings of Taylor expansion

Figure 5.3 presents an attempted polynomial approximation of the transfer curve of a transistor that saturates for higher voltages. Not only do all of the polynomials fail to
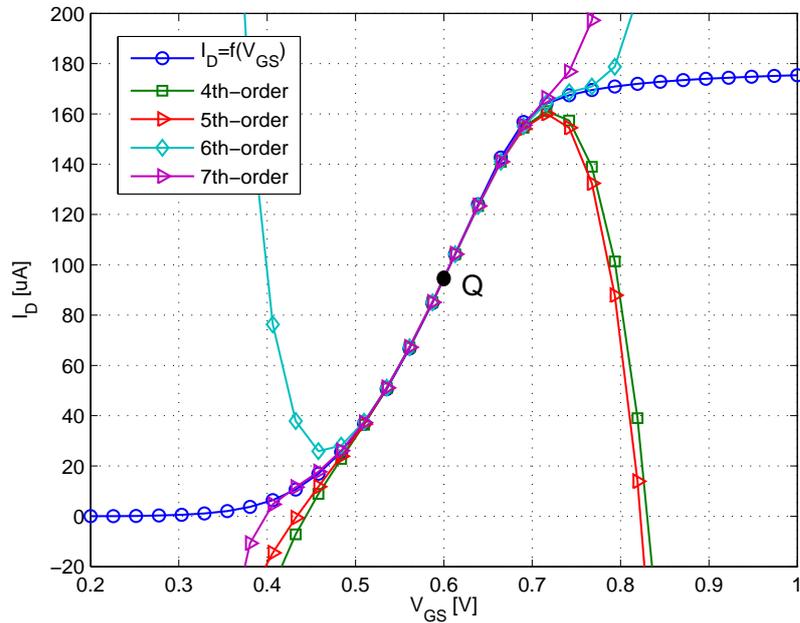
Figure 5.3: Failed approximation of saturated function.

converge in the cut-off region but also in the saturation range. This is due the afore-mentioned locality of Taylor's theorem, it converges only within a finite domain know as a *radius of convergence*. For certain types of non-linearity this radius approaches zero and a corresponding power series can't be found at all. One such example is a transfer function of a perfect bipolar switch, that can't be expressed by any means in terms of a polynomial. Thus, the power series approach is restricted to the functions called *soft* or *weak* non-linearities. Wambacq et al. [103] define this function as the one that in a vicinity of a bias point is sufficiently described using 3rd-order series only. In practice, as long as a bias point is set between cut-off and saturation points, the weakly non-linear behavior is observed and the power series expansion can be used. As long as the input amplitude does not move the bias-point towards one of the divergence ends, the power series description holds.

Another shortcoming of the Taylor series approach is a failure to describe non-linearities with memory effect i.e. the analysed function has to be static [103]. If capacitances or inductances are present in the circuit, the output signal at any given time

will depend also on previous time instants because of energy stored in these components. The solution of this problem is presented later in this chapter.

5.2.3   Polynomial description of oscillator

In the case of a standard oscillator, the signal amplitude is restricted by a non-linear mechanism like saturation. Thus, the power series description is not the most accurate method of predicting the amplitude. However, observing the polynomials from Figure 5.3 all functions start to diverge roughly for the same argument values hence indicating the points where strong non-linearity occurs. Analysing the curve $I_D = f(V_{GS})$ it can be seen that these points correspond to the cut-off voltage of approximately 450 mV and the saturation voltage larger than 700 mV. Thus, although this approach is not suitable to describe strong non-linear functions, the resulting polynomials can approximate with some error the points where oscillation amplitude will start to settle, a feature not available when using simple linear models.

A similar approach has been presented by Jardón-Aguilar et al. [104]. The authors used the polynomial description to find the large signal gain of an amplifier of feedback oscillator and then observing how it decreases to unity with an increasing signal amplitude. Based on trivial mathematical formulas the calculated amplitude prediction yielded results only 20% smaller than of these obtained using the Spice circuit simulator. Thus, although underestimating, the polynomial method allows one to analyse a circuit behavior through a set of closed form formulas first.

5.3   Volterra kernels method

In 1887, Italian mathematician and physicist Vito Volterra created a theory of functional series [105] that later has been extended by Wiener [106] to describe the behavior of non-linear electronic circuits. Wiener observed that if the system is weakly non-linear, the input is mapped to the output through a functional series in a similar manner as a real-valued power series describes the behavior of a linear circuit. This results in a well
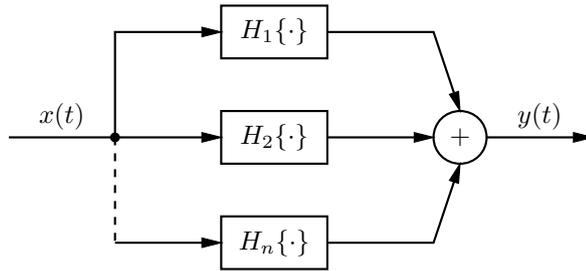
Figure 5.4: Non-linear system representation using n-th order Volterra functional series, known as Volterra-Wiener model [107].

known Volterra-Wiener model of a non-linear circuit depicted on Figure 5.4.

The coefficients $H_n\{x(t)\}$ are known as n^{th}-*order Volterra operators*. Each block represents a nth-degree functional [107], mapping $x(t)$ to $y(t)$, resulting in the following formula [103]

$$y(t) = H_1\{x(t)\} + H_2\{x(t)\} + H_3\{x(t)\} + \ldots + H_{n-1}\{x(t)\} + H_n\{x(t)\} \qquad (5.7)$$

where

$$H_n\{x(t)\} = \int\limits_{-\infty}^{+\infty} \cdots \int\limits_{-\infty}^{+\infty} k_n\left(\tau_1, \ldots, \tau_n\right) x\left(t - \tau_1\right) \cdots x\left(t - \tau_n\right) d\tau_1 \cdots d\tau_n \qquad (5.8)$$

The coefficient $k_n\left(\tau_1, \tau_2, \ldots, \tau_n\right)$ is called n^{th}-*order Volterra kernel*. Closer examination of (5.8) reveals that it resembles the *convolution integral* known from a linear circuit theory [108] and given by

$$y(t) = \int\limits_{-\infty}^{+\infty} h\left(\tau\right) x\left(t - \tau\right) d\tau \qquad (5.9)$$

where $h(\tau)$ is known as the *impulse response* of a linear time invariant circuit. The impulse response conveys unique information about the circuit, allowing to find the output signal $y(t)$ for any input excitation $x(t)$. Thus once the impulse response is known, the circuit is fully characterised and its behavior can be predicted. Now, because (5.8) represents a multidimensional convolution integral of a non-linear circuit, in this case $y(t)$ can also be predicted as long as the corresponding n^{th}-order impulse response functions (kernels) $k_n\left(\tau_1, \ldots, \tau_n\right)$ are known. Recalling the generic circuit from Figure 5.4 and

comparing to (5.8), it can be seen that $H_1\{\cdot\}$ represents the linear behavior of the system. Therefore $k_1(\tau_1)$ should be interpreted as a standard impulse response as in the case of any linear circuit. A second order operator multiplies an input signal by its time shifted version and scales it using two-dimensional impulse response $k_2(\tau_1, \tau_2)$. Thus, the last operator uses n time-shifted versions of the input signal with $\mathrm{n^{th}}$-dimensional input response. Thanks to this approach, despite the non-linear character of the system, the output response can be found using standard linear analysis tools.

A non-linear circuit described by (5.8) is defined in the time domain. In some applications, where the Fourier transform of an input signal can be calculated, it is more convenient to characterise the circuit in the frequency domain. Having defined the impulse responses, the corresponding Fourier transforms can be found from

$$K_n\left(\omega_1, \ldots, \omega_n\right) = \int\limits_{-\infty}^{+\infty} \cdots \int\limits_{-\infty}^{+\infty} k_n\left(\tau_1, \ldots, \tau_n\right) e^{-j(\omega_1\tau_1 + \ldots + \omega_n\tau_n)} \, d\tau_1 \, \cdots \, d\tau_n \qquad (5.10)$$

As an example of the frequency domain representation of non-linear circuits, consider a single sinusoid of $x(t) = A_0 \cos\left(\omega_0 t\right)$ applied to a basic $\mathrm{3^{th}}$-order non-linearity described with Volterra kernels, the output signal spectrum is found as [103]

$$\begin{aligned} y(t) = {}& A_0 \mathrm{Re}\left\{K_1(j\omega_0)e^{j\omega_0 t}\right\} + \\ & + \frac{A_0^2}{2}\mathrm{Re}\left\{K_2(j\omega_0, -j\omega_0)\right\} + \frac{A_0^2}{2}\mathrm{Re}\left\{K_2(j\omega_0, j\omega_0)e^{j2\omega_0 t}\right\} + \\ & + 3\frac{A_0^3}{4}\mathrm{Re}\left\{K_3(j\omega_0, j\omega_0, -j\omega_0)e^{j\omega_0 t}\right\} + \frac{A_0^3}{4}\mathrm{Re}\left\{K_3(j\omega_0, j\omega_0, j\omega_0)e^{j3\omega_0 t}\right\} \end{aligned} \quad (5.11)$$

showing contributions of harmonics at DC, ω_0, $2\omega_0$ and $3\omega_0$. All of these harmonic products are explained in more detail in Table 5.1 [103].

The main advantage of the Volterra kernels method over a standard power series description from Section 5.2.1 is its ability to characterise non-linear circuits with memory. This is due to the fact that an impulse response inherently conveys this information. Thus the method combines the basic features of the impulse response functions with the convenience of a power series description of non-linear circuits. However the method has also some restrictions [109]:

- The series is a sum that converges to a single value. If there are multiple possible output values (as in the case of hysteresis function of Schmitt trigger), the solution will converge only to one of the values.

- If higher order kernels dominate the non-linear behavior, the time to find them increases because kernels of lower order have to be computed first.

- If the sum diverges there is no solution (as in the case of Taylor series).

Table 5.1: Volterra kernels of a 3rd-order non-linear circuit driven by a single sinusoid [103].

Harmonic number	Response		
	frequency	amplitude	type
1	ω_0	$A_0|K_1(j\omega_0)|$	linear
2	$2\omega_0$	$\frac{1}{2}A_0^2|K_2(j\omega_0, j\omega_0)|$	second harmonic
	0	$\frac{1}{2}A_0^2|K_2(j\omega_0, -j\omega_0)|$	DC shift
3	$2\omega_0 - \omega_0 = \omega_0$	$\frac{3}{4}A_0^3|K_3(j\omega_0, j\omega_0, -j\omega_0)|$	compression or expansion
	$3\omega_0$	$\frac{1}{4}A_0^3|K_3(j\omega_0, j\omega_0, j\omega_0)|$	third harmonic

5.3.1 Calculation of kernels

For relatively simple circuits, the kernels and the corresponding Fourier transforms can be found from the Taylor series describing a non-linearity [110]. For more complex systems, kernels can't be found analytically however they can be extracted from the measurements, as described in detail by Boyd and Chua [111].

If a non-linear function is expressed in terms of a power series, kernels are found using a recursive method known as the *harmonic input method* [107, 112, 113], briefly described in this section. As the 1st-order kernels represent a linear behavior of the circuits these are found using standard methods, for example node analysis. In this

case the circuit is represented by its small-signal parameters i.e. the non-linearity is reduced to the first term of the describing polynomial.

For higher-order functions the input is shortened and the circuit is driven internally by the non-linear n[th]-order current probing sources. Each source is connected in parallel to the linearised version of the circuit used for the 1st-order kernel calculation. The corresponding transfer functions (kernels) are then found by solving the circuit using linear methods, although the excitations are now non-linear. Every time an nth-order kernel is calculated, (n-1)[th]-order functions are used. Thus, the procedure is recursive. More details are given in Section 5.4 where this methodology is employed to analyse a large signal behavior of the proposed circuit.

The formulae to calculate a non-linear probing sources up to an order of three, are presented in Table 5.2. Note that these expressions are only applicable to the one dimensional non-linear transconductance and conductance. The expressions are presented in a generic form and simplify in the case of a single signal excitation where $\omega_1 = \omega_2 = \omega_3 = \omega_0$.

Table 5.2: Calculation of non-linear probing sources [103].

Transconductance: $i_{out_k} \approx g_{1_k} v_{in_k} + g_{2_k} v_{in_k}^2 + g_{3_k} v_{in_k}^3$	
Order of probing source	Expression
2	$g_{2_k} K_{1_k}(j\omega_1) K_{1_k}(j\omega_2)$
3	$g_{3_k} K_{1_k}(j\omega_1) K_{1_k}(j\omega_2) K_{1_k}(j\omega_3) + \frac{2}{3} g_{2_k} \big[K_{1_k}(j\omega_1) K_{2_k}(j\omega_2, j\omega_3) +$ $+ K_{1_k}(j\omega_2) K_{2_k}(j\omega_3, j\omega_1) + K_{1_k}(j\omega_3) K_{2_k}(j\omega_1, j\omega_2) \big]$

5.3.2 Accuracy of kernels method

The complexity of a kernel description increases rapidly together with the complexity of the analysed non-linear function. As models of practical components are usually sophisticated, hand calculations based on these models are not possible. During design,

comprehensive results can be obtained using any circuit simulator able to solve steady state problems. Although accurate with the supplied models, simulators do not provide any analytical information about the influence of circuit parameters on non-linear behavior. On the contrary, as Volterra kernels are directly related to these parameters, this information is automatically conveyed with it. This leads to a trade-off between approximation error and the practical limits on description complexity. In this chapter, simplified models based on basic non-linear transconductances are used, assuming transistor capacitances being linear. The obtained results should be therefore treated as qualitative ones because more complex behavior is observed in practice due to the multi-dimensional non-linearities of actual circuits.

5.3.3 Volterra analysis of standard active inductor

After a basic introduction to the Volterra kernel technique given previously, this section presents the results of its application to a standard active inductor resonator. This comprehensive non-linear analysis was presented by Kaunisto in his doctoral dissertation [7]. To date, this work is the only complete source, documenting effects of large signal amplitudes on the performance of active inductor resonators.

Kaunisto starts the analysis assuming that single transistor amplifiers with a non-linear transconductance are used. He also modifies the Volterra kernels to fit the observed behavior of the investigated active inductors. It was achieved by changing polarities of an inverting amplifier and voltage controlling the feedback transconductor. As a result, the odd harmonic products have an opposite direction which promotes compression instead of expansion of a non-linear inductance. Due to the observed inductance compression, the resonance frequency increases when a signal amplitude gets larger. This causes the active inductor filter to work at higher frequency than designed by using a small signal approach. Thus, even if the transconductance amplifiers are still far from exceeding their maximum current and voltages or reaching saturation, the filter operates in the wrong bandwidth.

The outcome of the Volterra kernel method applied to the active inductor resonator

is a set of harmonic responses of the circuit on an increasing amplitude of the input signal, given in Table 5.3. All parameters correspond to a small signal model of the gyrator from Chapter 2 and the polynomial from Table 5.2. Kaunisto proved for the first time that the Volterra technique can be successfully employed to analyse the large signal behavior of a standard active inductor resonator. The next section presents the application of this methodology to the proposed resonator concept.

Table 5.3: Harmonic distortion components for the gyrator-based active inductor due to non-linear transconductances [7].

Type of response	Response i_{in}
fundamental	$v_{in} \frac{gm_1 gm_2}{j\omega C_g}$
second harmonic	$-\frac{1}{2} v_{in}^2 \left(\frac{g_{2,1} gm_2}{2j\omega_0 C_g} + \frac{g_{2,2} gm_1^2}{\omega_0^2 C_g^2} \right)$
third harmonic	$\frac{1}{4} v_{in}^3 \left(\frac{g_{3,1} gm_2}{3j\omega_0 C_g} - \frac{g_{3,2} gm_1^3}{j\omega_0^3 C_g^3} + \frac{g_{2,1} g_{2,2} gm_1}{\omega_0^2 C_g^2} \right)$
compression	$\frac{3}{4} v_{in}^2 \left[\frac{g_{3,1} gm_2}{j\omega_0 C_g} + \frac{g_{3,2} gm_1^3}{j\omega_0^3 C_g^3} - \frac{2g_{2,1} g_{2,2} gm_1}{3} \left(\frac{1}{2\omega_0^2 C_g^2} + \frac{2}{j\omega_g C_g} \right) \right]$

5.4   Non-linear analysis of a lossy degenerated gyrator

This section contains the main contribution of this chapter – the large signal analysis of the proposed resonator circuit. First, a generic model of the degenerated active inductor is described and characterised using Volterra kernels and the harmonic input method. The results are then used to show how the large signal swings affect the negative resistance and the resonant frequency of the circuit. The calculated kernels also allow the estimation of the harmonic distortion of the oscillator signal, as described in Section 5.5.

5.4.1 Circuit model

Figure 5.5 depicts a generic non-linear model of a lossy degenerated gyrator. Contrary to the Kaunisto approach [7], the orientation of the transconductors does not have to be modified as the observed behavior of the degenerated active inductor reveals an expansion of inductance in the presence of increasing input signal. As with Kaunisto, it is assumed that both transconductors are represented by a single transistor. This causes the input conductance G_i of such a simple gyrator to be dominated by gm of one of the amplifiers. Assuming that the non-linearity of the transistors is weak, polynomials describing active devices can be limited to the 3rd-order. Since the corresponding transconductances are the derivatives of these polynomials [103] they are non-linear as well (quadratic in this case). Thus, the input conductance G_i of the gyrator is approximately equal to Gm, the large signal transconductance of one of the amplifiers. This important observation has not been included in [7] and it is introduced in this thesis for the first time. In the following analysis G_i is represented by a non-linear conductance Gm_1 of the inverting amplifier.
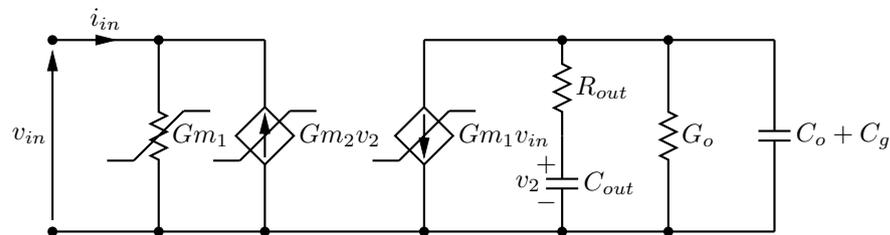
Figure 5.5: Simplified non-linear model of lossy degenerated gyrator.

5.4.2 Linear response

In the first step of the presented analysis the linear circuit response is calculated. In this case, the input conductance together with both transconductors are described by small signal parameters. This step yields exactly the same results as the small signal analysis presented in Chapter 4, Section 4.5. At this stage it is crucial to determine which quantities should be analysed in terms of Volterra kernels. For any gyrator

circuit two kernels for each of the considered orders have to be included. As the main function of interest is the large signal input admittance (the same as in linear case - this function conveys an essential information on the negative resistance and the simulated inductance), the input current has to be characterised as a function of the amplitude of the driving voltage. As the feedback transconductor is driven by the voltage at the output of the active inductor (either with the phase shifter or not), the kernel related to this voltage is also necessary in order to include the non-linear effects of the first amplifier.

Figure 5.6 depicts a linear model of a degenerated active inductor. As in Chapter 4, KVL and KCL equations are sufficient to analyse the circuit. The voltage v_2 driving the feedback transconductor is equal to

$$v_2(j\omega_1) = \frac{-gm_1 v_{in}(j\omega_1)}{j\omega_1 C_G + G_o - \omega_1^2 C_o C_{out} R_{out}} \tag{5.12}$$

The 1st-order kernel describing the dependence between the input and output of the active inductor is in fact the voltage gain of the forward path with the $R_{out}C_{out}$ phase shifter

$$K_{11}(j\omega_1) = \frac{v_2(j\omega_1)}{v_{in}(j\omega_1)} = \frac{-gm_1}{j\omega_1 C_G + G_o - \omega_1^2 C_o C_{out} R_{out}} \tag{5.13}$$

The 1st order input kernel represents the input admittance of the degenerated gyrator, and from Figure 5.6 this admittance is equal to

$$K_{in1}(j\omega_1) = gm_1 + \frac{-gm_2 v_2(j\omega_1)}{v_{in}(j\omega_1)} = gm_1 + \frac{gm_1 gm_2}{j\omega_1 C_G + G_o - \omega_1^2 C_o C_{out} R_{out}} \tag{5.14}$$

which corresponds with the results from Chapter 4 given by (4.20) for $G_i \approx gm_1$.

5.4.3   Second order kernels

The second harmonic response is found from the circuit presented on Figure 5.7. All the considered 2nd order effects are represented as non-linear current sources connected in parallel to the corresponding linear components. As indicated previously, the input is shorted, in this case setting v_{in2} to zero. This in turn causes both the parasitic
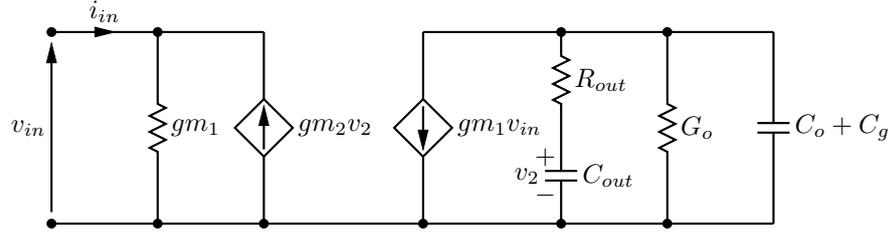
Figure 5.6: Linearised (1st-order) model of lossy degenerated gyrator.
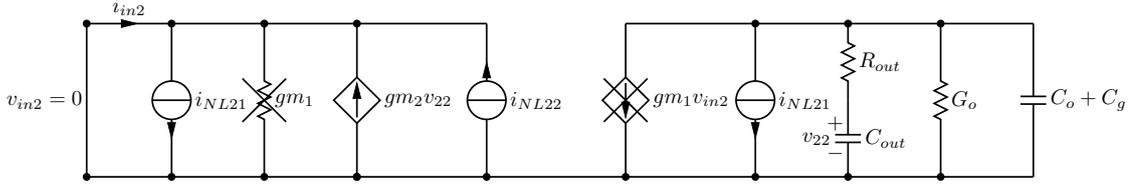
Figure 5.7: 2nd-order model of lossy degenerated gyrator.

lossy resistor of $1/gm_1$ and the voltage controlled current source of $gm_1 v_{in2}$ to be disconnected from the circuit. Despite this, a non-linear source i_{NL21} representing higher order distortion of first transconductor is left intact because shorting does not affect the ideal independent current sources. In addition, as $v_{in2} = 0$, no voltage gain nor input admittance can be defined for this circuit. It is important to recognise that the second order and higher kernels represent the response of the circuit to the imaginary stimuli rather than currents and voltages in a physical sense.

As before, the kernel of output voltage v_2 is found by analysing the output voltages, however for the reasons explained, the kernel no longer represents the voltage gain of the circuit. Note that the 2nd-order kernel is defined for two frequencies of ω_1 and ω_2. As suggested by (5.10), the Fourier transform of nth-dimensional impulse response results is a function of $\omega_1, \ldots, \omega_n$ frequency variables.

$$K_{12}(j\omega_1, j\omega_2) = v_{22}(j\omega_1, j\omega_2) = \frac{-i_{NL21}}{j(\omega_1 + j\omega_2)C_G + G_o - (\omega_1 + \omega_2)^2 C_o C_{out} R_{out}} \quad (5.15)$$

The 2nd-order kernel corresponding to a circuit response for the second harmonic is equal to a second harmonic current i_{in2} at the shortened input. Figure 5.7 reveals that

this function is equal to

$$K_{in2}(j\omega_1, j\omega_2) = i_{NL21} - gm_2 v_{22}(j\omega_1, j\omega_2) - i_{NL22} =$$

$$= i_{NL21} + \frac{gm_2 i_{NL21}}{j(\omega_1 + j\omega_2)C_G + G_o - (\omega_1 + \omega_2)^2 C_o C_{out} R_{out}} - i_{NL22}$$

$$(5.16)$$

The current sources i_{NL21} and i_{NL22} are found using the kernels from the previous step. As the non-linearity of the inverting amplifier depends only on the input voltage of the active inductor, i_{NL21} depends only on the coefficients of the polynomial describing this transconductance. In the case of a feedback amplifier, the non-linear response is proportional not only to the expansion polynomial but also to the non-linear voltage v_{22}. Thus, the expression for i_{NL22} is found according to the Table 5.2. The probing sources are therefore equal to

$$i_{NL21} = g_{21}$$

$$i_{NL22} = g_{22} K_{11}(j\omega_1) K_{11}(j\omega_2) =$$

$$= \frac{g_{22} gm_1^2}{\left(j\omega_1 C_G + G_o - \omega_1^2 C_o C_{out} R_{out}\right) \left(j\omega_2 C_G + G_o - \omega_2^2 C_o C_{out} R_{out}\right)} \qquad (5.17)$$

Finally, the 2nd-order kernels from (5.15) and (5.16) are found to be

$$K_{21}(j\omega_1, j\omega_2) = \frac{-g_{21}}{j(\omega_1 + j\omega_2)C_G + G_o - (\omega_1 + \omega_2)^2 C_o C_{out} R_{out}} \qquad (5.18)$$

and

$$K_{in2}(j\omega_1, j\omega_2) = g_{21} + \frac{gm_2 g_{21}}{j(\omega_1 + j\omega_2)C_G + G_o - (\omega_1 + \omega_2)^2 C_o C_{out} R_{out}} +$$

$$+ \frac{-g_{22} gm_1^2}{\left(j\omega_1 C_G + G_o - \omega_1^2 C_o C_{out} R_{out}\right) \left(j\omega_2 C_G + G_o - \omega_2^2 C_o C_{out} R_{out}\right)}$$

$$(5.19)$$

5.4.4 Third order kernels

The circuit necessary to calculate these kernels is similar to the one from the previous section and is depicted on Figure 5.8. The non-linear sources i_{NL31} and i_{NL32} represent a sources of third order distortion of the degenerated active inductor. As before, since

5.4 Non-linear analysis of a lossy degenerated gyrator
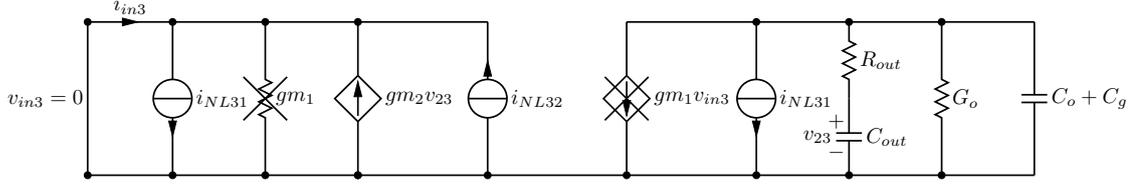
Figure 5.8: 3$^{\text{rd}}$-order model of lossy degenerated gyrator.

$v_{in3} = 0$, both the loss resistor $1/gm_1$ and the source gm_1v_{in3} can be suppressed. The 3$^{\text{rd}}$-order kernel of voltage v_{23} is derived as

$$K_{13}(j\omega_1, j\omega_2, j\omega_3) = \frac{-i_{NL31}}{j(\omega_1 + j\omega_2 + j\omega_3)C_G + G_o - (\omega_1 + \omega_2 + j\omega_3)^2 C_o C_{out} R_{out}}$$

(5.20)

The input kernel is found by applying KCL

$$i_{in3} = i_{NL31} - gm_2 v_{23}(j\omega_1, j\omega_2, j\omega_3) - i_{NL32} =$$

$$= i_{NL31} + \frac{gm_2 i_{NL31}}{j(\omega_1 + j\omega_2 + j\omega_3)C_G + G_o - (\omega_1 + \omega_2 + j\omega_3)^2 C_o C_{out} R_{out}} - i_{NL32}$$

(5.21)

As before the probing source i_{NL31} is equal to the third order coefficient of the polynomial approximating the non-linearity of the first transconductor. Similarly, i_{NL32} is found using Table 5.2, giving

$$i_{NL31} = g_{31}$$

$$i_{NL32} = g_{31}K_{11}(j\omega_1)K_{11}(j\omega_2)K_{11}(j\omega_3)+$$

$$+ \frac{2}{3}g_{21}\big[K_{11}(j\omega_1)K_{21}(j\omega_2, j\omega_3) + K_{11}(j\omega_2)K_{21}(j\omega_3, j\omega_1) +$$

$$+ K_{11}(j\omega_3)K_{21}(j\omega_1, j\omega_2)\big] =$$

$$= A_3 + B_3$$

(5.22)

where

$$A_3 = \frac{-g_{31}gm_1^3}{\big(j\omega_1 C_G + G_o - \omega_1^2 C_o C_{out} R_{out}\big)\big(j\omega_2 C_G + G_o - \omega_2^2 C_o C_{out} R_{out}\big)} \times$$

$$\times \frac{1}{\big(j\omega_3 C_G + G_o - \omega_3^2 C_o C_{out} R_{out}\big)}$$

(5.23)

and

$$B_3 = \frac{2g_{22}gm_1g_{21}}{3\left(j\omega_1 C_G + G_o - \omega_1^2 C_o C_{out} R_{out}\right)} \times$$

$$\times \frac{1}{j(\omega_2 + \omega_3)C_G + G_o - (\omega_2 + \omega_3)^2 C_o C_{out} R_{out}} +$$

$$+ \frac{2g_{22}gm_1g_{21}}{3\left(j\omega_2 C_G + G_o - \omega_2^2 C_o C_{out} R_{out}\right)} \times$$

$$\times \frac{1}{j(\omega_3 + \omega_1)C_G + G_o - (\omega_3 + \omega_1)^2 C_o C_{out} R_{out}} +$$

$$+ \frac{2g_{22}gm_1g_{21}}{3\left(j\omega_3 C_G + G_o - \omega_3^2 C_o C_{out} R_{out}\right)} \times$$

$$\times \frac{1}{j(\omega_1 + \omega_2)C_G + G_o - (\omega_1 + \omega_2)^2 C_o C_{out} R_{out}} \tag{5.24}$$

Substituting (5.23) and (5.24), the 3$^{\text{nd}}$-order kernels described by (5.21) are equal to

$$K_{13}(j\omega_1, j\omega_2, j\omega_3) = \frac{-g_{31}}{j(\omega_1 + j\omega_2 + j\omega_3)C_G + G_o - (\omega_1 + \omega_2 + j\omega_3)^2 C_o C_{out} R_{out}} \tag{5.25}$$

and

$$K_{in3}(j\omega_1, j\omega_2, j\omega_3) = \frac{gm_2 g_{31}}{j(\omega_1 + j\omega_2 + j\omega_3)C_G + G_o - (\omega_1 + \omega_2 + j\omega_3)^2 C_o C_{out} R_{out}} +$$

$$+ \frac{g_{31}gm_1^3}{j\omega_1 C_G + G_o - \omega_1^2 C_o C_{out} R_{out}} \times$$

$$\times \frac{1}{j\omega_2 C_G + G_o - \omega_2^2 C_o C_{out} R_{out}} \times$$

$$\times \frac{1}{j\omega_3 C_G + G_o - \omega_3^2 C_o C_{out} R_{out}} + g_{31} + B_3 \tag{5.26}$$

5.5   Harmonic response of degenerated gyrator

The kernels describing the input current of the degenerated gyrator allow us to approximately describe the behavior of this circuit in the presence of a large signal amplitude. From Table 5.1, the corresponding higher order harmonic effects can be found. Second and third order harmonics are obtained by substituting $\omega_1, \omega_2, \omega_3 \equiv \omega_0$ in (5.14), (5.19) and (5.26) respectively. The admittance expansion/compression due to odd harmonics can be also found if $\omega_1, \omega_2 \equiv \omega_0$ and $\omega_3 = -\omega_0$. The presence of non-zero G_o is necessary

for several reasons. Firstly, it is required to simulate correct response at lower resonant frequencies, as presented in Chapter 4. Secondly, because in general the DC gain of submicron CMOS transistors is finite, omitting G_0 usually yields overestimated large signal performance of the circuit. Finally, as the symbolic mathematics tools available today allow us to work and simplify otherwise cumbersome functions, there is not much more workload required to derive and then process the complicated formulas as presented in this chapter. Expressions can be simplified by dropping these terms that even for large signal amplitudes (in the case of CMOS gyrator in the range of few hundred mV) do not contribute much to overall behavior. However, this does not automatically imply that G_o can or should be omitted where possible.

Table 5.4 contains the calculated higher order responses of a degenerated gyrator using the proposed nonlinear model from Figure 5.5 and related kernels. Based on this, the subsequent sections present the main conclusions on the large signal performance of a negative resistance active inductor derived from the new analysis presented in this dissertation.

5.5.1   Large signal resonant frequency

The resonant frequency of an active inductor tank changes with signal amplitude through the effect of the non-linear transconductances. Large signal swings cause frequency shifts that usually are unacceptable when the resonator is used in a filter. Ideally this filter has to have the same response for all of the signal amplitudes within the dynamic range of the circuit. Thus the dynamic range of the active inductor circuit is always much more restricted than that of a passive resonators [7, 46].

In the case of an oscillator this problem is not as severe as the circuit produces a single, constant amplitude signal at a given resonant frequency. However, the instantaneous frequency still varies with the input signal, as in the case of a passive tank with a varactor. Thus, when analysing the large signal behavior of a degenerated gyrator based oscillator, this effect can't be neglected because, as shown in Chapter 4, Section 4.3, a negative conductance is also a function of signal frequency.

Table 5.4: Harmonic distortion components of a lossy degenerated gyrator.

Type of response	Response i_{in}
fundamental	$v_{in}\left(gm_1 + \dfrac{gm_1 gm_2}{j\omega_0 C_G + G_o - \omega_0^2 C_o C_{out} R_{out}}\right)$
second harmonic	$\dfrac{1}{2}v_{in}^2\left(g_{21} + \dfrac{gm_2 g_{21}}{j2\omega_0 C_G + G_o - (2\omega_0)^2 C_o C_{out} R_{out}} - \dfrac{gm_1^2 g_{22}}{\left(j\omega_0 C_G + G_o - \omega_0^2 C_o C_{out} R_{out}\right)^2}\right)$
DC shift	$\dfrac{1}{2}v_{in}^2\left(g_{21} + \dfrac{gm_2 g_{21}}{G_o} - \dfrac{gm_1^2 g_{22}}{\omega_0^2 C_G^2 + \left(G_o - \omega_0^2 C_o C_{out} R_{out}\right)^2}\right)$
third harmonic	$\dfrac{1}{4}v_{in}^3\left(g_{31} + \dfrac{gm_2 g_{31}}{j3\omega_0 C_G + G_o - (3\omega_0)^2 C_o C_{out} R_{out}} + \dfrac{g_{32} gm_1^3}{\left(j\omega_0 C_G + G_o - \omega_0^2 C_o C_{out} R_{out}\right)^3} - \dfrac{g_{21} g_{22} gm_1}{\left(j\omega_0 C_G + G_o - \omega_0^2 C_o C_{out} R_{out}\right)\left(j2\omega_0 C_G + G_o - (2\omega_0)^2 C_o C_{out} R_{out}\right)}\right)$
Approx. third order harmonic compression or expansion at ω_0	$\dfrac{3}{4}v_{in}^3\left(g_{31} + \dfrac{gm_2 g_{31}}{j\omega_0 C_G + G_o - \omega_0^2 C_o C_{out} R_{out}} - \dfrac{4 g_{22} gm_1 g_{21}}{3\left(j\omega_0 C_G + G_o - \omega_0^2 C_o C_{out} R_{out}\right) G_o} + \dfrac{g_{32} gm_1^3}{\left(j\omega_0 C_G + G_o - \omega_0^2 C_o C_{out} R_{out}\right)^2\left(-j\omega_0 C_G + G_o - \omega_0^2 C_o C_{out} R_{out}\right)}\right)$

To find how a resonant frequency changes with increasing amplitude, the response of the circuit at the fundamental frequency has to be first found. The resonant frequency is the one for which the imaginary part of the resonator admittance reaches zero, for given circuit parameters and a signal amplitude. Using Table 5.4 this frequency can be found by solving the following

$$\omega_{0Lndg}C_T + \Im\left\{\frac{i_{inLin}(\omega_{0Lndg})}{v_{in}} + \frac{i_{inComp/Exp}(\omega_{0Lndg})}{v_{in}}\right\} = 0 \qquad (5.27)$$

where C_T is a total tank capacitance, $i_{inLin}(\omega_{0Lndg})$ and $i_{inComp/Exp}(\omega_{0Lndg})$ are respectively: the linear and compression/expansion circuit responses from Table 5.4. Equation (5.27) yields an implicit function that can't be presented in a simple form like (4.13) for the small signal model from Chapter 4. However, for given circuit parameters, the result can be found numerically. The non-linear parameters are approximated from a circuit simulator, by first finding a $I - V$ curve and quiescent points for a single transconductor with an active load. This approach allows us to find the saturation curves that approximate the actual amplifier behavior. The corresponding derivatives can then be calculated using MATLAB (function *diff()* that returns a vector of differences between adjacent elements of the input vector $I = f(V)$) [96]. Table 5.5 presents the parameter for the transistor with the drawn length L of 250 nm.

Table 5.5: Non-linear parameters of a single MOS transconductor with active load.

gm_i	g_{2i}	g_{3i}
mA/V	mA/V^2	mA/V^3
5	-17.7	-170
10	11.9	-130
15	-31.9	-82

Note, the calculation error increases for derivatives of higher order and can be minimised by larger number of calculation points of $I - V$ curve. The presented values should be treated as an example only since they depend strongly on amplifier architecture and its bias circuit, and also on transistor dimensions. Using the small signal parameters from Chapter 4 (Table 4.5), together with the coefficients of Taylor expansion given in Table 5.5, the resonant frequency as a function of signal amplitude was

calculated. The corresponding curves are depicted on Figure 5.9. All curves were found
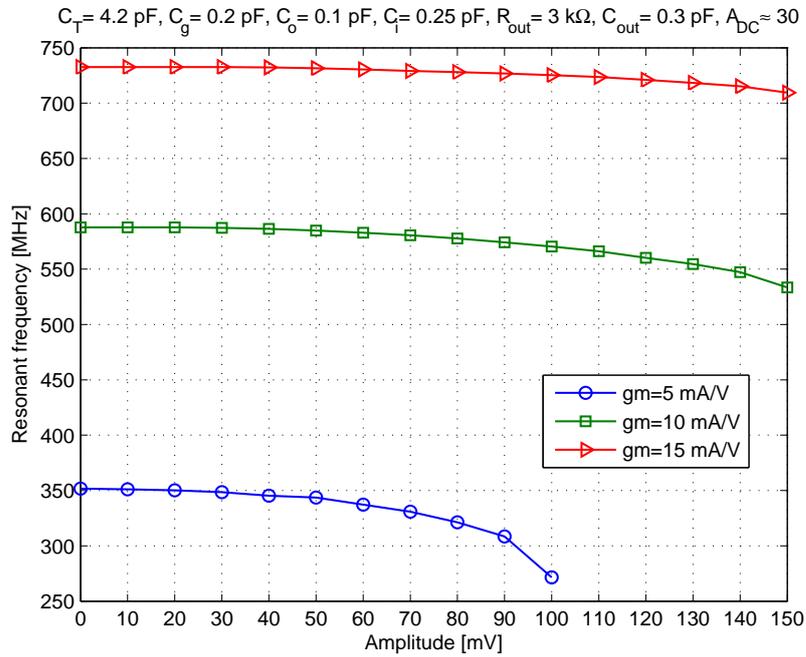
Figure 5.9: Resonant frequency as a function of signal amplitude.

by increasing the driving signal amplitude until the calculated frequency becomes a complex quantity. This is due to the dependence of the parallel equivalent inductance on the negative resistance and at a certain point equation (5.27) does not have any real and positive solution. From a practical point of view, the actual resonant frequency is in fact an average of presented curves for any of the considered transconductance values. This can be explained as follows. For each oscillation cycle, the signal swings through three zero-crossing points and two points where its amplitude reaches a maximum absolute value. Close to the zero-crossings, the frequency of the signal equals the value found from a small signal model. At maximum amplitude, frequency decreases through a harmonic compression of the inductance. As a result, the frequency observed through a single oscillation period lies between the small signal and the large signal values. Thus a degenerated active inductor based oscillator, generates a signal at lower frequency than the designed, not only due to the parasitic capacitances but also due to a non-linearities of the gyrator amplifiers. Looking at Figure 5.9, for the considered

140

parameter values, the frequency averaged over one oscillation period is 10% less than its small signal value. In practice the expected frequency drop is higher due to the non-linear capacitance of transistors that, for simplicity, has not been included in this analysis.

5.5.2 Large signal conductance

To observe how the generated negative resistance changes with signal amplitude, the real part of the input admittance at the resonant frequency has to be found. As previously, higher order effects, in addition to the amplitude dependent resonance frequency, are also considered here. The main point of interest is the signal level for which the effective input conductance of a resonant tank approaches zero. For this amplitude, circuit losses are equal to the compensating negative conductance and therefore the oscillator signal amplitude settles. As indicated previously, because the polynomial approximation methods fail for strong non-linearities (i.e. when the amplifier saturates), the presented results should be treated as indicative rather than as providing exact values. Using Tables 5.4, 5.5 and 4.6, together with the instantaneous frequencies calculated from (5.27), the input admittance of a self oscillating active inductor can be analysed. Figure 5.10 depicts the real part of this admittance for $\Re\{y_{in}\} \leq 0$.

Using Figure 5.10 as a reference, the behavior of a degenerated gyrator can be explained as follows. Under the linear conditions defined by Barkhausen criteria from Chapter 4, the effective equivalent parallel conductance is negative and oscillations start to build up. Depending on the chosen bias point i.e. transconductance and its derivatives, the increasing signal amplitude decreases this negative conductance due to a compression of admittance caused by the odd-order harmonics, limiting signal amplitude growth. Another contributor to the shape of the curves is the instantaneous frequency which changes the negative term of $G_o - \omega^2 C_o C_{out} R_{out}$. This is more pronounced for smaller gm values because, as shown on Figure 5.9, the frequency drop due to an increasing signal amplitude is the steepest in that case. In the case where transconductance is set to the maximum (15 mA/V), the effective input conductance

141

decreases rapidly due to a reduced G_o, as high bias currents decrease the DC gain of the transistor (Figure 4.12). Secondly, the rate of change of gm with input signal is the fastest for maximum transconductances in the amplifier with the active load. To prove this, consider Figure 5.11 which presents the normalised $I - V$ curves of an ideal single NMOS transistor with PMOS current source, together with its calculated gm for three different peak values. It can be seen that for the transconductance of 15 mA/V the slope of curve is the steepest. Therefore, for both minimum and maximum gm, the generated signal amplitude is smaller at both ends of the tuning range of the active inductor VCO. As a result, reduced signal power and higher phase noise will be observed in these areas. As the expected oscillation amplitude is in the range of 50 mV to 150 mV, a degenerated gyrator always has (as all gyrator based circuits) an inferior phase noise to any comparable passive LC tank VCO, not only due to a generally higher noise but also due to the non-linear character of the active resonator which limits available oscillation amplitude.
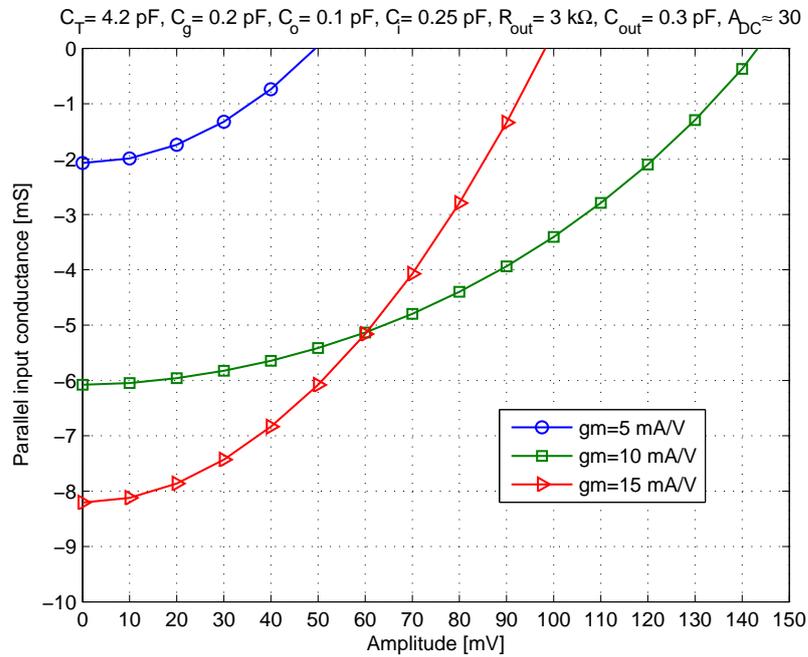
Figure 5.10: Large signal input conductance of a degenerated active inductor.
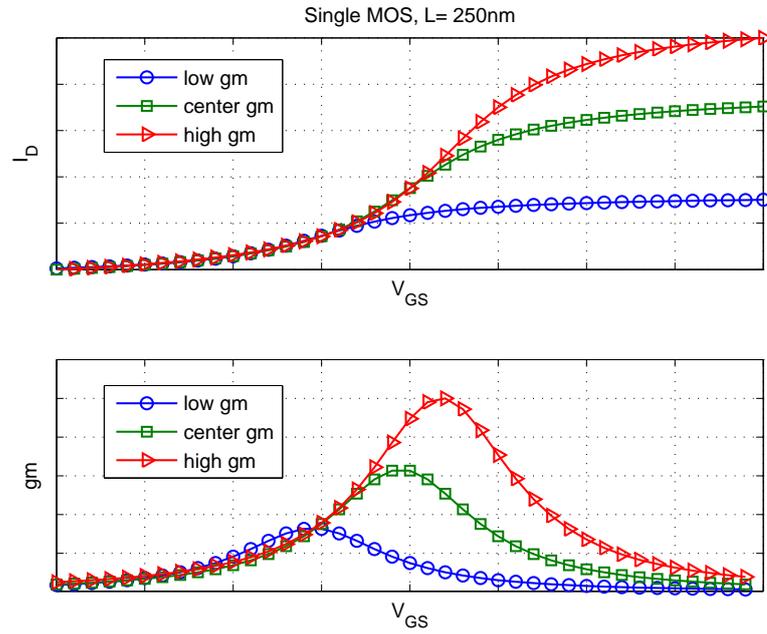
Figure 5.11: Normalised $I - V$ and gm curves of an ideal, single MOS transconductor with active load.
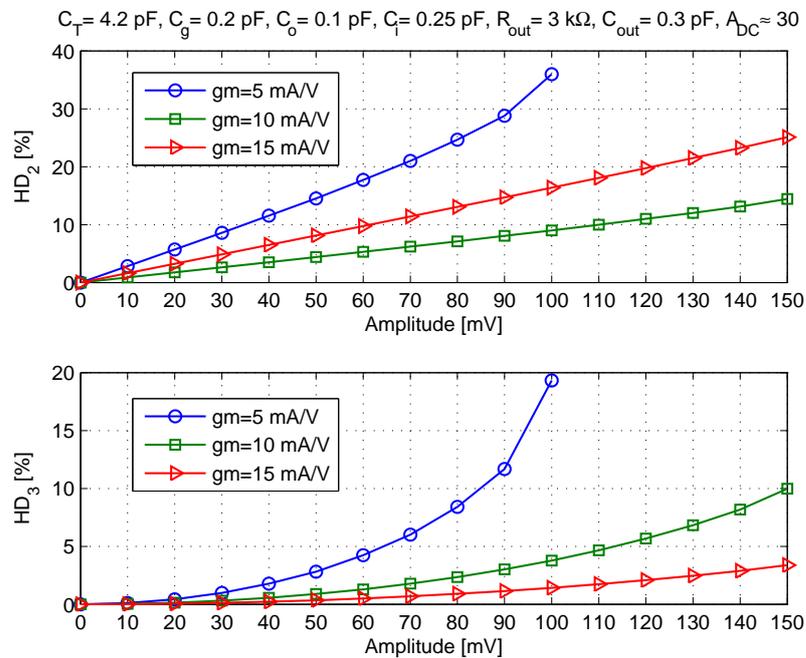
Figure 5.12: Harmonic distortion products of degenerated active inductor resonator

5.5.3   Harmonic distortion

Harmonic distortion is a measure of the relative magnitude of higher frequency products to the linear response of the circuit. Using kernels and the corresponding harmonic components from Table 5.4, the signal distortion can be found from a standard definition as [103]

$$HD_2 = \frac{1}{2}v_{in}\left|\frac{K_{in2}(j\omega_0, j\omega_0)}{K_{in1}(j\omega_0)}\right| : \text{ second order distortion} \qquad (5.28)$$

$$HD_3 = \frac{1}{4}v_{in}^2\left|\frac{K_{in3}(j\omega_0, j\omega_0, j\omega_0)}{K_{in1}(j\omega_0)}\right| : \text{ third order distortion} \qquad (5.29)$$

Figure 5.12 depicts a calculated harmonic distortion of the degenerated gyrator as a function of input voltage amplitude for the same parameter values as in previous section. Referring to the Volterra kernel analysis results from Table 5.4, it can be seen that all of the harmonic products are inversely proportional to the signal frequency. For this reason, the harmonic distortion increases faster for a smaller gm as this transconductance sets the resonant frequency low. When the signal amplitude reaches values for which the total negative conductance is zero (Figure 5.10), HD_2 and HD_3 products do not exceed 15%. This proves that although the generated signal amplitudes are only a fraction of the circuit supply voltage (VDD of 1.8 V for 180 nm CMOS process is used throughout this thesis) the non-linear active resonator introduces considerable signal distortion. Even if an active inductor is designed such that it has a wide voltage headroom, the increasing harmonics inevitably will restrict large signal performance (due to the significant frequency shifts and distortion). Only few published works refer to this issue. This thesis builds off the work of Abidi [46] and Kaunisto [7] on standard gyrator resonators to, the previously unexplored, area of self-oscillating active inductors.

The last type of distortion is a DC shift caused by even-order harmonics. For the circuit parameters considered here, the average magnitude of this shift for each transconductance, resonant frequency and signal amplitude is in the range of 10%. This type of signal distortion, together with other even-order products i.e. $HD_2, HD_4, ..., HD_{2n}$ can be significantly minimised if a differential resonator is used and the signal is then com-

bined in a single ended buffer amplifier. The drawback is an increase in the odd-order products and the single-ended output from the circuit that occupies a double chip area in comparison with a single active inductor resonator.

5.6 Validation of presented analysis

As mentioned previously, the presented model of degenerated gyrator assumes that transconductance amplifiers are the only source of non-linearity. In practice, transistor capacitances and conductances are also non-linear, however their inclusion in the model would dramatically increase the complexity of the calculations. Also, most of the transistor parasitics are typically multidimensional i.e. their value depends on other circuit parameters [103]. As a result, no analytical model can be found if complete component models are required to be used.

Although only qualitative, the proposed model is validated in Chapter 7, Section 7.6, where the practical CMOS degenerated gyrator circuit is designed and simulated. The circuit consists of a single transistor transconductance amplifier, biased using current mirrors and is therefore well suited to compare with the simple non-linear model presented in this chapter. Figures 7.17 and 7.18 present the total input conductance and the parallel equivalent inductance as a function of signal amplitude. It can be seen that the negative conductance has the same character as predicted from a highly simplified model. As calculated, the smallest compression rate is obtained for medium values of gm, as predicted in Figure 5.10. The parallel inductance from Figure 7.18 undergoes the expected harmonic expansion and reduces the resonant frequency of the oscillator (Figure 7.19).

The harmonic distortion of the practical circuit was also simulated (Table 7.5). As predicted, when oscillation frequency increases, total harmonic distortion decreases due to the reduced HD_2 and HD_3 products for larger gm. Thus, although only one-dimensional non-linearities were used in the mathematical model derived in this thesis, the results of comparison to a more sophisticated CMOS circuit give an indication of

the validity of the presented large signal model.

5.7   Chapter summary

This chapter presented the non-linear analysis of a degenerated active inductor resonator. First, the basic theory of non-linear circuits was discussed, together with the fundamentals of Volterra kernels technique. Using the results previously published by Kaunisto [7], it was shown that the kernel method is suitable to describe the behavior of a standard active inductor resonator. Finally, an extended non-linear analysis of the proposed degenerated gyrator was presented, with special emphasis on the following:

- A new non-linear model of the active resonator. The crucial modifications over a standard gyrator circuit include: adding RC phase shifter at the output node and recognising an important problem of gm-dependent input losses of the resonator. Thus, although much simpler than a practical integrated circuit, the proposed model allows us to analyse circuit behavior under large signal excitation.

- A step by step Volterra kernel technique was presented. Though the method is well documented in the literature [103] it is usually given in more generic form. To explain how the results were obtained it was important to lead the reader through each step separately. As a result, this chapter can be used as a reference if other type of weakly non-linear circuits, not only gyrators, have to be analysed.

- The large signal response of degenerated gyrator resonator. It was shown the negative resistance generated using the passive RC shifter is compressed due to harmonic signals originating from non-linear amplifiers of the gyrator. When the oscillations build up, the increasing amplitude reduces negative resistance until its value equals the circuit losses. This phenomenon is caused by the weak non-linearity of transconductors rather than their saturation (which typically requires larger amplitudes). The harmonic compression is also responsible for lower oscillation frequency than predicted by the small signal model. For large amplitudes,

the simulated inductance is larger, shifting the resonant frequency down. This proves the importance of the large signal analysis presented in this thesis. These conclusions were confirmed by the simulation results of the practical circuit in Chapter 7.

- Harmonic distortion of signals of the proposed oscillator. As presented in this chapter, the kernels convey information on magnitude of harmonic products generated by the circuit. It was shown that when the signal amplitude increases, this results in higher harmonic distortion. This effect becomes more pronounced for low resonant frequencies and transconductance values. Note that the proposed simplified non-linear model was able to capture this behavior, comparable with the simulation results from Chapter 7.

The chapter also enabled the investigation of the practical range of amplitudes of the oscillator signal. Together with the study of noise from Chapter 4, the qualitative observations of the non-linear model lead to phase noise analysis of the proposed oscillator. The next chapter is dedicated to this important aspect of oscillator performance.

Chapter 6

Phase noise of degenerated gyrator

6.1 Introduction

As discussed in Chapter 2, the phase noise level of an oscillator is one of the most important parameters determining the performance of a circuit. It was shown that phase noise causes a reciprocal mixing in RF receivers and spurious emission in radio transmitters. To create a complete description of the proposed self-oscillating active inductor resonator it is therefore essential to create a phase noise model of the degenerated gyrator. This chapter consists of three parts:

- Section 6.2 presents an overview of the most important of the existing phase noise analysis methods. Both linear and non-linear phase noise models are discussed. The linear approach yields intuitive results, whereas the non-linear methods require large computational effort and do not provide any analytical formulas. The linear methods presented in this chapter include the famous Leeson's equation [114, 115], a staple phase noise model of feedback oscillators for the last fifty years. Also, a linear time variant approach of Hajimiri and Lee is discussed [45, 116–118]. Finally, a non-linear approach to phase noise modelling based on a well established harmonic balance method is presented. Each of the aforementioned methods is described focusing on its advantages, weaknesses and

accuracy of phase noise estimation. This part contributes to the thesis through a brief, yet informative, introduction to phase noise analysis of oscillators.

- In Section 6.3 a new linear time invariant phase noise model of the proposed circuit is derived. Using the methodology of Razavi [26] together with the proposed noise model for active inductor resonators from Chapter 4, a closed form analytical phase noise model of the degenerated gyrator resonator is obtained. This is the main contribution of this chapter as no similar models have been published yet. Calculations using the new LTI model are compared to the simulation results for the practical circuit from Chapter 7. This comparison shows only a few dB difference to a more complex numerical and non-linear phase noise model used by Eldo RF simulator, proving usability of the proposed LTI phase noise model of the degenerated active inductor resonator.

- In Section 6.4 the model derived in the previous section is discussed. Although highly simplified, the proposed analytical phase noise model provides valuable design insights into the basic dependencies between phase noise levels and active resonator components. As a result, the presented analysis clearly indicates the main sources of the inferior phase noise performance of the active inductor resonator in comparison to a standard integrated LC oscillators using passive spiral inductors.

The methodology used throughout this chapter requires some clarification. The term "phase noise level" corresponds to a standard definition i.e. it represents a relative power spectral density given in dBc (dB related to the power of the carrier signal) in a bandwidth of 1 Hz at some offset frequency ω_m from the carrier to the total power of this carrier signal [28]. Although phase fluctuations do not transmit any power, the noise current and voltages causing these fluctuations do. As a result, phase uncertainties can be described in the frequency domain through power spectral density functions related to the corresponding noise sources. If not otherwise indicated, noise sources are described using power, as in the case of the analyses from Chapters 2, 3 and 4.

6.2 Overview of phase noise models

6.2.1 Linear models

6.2.1.1 Time invariant approach (LTI) – Leeson's model

This approach known as *Leeson's model* after it's author D. B. Leeson, who published in a landmark paper presenting a simple model of LC feedback oscillator phase noise in 1966 [114]. The model consists of a linear amplifier described with noise figure F, and a simple LC resonator with a finite quality factor Q_0, illustrated in Figure 6.1. Leeson showed that in the case of an LC oscillator, the unloaded quality factor of the resonator is a critical parameter determining phase noise performance. In the Leeson model, two main noise sources are considered: white noise and flicker noise. Both noise sources modulate the oscillator phase and therefore the instantaneous frequency of the signal (as the frequency is a derivative of phase). Thus, the oscillator undergoes a AM-PM noise conversion. The phase of the signal is modulated with rates (ω_m) proportional to the frequency components of each of the noise sources. If that rate is small, flicker noise becomes the main phase modulating source whereas white noise source becomes
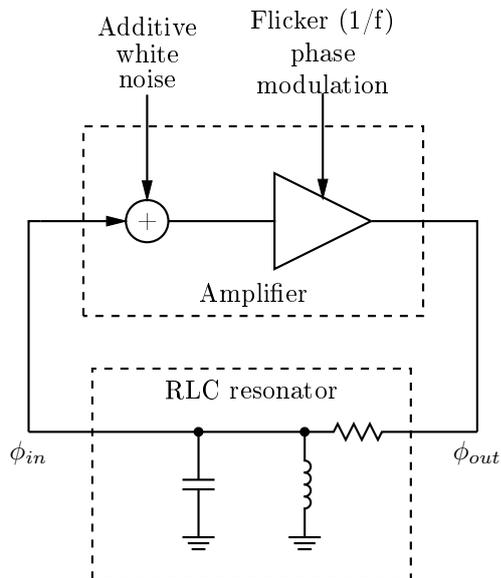
Figure 6.1: Leeson's phase noise model of feedback oscillator [41].

dominant at higher ω_m. Leeson expressed the combination of these two noise sources in terms of a double side band relative power spectral density expressed as

$$S_{\Delta\phi}(\omega_m) = \frac{2FkT}{P_s}\left(1 + \frac{\omega_3}{\omega_m}\right) \tag{6.1}$$

where F is a noise factor of the amplifier, k is Boltzmann's constant, T is the temperature in Kelvins, P_s is a carrier signal power and ω_3 is the frequency for which the level of a flicker noise is equal to the white noise (called *corner frequency*). Noise factor of the amplifier is defined as a ratio of signal to noise ration on the output of the amplifier to the signal to noise ration at its input. Leeson proposed that (6.1) can be considered as a single noise source representing a power spectral density of phase uncertainty $\Delta\phi$ of the LC oscillator [114]. The factor of 2 in (6.1) comes from the fact that amplitude changes due to noise are not included in the model. This assumption is valid because oscillators have an inherent mechanism of stabilising amplitude as explained previously in detail in Chapter 2, Section 2.3.1. The value of 2 is an estimate derived from the *equipartition theorem* [32] which states that a noise influence on the oscillator signal can be equally divided between phase and amplitude perturbations.

As the LC tank is a bandpass filter, it attenuates signals that are offset from the resonant frequency, acting like a low pass filter for frequency variations caused by the noise source (6.1). The attenuation of this low pass filter is proportional to the half bandwidth of the LC resonator

$$\beta_{half} = \frac{\omega_0}{2Q_0} \tag{6.2}$$

Leeson recognised that for values of ω_m within the half bandwidth of the tank, the PSD of ϕ_{out} phase fluctuations on the output of the amplifier can be found from

$$S_{\phi_{out}}(\omega_m) = \left.\frac{\beta_{half}^2}{\omega_m^2}S_{\Delta\phi}(\omega_m)\right|_{\substack{\omega_m < \beta_{half} \\ \omega_m \ll \omega_0}} \tag{6.3}$$

In the case of ω_m larger than the resonator β_{half}, frequency variations are substantially attenuated and do not propagate around the feedback loop [41]. However, they are still present at the amplifier output (i.e. the point between the amplifier and the resonator).

In this case the PSD of these phase variations is equal to (6.1) [114, 115]

$$S_{\phi_{out}}(\omega_m) = S_{\Delta\phi}(\omega_m)\Big|_{\omega_m > \beta_{half}} \tag{6.4}$$

Combining (6.1) with (6.4) the total phase noise spectrum of ϕ_{out} is described by

$$S_{\phi_{out}}(\omega_m) = \frac{2FkT}{P_s}\left(1 + \frac{\omega_3}{\omega_m}\right)\left(1 + \frac{1}{4Q_0}\frac{\omega_0^2}{\omega_m^2}\right) =$$
$$= \frac{2FkT}{P_s}\left(\frac{1}{\omega_m^3}\frac{\omega_0^2\omega_3}{4Q_0} + \frac{1}{\omega_m^2}\frac{\omega_0^2}{4Q_0} + \frac{\omega_3}{\omega_m} + 1\right) \tag{6.5}$$

Additionally, the PSD of ϕ_{in} variations for any value of ω_m can be found [115]

$$S_{\phi_{in}}(\omega_m) = \frac{2FkT}{P_s}\left(1 + \frac{\omega_3}{\omega_m}\right)\frac{1}{4Q_0}\frac{\omega_0^2}{\omega_m^2} \tag{6.6}$$

Leeson's model from (6.5) can be considered as a combination of four different noise sources [28]. The first source represents an up-converted flicker noise of the amplifier and is proportional to ω_m^{-3}. The second term represents thermal FM noise and decreases with ω_m^{-2}. The third source is the flicker phase noise whereas the last term represents the thermal noise floor of the oscillator. These four sources combined represent a generic solution and therefore require some practical assumptions about ω_3 and Q_0 values to emulate the actual behavior of an oscillator.

If the LC resonator has low Q_0 or low ω_3, the half-bandwidth of the tank is larger than the flicker noise corner. In this case, the output phase noise spectrum consists of three components depicted in Figure 6.2. All the parameters used for calculation of noise from (6.5) are included in the plot. Note that the angular frequency ω_m is transformed to a frequency f_m for convenience, however it does not affect any aspect of the Leeson model analysis. For the considered case, the phase noise spectrum is a combination of all components indicated by (6.5). Thus, the curve f_m^{-3} represents the up-converted flicker noise component, f_m^{-2} illustrates the thermal FM noise contribution as described previously. Figure 6.2 depicts the typical shape of phase noise spectrum for a typical LC oscillator built using integrated resonant tanks with either spiral inductors or gyrators.
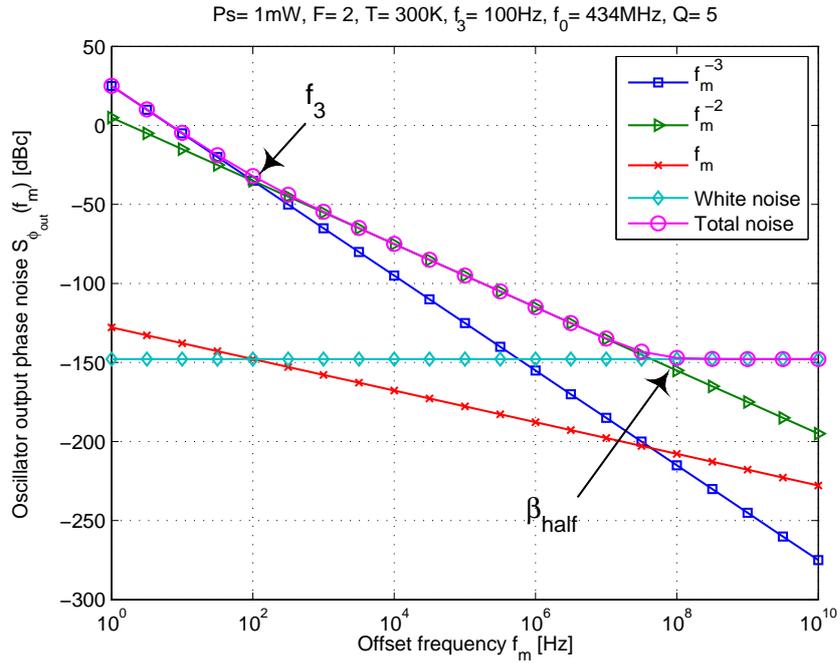
Figure 6.2: Phase noise model for low Q_0 or low f_m LC feedback oscillator.
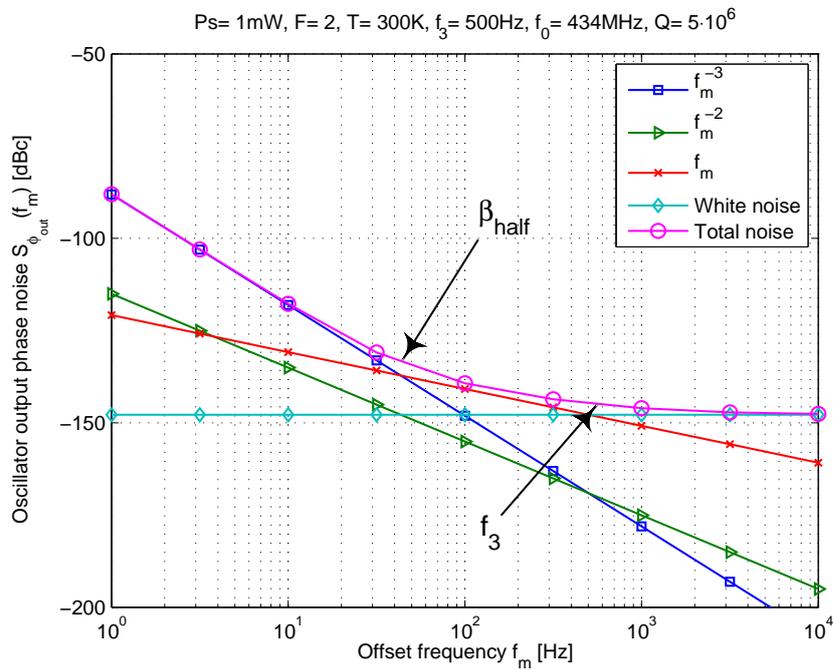
Figure 6.3: Phase noise model for high Q_0 or high f_m LC feedback oscillator.

When the resonant tank has either high Q_0 or high ω_3 (f_m), the phase noise spectrum is similar to that presented in Figure 6.3. The spectrum also consists of three components, however now the thermal FM noise of f_m^{-2} is superimposed by the remaining sources from (6.5). Note that a Q_0 of $5 \cdot 10^6$ can't be obtained by any means in any practical integrated circuit and is used only to simulate the behavior of an oscillator with the extremely high quality factor.

6.2.1.2 Strengths and limitations of Leeson model

The presented linear time invariant method represents a fundamental model of phase noise in oscillators. A closer look at (6.5) reveals ways to minimise phase noise of an LC oscillator [41]:

- White noise spectral density has to be small. This requirement ensures a small FM modulation of the output signal due to thermal noise generated in the resonator. This also minimises the noise floor of the system because at large frequency offsets ω_m minimising effects of reciprocal mixing. As the majority of noise in the oscillator originates from the amplifier, it is crucial to use active circuits with the lowest noise figure possible.

- Oscillator signal power P_s should be large. If the oscillation amplitude is large then the signal to noise ratio of the oscillator improves. As a result, phase noise is smaller because it represents a relative measure of noise power to the power of the generated signal. In practice, the signal to noise ratio does not improve indefinitely with increasing signal amplitude. At a certain point the circuit can't exceed the maximum signal level (due to breakdown voltage of transistors or the maximum current specification). The attempts to further increase it usually boost noise levels which in turn reduces the phase noise performance of the oscillator.

- Resonator Q_0 should be large. Large quality factor decreases half-bandwidth of the resonator, improving attenuation of noise at small frequency offsets ω_m from the carrier. However as shown in Chapters 2 and 3 this requirement is valid only

for the tanks using passive inductors. When gyrators are employed phase noise becomes proportional to Q_0 [47] and for this reason the Leeson model can't be directly employed to predict the behavior of these circuits.

- Flicker corner frequency ω_3 should be small. This is an indication that the circuit should contain a relatively low flicker noise component. Smaller flicker noise frequency reduces noise from ω_m^{-3} and ω_m^{-1} regions of (6.5). As a result, phase noise close to the carrier is reduced, that improving significantly the spectral purity of the oscillator signal.

- If phase noise at large ω_m is important, the oscillator output should be taken from the output of the resonator (ϕ_{in} from Figure 6.1) to take advantage of the extra filtering in the resonator as suggested by (6.6). However, post-oscillator circuits (e.g. buffer amplifiers, frequency multipliers, frequency dividers or phase-noise analysers) can contribute flicker or white noise levels sufficient to mask this behavior, thus further circuit simulations have to be conducted to confirm the proper choice of oscillator output node.

Some shortcomings of the Leeson phase noise model have been reported. Firstly, the signal power P_s, corner frequency ω_3 and noise factor F parameters have to be known prior to the calculations. As suggested in the original paper [114], they are found empirically such that the calculated model fits measured data for the given oscillator. Thus the model can't predict the phase noise levels of an unknown oscillator circuit directly and should be treated as a qualitative analysis. Secondly, Leeson presents a model based on a linear amplifier which is not true in general. For example, harmonic effects are not included and hence noise effects related to harmonics are not included. Finally, as the model deals only with the LC feedback oscillator circuit it can't explain the phase noise behavior of ring oscillators [41, 119].

6.2.1.3 Time variant approach (LTV) – Hajimiri-Lee model

The basic shortcoming of Leeson's approach is an assumption of stationary behavior for oscillators. With this assumption, an amplifier introduces the same amount of noise equally over the period of oscillations. In general this is not true, since in each cycle a standard LC resonator receives energy from the amplifier in the form of short pulses. The noise is injected to the tank during this short period of time also. Therefore, the phase modulation of the oscillator signal due to noise depends also on time instant when the noise has been introduced to the circuit. As a result, oscillator behavior in the presence of noise is time variant as opposed to the Leeson approach.

This problem was recognized and described by Hajimiri and Lee [45, 116–118]. In general, if a pulse perturbation (or any signal including noise) is injected into oscillating resonator, it causes variations of both amplitude and phase, as illustrated on Figure 6.4. If the perturbation occurs when an oscillation reaches the peak magnitude,
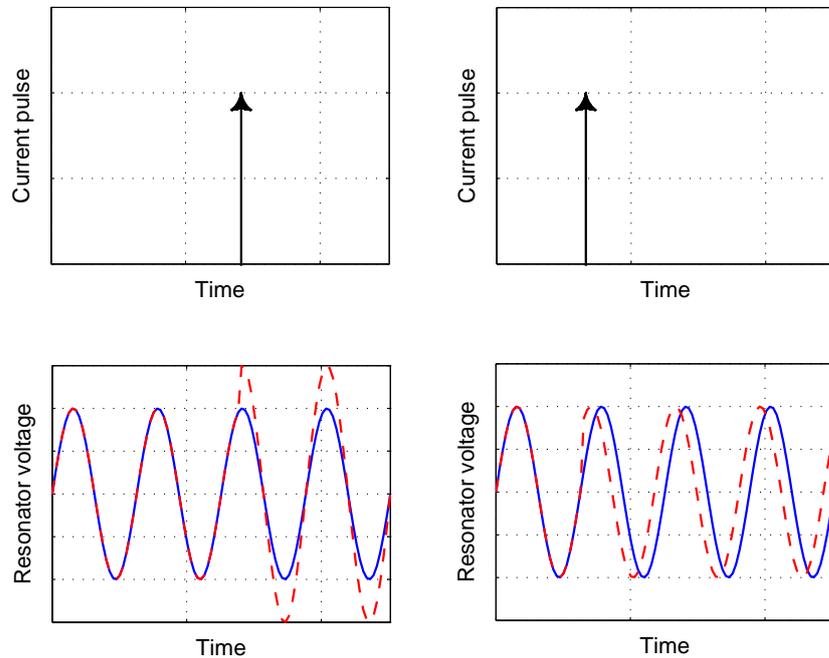
Figure 6.4: Response of oscillating resonator to injected current disturbance [116].

the amplitude of the signal is changed, however the phase is not affected. On contrary, if the same perturbation is injected during the zero crossing, phase changes instantly but the amplitude is not. Thus, it can be seen that the phase noise of the oscillator depends on the time instant when the noise is introduced in the resonator. Hajimiri and Lee proposed the *impulse sensitivity function* (ISF for short or $\Gamma(x)$), to represent the described behavior of phase fluctuations. It is a dimensionless, amplitude independent and periodic function with period of 2π. It is measured as a relative phase change to a signal period for different injection instants of the single test pulse of known amount of electrical charge. The ISF reaches the maximum when the pulse is introduced during zero crossings and equals zero when the perturbation is applied at the peak of oscillations. Once the ISF is derived, it is expanded in terms of a Fourier series with real coefficients. These coefficients are then used to express the phase noise equation in a logarithmic scale as [116]

$$S_{\phi_{out}}(\omega_m) = 10 \log \left(\frac{c_0^2 \cdot \overline{i_n^2}/\Delta\omega}{4q_{max}^2} \cdot \frac{\omega_{1/f}}{\omega_m^3} + \frac{\Gamma_{RMS}^2}{2q_{max}^2} \cdot \frac{\overline{i_n^2}/\Delta\omega}{\omega_m^2} \right) \qquad (6.7)$$

where c_0 is the first coefficient of Fourier expansion of ISF, q_{max} is a maximum charge stored in a tank capacitor, $\overline{i_n^2}/\Delta\omega$ is a noise PSD of a single source, ω_m is an offset frequency from the carrier, $\omega_{1/f}$ represents a flicker corner frequency of an amplifier and Γ_{RMS} is a RMS value of a periodic function $\Gamma(x)$.

The use of electrical charge q_{max} as a quantity controlling the phase noise is not coincidental. Hajimiri and Lee observed that although oscillators are non-linear in a sense of current and voltage transfer functions, phase fluctuations are proportional to the amount of charge injected by the noise sources to the resonator. This relationship remains linear and therefore standard impulse response functions known from the linear circuit analysis can be used to derive (6.7).

6.2.1.4 Strengths and limitations of Hajimiri-Lee model

The main strength of the discussed approach lies in its ability to capture non-linear effects taking place in practical oscillators. A harmonic distortion of a generated signal

produces also corresponding harmonics of the ISF function. As (6.7) is derived using Fourier coefficients of the impulse sensitivity function, the resulting phase noise includes effects of non-linear distortion caused in the oscillator. This qualitative conclusion can't be obtained using the simple Leeson model.

The main disadvantage of this method is a tedious calculation of ISF, valid only to the particular circuit under test [28]. In addition, as indicated [116], an exact analytical derivation of $\Gamma(x)$ can't be found for any but the simplest oscillators and hence have to be usually solved numerically. Also, the amplitude of the testing impulse is not specified explicitly and additional testing is needed to ensure linearity between charge and phase fluctuations.

The Hajimiri-Lee model delivers a following set of qualitative oscillator rules:

- Active circuit providing energy restoration to the resonator should be on only during a zero crossings of ISF. These pulses should be relatively short in comparison to the oscillation period.

- If possible the ISF should be symmetrical to reduce its DC component and hence any flicker noise up-conversion caused by it. This is especially important for technologies with poor $1/f$ performance.

- The main conclusions of the time-invariant model are still valid. Q_0 and signal amplitude should be maximised, as in the case of the Leeson model.

Although extensively cited, the linear time-variant method briefly presented here is not widely used in practical oscillator design. Firstly, most of the observations published by Hajimiri and Lee are sufficient to establish a set of qualitative design rules for both LC and ring oscillators. As ISF is not usually given in a form of analytical formula consisting of various circuit parameters, it is impossible to predict how $\Gamma(x)$ changes with these parameters. Thus, if one of these parameters is modified usually ISF have to be derived again together with its Fourier series coefficients. For this reasons, commercially

available circuit simulators use a more complex, non-linear approach presented in the following section.

6.2.2 Nonlinear phase noise model – harmonic balance method

The non-linear phase noise model requires substantial computational power and does not yield closed form solutions, however results in more accurate phase noise estimation than the linear methods described previously. The calculation can be either conducted in the time or frequency domain. The latter approach is more common, since typical large signal circuits can be successfully solved using Fourier series.

The phase noise calculation method using the non-linear circuit model is based on a solution of Kirchhoff's equations in the presence of a perturbing signal. In, fact this is a modified version of the standard *harmonic balance technique*, or HB, used to solve large signal problems in the frequency domain. The main difference between analysis of oscillators and amplifiers or mixers is that the former is an autonomous circuit, and therefore there are no excitation signals. The oscillation frequency is therefore not known and must be estimated prior to further calculations, either by a random guess or by more elaborate iterative continuation methods [110].

The HB method can be briefly explained as follows. First, linear and non-linear components of an oscillator circuit are found and grouped respectively into linear and non-linear sub-networks. These sub-networks are then connected together through a finite number of ports [110]. At this stage, the circuit is considered noiseless. A linear subcircuit is represented by a Norton equivalent network, described by an admittance matrix, and can be directly solved in the frequency domain. The non-linear components are represented in the time domain where the responses corresponding to each of the ports are calculated and then transferred into the frequency domain. The total response of the circuit is found when for each interconnecting port and harmonic frequency the current of the linear network equals the current from the non-linear block.

Once frequency and amplitude of the fundamental and harmonic components are found, noise sources are connected to the circuit in the form of current and voltage

generators placed between linear and non-linear sub-networks. The presence of noise disturbs an ideal solution, and therefore it has to be modified to satisfy Kirchhoff's laws. Noise sources close to the carrier modulate the signal frequency producing sidebands around the carrier [28]. At higher offsets, the oscillator acts as a mixer converting low frequency noise sources around the harmonics of the oscillating signal [110].

The main advantage of this phase noise calculation method is its ability to capture noise effects in non-linear autonomous circuit, providing that noise models are well characterised and available for the circuit designer. For this reason the technique is widely used in commercial circuit simulators. The disadvantage is a lack of any analytical insight into phase noise generation mechanisms and therefore the circuit parameters have to be optimised through a number of numerical simulations.

6.2.3   Comparison of presented methods

Table 6.1 presents a short summary of the presented phase noise modelling methods. Each approach is characterised by its complexity, accuracy and ability to provide a closed form solution. Although the time invariant method proposed by Leeson is the least accurate, it allows us to establish performance limitations through noise analysis of a linear circuit. The main purpose of this chapter is the derivation of a closed form phase noise model to capture fundamental relationships between phase noise and circuit parameters. For this reason, the existing LTI approach is sufficient, however the accuracy of phase noise calculation is low and should be treated as qualitative.

Table 6.1: Comparison of existing oscillator phase noise models.

Name	Type	Complexity	Closed form solution	Accuracy
Leeson	linear/invariant	low	yes	poor
Hajimiri-Lee	linear/variant	medium	very limited	fair
Harmonic balance	non-linear/variant	high	no	very good

6.3   Proposed LTI phase noise model of degenerated active inductor oscillator

This section presents the main contribution of this chapter, the proposed LTI model of the degenerated active inductor oscillator. First, the methodology of model derivation is presented, focusing on the linear methods of noise analysis. This leads to the derivation of the phase noise model with special emphasis on the contribution of all considered noise sources. Finally, the model is discussed and compared to a non-linear numeric algorithm implemented in Eldo RF [120].

6.3.1   Methodology description

To clarify the way the model is obtained it is important to investigate existing LTI models published in the literature. As the Leeson's model describes only a phase noise of the standard LC feedback oscillator, Razavi [121] derived the linear time invariant models of inductorless architectures as ring or relaxation oscillators. This methodology was used by Craninckx [47] to describe the phase noise of the oscillator with a standard active inductor, detailed in Chapter 3, Section 3.4.3. The proposed LTI model will be derived using the same approach.

The method uses noise transfer functions, previously described in Chapters 3 and 4 to study noise properties of active inductor and degenerated gyrator resonators. Recalling (3.30) from Chapter 3 to calculate phase noise at a given frequency offset ω_m the noise power at this frequency has to be found and then compared to the signal power at the resonant frequency ω_0. The calculation of noise in resonators at ω_m using a noise transfer function is not trivial. In oscillating circuits, where all of the losses are compensated, these functions become infinite, as indicated in Chapter 3, Section 3.3.2.2. This behavior is expected as in a fully compensated resonator the signal would increase indefinitely if it was not limited by the amplifier non-linearity. To circumvent this, Razavi proposed linearisation of transfer functions around the resonant frequency using the first two terms of the Taylor series. If the offset frequency ω_m is much less than

6.3 Proposed LTI phase noise model of degenerated active inductor oscillator

oscillation frequency ω_0, then the noise transfer function is estimated by a tangent line approximation from

$$H_n(\omega_m)\Big|_{\omega_m \ll \omega_0} \approx H_n(\omega_0) + \omega_m \frac{\partial H_n(\omega)}{\partial \omega}\Big|_{\omega=\omega_0} \tag{6.8}$$

where $H_n(\cdot)$ is the noise transfer function. Thus although $H_n(\omega_0)$ is still infinite at resonant frequency, the second term is not. Note that without additional analysis (6.8) can't be calculated as the first term is infinite. Craninckx [47] suggested that since infinite impedance corresponds to zero admittance, it is possible to use admittance noise transfer functions instead, however without giving any proof that such an assumption is valid. An original proof is derived in this dissertation to validate this statement.

The relationship between impedance and admittance of any linear circuit is given by

$$Z(\omega_m) \equiv \frac{1}{Y(\omega_m)} \tag{6.9}$$

then, according to (6.8) it can be rewritten as

$$Z_n(\omega_0) + \omega_m \frac{\partial Z_n(\omega)}{\partial \omega}\Big|_{\omega=\omega_0} = \frac{1}{Y_n(\omega_0) + \omega_m \frac{\partial Y_n(\omega)}{\partial \omega}\Big|_{\omega=\omega_0}} \tag{6.10}$$

Grouping the functions on the left hand side this yields the following

$$Z_n(\omega_0)Y_n(\omega_0) + Y_n(\omega_0)\omega_m \frac{\partial Z_n(\omega)}{\partial \omega} + Z_n(\omega_0)\omega_m \frac{\partial Y_n(\omega)}{\partial \omega} + \omega_m^2 \frac{\partial Z_n(\omega)}{\partial \omega} \frac{\partial Y_n(\omega)}{\partial \omega} = 1 \tag{6.11}$$

Substituting impedance with conductance ($Z = 1/Y$), (6.11) transforms to

$$1 + Y_n(\omega_0)\omega_m \frac{\partial\left(\dfrac{1}{Y_n(\omega)}\right)}{\partial \omega} + \frac{\omega_m}{Y_n(\omega_0)} \frac{\partial Y_n(\omega)}{\partial \omega} + \omega_m^2 \frac{\partial\left(\dfrac{1}{Y_n(\omega)}\right)}{\partial \omega} \frac{\partial Y_n(\omega)}{\partial \omega} = 1 \tag{6.12}$$

Using a reciprocal rule

$$-Y_n^2(\omega) \frac{\partial\left(\dfrac{1}{Y_n(\omega)}\right)}{\partial \omega} = \frac{\partial Y_n(\omega)}{\partial \omega} \tag{6.13}$$

6.3 Proposed LTI phase noise model of degenerated active inductor oscillator

expression (6.12) simplifies to

$$1 - \frac{\omega_m^2}{Y_n^2(\omega_0)} \frac{\partial Y_n(\omega)}{\partial \omega} \frac{\partial Y_n(\omega)}{\partial \omega} = 1 \tag{6.14}$$

Equation (6.14) is true only if $\omega_m \to 0$. In practice, for non-zero offset frequencies in the range up to a few MHz from RF carrier, the reminder on the left-hand side of (6.14) is negligible and both sides of (6.14) are still approximately equal. As a result, the noise transfer function can now be represented by a linearised version of its reciprocal from (6.9)

$$Z_n(\omega_m)\bigg|_{\omega_m \ll \omega_0} \approx \frac{1}{Y_n(\omega_0) + \omega_m \dfrac{\partial Y_n(\omega)}{\partial \omega}} \approx \frac{1}{\omega_m \dfrac{\partial Y_n(\omega)}{\partial \omega}}\bigg|_{Y_n(\omega_0)=0} \tag{6.15}$$

The proposed proof completes the discussed methodology used previously by Razavi [121] and Craninckx [47]. To calculate the phase noise of degenerated gyrator, the noise transfer functions corresponding to each of the noise sources of the gyrator circuit have to be found first. As presented in Chapters 3 and 4, these functions have typically an impedance character. Assuming $\omega_m << \omega_0$, (6.15) can be used to find noise transfer functions at the offset frequency, despite the fact that the impedance of a fully compensated resonator is infinite. After the functions are characterised, the noise power due to noise sources can be calculated for the frequency of ω_m. This power compared to the power of the oscillator signal (that can be estimated from the large signal model presented in Chapter 5) results in the phase noise at given offset frequency.

6.3.2   Noise model of fully compensated resonator circuit

Although the noise calculation methodology presented in this chapter is widely known, the following LTI model for a degenerated active inductor derived using this approach is novel. To find the noise transfer functions of a fully compensated resonant tank, consider the degenerated gyrator resonator model illustrated on Figure 6.5. In fact, this is the modified version of a generic noise model from Figure 4.15 described in Chapter 4, Section 4.6.1. During oscillations, all circuit losses, including load, are compensated by

6.3 Proposed LTI phase noise model of degenerated active inductor oscillator
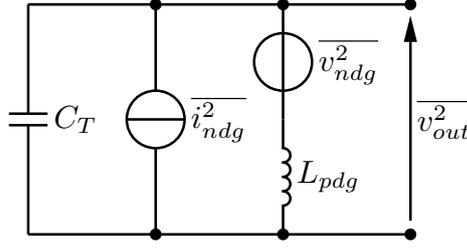
Figure 6.5: Fully compensated noisy degenerated gyrator resonant tank.

a negative resistance generation mechanism and full compensation occurs. As a result, the circuit can be simplified into a parallel connection of single capacitor and inductor. Note that all of the noise sources are still present as these are not affected by the negative resistance compensation mechanism.

Applying KVL to the circuit from Figure 6.5, the output voltage produced by noise sources is found as

$$v_{outFC} = i_{ndg}Z_{ndgFC}\left(j\omega\right) + v_{ndg}A_{ndgFC}\left(j\omega\right) \tag{6.16}$$

where

$$Z_{ndgFC}\left(j\omega\right) = \frac{j\omega L_{pdg}}{1 - \omega^2 L_{pdg}C_T} = \frac{1}{j\left(\omega C_T - \dfrac{1}{\omega L_{pdg}}\right)} \tag{6.17}$$

$$A_{ndgFC}\left(j\omega\right) = \frac{1}{1 - \omega^2 L_{pdg}C_T} = \frac{Z_{ndgFC}\left(j\omega\right)}{j\omega L_{pdg}} \tag{6.18}$$

Note that (6.17) and (6.18) are equal to the transfer functions (4.45) and (4.46) from Chapter 4 when $R_T \to \infty$ i.e. when the tank is fully compensated. As i_{ndg} and v_{ndg} are correlated through the resistor R_{out} from the phase shifter, it is important to expand these sources to independent uncorrelated terms.

Recalling (4.43) from Chapter 4, substituting it into (6.16) and grouping terms, the output voltage v_{outFC} consists of

$$v_{outFC} = \left(i_{d2} + v_{nR}\frac{gm_2}{j\omega C_{out}R_{out} + 1}\right)Z_{ndgFC}\left(j\omega\right) +$$

$$+ \frac{1}{gm_1}\left(i_{d1} + v_{nR}\frac{j\omega C_{out}}{j\omega C_{out}R_{out} + 1}\right)A_{ndgFC}\left(j\omega\right) \approx$$

6.3 Proposed LTI phase noise model of degenerated active inductor oscillator

$$\approx i_{d2}Z_{ndgFC}\left(j\omega\right) + \frac{i_{d1}}{gm_1}A_{ndgFC}\left(j\omega\right) +$$

$$+ v_{nR}\left(\frac{C_{out} + gm_1gm_2L_{pgd}}{gm_1C_{out}R_{out}}\right)A_{ndgFC}\left(j\omega\right)\bigg|_{\omega\gg 1/C_{out}R_{out}} \tag{6.19}$$

and the contribution of each of these noise sources can now be analysed separately: i_{d2}, i_{d1} and v_{nR} of the phase shifter resistor. Note that the noise transfer function from R_{out} is derived assuming low-pass noise shaping in the phase shifter, also described in detail in Chapter 4, Section 4.6.

6.3.3   Noise from transconductance amplifiers

Here the methodology described in Section 6.3.1 is applied in practice. First, the noise transfer function of i_{d2} source originating from the feedback transconductor is analysed. The reciprocal of the noise transfer function (6.17) is equal to

$$Y_{ndgFC}\left(j\omega\right) = \frac{1}{Z_{ndgFC}\left(j\omega\right)} = \frac{1 - \omega^2 L_{pdg}C_T}{j\omega L_{pdg}} = j\left(\omega C_T - \frac{1}{\omega L_{pdg}}\right) \tag{6.20}$$

As shown by (4.9) in Chapter 4, L_{pdg} is a function of frequency. This dependency becomes important because even for a relatively small change of inductance, its derivative is non-zero. When omitted, the phase noise level can be underestimated by a few dB, decreasing the accuracy of the already simplified LTI model.

According to (6.15), to find the noise transfer function at ω_m, the derivative of the conductance has to be found first

$$\frac{\partial Y_{ndgFC}\left(\omega\right)}{\partial\omega} = j\left(C_T + \frac{1}{\omega^2 L_{pdg}} + \frac{1}{\omega L_{pdg}^2}\frac{\partial L_{pdg}}{\partial\omega}\right) \tag{6.21}$$

As the inductance is a function of frequency, its derivative is found using the auxiliary parameters of a parallel degenerated resonator model from Section 4.5. Using (4.25), (4.26) and (4.27) this is calculated as

$$\frac{\partial L_{pdg}}{\partial\omega} = \frac{2C_G}{gm_1gm_2}\left(\frac{\omega}{\omega_{z2}^2} - \frac{\omega_{z1}^2}{\omega^3}\right) \approx \frac{2C_G}{gm_1gm_2}\frac{\omega}{\omega_{z2}^2} \tag{6.22}$$

6.3 Proposed LTI phase noise model of degenerated active inductor oscillator

The conductance Y_{ndgFC} at ω_m can be found by substituting (6.21) and (6.22) to (6.8)

$$Y_{ndgFC}\left(\omega_m\right) \approx Y_{ndgFC}\left(\omega_0\right) + \omega_m \frac{\partial Y_{ndgFC}\left(\omega\right)}{\partial \omega} = 2j\omega_0 C_T \left(1 + \frac{C_T C_G}{gm_1 gm_2} \cdot \frac{\omega_0^4}{\omega_{z2}^2}\right) \cdot \frac{\omega_m}{\omega_0}$$

(6.23)

Finally, using the mathematical proof (6.15), the impedance noise function $Z_{ndgFC}\left(\omega_m\right)$ necessary to calculate the contribution of i_{d2} is derived as

$$Z_{ndgFC}\left(\omega_m\right) \approx \frac{1}{2j\omega_0 C_T} \cdot \frac{1}{1 + \dfrac{C_T C_G}{gm_1 gm_2} \cdot \dfrac{\omega_0^4}{\omega_{z2}^2}} \cdot \frac{\omega_0}{\omega_m}$$

(6.24)

The noise contribution from the direct path transconductor is derived in a similar fashion. The reciprocal of the corresponding noise transfer function (6.18) is first calculated

$$K_{ndgFC}\left(j\omega\right) = \frac{1}{A_{ndgFC}\left(j\omega\right)} = 1 - \omega^2 L_{pdg} C_T$$

(6.25)

and approaches zero at resonant frequency. In the next step of the analysis described in Section 6.3.1, the derivative of $K_{ndgFC}\left(j\omega\right)$ is found

$$\frac{\partial K_{ndgFC}\left(\omega\right)}{\partial \omega} = -2\omega L_{pdg} C_T - \omega^2 C_T \frac{\partial L_{pdg}}{\partial \omega} = -2\left(\omega L_{pdg} C_T + \frac{\omega^2 C_T C_G}{gm_1 gm_2} \frac{\omega}{\omega_{z2}^2}\right)$$

(6.26)

Note that again (6.22) was used. As a result K_{ndgFC} at ω_m is therefore equal to

$$K_{ndgFC}\left(\omega_m\right) \approx -2\left(\omega_0^2 L_{pdg} C_T + \frac{\omega_0^2 C_T C_G}{gm_1 gm_2} \frac{\omega_0^2}{\omega_{z2}^2}\right) \cdot \frac{\omega_m}{\omega_0} =$$

$$= -2\left(1 + \frac{C_T C_G}{gm_1 gm_2} \cdot \frac{\omega_0^4}{\omega_{z2}^2}\right) \cdot \frac{\omega_m}{\omega_0}$$

(6.27)

Finally, at offset frequency ω_m, the noise transfer function of the i_{d1} generator is given by

$$A_{ndgFC}\left(\omega_m\right) \approx \frac{1}{K_{ndgFC}\left(\omega_m\right)} = -\frac{1}{2} \cdot \frac{1}{1 + \dfrac{C_T C_G}{gm_1 gm_2} \cdot \dfrac{\omega_0^4}{\omega_{z2}^2}} \cdot \frac{\omega_0}{\omega_m}$$

(6.28)

Note that in both (6.24) and (6.28) noise transfer functions are derived in terms of ω_0/ω_m by the use of factorisation. Therefore the presented results follow the conventional phase noise representation found throughout the literature.

6.3 Proposed LTI phase noise model of degenerated active inductor oscillator

The noise transfer function (6.24), corresponding to the noise source i_{d2} of the feedback transconductor, is inversely proportional to the total tank capacitance C_T. This is expected behavior since, as presented in Chapter 4, the noise power spectral density of a degenerated active inductor has kT/C_T characteristics. Both transfer functions (6.24) and (6.28) have the common term that seems to be strongly and inversely proportional to the carrier frequency and possibly can be minimised for large ω_0. In practice however, this is not the case and it can be explained as follows. As the parallel inductance of a degenerated active inductor is

$$L_{pdg} \propto \frac{C_G}{gm_1 gm_2} \tag{6.29}$$

and

$$\omega_0^2 \propto \frac{1}{L_{pdg} C_T} = \frac{gm_1 gm_2}{C_G C_T} \tag{6.30}$$

then the described term can be roughly approximated by

$$\frac{1}{1 + \dfrac{C_T C_G}{gm_1 gm_2} \cdot \dfrac{\omega_0^4}{\omega_{z2}^2}} \approx \frac{1}{1 + \dfrac{\omega_0^2}{\omega_{z2}^2}} \tag{6.31}$$

At sub-GHz frequencies, the parameter values in the range described in Chapter 4 by Tables 4.4 and 4.6) result in the ratio of ω_0^2/ω_{z2}^2 between 0.5 and 1.5. This is due to the dependence of the resonant frequency on ω_{z2} given by (4.13). Thus, the dependency between (6.31) and the resonant frequency is not strong.

6.3.4 Noise from phase shifter

The last noise contribution comes from the phase shifter used for negative resistance generation. Assuming higher resonance frequency than of a 3 dB corner of $C_{out} R_{out}$, the reciprocal of the noise transfer function of source v_{nR} from (6.19) is

$$N_{ndgFC}(j\omega) = \frac{gm_1 C_{out} R_{out}}{(C_{out} + gm_1 gm_2 L_{pgd}) A_{ndgFC}(j\omega)} = \frac{gm_1 C_{out} R_{out} (1 - \omega^2 L_{pdg} C_T)}{C_{out} + gm_1 gm_2 L_{pgd}} \tag{6.32}$$

6.3 Proposed LTI phase noise model of degenerated active inductor oscillator

Using the quotient rule and reduction the derivative of (6.32) is equal to

$$
\frac{\partial N_{ndgFC}\left(\omega\right)}{\partial \omega} = \frac{gm_1 C_{out} R_{out} \left(-2\omega L_{pdg} C_T - \omega^2 C_T \dfrac{\partial L_{pdg}}{\partial \omega}\right)}{C_{out} + gm_1 gm_2 L_{pgd}} +
$$

$$
+ \frac{gm_1 C_{out} R_{out} \left(1 - \omega^2 L_{pdg} C_T\right) gm_1 gm_2 \dfrac{\partial L_{pdg}}{\partial \omega}}{\left(C_{out} + gm_1 gm_2 L_{pgd}\right)^2} \tag{6.33}
$$

At resonant frequency second term of (6.33) equals zero, and by substituting (6.22) and factorising for ω_m/ω_0, N_{ndgFC} is given by

$$
N_{ndgFC}\left(\omega_m\right) \approx \frac{-2gm_1 \omega_0^2 C_T C_{out} R_{out} \left(\omega_0^2 L_{pdg} C_T + \dfrac{\omega_0^2 C_T C_G}{gm_1 gm_2} \cdot \dfrac{\omega_0^2}{\omega_{z2}^2}\right)}{\omega_0^2 C_T C_{out} + gm_1 gm_2} \cdot \frac{\omega_m}{\omega_0} =
$$

$$
= \frac{-2gm_1 \omega_0^2 C_T C_{out} R_{out} \left(1 + \dfrac{C_T C_G}{gm_1 gm_2} \cdot \dfrac{\omega_0^4}{\omega_{z2}^2}\right)}{\omega_0^2 C_T C_{out} + gm_1 gm_2} \cdot \frac{\omega_m}{\omega_0} \tag{6.34}
$$

and the noise transfer function of voltage source v_{nR} from phase shifter at offset frequency is obtained

$$
A_{nRFC}\left(\omega_m\right) \approx \frac{1}{N_{ndgFC}\left(\omega_m\right)} = -\frac{\omega_0^2 C_T C_{out} + gm_1 gm_2}{2gm_1 \omega_0^2 C_T C_{out} R_{out} \left(1 + \dfrac{C_T C_G}{gm_1 gm_2} \cdot \dfrac{\omega_0^4}{\omega_{z2}^2}\right)} \cdot \frac{\omega_0}{\omega_m} =
$$

$$
= -\frac{1 + \dfrac{gm_1 gm_2}{\omega_0^2 C_T C_{out}}}{2gm_1 R_{out}} \cdot \frac{1}{1 + \dfrac{C_T C_G}{gm_1 gm_2} \cdot \dfrac{\omega_0^4}{\omega_{z2}^2}} \cdot \frac{\omega_0}{\omega_m} \tag{6.35}
$$

As in (6.24) and (6.28), the noise transfer function (6.35) contains the term described by (6.31) that is not strongly dependent on the resonant frequency. The remaining term is controlled directly by the phase shifter parameters R_{out} and C_{out}. The first conclusion is that noise level at ω_m can be decreased for larger values of R_{out}. This behavior follows the assumption that the 3 dB corner frequency of the phase shifter

6.3 Proposed LTI phase noise model of degenerated active inductor oscillator

is lower than the resonant frequency of the oscillator. As described in Chapter 4, in this case less noise is injected into the resonator due to the low pass characteristics of the RC circuit. This feature can't be exploited for large values of R_{out}. If R_{out} is excessive, the cut-off frequency of the phase shifter is too low and there is no signal fed back to the gyrator input. As a result, negative conductance generated at higher resonant frequencies may not be sufficient to compensate the circuit. This behavior has been discussed in Chapter 4, Section 4.5, where the bandwidth over which the negative resistance is available was analysed. As (6.35) shows, the noise level at ω_m is inversely proportional to C_{out} as well. This dependence has the same character as in the case of R_{out} with all the consequences described previously i.e. excessive capacitance values decrease noise but at the same time reduce the amount of negative conductance generated at resonant frequency.

The noise contribution of the phase shifter is also inversely proportional to gm_1 and the total tank capacitance C_T. Thus to reduce the noise both gm_1 and C_T have to be increased. As presented previously in Chapters 3 and 4 this requirement causes large power consumption at a given resonant frequency. One may also conclude that the noise contribution of the RC circuit can also be controlled by the $gm_1 gm_2$ product, as shown by (6.35). However, as $\omega_0^2 \propto gm_1 gm_2$, change in the two transconductances causes a proportional change of the resonant frequency ω_0, thus not affecting the noise transfer function.

6.3.5   Total noise at offset frequency ω_m

After the respective noise transfer functions have been calculated, the total output noise PSD at offset frequency ω_m of the degenerated gyrator can be found. As the noise sources of the transconductors and the phase shifter are uncorrelated the total noise is found from

$$
\frac{\overline{v_{ndgFC}^2\left(\omega_m\right)}}{\Delta f} = \frac{\overline{i_{d2}^2}}{\Delta f}\left|Z_{ndgFC}\left(\omega_m\right)\right|^2 + \frac{\overline{i_{d1}^2}}{\Delta f}\frac{1}{gm_1^2}\left|A_{ndgFC}\left(\omega_m\right)\right|^2 +
$$
$$
+ \frac{\overline{v_{nR}^2}}{\Delta f}\left|A_{nRFC}\left(\omega_m\right)\right|^2 \tag{6.36}
$$

6.3 Proposed LTI phase noise model of degenerated active inductor oscillator

and substituting (6.24), (6.28) and (6.35), equation (6.36) is transformed into

$$
\frac{\overline{v_{ndgFC}^2(\omega_m)}}{\Delta f} \approx \frac{\overline{i_{d2}^2}}{\Delta f} \frac{1}{4\omega_0^2 C_T^2 \left(1 + \dfrac{C_T C_G}{gm_1 gm_2} \cdot \dfrac{\omega_0^4}{\omega_{z2}^2}\right)^2} \cdot \frac{\omega_0^2}{\omega_m^2} +
$$

$$
+ \frac{\overline{i_{d1}^2}}{\Delta f} \frac{1}{4gm_1^2 \left(1 + \dfrac{C_T C_G}{gm_1 gm_2} \cdot \dfrac{\omega_0^4}{\omega_{z2}^2}\right)^2} \cdot \frac{\omega_0^2}{\omega_m^2} +
$$

$$
+ \frac{\overline{v_{nR}^2}}{\Delta f} \frac{\left(1 + \dfrac{gm_1 gm_2}{\omega_0^2 C_T C_{out}}\right)^2}{4gm_1^2 R_{out}^2 \left(1 + \dfrac{C_T C_G}{gm_1 gm_2} \cdot \dfrac{\omega_0^4}{\omega_{z2}^2}\right)^2} \cdot \frac{\omega_0^2}{\omega_m^2} \qquad (6.37)
$$

All the noise sources are characterised by the corresponding thermal noise PSD

$$
\frac{\overline{i_{d1}^2}}{\Delta f} = 4kT\gamma gm_1
$$

$$
\frac{\overline{i_{d2}^2}}{\Delta f} = 4kT\gamma gm_2
$$

$$
\frac{\overline{v_{nR}^2}}{\Delta f} = 4kTR_{out} \qquad (6.38)
$$

When common terms are found, (6.37) becomes

$$
\frac{\overline{v_{ndgFC}^2(\omega_m)}}{\Delta f} \approx \frac{kT\gamma \left[\dfrac{gm_2}{\omega_0^2 C_T^2} + \dfrac{1}{gm_1} + \dfrac{1}{gm_1^2 R_{out}\gamma}\left(1 + \dfrac{gm_1 gm_2}{\omega_0^2 C_T C_{out}}\right)^2\right]}{\left(1 + \dfrac{C_T C_G}{gm_1 gm_2} \cdot \dfrac{\omega_0^4}{\omega_{z2}^2}\right)^2} \cdot \frac{\omega_0^2}{\omega_m^2} \qquad (6.39)
$$

and phase noise can be calculated from this formula for a single sided phase noise PSD given by (3.30) i.e. $\mathcal{L}(\omega_m) = S_{out}(\omega_m)/V_{out}^2/2$. Note that (6.39) contains both phase and amplitude noise contributors. To estimate only the phase noise contribution, the equipartition theorem can be used (described previously in Section 6.2.1.1) which reduces the value calculated from (6.39) by the factor of 2.

170

6.4   Model verification and design insights

This section presents a comparison of the proposed noise model given by (6.39) to the simulation results of the practical circuit presented in Chapter 7. The model parameters presented in Table 6.2a have been extracted from the circuit schematics using Eldo RF DCOP (DC Operating Point) analysis. All the details on circuit design and simulations are thoroughly discussed in the next chapter.

The circuit has been simulated using UMC 180nm 1P6M process libraries under the large signal steady state conditions including the noise generated in all components. The results of the simulation include the signal amplitude and the corresponding phase noise at the resonant frequency. As the generated gyrator can be tuned via the bias current of the transconductance amplifiers, the aforementioned simulation has been conducted for three different operational points.

To calculate the phase noise using (6.39), the signal amplitude has to be known. At the design stage, the non-linear model of the degenerated active inductor resonator derived in Chapter 5 can be used. In this example, however the signal amplitude obtained from Eldo RF simulations is used to calculate this amplitude. The goal is to compare the proposed noise model to the complex non-linear phase noise calculation algorithm of the circuit simulator assuming that in both cases the signal amplitude is the same. Once the phase noise power is found using (6.39) it is compared to the square of the oscillation amplitude according to (3.30) discussed previously. The results are presented in Table 6.2b where the phase noise levels are calculated and simulated for a 1 MHz offset frequency from the corresponding carrier. Figure 6.6 depicts the phase noise plots obtained in Eldo RF for the circuit in Chapter 7, Section 7.7.4 and MATLAB for the proposed LTI model. It can be seen that in comparison to the much more complicated phase noise model from the circuit simulator, the proposed phase noise LTI achieves good accuracy. In the case of the lowest resonant frequency of 300 MHz the calculated phase noise level is underestimated by 7 dB. This is due to an increased harmonic distortion of the signal at this frequency that in turn increases phase noise

Table 6.2: Comparison of phase noise levels simulated in Eldo RF for the oscillator circuit from Chapter 7 and calculated using the proposed LTI model.

(a) Model parameters

Parameters						
R_{out}	C_{out}	C_g	C_o	C_i	C_t	A_{DC}
kΩ	pF					–
3.52	0.2*	0.2	0.25		4	34
*−fixed 150 fF and 50 fF of NMOS parasitics						

(b) Results showing phase noise at 1 MHz offset from oscillation frequency

I_B	gm_1	gm_2	f_0	Amplitude	Simulated PN	Calculated PN
µA	mA/V		MHz	mV	dBc/Hz	
300	5.5		226	80	-92.5	-99.3
900	12		430	106	-99.5	-101
1400	15.5		580	76	-98.4	-99
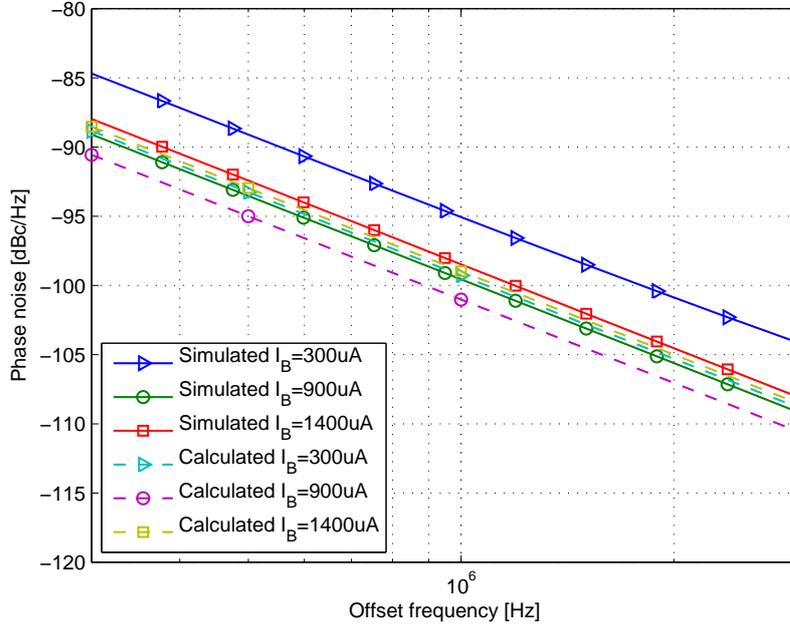
Figure 6.6: Graphical comparison of phase noise levels simulated in Eldo RF for the oscillator circuit from Chapter 7 and calculated using the proposed LTI model.

due to mixing effects in practical oscillators [121]. As the LTI model assumes a linear operation of the oscillator these effects are not captured, resulting in the lower phase noise level.

The accuracy improves for the bias current I_B of 900 μA because, as presented in Chapter 7 in Table 7.5, the harmonic distortion of the circuit is reduced approximately by half for this bias condition. In this case, the difference between the simulation results and LTI model calculations is 1.5 dB. The same behavior can be seen at the highest considered oscillation frequency of 580 MHz, where the difference between the proposed model and the simulation is only 0.6 dB. Although the proposed model tends to underestimate phase noise levels by a few dB, it is useful as it allows us to observe the influence of various circuit parameters on the phase noise of the degenerated oscillator before the actual circuit is designed at transistor level.

6.4.1 Design insights

Using the proposed phase noise model, some design recommendations can be formulated. The following tables present phase noise calculations for various parameter values of an example VCO for the sub-GHz frequency band. In all discussed cases, Barkhausen criteria are met, based on (4.39) and (4.40) from Chapter 4. An oscillation amplitude has been approximated also, assuming single transistor transconductors with finite losses and each biased with active load. Phase noise at 1 MHz is calculated for each resonant frequency of VCO.

In the first case, Table 6.3a, the chosen parameters represent a trade-off between the power consumption and chip area. Resulting phase noise averages around -103 dBc/Hz (calculated as dB value of arithmetic average of the phase noise levels in the linear scale). As suggested in this chapter and Chapter 4, the total noise of a degenerated active inductor resonator can be improved if the total tank capacitance C_T is increased. The same applies to noise at offset frequencies. Table 6.3b shows the situation where C_T was doubled (from 4.2 pF to 8.4 pF) in comparison with the previous case. On average, 5 dB phase noise improvement for each of considered resonant frequencies is

observed. The cost are both increased circuit size and power consumption. Finally, Table 6.3c represents an attempt to decrease a tank capacitance using larger phase shifter capacitor (C_{out} of 500 fF) and for constant power consumption. In this case phase noise deteriorates by 1 dB from the one of large C_T.

For all considered parameter values, calculated phase noise levels do not meet requirements for a high-performance wireless communication system like GSM 1800 for example. The reason for it is mostly a very limited oscillation amplitude caused by non-linear effects of CMOS transistors. In general, the performance of integrated degenerated active inductor VCOs do not exceed that of ring oscillators. As ring VCOs are switching circuits, voltage swing is practically limited to power supply at the cost of a high THD in the output signal. To achieve the phase noise levels comparable to a passive LC-oscillator, a degenerated gyrator has to use relatively very large capacitors or transconductors with high linearity. Assuming a target of -120 dBc/Hz at 1 MHz from carrier frequencies considered in this chapter, the tank capacitance C_t approaches 70 pF and its silicon area would match the one of spiral inductor. In addition, the transconductance values have to be increased to the range of 30-85 mA/V. In the available 180 nm process, typically NMOS transistors in strong inversion require power of at least 0.33-0.5 mW per 1 mA/V of transconductance. To set gm for a low phase noise operation, power consumption of 25-40 mW per single transistor is necessary, a value far beyond any practical implementation of an integrated oscillator. Similar conclusions have been drawn by Craninckx [47] who analysed the power consumption requirements for low phase noise of a standard active inductor oscillator. As the proposed circuit is a derivative of a gyrator, it shares the same performance limitations, proved by the thorough analysis of the phase noise model derived in this dissertation.

The second possible solution is a maximising output signal level. For the parameters considered here, an amplitude in the range of 500 mV allows improvement in phase noise to the required values without an excessive increase in power consumption or circuit size. However, this also implies large dynamic range of the gyrator, that can't be obtained in sub-micron architectures. For these reasons the presented large signal and phase noise

Table 6.3: Phase noise simulations using the proposed LTI model in function of circuit parameter.

(a) Phase noise for nominal parameter values

gm_1, gm_2	Resonant frequency	Signal amplitude	Phase noise at 1 MHz offset
mA/V	MHz	mV	dBc/Hz
5	363	50	-100
10	580	140	-108.4
15	756	90	-104
$C_T = 4.2 \ pF, \ C_{out} = 300 \ fF, \ R_{out} = 3 \ k\Omega$ $C_g = 200 \ fF, \ C_o = 100 \ fF, \ A_{DC} \approx 30, \ \gamma = 2.5$			

(b) Phase noise for doubled tank capacitance C_t

gm_1, gm_2	Resonant frequency	Signal amplitude	Phase noise at 1 MHz offset
mA/V	MHz	mV	dBc/Hz
7.2	369	75	-105.7
14	582	190	-113.2
20.8	750	150	-110.5
$\mathbf{C_T = 8.4 \ pF}, \ C_{out} = 300 \ fF, \ R_{out} = 3 \ k\Omega$ $C_g = 200 \ fF, \ C_o = 100 \ fF, \ A_{DC} \approx 30, \ \gamma = 2.5$			

(c) Phase noise for increased phase shifter capacitance C_{out}

gm_1, gm_2	Resonant frequency	Signal amplitude	Phase noise at 1 MHz offset
mA/V	MHz	mV	dBc/Hz
7.2	364	70	-105.6
14	569	170	-111.8
20.8	730	120	-107.7
$\mathbf{C_T = 5.2 \ pF}, \ \mathbf{C_{out} = 500 \ fF}, \ R_{out} = 3 \ k\Omega$ $C_g = 200 \ fF, \ C_o = 100 \ fF, \ A_{DC} \approx 30, \ \gamma = 2.5$			

analyses prove that a degenerated active inductor can't easily obtain low phase noise operation, at least in an available nanometer CMOS technology.

6.5 Chapter summary

This chapter presented the phase noise model of the degenerated gyrator oscillator. As the concept of a self-oscillating active inductor has not been researched in the existing literature, there is a need to analyse the proposed oscillator in terms of phase noise.

First, the most important phase noise analysis methods have been described, with special emphasis on the accuracy, complexity and practicality. It was shown that although not highly accurate, the linear time invariant approach can be used to deliver the analytical phase noise model of the oscillator. As the main goal of this chapter was to analyse how each of the circuit parameters contributes to the phase noise of the proposed oscillator, the LTI approach has been chosen over the more complex Hajimiri-Lee or harmonic balance methods, described in Sections 6.2.1.3 and 6.2.2.

The next part of the chapter focused on the methodology used to derive a LTI model. Based on previous work of Razavi [121] and Craninckx [47], the described methodology has been presented in a clear, step by step manner with rigorous proofs. It was shown that the noise analysis of fully compensated resonators requires a different approach than the calculation of noise in a lossy circuit from Chapters 3 and 4. For the first time, it was proved mathematically that, for the convenience of circuit analysis, phase noise can be approximated using admittance and impedance noise transfer functions interchangeably, as long as the offset frequency ω_m is much smaller than the carrier frequency ω_0.

Based on the described methodology, a new LTI phase noise model of the degenerated active inductor oscillator has been derived. First, all of the main noise sources of the gyrator circuit have been indicated, leading to the calculation of the corresponding noise transfer functions. Based on this, the total noise at a frequency offset from the carrier has been derived in a closed form given by (6.39).

Finally, the proposed phase noise model has been validated, using the simulation results of a practical circuit design presented in Chapter 7, Section 7.7.4. It was shown that accuracy of the derived LTI model, decreases with increasing harmonic distortion of the oscillator signal. This behavior is expected since linear models fail to capture non-linear effects in oscillators. The benefit however is a closed form phase noise equation, not available in circuit simulators, clearly showing the dependence of phase noise on various circuit parameters.

The proposed phase noise model has also been used to formulate some design recommendations for degenerated active inductor oscillators. It was shown that for a low phase noise operation, the circuit realised in CMOS requires excessive power consumption and for this reason it is not possible to obtain an oscillator meeting a stringent requirements of modern digital communications systems, such as GSM 1800 for example. This is however due to the nature of gyrator circuits in general since the proposed circuit follows the same trade-off between the power and phase noise as standard active inductor circuits.

This chapter concludes a theoretical discussions presented also in Chapters 4 and 5. The next chapter of this dissertation leads to the practical design of the oscillator following the similar methodology: first the circuit is designed using the small signal model, then simulated under large signal conditions and noise of all components.

Chapter 7

Degenerated active inductor oscillator design

7.1 Introduction

This chapter presents a complete design procedure for experimental CMOS circuits based on the proposed degenerated gyrator concept. The first circuit, a 434 MHz wideband oscillator is designed and simulated in Mentor Graphics IC Studio software suite using UMC 1P6M 180 nm process libraries. The second circuit, a 434 MHz OOK transmitter, is designed using UMC 1P9M 90 nm RF process that became recently available. The choice of 434 MHz bandwidth is not coincidental. This unlicensed band is intended for the use of a low power ISM (industrial, scientific and medical) systems and therefore one does not require any government permit to utilise this frequency spectrum. As indicated in Chapter 2, the use of the modern CMOS nanoscale processes to realise integrated VCO operating at sub-GHz frequencies can be challenging due to the following:

- Capacitors and inductors are optimised for much higher frequencies at the cost of the performance reduction at frequencies less than 1 GHz. For example, in the described 180 nm process, inductors reach their maximum Q of 11 at 5 GHz,

whereas at 500 MHz the quality factor drops by 80%. This in turn translates to more static power necessary to compensate the resonant tank.

- As the oscillation frequency is small, the required values of LC components are relatively high. The largest inductor available in the presented 180 nm process has the inductance of 14 nH and occupies the area of 250 µm by 250 µm. To design the oscillator operating under 500 MHz, the required tank capacitance value is larger than 7 pF, which corresponds to the physical size of 85 µm by 85 µm. As a result, the integrated LC tank requires nearly 70000 µm^2 of the silicon area.

Thus it is beneficial to explore the possibilities of a sinusoidal oscillator integration using the self-oscillating gyrator circuit presented in this thesis.

The chapter describes in detail all of the necessary design steps, including:

- DC and small signal analysis. Here, the problems of the circuit bias in the presence of a relatively low supply voltage are addressed. Various active inductor configurations are discussed focusing primarily on the ease of implementation and the practical use in the proposed oscillator circuit. The small signal analysis is then used to fine tune the parameter values calculated previously in Chapter 4 from the proposed theoretical model of the degenerated gyrator.

- Large signal behavior of the proposed circuit is simulated in both the frequency and time domain. This part confirms the proposed Volterra kernel model from Chapter 5, Section 5.5 and LTI phase noise model from Chapter 6, Section 6.3. Both signal amplitude and phase noise levels are discussed based on a steady state analysis of autonomous circuits available in Eldo RF circuit simulator.

- The designed circuit presented in this chapter consists of an oscillator core and an output buffer amplifier required to drive a load. This allows the analysis of the power of RF signal generated in the circuit and the harmonic distortion experienced by the load.

- The performance of the oscillator due to temperature and process variation is presented and thoroughly discussed. In each case, the circuit is simulated in terms of frequency range, phase noise and output signal power. Although this type of analysis is commonly omitted in the literature on active inductor circuits, it is presented here to complete the thorough discussion on strengths and weaknesses of the proposed oscillator circuit.

The described methodology presented in this chapter represents a standard way for negative resistance oscillator design and therefore can be applied to any, not only active inductor, VCO circuit. For this reason, one can use this chapter as an oscillator design guide which increases an overall value of this doctoral dissertation.

The active inductor circuit used to confirm the proposed theory of passive RC compensation is a modified version of the circuit presented by Hsiao et al. [99]. In the paper the authors employed a single resistor to improve the quality factor of the inductor, relying only on highly-nonlinear transistor capacitances. No noise and large signal design insights were given. In following years, Wu et al. [122] and Mukhopadhyay et al. [80, 123] designed a standard CMOS VCO based on Hsiao circuit. Although this time the authors attempted to analyse circuit noise, the large signal properties were not disclosed. The performance of both VCOs are compared with the degenerated gyrator oscillator presented in this chapter.

7.2   Gyrator architecture

As shown previously in Chapter 3, Section 3.2.1, for proper operation, any gyrator requires one non-inverting and one inverting transconductor. Therefore, using NMOS and PMOS transistors, there are eight possible architectures of two transistor gyrators available, depicted on Figure 7.1. In all cases the inverting transconductor is a CS amplifier, whereas the non-inverting stage is either a CD or CG amplifier. To choose the proper configuration for the oscillator design, the following criteria have to be considered:

- Voltages for given CMOS process: Due to miniaturisation, all maximum transistor voltages are scaled down as well, however the magnitude of these changes is different for every process. For example, for a long channel 1 µm process, typical values of drain and threshold voltages were 5 V and 800 mV respectively [27]. The same voltages in 180 nm are equal to 1.8 V and 500 mV. As a result, the available headroom to keep transistors in the saturation region is reduced. A smaller headroom also limits the number of devices that can be stacked together which becomes especially important if the circuit operates in a large signal regime.

- Bias configuration: Since transconductors are connected in a feedback loop, depending on configuration used, each stage can provide DC bias for other amplifiers at the same time. Proper choice of the quiescent point not only allows to control a transconductance value but also ensures sufficient headroom for a large signal swing. If each stage has to be powered separately through dedicated bias networks and DC blocking capacitors, the circuit size inevitably increases.

Due to the low voltage power supply in our chosen submicron processes, the CS-CG circuits from Figures 7.1e and 7.1f can suffer from a reduced voltage headroom. Although oscillators using these circuits were reported previously, they used either a large supply voltage [53] or excessive power consumption [82] to achieve lower phase noise at the cost of a severely distorted output signal. In addition, stacked devices reduce available transconductance values due to reduced drain to source voltage on each of devices. The main advantage of the circuits from Figures 7.1e and 7.1f is current reuse. This allows the use of a single source to bias both transconductors.

Not all of the presented circuits are suitable for the mutual bias scheme. For example, the gyrator from Figure 7.1c requires the following bias conditions

$$V_{GS2} = V_{SD1} \tag{7.1}$$

$$V_{SG1} = V_{GS2} - V_{DS2} > 0 \tag{7.2}$$

(a) N-N, CS-CD

(b) P-P, CS-CD

(c) N-P, CS-CD

(d) P-N, CS-CD

(e) N-N, CS-CG

(f) P-P, CS-CG

(g) N-P, CS-CG

(h) P-N, CS-CG
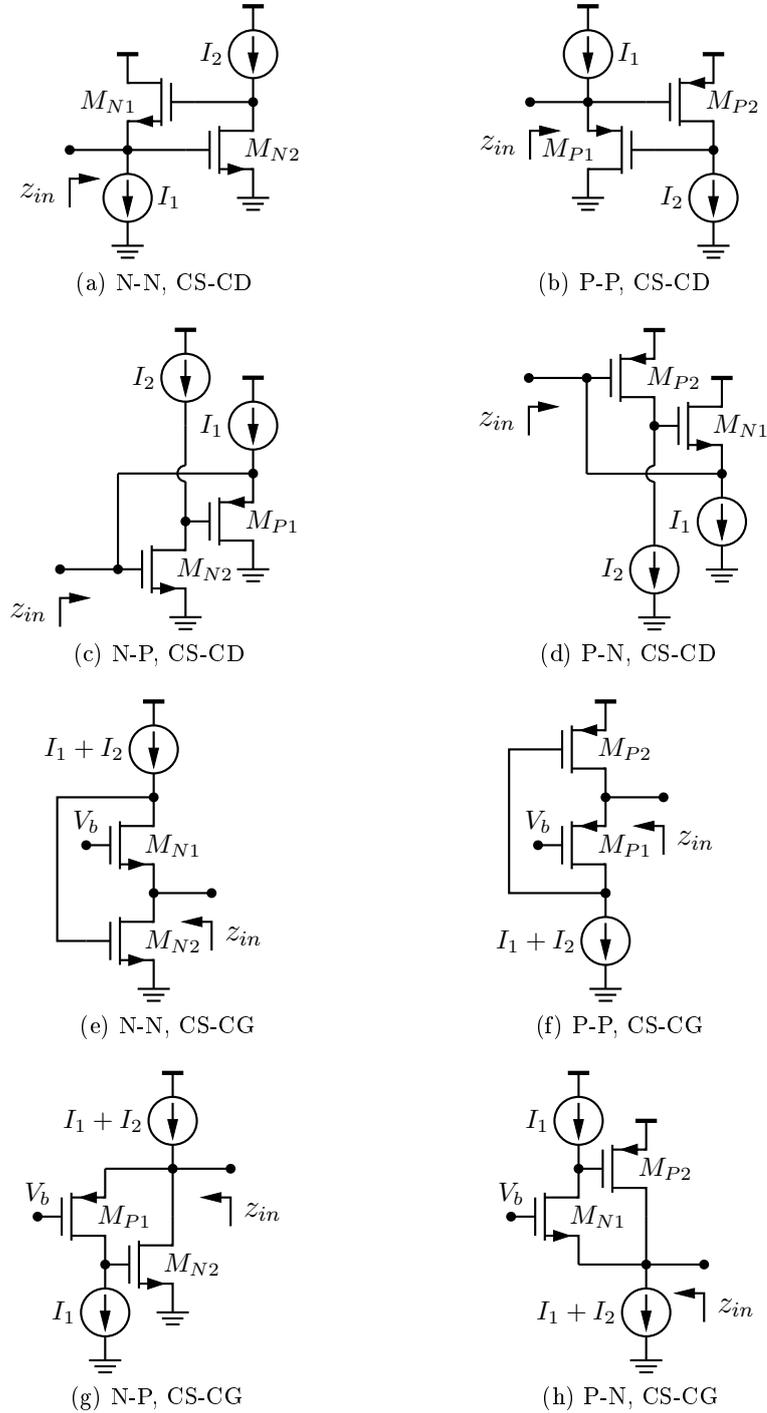
Figure 7.1: Possible configurations of two transistor CMOS gyrators.

As a result transistor M_2 is biased close to the boundary between linear and saturation regimes that may then result in small oscillation amplitudes and increased harmonic distortion. The same rules apply to the circuit from Figure 7.1d. The same analysis can be applied to CS-CG circuits from Figures 7.1e and 7.1f. It can be seen that for these NMOS-only or PMOS-only configurations, the common source amplifier has to be biased with gate voltage of $V_{GS} = V_{DS1} + V_{DS2}$ which can shift transistor M_1 close to the triode region boundary.

Among the presented circuits, the NMOS and PMOS configurations from Figures 7.1a and 7.1b are convenient for mutual bias together with an adequate headroom for oscillation purposes. For the reminder of the discussion, the circuit from Figure 7.1a will be described as a *NMOS gyrator* whilst the term *PMOS gyrator* will apply to the circuit from Figure 7.1b. The choice between transistor type depends on two factors: parasitics and noise. For the same transconductance, overdrive voltage and drain current, the width of a PMOS transistor is typically at least two times larger than that of an NMOS counterpart. This in turn increases C_{gs} and C_{gd} and affects both the maximum frequency of operation and the negative resistance generation mechanism when used in a degenerated gyrator circuit. If the dimensions of the N and P devices are the same, PMOS amplifiers produce smaller gm, leading to increased inductance value for the active inductor. To keep the resonant frequency constant, the tank capacitance has to be made smaller than in the case of an NMOS gyrator. Thus, although PMOS transistors produce smaller thermal noise than NMOS devices (due to reduced gm), this does not automatically translate to a lower phase noise of degenerated gyrator oscillator.

7.3   Gyrator bias

To provide a sufficient voltage headroom for both amplifiers using the mutual bias described previously, the bias voltages of an NMOS gyrator are chosen as shown on Figure 7.2. This scheme supplies equal voltages to both transconductors. Note that the voltages on the current sink and source are also equal. The proposed biasing ar-

rangement can be fine-tuned to compensate for the body effect of the non-inverting transconductor. As the bulk of the NMOS transistor of a CD amplifier has a different potential than the source node, the threshold voltage of the device is larger than of the second transistor. As a result, for the same gate voltage the non-inverting amplifier conducts less current than the common source transconductor. To compensate, either a wider CD device can be used keeping a bias constant or a larger overdrive has to be supplied at the cost of a reduced voltage headroom on one of the current sources. Typically a change of gate potential up or down within 15% of an original voltage division ratio from Figure 7.2 is sufficient for the described bias fine-tuning. The actual bias voltages are presented later in this chapter.
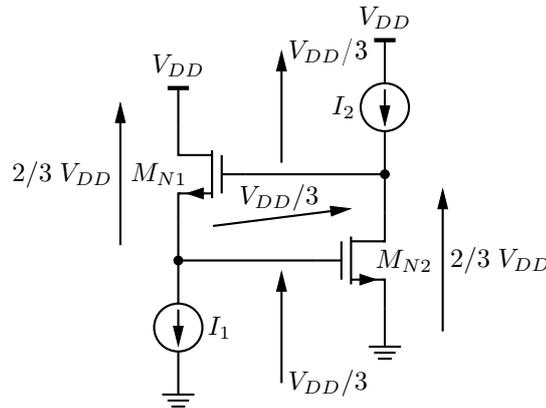
Figure 7.2: Bias scheme of CS-CD active inductor

7.4 DC analysis

The design methodology for the degenerated active inductor oscillator starts from an analysis of a standard gyrator first i.e. without the RC phase shifter. This is possible if one assumes that the RC circuit does not affect DC bias conditions of the complete circuit. The dimensions of transistors are determined by transconductance values required for the simulated inductance values in the range of a few tens of nH. As described previously in Chapters 4 and 6, the choice of gm values is also governed by the trade-off between circuit parasitics, power consumption and noise: a small gm allows the use of

smaller transistors and less power, however it increases the noise of the resonator. On the contrary, a large gm imposes proportionally larger transistors and power consumption but can improve the noise of the tank. For the sub-GHz frequency band considered in this chapter, a maximum gm value in the range of 15 mA/V was chosen as a practical trade-off between power, circuit size and noise.

For the 180 nm process used in the thesis, the threshold voltage V_{th} of NMOS devices without the body effect is approximately 470 mV and a maximum drain to source voltage V_{DSmax} is 1.8 V. Assuming the voltage division from Figure 7.2, both transconductors are biased such that their gate to source voltage V_{GS} is 600 mV and the drain to source voltage V_{DS} is 1.2 V. Thus, it is possible to set the overdrive voltage in the range of 130 mV for each NMOS device and still provide sufficient headroom for both bias current sources. Although the standard formulas for long channel transistors do not describe well the behavior of sub-micron devices, they can be still used as a first order calculation. The obtained values can then be further optimised in a circuit simulator for a given performance.

7.4.1   Transconductors

The drain current of the CS amplifier, necessary to provide conductance of 15 mA/V for the overdrive voltage of 130 mV is found from

$$I_D = \frac{gm \cdot V_{OV-CS}}{2} = \frac{15 \; mA/V \cdot 130 \; mV}{2} = 975 \; \mu A \qquad (7.3)$$

The *process transconductance parameter*, $k' = \mu_o C_{ox}$ [97] for NMOS device in the described process is approximately equal to 300 µA/V^2. As discussed previously in Section 4.5.2, to increase the DC gain of the transconductor the drawn length of the device L is increased to 250 nm from the minimum of 180 nm given by the technology. The value of 250 nm allows us to obtain a DC gain in the range of 30 while keeping a relatively small area of NMOS devices. For the drain current calculated from (7.3), the

estimated transistor width W is equal to

$$I_D = \frac{k'}{2}\frac{W}{L}V_{OV-CS}^2 \Longrightarrow W = L\frac{2I_D}{k'V_{OV-CS}^2} \approx 96\ \mu m \qquad (7.4)$$

To improve gate resistance and to use silicon area more effectively through drain-source sharing, the high aspect ratio transistor is split into a number of smaller devices with multiple gate fingers [26, 124]. In this case, the width of 96 µm has been divided into 4 parallel transistors with 6 fingers of 4 µm gate width each. Using the DCOP (DC Operating Point) simulation in Eldo RF, the results presented in Table 7.1a were obtained. It can be seen that though the required drain current is 30% larger than initially assumed, the transistor delivers the chosen gm value.

The size of the common drain (CD) device can be found through a DCOP simulation using (7.4) to estimate a proper size of the transistor. Due to the body effect described previously, the gate potential of the transistor has to be larger than in the case of CS transconductor to keep V_{OV-CD} constant. As depicted on Figure 7.2, $V_{GS-CD} = V_{DS-CS} - V_{GS-CS}$ and hence drain to source voltage of CS amplifier has to increase by approximately 100 mV to provide proper gate potential. Simulated results are presented in Table 7.1.

Figure 7.3 presents the circuit schematics used for a DCOP analysis whereas the test bench circuit is depicted on Figure 7.4.

Table 7.1: Simulated small signal parameters of amplifiers.

(a) Inverting transconductor.

Parameter	Value	Unit
V_{GS-CS}	600	mV
V_{DS-CS}	1.2	V
V_{th-CS}	485.3	mV
V_{OV-CS}	114.7	mV
I_{D-CS}	1.3	mA
gm_{CS}	15.2	mA/V

(b) Non-inverting transconductor.

Parameter	Value	Unit
V_{GS-CD}	700	mV
V_{DS-CD}	1.2	V
V_{th-CD}	581.5	mV
V_{OV-CD}	118.5	mV
I_{D-CD}	1.36	mA
gm_{CD}	15.49	mA/V

Figure 7.3: Gyrator circuit configured to DC simulation.
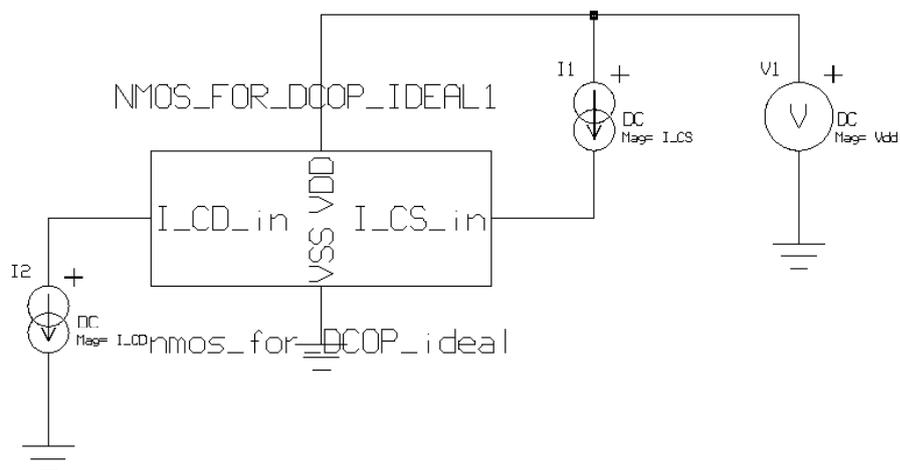
Figure 7.4: DC test bench circuit using ideal current sources.

7.4.2 Current source and sink

In practical gyrators, ideal current sources are approximated by the use of current mirrors. Within specified voltage range, the current mirror is able to keep the DC current (supplied to the transconductors) constant for the varying voltage on its output. Hence, the current mirror mimics the operation of an ideal current source.

Initially the dimensions of each of the transistors used as a current source or sink can be made equal to one of the corresponding transconductors. However, as shown on Figure 7.2 the available V_{DS} for these transistor is smaller than the drain to source voltage reserved for the amplifiers. Thus the total width of these devices require further corrections. In general, the performance of the bias circuit is a trade-off between noise, parasitics and the available voltage range. Wider transistors better suit reduced voltage headroom because, for a given current, they require a smaller overdrive. As a result they are biased further away from a triode region. Flicker noise is also smaller due to its inverse proportionality to $W \cdot L$ product [26, 44]. On the other hand, narrow transistors require larger overdrive and hence have smaller gm, generating less thermal noise current.

In the circuit of Figure 7.2, the CS amplifier is biased through the PMOS current source with available source to drain voltage V_{SD-P} of 520 mV and a drain current of 1.3 mA. In the case of the CD amplifier a NMOS sink is used. A drain to source voltage V_{DS-N} of 600 mV and a current of 1.36 mA are required. The width of the NMOS sink could be reduced by half in comparison with the transconductor due to a sufficient voltage headroom from a minimum saturation voltage, V_{SAT-N}. The results of the DCOP analysis are presented in Table 7.2 and the complete gyrator circuit is depicted in Figure 7.5

7.4.3 Transconductance tuning

The transconductance of both amplifiers is controlled by feeding a reference current I_B to both mirrors. In the presented configurations, the mirrors are referenced to

Table 7.2: Parameters of PMOS source and NMOS sink.

PMOS			NMOS		
Parameter	Value	Unit	Parameter	Value	Unit
V_{SG-P}	830	mV	V_{GS-N}	695	mV
V_{SD-P}	520	mV	V_{DS-N}	598	mV
V_{SAT-P}	309.7	mV	V_{SAT-N}	195.2	mV
V_{th-P}	536.8	mV	V_{th-N}	500	mV
V_{OV-P}	293.2	mV	V_{OV-N}	195	mV
I_{D-P}	1.3	mA	I_{D-N}	1.36	mA
gm_P	7.2	mA/V	gm_N	10.72	mA/V
W_P	96	µm	W_N	48	µm

different supply potentials (the NMOS sink to the ground and the PMOS source to VDD). In practice I_B is delivered from a circuit able to sink and source the reference current concurrently as a band gap circuit. Assuming that I_B can be supplied to both amplifiers, the transconductance is controlled simultaneously, as shown on Figure 7.6. It can be seen that the gm of the CD and CS transconductors can be tuned with mismatch less than 3%. The shape of the curve follows a typical pattern for sub-micron devices, deviating from the quadratic behavior of long channel transistors. For VDD=1.8 V, the static power required to deliver transconductance of 15 mA/V is in the range of 3 mW. For the currents smaller than 250 µA, the amplifiers move to a subtreshold regime that is not suitable for large signal operation of the considered circuit.

This simulation concludes the DC analysis of the gyrator circuit. As indicated previously, from a bias perspective there is no difference between the standard and degenerated gyrator as the RC phase shifter does not affect DC operation of the circuit.

7.5 Small signal AC analysis

Before the RC shifter will be connected, the standard gyrator is analysed for AC signal to ensure that the circuit operates below its self resonant frequency. As the self resonance depends on parasitic capacitances it is hard to control due to process variations. After this, a complete degenerated active inductor resonator is designed and simulated in
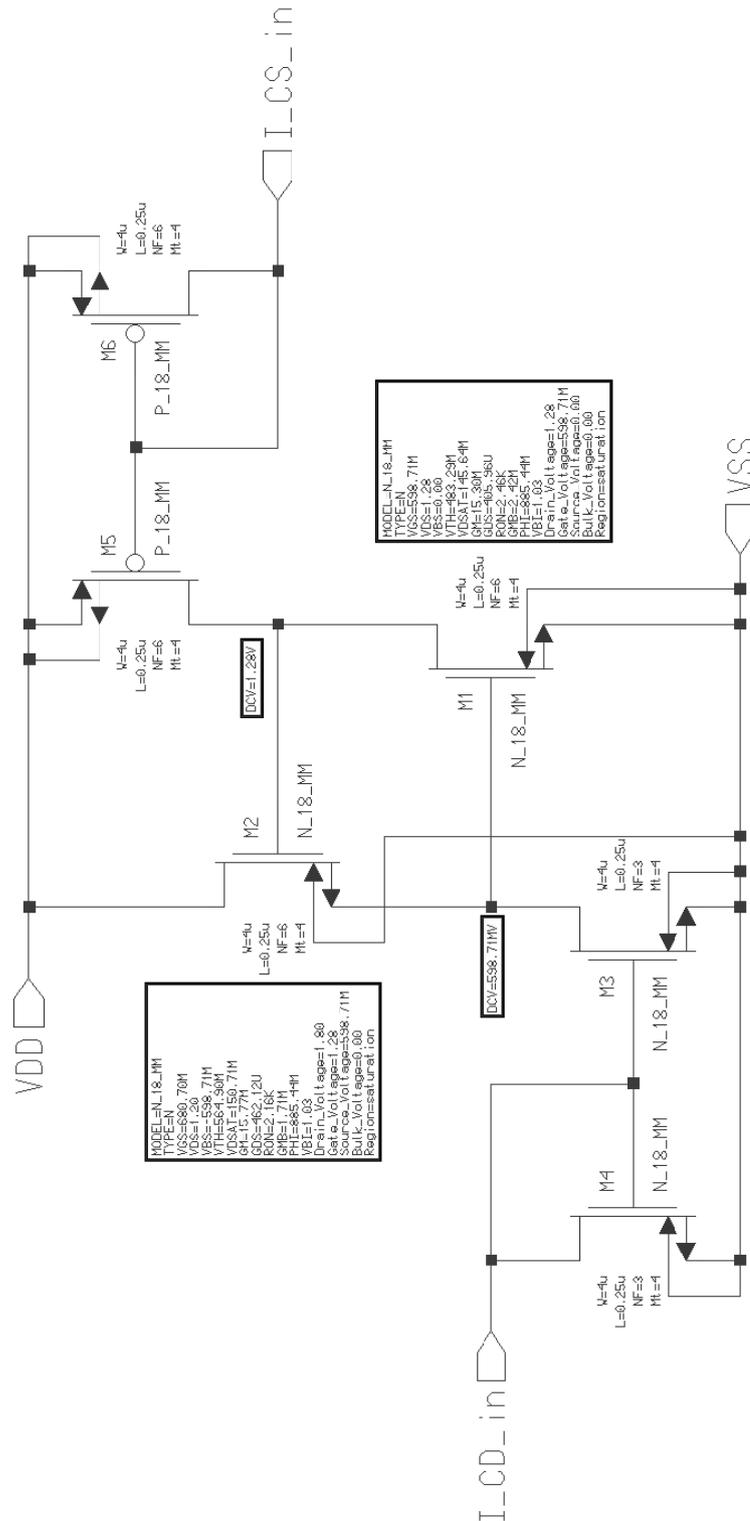
Figure 7.5: Complete gyrator circuit configured for DC simulation.

order to verify the Barkhausen criteria for oscillation. All of the results have been obtained in Eldo RF using an AC small signal simulator.

7.5.1 Gyrator without RC phase shifter

The circuit is analysed for three I_B values: 300 µA, 750 µA and 1500 µA, respectively. This allows us to observe the behavior of the circuit for different gm values. Figure 7.7 presents the active inductor circuit where the gate of the non-inverting transconductor has been disconnected from the output of CS amplifier. If a short circuit is connected between CD_G to gyr_out nodes, the gyrator operates as a standard active inductor. In the case of the degenerated gyrator, the short circuit is substituted by an RC shifter.

The small signal simulation has been set as follows. An AC test signal generator has been connected to the inverting amplifier input. A frequency sweep has been set from 100 MHz to 1000 MHz. The result of this simulation allows the analysis of the input admittance (or impedance), assuming linear behavior around the DC quiescent
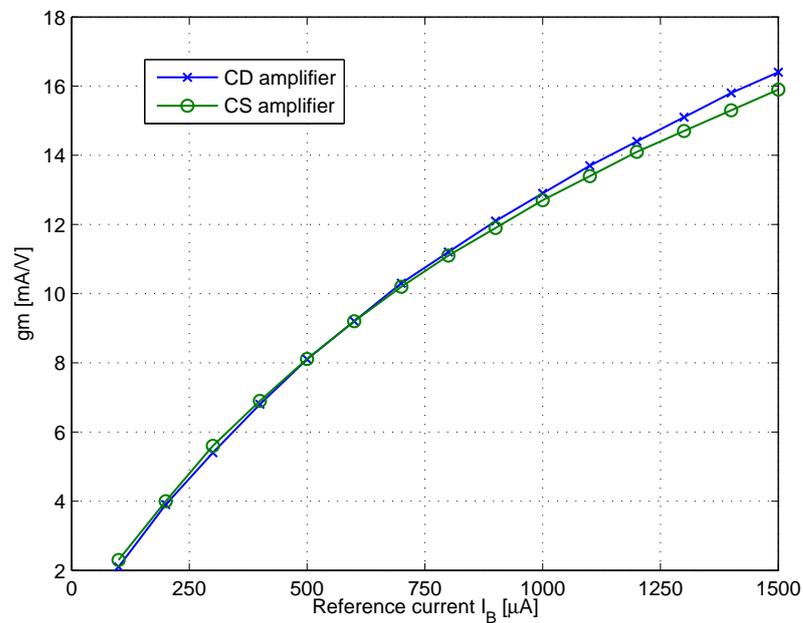
Figure 7.6: Transconductance of gyrator amplifiers as functions of reference current I_B.

point found in the previous design step. The circuit simulator calculates the real and imaginary parts of a complex immitance of the tested circuit separately. Figure 7.8 depicts the test bench circuit of a gyrator from Figure 7.7. Capacitor C_g represents the gyrated capacitance connected to the output of the active inductor. R_{out} and C_{out} allow control of the negative resistance generation mechanism.

First, the circuit has been simulated for R_{out} of 0 Ω, C_{out} of 0.15 pF and C_g of 0.2 pF. In this case a standard gyrator is obtained with the total load capacitance provided by MOS parasitics, C_g and C_{out}. If the capacitors are too small, then the circuit parasitics dominate which in turn increases circuit sensitivity for process variations. When C_g and C_{out} are large, the simulated inductance increases, typically also decreasing the self resonant frequency of the circuit. The analysis presented in Chapter 4, Section 4.5, shows that for operation in sub-GHz frequencies both capacitors are in the range from 0.2 pF to 0.5 pF. More details about a choice of C_{out} values are discussed later in this section.

Figure 7.9 illustrates real and imaginary parts of input admittance, together with the calculated inductance as a function of signal frequency. To explain the behavior of the circuit, one has to consider different frequency ranges. At low frequencies, the circuit losses increase dramatically due to a relatively small simulated inductance that in turn causes low unloaded Q. This is most severe for high transconductances because inductance is inversely proportional to the square root of gm. This issue can be improved using a larger gyration capacitance that shifts the peak of resistive losses into lower frequencies at the cost of reduced tuning range at high frequencies. At high frequencies the input conductance reaches its limit of $1/gm$ due to the architecture of the gyrator, as discussed in Chapter 4.

7.5.2 Complete degenerated gyrator circuit

In this section the RC phase shifter is connected to the circuit. As a result, the degenerated gyrator is obtained and a negative resistance is generated. To fully analyse the circuit behavior the input conductance and susceptance are simulated separately
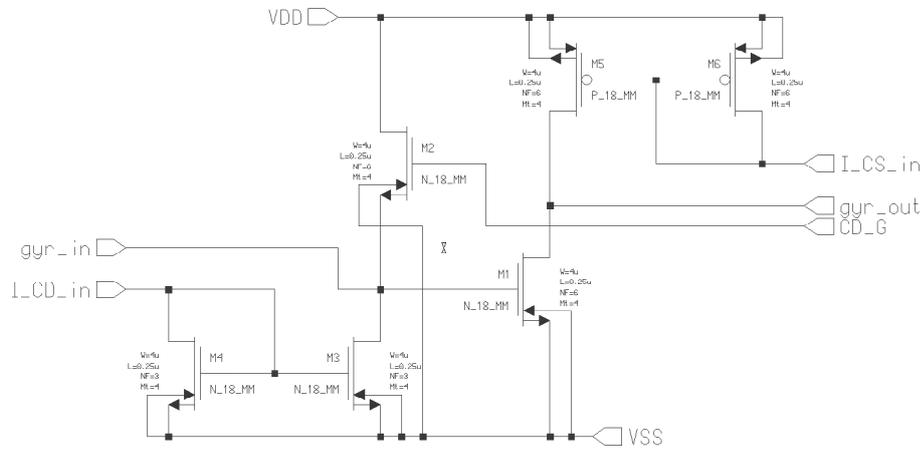
Figure 7.7: Gyrator circuit for AC simulation.
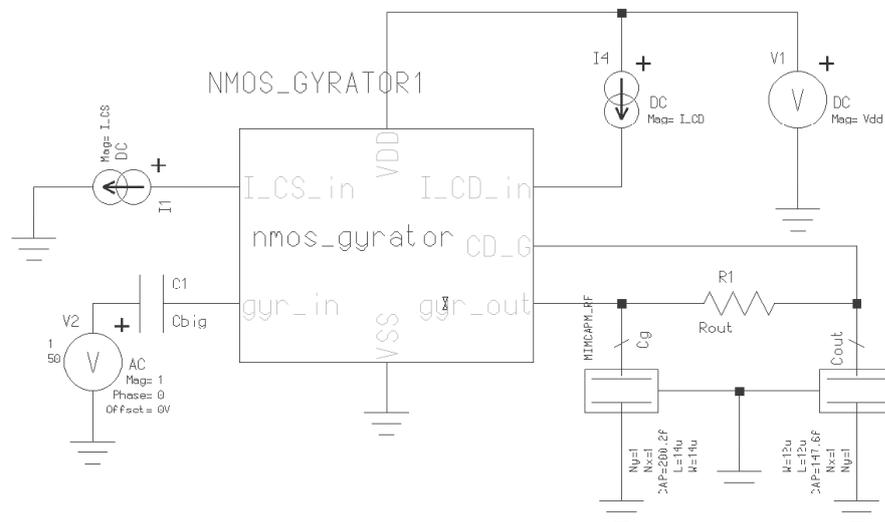
Figure 7.8: Test bench circuit.
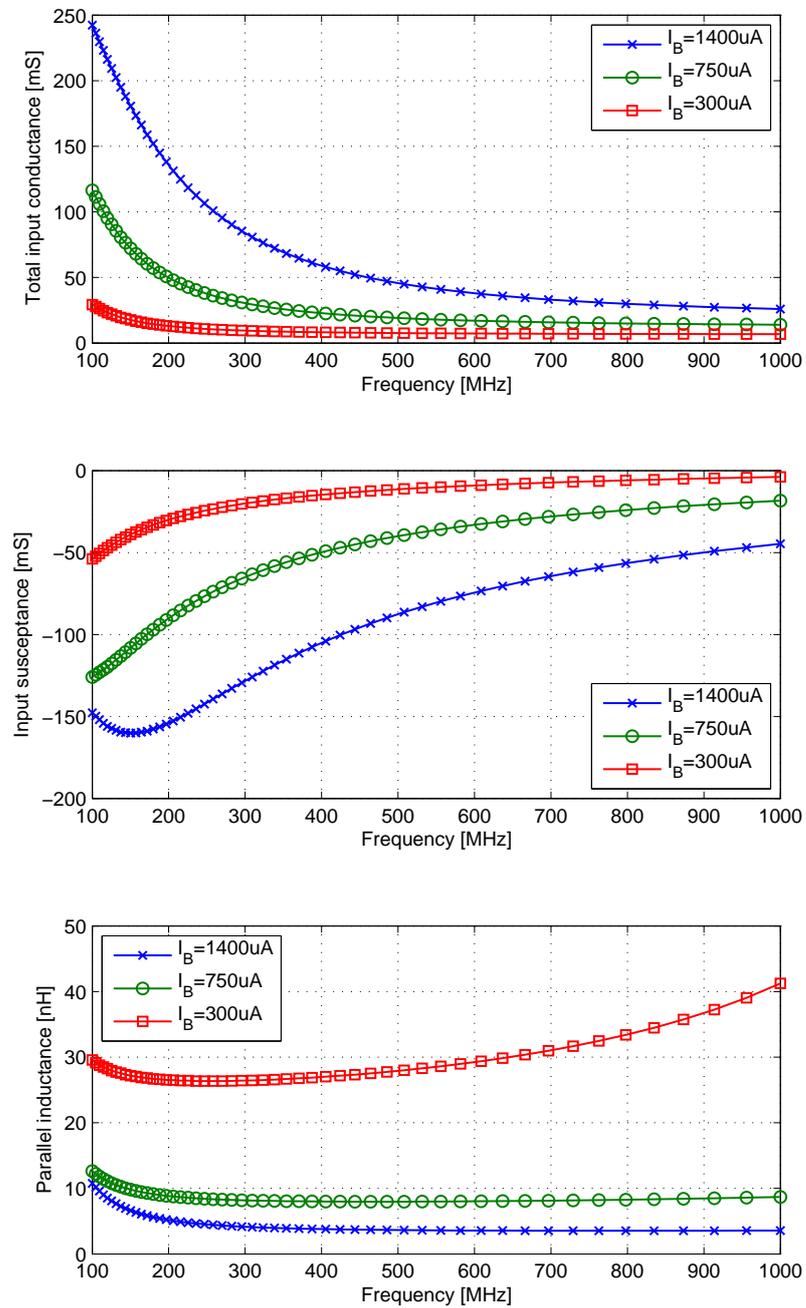
Figure 7.9: Simulated input admittance of active inductor without RC phase shifter.

for different values of the RC phase shifter components. Finally, the tank capacitance necessary for oscillations is found using a new and relatively simple graphical method, described in detail later in this section.

7.5.2.1   Input conductance

First, the real part of the input admittance as a function of frequency and the shifter resistance R_{out} is analysed. As previously, three bias current values are considered. Figure 7.10 presents the evolution of negative conductance over an increasing resistance of the phase shifter. For R_{out} of 1 kΩ, negative conductance is generated only for two of the considered bias currents. Also, circuit losses are cancelled only for the frequencies over 500 MHz. When R_{out} increases, the phase shift between the output voltage of the CS amplifier and input voltage of CD stage increases. As a result, more negative conductance is produced.

The frequency bandwidth over which a negative conductance is generated is inversely proportional to R_{out}. This behavior can be explained by (4.42), the equation defining the described frequency range in terms of ω_{RnegL} and ω_{RnegH}, the frequencies defining the low and the high limits of the described frequency range. The ratio of the two frequencies has the form of

$$\frac{\omega_{RnegH}}{\omega_{RnegL}} = \frac{f(R_{out}) + g(R_{out})}{f(R_{out}) - g(R_{out})} \tag{7.5}$$

and closer analysis reveals that when all the other parameters are constant, $f(R_{out})$, $g(R_{out})$ are inversely proportional to the resistance of R_{out}. As a result both ω_{RnegL} and ω_{RnegH} decrease as well as their ratio, reducing the bandwidth of the negative conductance.

For the parameter values chosen for the design presented in this thesis, a value of R_{out} in the range of 3.5 kΩ represents the best trade-off between the bandwidth and amount of negative conductance required for compensation of the resonator.

The input conductance is also controlled by C_{out}. For the chosen R_{out}, the circuit has been simulated for three capacitance values: 0.15 pF, 0.26 pF and 0.4 pF as depicted

on Figure 7.11. Increasing the value of C_{out} shifts the negative conductance bandwidth into lower frequencies, reducing its width. The magnitude of the negative conductance also becomes smaller.
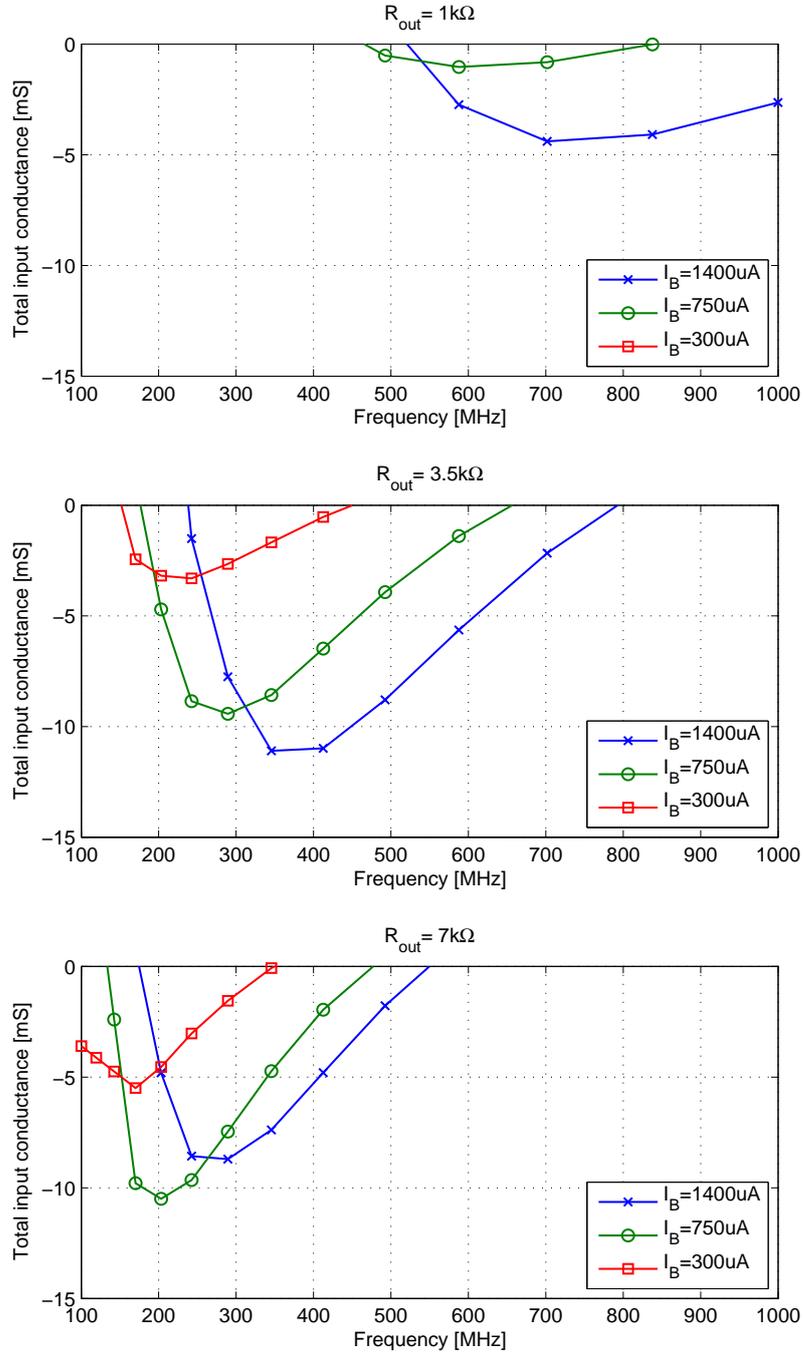
Figure 7.10: Total input conductance as a function of frequency and R_{out} for three different bias currents.
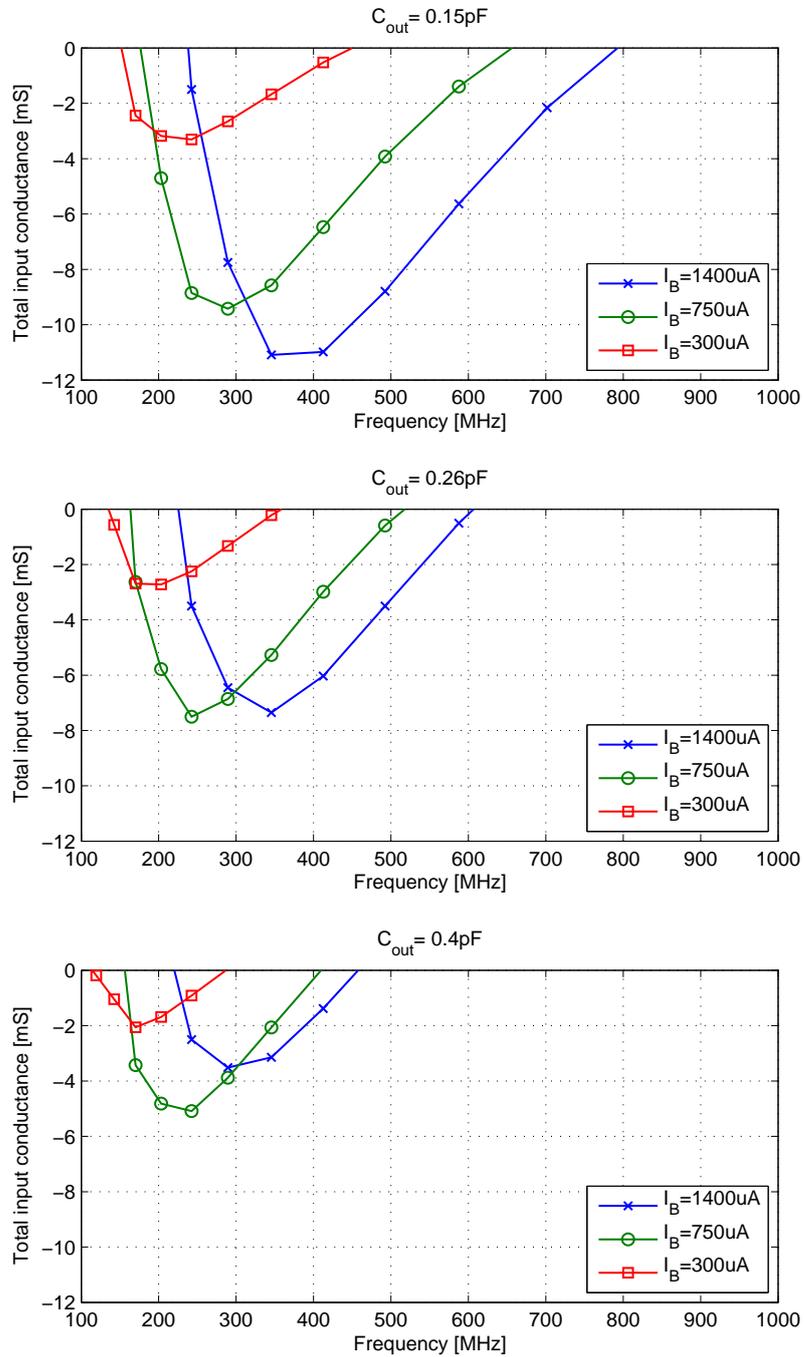
Figure 7.11: Total input conductance as a function of C_{out}.

7.5.2.2 Susceptance

As indicated previously, the AC analysis allows us to analyse the circuit susceptance separately from the conductance. As a result it is possible to observe how the inductive impedance changes with frequency and the circuit parameters. Figure 7.12 illustrates a simulated susceptance as a function of frequency. It can be seen that the circuit generates an inductive susceptance within the considered frequency band. As in the case of the standard gyrator described previously, the susceptance is proportional to I_B and therefore gm of the transconductors. Thus, the proposed degeneration technique allows us to retain a tunable inductive admittance whilst introducing negative resistance, as predicted in Chapter 4. The increase of R_{out} causes a decrease of the susceptance and the simulated inductance becomes larger than that of a standard gyrator, reducing the resonance frequency of the circuit. In this case, R_{out} of 3.5 kΩ prevents excessive inductance values (Figure 7.14), especially for small gm values. This in turn, allows the use of tank capacitances in the range of pF at sub-GHz frequencies and therefore improve the noise produced by the resonator (Chapter 4). The influence of C_{out} on the circuit susceptance has been also analysed, as depicted on Figure 7.13. The observed behavior is the same as in the case of a changing R_{out}, shifting the self-resonance frequency of the circuit down for an increasing value of the phase shifter capacitance. In the presented design, a value of 0.15 pF has been chosen to avoid excessive inductance at the frequencies of interest for all the bias currents used.

7.5.2.3 AC behavior verification

The input conductance plots depicted in Figures 7.10 and 7.11 are compared to Figure 4.13. In the case of R_{out} equal to 3.5 kΩ and C_{out} of 150 fF, the shape of the curves and the magnitude of the negative conductance produced by the practical circuit correspond to these obtained from the mathematical model from Chapter 4. In the actual circuit, the frequency range where the resonator is fully compensated is reduced by about 20% due to the parasitic capacitances of the transistors and current mirrors.
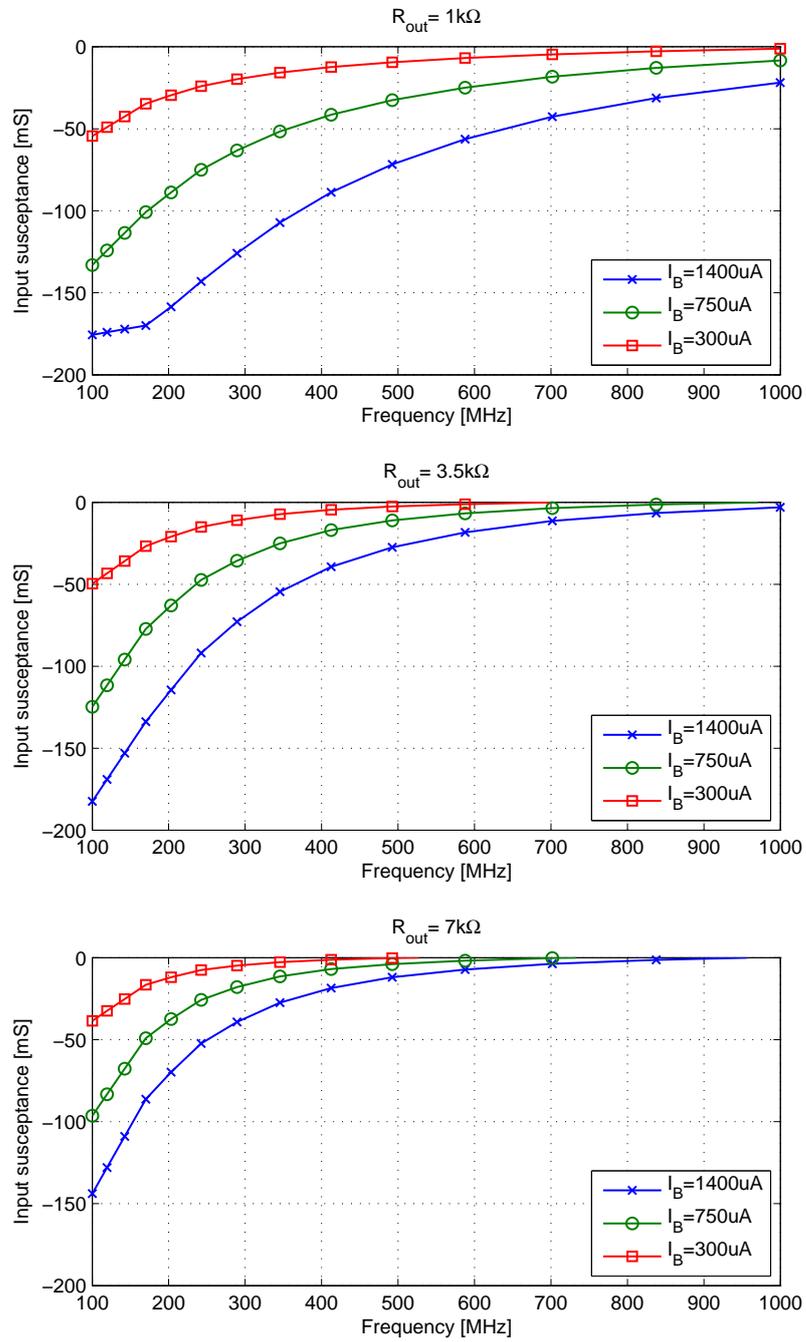
Figure 7.12: Input susceptance of the circuit for three different bias currents and R_{out} values .
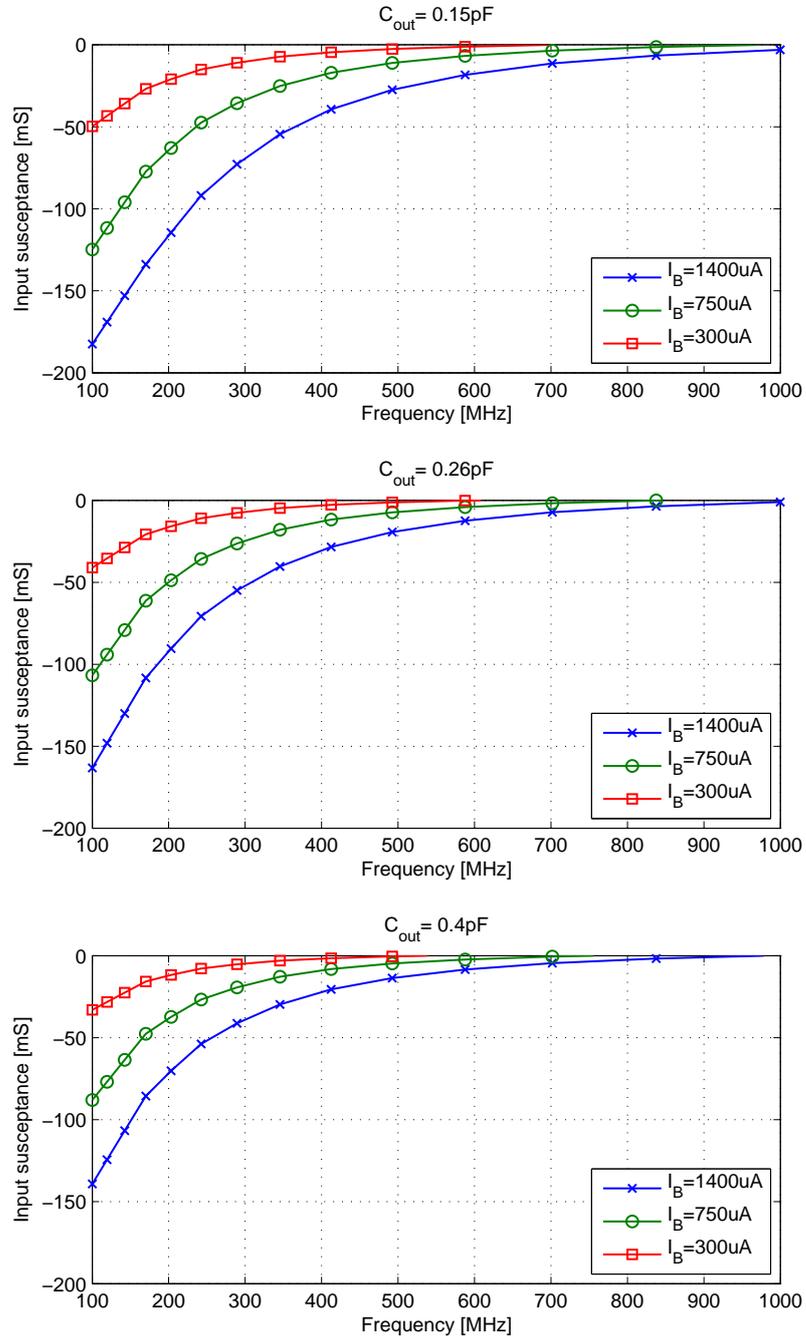
Figure 7.13: Input susceptance as a function of C_{out}.
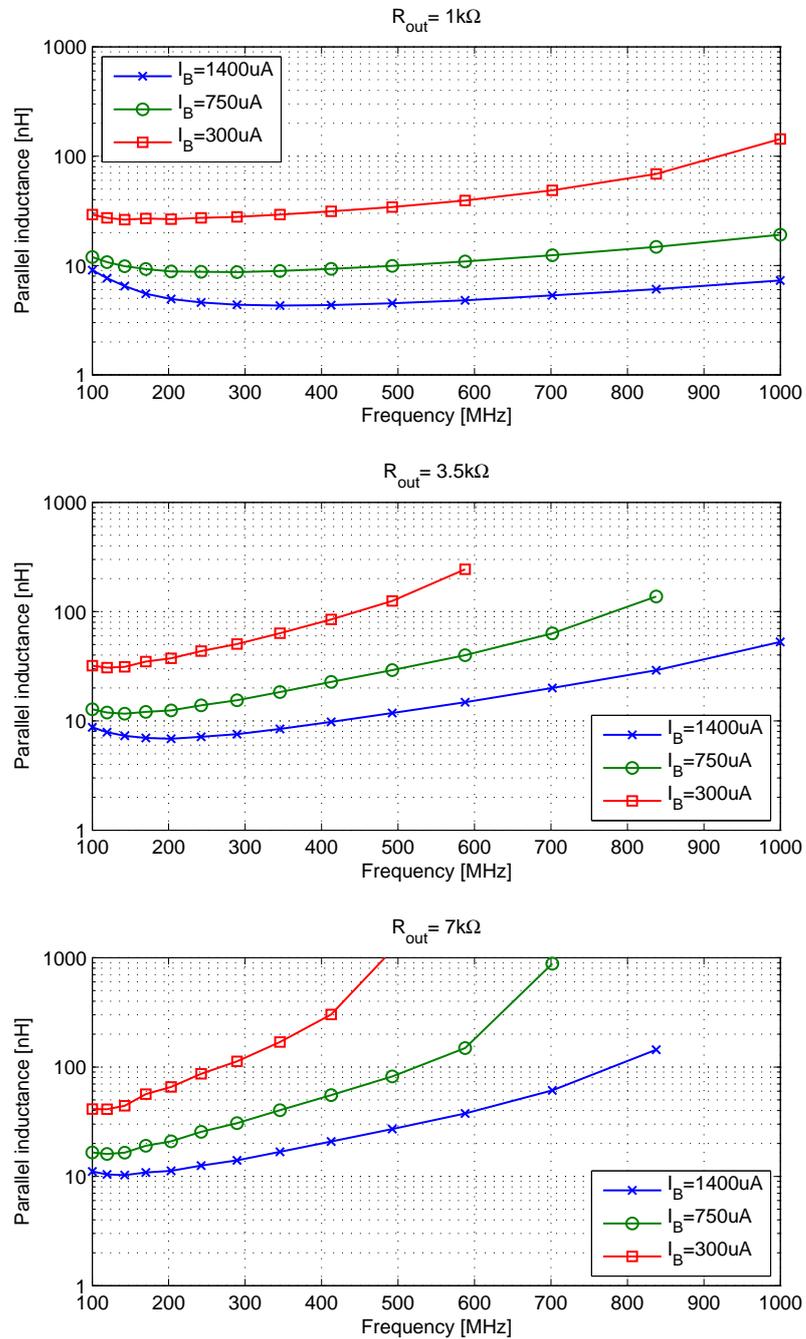
Figure 7.14: Simulated parallel inductance.

Note that the simulated lower limit of this frequency band, is approximately equal to 200 MHz, as calculated previously in Chapter 4. This proves that the gyrator losses represented by G_o are the main cause for the reduction of the negative conductance at low frequencies, as predicted by the mathematical model and shown in Figure 4.9.

In the case of the equivalent parallel inductance depicted in Figure 7.14, the CMOS gyrator follows the behavior of a generic theoretical model from Section 4.2.1.2, Figures 4.4 and 4.6. It can be seen, that the proposed theoretical model predicts correctly the behavior of the practical circuit in terms of the magnitude of the simulated inductance (refer to the case for R_{out} of 1 kΩ) its increase with frequency and inverse proportionality to gm.

Note that in the practical oscillator, the value of the phase shifter C_{out} has been halved in comparison to the mathematical model from Chapter 4, Table 4.6. This is due to the parasitic capacitances of the CD amplifier and the current mirror that are represented by single capacitors in the mathematical model. More details on the influence of the parasitics on a degenerated gyrator circuit are presented by Szczepkowski et al. [125]. Although, the considered circuit is far from ideal and does have more complex parasitic structure than initially assumed, the overall AC behavior follows the one predicted mathematically from the proposed circuit model.

7.5.3 Resonant frequency of the oscillator and choice of a tank capacitor value

To create the conditions for instability, the circuit has to be in resonance while negative conductance fully compensates the resonator losses. Proper calculation of the resonant frequency therefore requires a thorough simulation of the most important circuit parasitics. To simplify the process, a new, simple and intuitive graphical method is proposed. The method can be described as follows. First, plots of the real and imaginary parts of input admittance from Figure 7.10 and 7.12 can be displayed on a single sheet. Figure 7.15 presents both characteristics for R_{out} and C_{out} of 3.5 kΩ and
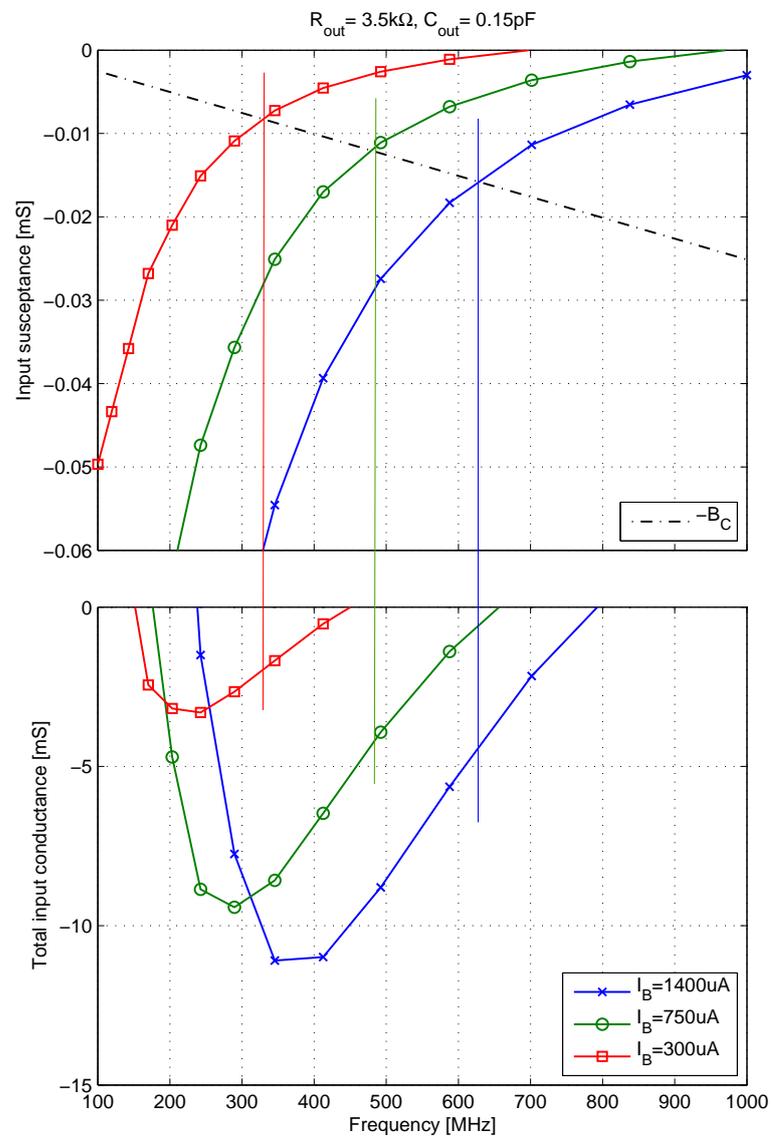
Figure 7.15: Finding tank capacitance and resonant frequency using graphical method.

Table 7.3: Resonant frequency and total negative conductance for degenerated gyrator with tank capacitance C_t of 4 pF.

I_B	f_0	G_{pdg}
µA	MHz	mA/V
300	330	-1.95
750	480	-3.8
1400	640	-4.7

0.15 pF, respectively. As the circuit simulates a parallel resonator, the tank capacitance can be described by the susceptance $jB_C = j\omega C_t$ that adds directly to the input susceptance of the gyrator. When the sum is zero in total, the tank is at resonance as both susceptances have the same magnitudes. Thus, to graphically determine the resonant frequency, B_C can be projected on Figure 7.15 as a $-B_C$, represented here as a dashed line. The points where this line intersects the gyrator susceptance curves for different I_B, indicates the resonant frequency. If at the same time, negative resistance is generated, the circuit will become unstable. Note that the described graphical method can be used for any other negative resistance oscillator circuit where the similar sets of plots are available.

Setting B_C to different values, changes the slope of the line, making it steeper for larger tank capacitor values. In Figure 7.15, $C_t = 4$ pF has been used. For the considered parameters, the calculated resonant frequency and negative resistance values are presented in Table 7.3. The available total tuning range of 310 MHz around the centre frequency of 480 MHz results in a relatively wide fractional bandwidth of about 64%, a result beyond the capabilities of an oscillator using a single passive LC tank.

7.6   Large signal analysis

This section presents a large signal analysis of the oscillating circuit. As an oscillator is non-linear and operates with a periodic signal, harmonic balance methods are used to find a steady state solution. One of the best known harmonic balance approaches implemented in circuit simulators like Eldo RF is the *probe method* [126].

The circuit simulator introduces a harmonic source (series voltage or parallel current) between nodes for which oscillatory behavior is suspected. The probe is defined by amplitude and frequency, where the latter can be set as an initial guess, close to the expected, theoretical value. During simulation, the probe parameters are varied until their values allow us to reach a converging solution within a specified error. The steady-state conditions of the analysed circuit are therefore given by the probe amplitude and

frequency. The SST (steady state) simulator in Eldo RF allows one to find the large signal voltages and currents, the oscillation frequency and phase noise of the circuit. Figure 7.16 illustrates the test bench circuit used for this simulation. The tank capacitor and phase shifter are designed using MIM capacitors. The resistor R_{out} employs a high resistance device optimised for RF frequencies with a non-salicide polysilicon conductive path. The related design parameters are displayed in Table 7.4. Once the simulation is set, the probe is placed automatically between the nodes gyr_in and VSS, that is at the gyrator input.

7.6.1   Large signal input admittance

As described in Chapter 5, the small signal AC model of a degenerated gyrator is not sufficient to describe its behavior in the presence of oscillations. It was shown that increasing signal amplitude causes a compression of the negative conductance and changes the resonant frequency due to expansion of the inductance. To confirm this behavior, the input admittance of the circuit has been simulated as a function of the amplitude of the input signal applied between the nodes gyr_in and VSS. The results, in a form of the total input conductance and parallel inductance are illustrated on Figures 7.17 and 7.18, respectively. At this stage the circuit is analysed as being driven by an external signal source, defined by frequency and amplitude. Thus, for the purpose of this particular simulation it is assumed that the degenerated gyrator is not considered an autonomous circuit.

When the signal amplitude is relatively small, less than 1 mV, the values correspond to the ones found using the AC signal analysis in Section 7.5, Table 7.3. When the signal amplitude increases, the circuit behaves as predicted by the proposed Volterra kernel model from Chapter 5, Table 5.4. Note, that although the proposed non-linear model is much simplified, the observed curves correspond to the mathematical results depicted previously on Figure 5.10. The negative conductance starts to decrease until its value reaches zero. At this point oscillations should settle however the presented amplitude values should be treated only as qualitative. Due to the nature of simulation setup in
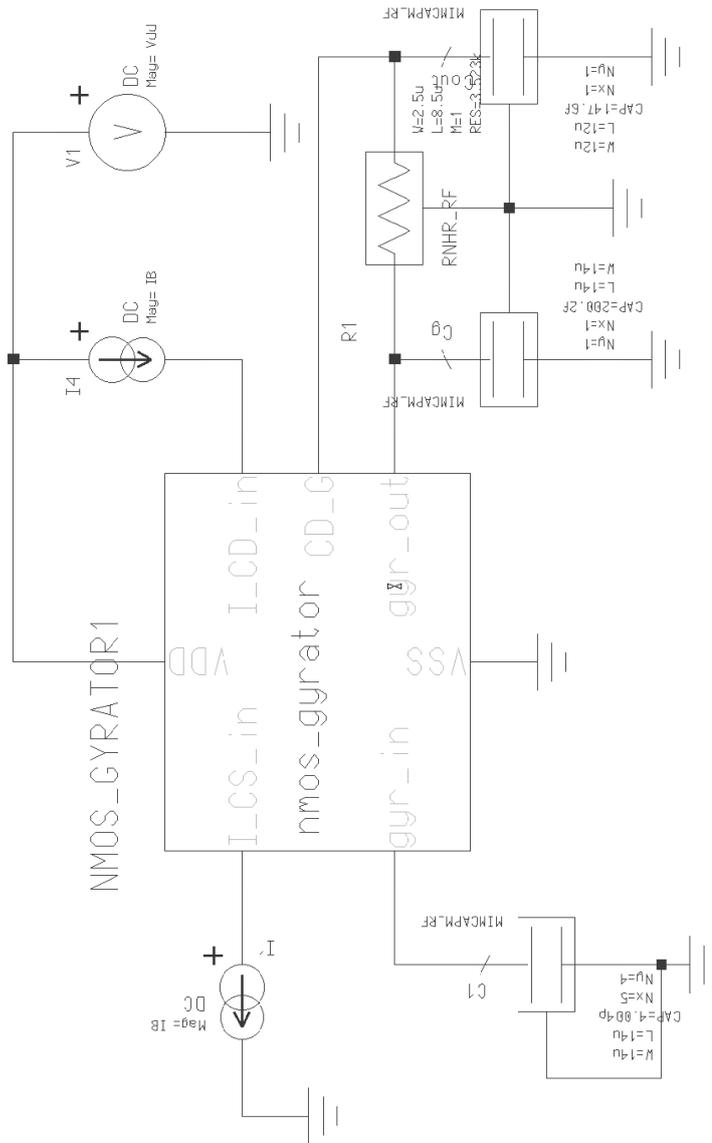
Figure 7.16: Test bench circuit for SST and time domain simulations.

Table 7.4: Design parameters of passive components

Component	Model	Value	Unit	W	L	Unit
R_{out}	RNHR_RF	3.523	kΩ	8.5	2.5	
C_{out}		0.15		12	12	
C_g	MIM	0.2	pF	14	14	μm
C_t		4		60	48	
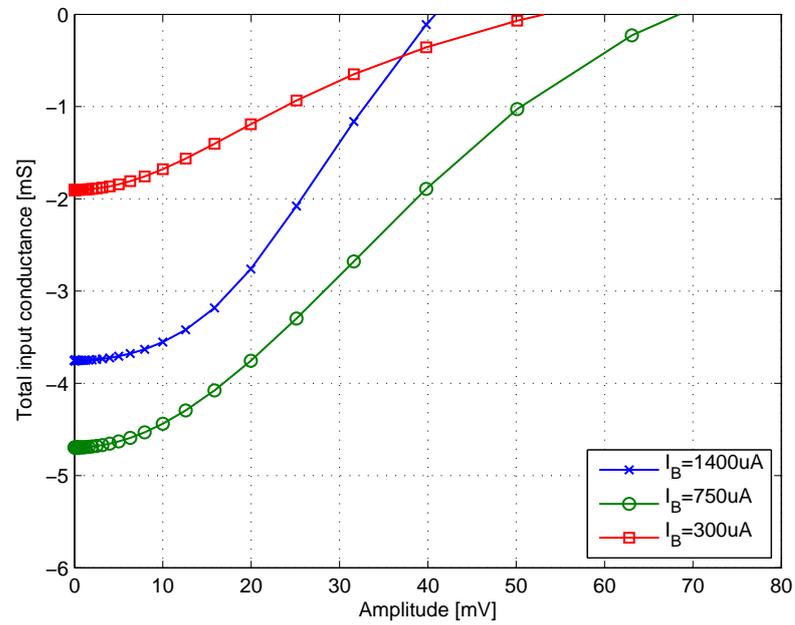
Figure 7.17: Large signal input conductance of degenerated active inductor resonator
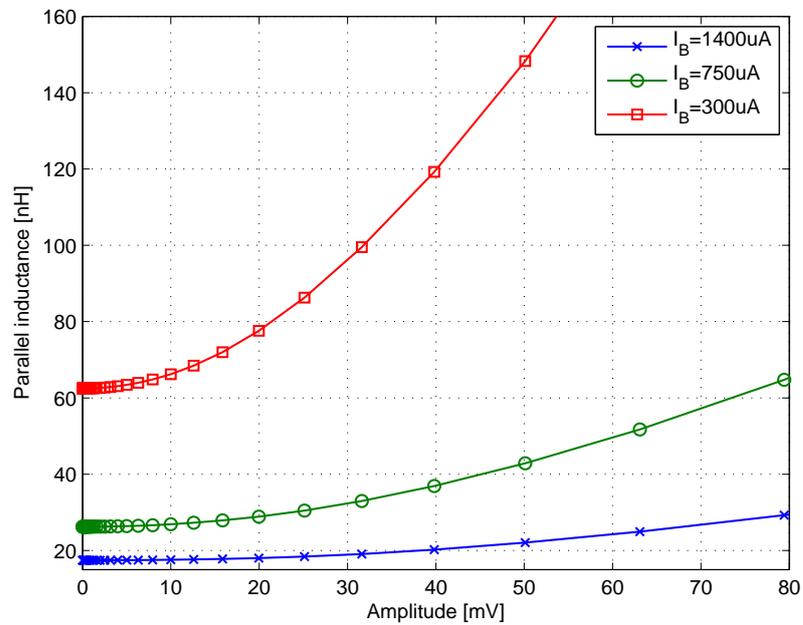
Figure 7.18: Large signal inductance of degenerated active inductor resonator

Eldo RF it was assumed that the resonant frequency was constant for each curve and equal to the small signal value from Table 7.3. In general, as explained in detail in Sections 5.5.1 and 5.5.2, such an assumption is false, as due to the expansion of the inductance (proved by Figure 7.18), the resonant frequency decreases with increasing amplitude. However, the simulation of each point at the presented plots, would require a separate calculation of the resonant frequency and recursive simulation in Eldo RF. The proper values of oscillation amplitudes are found using the probe method described previously, however in this case one can't obtain the plots depicted in Figures 7.17 and 7.18. Thus, these plots should be treated only as illustrative. It will be showed later that the numerical results obtained from the SST simulation are much closer to the calculated values from Chapter 5.

7.6.2 Tuning range

Figure 7.19 depicts the tuning curve of the oscillator. Each point represents the oscillation frequency for I_B between 300 µA and 1400 µA with a 100 µA step. It can be seen that SST simulator was able to find instability leading to oscillations for all of the considered bias conditions. Thus, the degenerated gyrator generates a signal without any external compensation circuit, as predicted in small signal analysis.

The dashed line represents the resonant frequency approximated using the graphical method and the small signal simulation results. One observation made is that the signal frequency found in a large signal regime is lower than expected for small signal behavior. This is caused by two factors. First, as predicted in Chapter 5, Table 5.4 and shown on Figure 7.18, due to harmonic distortion of an increasing signal amplitude, the simulated inductance value becomes expanded. As a result, the average value for the inductance over one oscillation cycle is somewhat larger than the small signal value determined from the AC model. Secondly, all of the transistor parasitic capacitances are voltage dependent and vary with oscillation signal.

The tuning range of the oscillator found using the SST analysis is equal to 354 MHz, spanning from 226 MHz to 580 MHz. Assuming the centre frequency of the oscillator
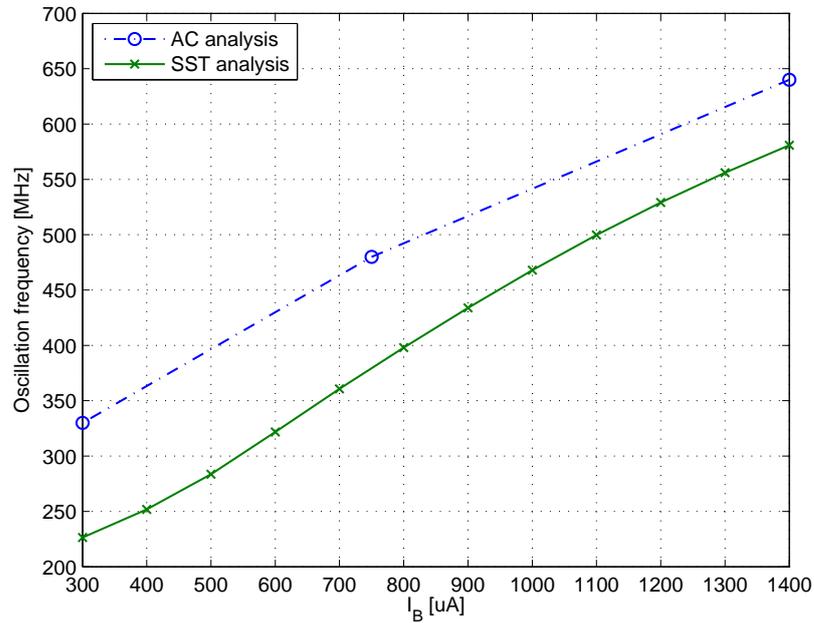
Figure 7.19: Tuning curve of the oscillator.

at 434 MHz for I_B of 900 µA, this value results in a relatively wide, fractional tuning range of 81.5%. No switched capacitors and varactors are used. It is also worth noting that the tuning curve is less distorted than in the case of circuits tuned by varactor diodes.

As the proposed oscillator is controlled by the bias current, the tuning constant is expressed in Hz/A. The average value of the tuning constant for the circuit is equal to 320 kHz/µA.

7.6.3 Spectral and transient simulation of output signal

This section presents the spectral properties of the oscillator output signal as a function of bias current. The result has been extracted from SST simulation for five different I_B values and five harmonic frequencies. In general, the oscillator signal can be extracted from either the *gyr_in* or the *gyr_out* nodes (refer to Figure 7.16). The practical choice of the output is dictated by the type of load, required output signal power and the buffer amplifier architecture. More details will be given in subsequent sections.

Table 7.5: Output signal spectrum for five different reference currents.

(a) I_B =300 µA.

f_0 =226 MHz		
Output	gyr_in	gyr_out
Component	Amplitude	
	mV	
DC	490	891
f_0	80	447
$2f_0$	28	130
$3f_0$	9	48
$4f_0$	2.2	19
$5f_0$	0.8	7
THD (%)	37	31

(b) I_B =750 µA.

f_0 =380 MHz		
Output	gyr_in	gyr_out
Component	Amplitude	
	mV	
DC	532	1037
f_0	109	683
$2f_0$	29	135
$3f_0$	4	39
$4f_0$	0.68	17
$5f_0$	0.48	6
THD (%)	27	21

(c) I_B =900 µA.

f_0 =434 MHz		
Output	gyr_in	gyr_out
Component	Amplitude	
	mV	
DC	544	1100
f_0	106	653
$2f_0$	21	95
$3f_0$	1.2	32
$4f_0$	0.9	12
$5f_0$	0.14	1.7
THD (%)	20	16

(d) I_B =1200 µA.

f_0 =530 MHz		
Output	gyr_in	gyr_out
Component	Amplitude	
	mV	
DC	568	1200
f_0	92	558
$2f_0$	9	46
$3f_0$	0.8	22
$4f_0$	0.26	4
$5f_0$	0.03	2
THD (%)	10	9

(e) I_B =1400 µA.

f_0 =580 MHz		
Output	gyr_in	gyr_out
Component	Amplitude	
	mV	
DC	584	1250
f_0	76	477
$2f_0$	4	32
$3f_0$	0.62	15
$4f_0$	0.09	2.8
$5f_0$	0.02	1.8
THD (%)	5.3	7.3

Table 7.5 presents the simulated results of SST simulation in the frequency domain. Each sub-table contains the signal amplitudes at the carrier frequency and the corresponding harmonics, simulated for each of the two possible oscillator outputs, the *gyr_in* and the *gyr_out* nodes. The available amplitudes on the *gyr_in* node correspond to the results of theoretical derivations presented in Chapter 5, in Figure 5.10, proving that the Volterra kernels method applied for a simplified model of the degenerated gyrator can predict correct large signal behavior. Note that the output amplitudes from *gyr_out* were not analysed by the theoretical model. Their levels are significantly larger due to the imbalance introduced by the phase shifter and different voltage gains of the CS and CD amplifiers. In addition, note that the oscillator signal becomes less distorted for the increasing bias current (i.e. increasing gm). This behavior has been predicted by the proposed large signal model (indicated by Figure 5.12) and also thoroughly explained in Chapter 5. Large THD for the low transconductance values can be improved if the oscillator signal can be filtered by the use of tuned buffer amplifier. This approach is discussed in detail later in the chapter.

The time domain behavior has also been analysed. The simulation time was set to 300 ns (which corresponds to 130 periods of 434 MHz sinusoid) with approximately 90 points per period for accuracy and simulation speed. Figures 7.20 and 7.21 show a 434 MHz signal at *gyr_in* and *gyr_out* nodes, respectively. Each figure presents three plots where the center one represents a simulated output voltage for a total specified time. The top plot depicts the transient behavior of the oscillator signal. Note that the oscillator start-up time is not representative due to the use of an always-on ideal DC source as the power supply voltage VDD. As a result, the circuit simulator requires more iterations before reaching stable solution. In practice, oscillators are triggered by the relatively abrupt switch on of a power supply which in turn causes faster oscillation buildup. For the basic setup of SST simulation in Eldo RF, the use of a pulsed DC sources to simulate this state is not allowed by the program. Figures 7.20 and 7.21 also depict a magnified version of the simulated signal once the oscillator operates in the steady state. It can be seen that amplitudes predicted during SST simulation
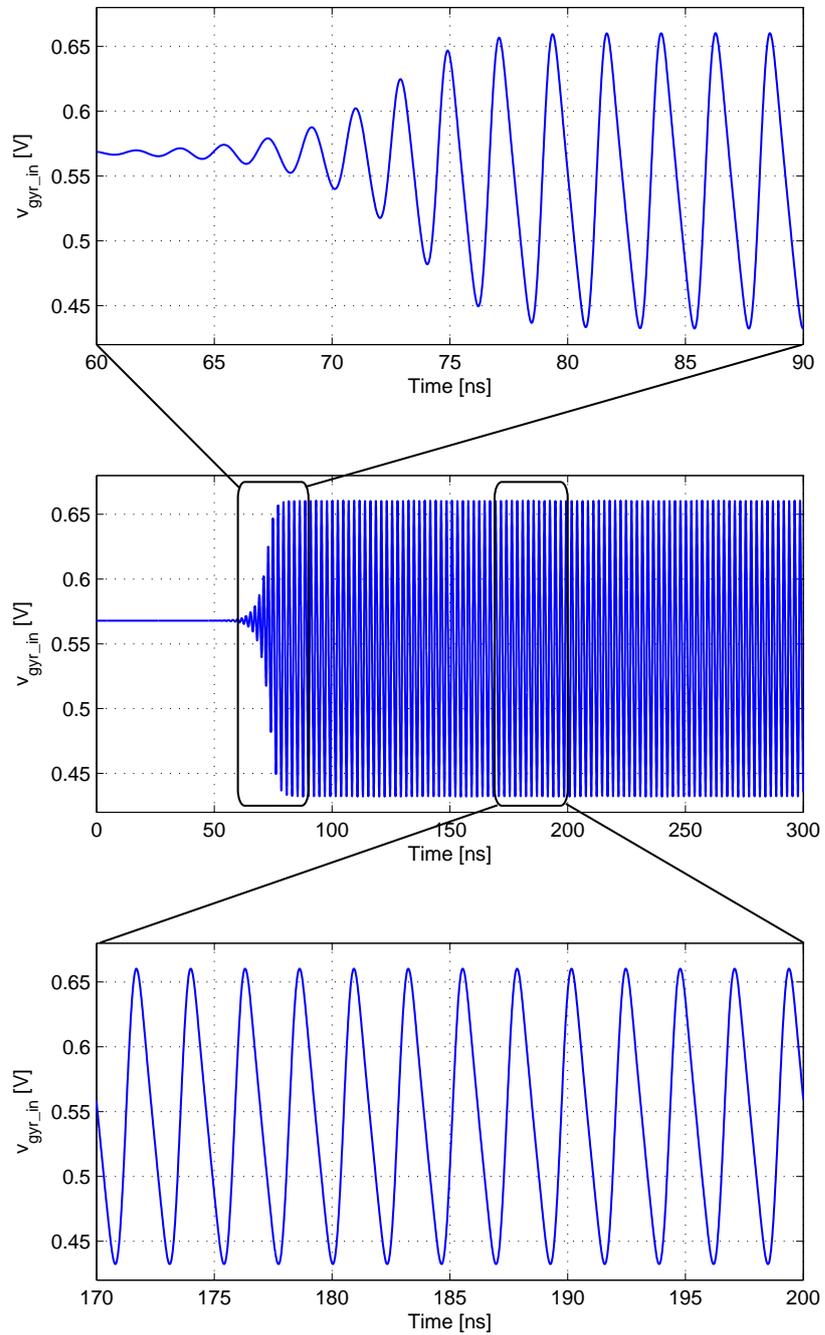
Figure 7.20: Generated 434 MHz signal at *gyr_in* node.
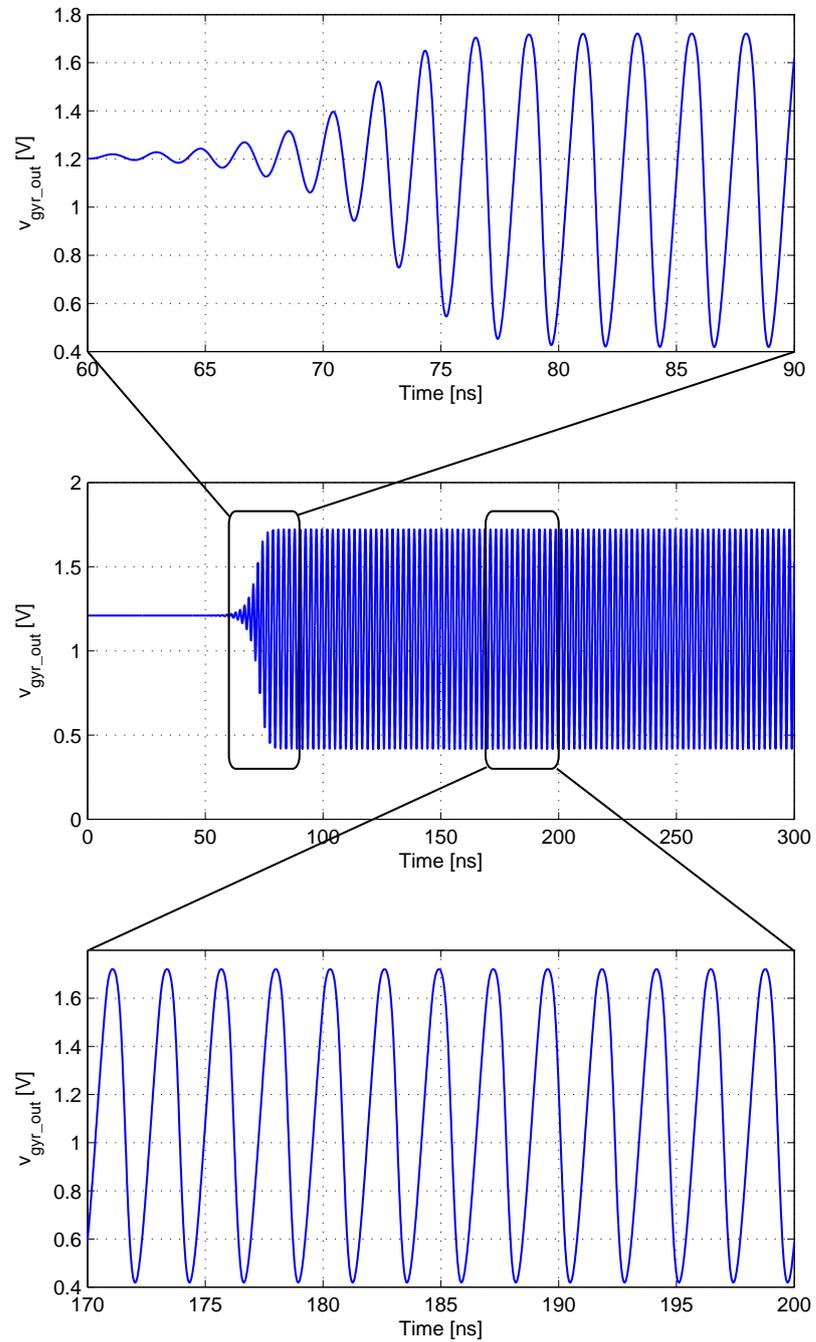
Figure 7.21: Generated 434 MHz signal at *gyr_out* node.

for $I_B = 900$ µm presented in Table 7.5 are equal to those found from time domain simulations. The frequency of a steady state voltage is equal to 434.783 MHz.

7.6.4 Oscillator phase noise

The phase noise has been simulated for frequency offsets spanning over two decades, between 30 kHz to 3 MHz. The Eldo RF algorithm computes phase noise according to [120]

$$S_{phi_{EldoRF}} = \frac{S_{\omega_0 + \Delta\omega_m} + S_{\omega_0 - \Delta\omega_m} - 2\Re\{S_{corr}e^{2j\phi_{SS}}\}}{V_{SS}^2} \qquad (7.6)$$

$S_{\omega_0 + \Delta\omega_m}$ and $S_{\omega_0 - \Delta\omega_m}$ represent the PSD of noise at $+\omega_m$ and $-\omega_m$ offsets from the carrier, respectively. S_{corr} is a correlation between the noise components at $\omega_0 + \omega_m$ and $\omega_0 - \omega_m$, whereas ϕ_{SS} and V_{SS} are signal phase and amplitude extracted from the steady state large signal simulation [120]. The circuit simulator inserts a phase noise probe between two nodes of the circuit. In the considered case, the phase noise has been extracted between *gyr_in* and the ground nodes first and then compared to the phase noise simulated between *gyr_out* and the ground. As indicated previously, an oscillator load can be connected to *gyr_in* or *gyr_out* and therefore it is important to analyse the phase noise levels at both these nodes. During SST simulation it was observed that at the described nodes phase noise magnitudes were equal and, from a noise perspective, one point is not preferred over the other to provide the output signal.

Figure 7.22 presents a single sideband phase noise spectrum for the five considered I_B values extracted from the *gyr_out* node. The lowest phase noise level approximately of -100 dBc/Hz has been obtained for 750 µA and 900 µA bias currents. At larger currents, phase noise deteriorates due to increased signal frequency and reduced signal amplitude. At 300 µA, signal amplitude is the smallest in connection with a high harmonic distortion. This results in the highest phase noise level. The phenomenon of phase noise increase due to harmonics has been studied by Razavi [119], and Hajimiri

Figure 7.22: Simulated single sideband phase noise spectrum as a function of I_B.

and Lee [116] where it is shown that high order distortion components fold (alias) noise components from higher frequencies into the bandwidth close to the carrier.

It can be seen that simulated phase noise level is on average a few dB higher in comparison with the proposed theoretical model from Chapter 6. The results of comparison are summarised in Section 6.4, in Table 6.2 and Figure 6.6. The difference comes from the fact that the phase noise model does not account for a non-linear folding phenomenon described above. The proposed phase noise model does not account for noise injected by non-ideal current sources and time variance of the oscillator. Nevertheless, the simple linear model developed in Chapter 6 is sufficient to predict correct orders of phase noise magnitudes for degenerated gyrator oscillators.

7.7 Output signal of loaded oscillator

As indicated before, a signal can be extracted from the oscillator from two nodes: *gyr_in* or *gyr_out*. In practice, an oscillator is used to drive a mixer and therefore the

load is typically capacitive. In other applications, for example continuous wave (CW) transmitters, the load can be resistive (antenna and matching circuits). Typically, the output power of RF amplifier is determined using a 50 Ω termination. This load can't be connected directly to the degenerated gyrator for two reasons. First, the influence of the load has to be minimised to avoid excessive frequency pulling. Secondly, resistance in the range 50 Ω represents significant losses that would require much more power to compensate. Thus an output buffer has to be used.

7.7.1   Choosing oscillator output and buffer amplifier

In general, the buffer amplifier can have any known configuration as long as its influence on the oscillator circuit is well characterised. If the oscillator signal is too small it can be boosted through a CS amplifier. If a simple one transistor amplifier is employed, a Miller capacitance will introduce significant capacitive load. This effect can be minimised by using a two transistor cascode. Observing oscillator signals depicted previously in Figures 7.20 and 7.21, it can be seen that gyr_in node delivers 5 to 6 times smaller amplitude than the gyr_out port. This asymmetry comes from the fact that both transconductors have the same gm however the capacitances at gyrator ports are not equal. As shown in Chapter 4, the RC shifter contributes to the magnitude of the simulated inductance, resulting in the gyration capacitance C_g being smaller than the total tank capacitance C_T. Thus, the voltage produced at the gyr_out port is larger than that of the gyr_in node.

If the oscillator is loaded from the gyr_in port, the main advantage of this approach is that any parasitic capacitance of the buffer input is connected in parallel to the total tank capacitance C_T. As a result, the buffer parasitics do not contribute to the negative resistance generation mechanism of the degenerated gyrator. The downside is that the signal from the gyr_in node has much smaller amplitude and requires additional gain.

On the contrary, if the output signal is extracted from the gyr_out port, then a significantly larger signal amplitude is available and further gain may not be required at all. The parasitic input capacitance of the buffer is now in parallel to the gyration

capacitor C_g and therefore contributes to the loss compensation mechanisms as well as simulated inductance. These observations lead to a source follower (CD) configuration for the output buffer as this circuit has a high input impedance (i.e. a relatively small input capacitance) and is suitable to directly drive high loads in the range of 50 Ω with 0 dB voltage gain. Care has to be taken in the presence of capacitive loads, because they can form a positive feedback network together with the transistor gate to source capacitance [32]. In extreme cases this can result in unintended negative resistance being generated as in the case of single transistor compensation circuit described in Chapter 2.

In addition to the described requirements, the gain-bandwidth product of the amplifier should also be considered. As the oscillator bandwidth is centered around 434 MHz and spans from 226 MHz to 580 MHz it is not necessary to provide substantial buffer gain beyond this frequency range. Thus, an output buffer can be realised using a tuned amplifier i.e. loaded with a resonant tank tuned to the center frequency of the considered bandwidth. The drawback of this approach is the use of a second resonator however due to the use of a inductor in the load, MOS transistor can be biased with $V_{DS} = V_{DD}$, the maximum available headroom.

The use of an additional passive LC tank potentially destroys the benefit of the proposed oscillator, the reduction of chip area. This conclusion is not true. To obtain a high performance output buffer (crucial at RF frequencies) operating with low supply voltage the use of inductors is fundamental, regardless of the architecture of the LC oscillator one intends to use. Thus, even if not much can be done to avoid a relatively large passive LC tank in the buffer, the oscillator area can be still reduced by the use of the degenerated active inductor.

At the same time, the question arises if instead of a spiral inductor, a gyrator can be used in the buffer. Unfortunately, this can't be done without a serious compromise of the amplifier performance. The main advantage of a spiral inductor is its zero DC voltage drop that in turn spares the voltage headroom left for the buffer transistor. As shown in this thesis, an active inductor requires DC power to operate and would reduce
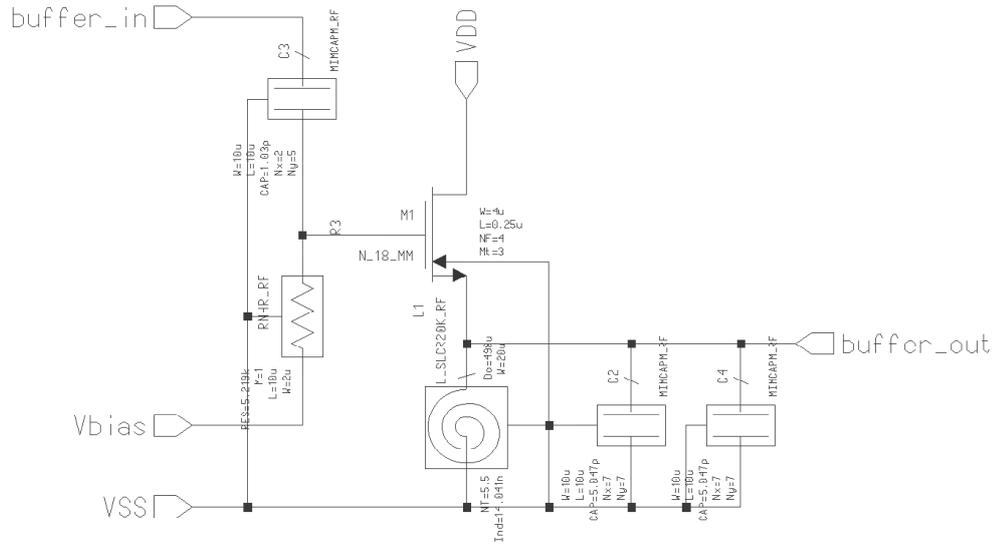
Figure 7.23: Tuned buffer amplifier circuit with integrated resonator.

dramatically the available voltage range for the amplifier. Also, such a circuit would be highly non-linear under large signal operation, in comparison to the approach using a passive LC tank described in this section. Thus, the use of a gyrator in place of a spiral inductor is not practical for the buffer application.

Figure 7.23 illustrates a tuned source follower employing an integrated resonator with spiral inductor and MIM capacitors. The size of the transistor is set such for the considered bias point of V_{gs} =1.1 V and V_{ds} =1.8 V, device transconductance is equal to 20 mA/V. As the output resistance of the source follower is equal to $1/gm$, this allows us to match the amplifier to the 50 Ω load. The cost however is increased power consumption of approximately 16 mW because the amplifier operates as a class-A circuit (i.e. low efficiency but high linearity). The amplifier is biased separately from the oscillator through a large resistor to prevent excessive loading of the core. Also, a 1 pF blocking capacitor is used to separate both circuits at low frequencies. As before, to exploit the larger DC gain of the transistor, the drawn length L of the NMOS device has been set to 250 nm. The total width of the transistor equals 48 µm using 3 parallel devices with 4 fingers and 4 µm width per single finger. The diameter of the inductor is equal to 500 µm with 5.5 turns of 20 µm metal conductor and inductance of 14 nH.
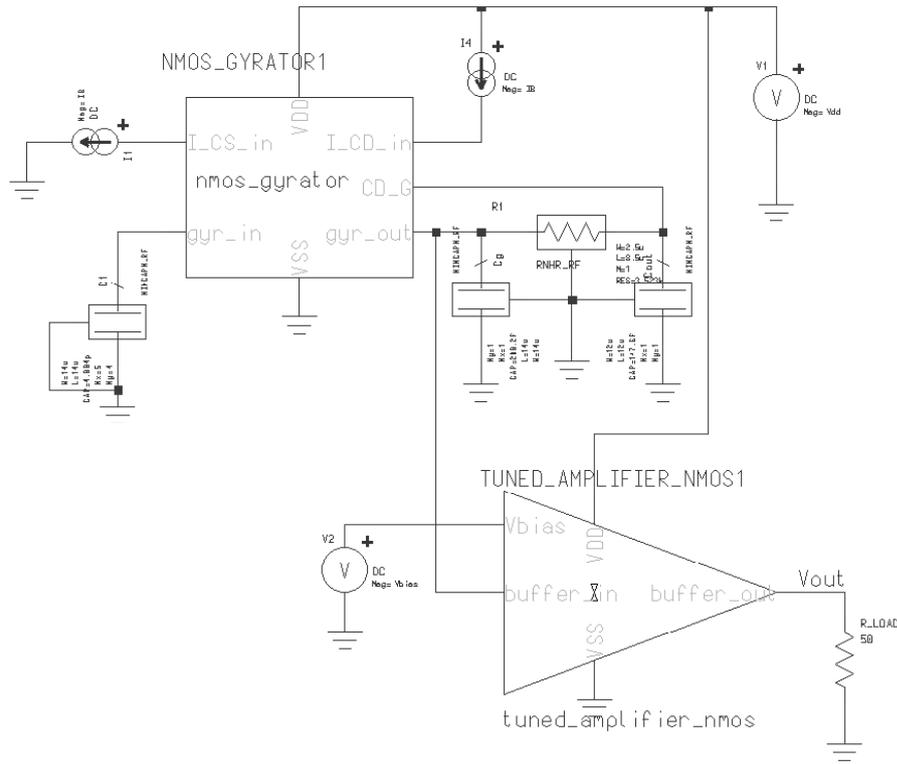
Figure 7.24: Complete oscillator circuit with output buffer.

The resonator capacitance is composed of two 5 pF capacitors in parallel, each being a 70 μm per 70 μm square. Loaded Q of this resonator is approximately equal to 1 which ensures a wide band operation around the carrier frequency.

Figure 7.25 presents how the tuning range of the oscillator changes as a result of 50 Ω load. As before, a SST simulation has been carried out for different values of bias current I_B. It can be seen that connecting the buffer at the *gyr_out* node affects the lower boundary of the tuning range. This is due to additional RC components introduced by the amplifier. To increase the tuning range at high frequencies, the maximum I_B has been increased from 1400 μA to 1600 μA. As a result, the tuning constant is smaller than in the unloaded case, approximately 250 kHz/μA.

The next plot (Figure 7.26) depicts a transient simulation results of 434 MHz output signal for $I_B = 920$ μA. The DC component of 10 mV is a result of resistive losses of a spiral inductor from the buffer and even order harmonics of the oscillator signal.
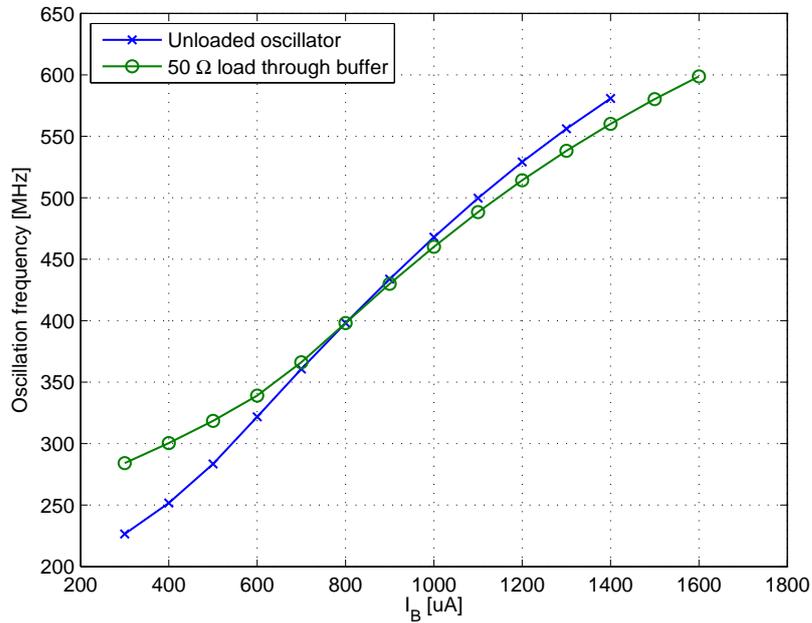
Figure 7.25: Tuning curve of loaded oscillator.

A spectral analysis of the output signal has been carried out. As for the unloaded oscillator, the results are summarized in Table 7.6. It can be seen that in comparison to the results from Table 7.5, the tuned buffer reduces THD of the output signal by 50 % despite the relatively poor Q factor of the passive inductor used. Also, the amplitude is reduced in comparison with unloaded gyr_out output. The attenuation comes from the amplifier output resistance of 50 Ω and therefore only half of the input voltage is available for the load resistor.

7.7.2 Output power

Finally, the signal amplitudes at f_0 are used to calculate the output RF power of the oscillator using the following formula for a real power of a sinusoidal signal

$$P_{AC} = \frac{V_{RMS}^2}{R} = \frac{V_{MAX}^2}{2R}$$
$$P_{ACdBm} = 10 \cdot log\left(\frac{P_{AC}}{1mW}\right) \tag{7.7}$$

At 50 Ω load resistance, (7.7) yields the results presented in Table 7.7.
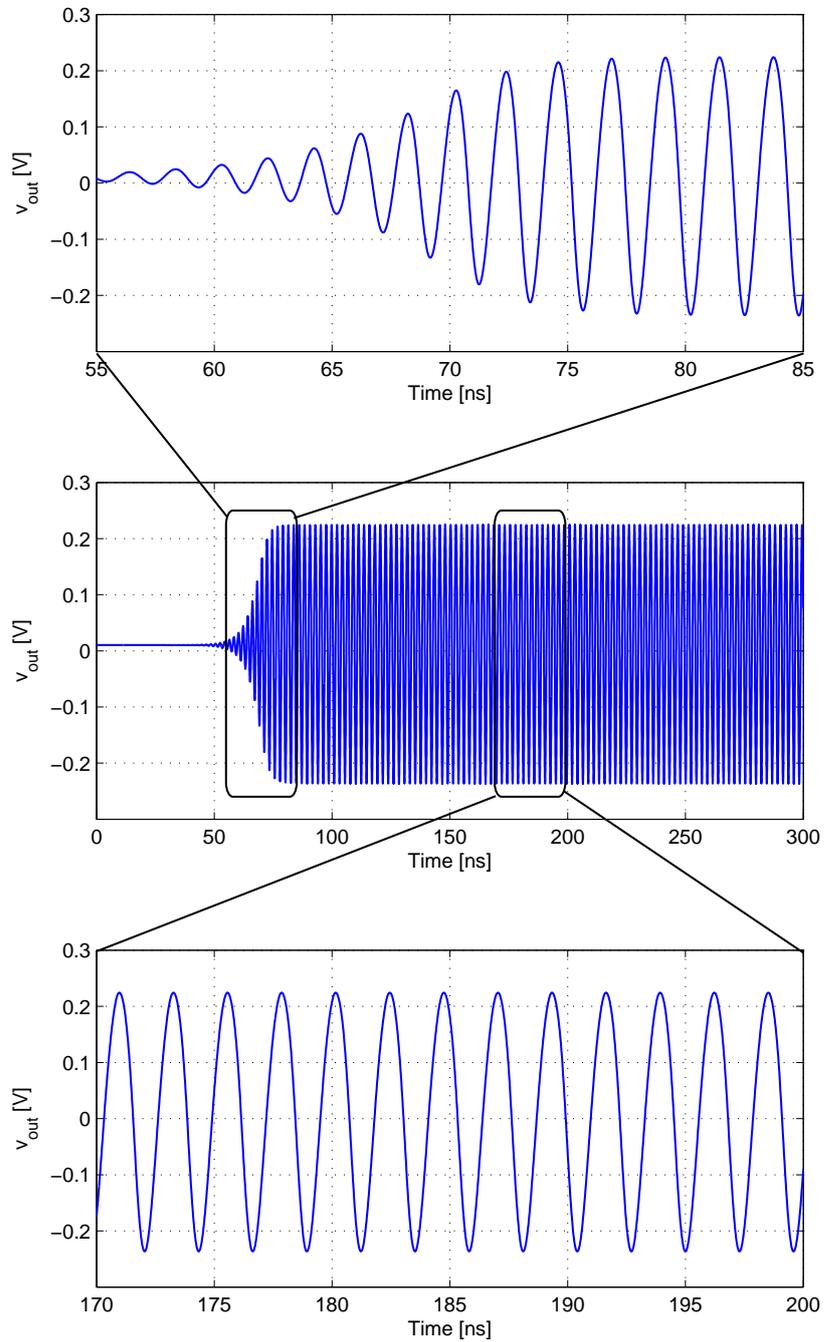
Figure 7.26: Generated 434 MHz output signal at 50 Ω load.

Table 7.6: Output signal spectrum of loaded oscillator for five different reference current values.

(a) $I_B =$ 400 µA.

$f_0 =$ 300 MHz	
Component	Amplitude
	mV
DC	10.3
f_0	120.4
$2f_0$	24.6
$3f_0$	4.2
$4f_0$	0.7
$5f_0$	0.12
THD (%)	20

(b) $I_B =$ 750 µA.

$f_0 =$ 375 MHz	
Component	Amplitude
	mV
DC	10.3
f_0	230.4
$2f_0$	35
$3f_0$	5.8
$4f_0$	1.3
$5f_0$	0.324
THD (%)	15

(c) $I_B =$ 900 µA.

$f_0 =$ 430 MHz	
Component	Amplitude
	mV
DC	10.3
f_0	230.5
$2f_0$	23
$3f_0$	3.3
$4f_0$	1
$5f_0$	0.27
THD (%)	10

(d) $I_B =$ 1200 µA.

$f_0 =$ 514 MHz	
Component	Amplitude
	mV
DC	10.3
f_0	197
$2f_0$	7.3
$3f_0$	2
$4f_0$	0.6
$5f_0$	0.05
THD (%)	4

(e) $I_B =$ 1600 µA.

$f_0 =$ 600 MHz	
Component	Amplitude
	mV
DC	10.1
f_0	131
$2f_0$	2.4
$3f_0$	0.93
$4f_0$	0.2
$5f_0$	0.05
THD (%)	2

Table 7.7: RF power at 50 Ω load resistor

I_B	f_0	P_{RF}	
µA	MHz	mW	dBm
400	300	0.145	-8.4
750	375	0.53	-2.75
900	430	0.53	-2.75
1200	514	0.4	-4
1600	600	0.17	-7.65

7.7.3 Power consumption

The power consumption depends on two factors: DC current necessary to bias the degenerated gyrator and the energy required for proper operation of the output buffer. When the circuit is tuned, the power consumption of the oscillator core changes as it depends on the bias current I_B supplied to both transconductance amplifiers through the current mirrors. In the case of the buffer amplifier, its power consumption remains constant and independent from the core due to the use of a decoupling capacitor.

To tune the oscillator to 600 MHz, a bias current of 1600 µA is required. For the supply voltage V_{DD} of 1.8 V this results in the total power consumption of 26.72 mW for the complete oscillator circuit. This includes 5.76 mW for the oscillator core, 5.76 mW for bias mirrors and 15.2 mW dissipated by the buffer. At 434 MHz, the total power reduces to 21.7 mW as I_B is decreased. Note that at this frequency the output amplifier consumes 70% of the total power due to its required low output impedance of 50 Ω. Finally, the minimum power required for the operation of the complete oscillator circuit is equal to 18.1 mW.

The presented power consumption performance is compared to other oscillator circuits later in this chapter.

7.7.4 Phase noise of loaded oscillator

Simulations of the buffered circuit do not reveal any significant changes of phase noise in comparison to the unloaded case presented in Figure 7.22. On average, for considered I_B values between 400 µA and 1600 µA, the phase noise level does not increase more

than 0.5 dB. However, for $I_B = 300$ μA phase noise has increased by 4 dB, mostly due to smaller amplitude generated from the core. The phase noise extraction probe has been connected between the ground and V_{out} nodes (Figure 7.24).

7.8 Process and temperature variations

The last section of circuit analysis shows how the loaded oscillator behaves when design parameters differ from their nominal values. Three typical scenarios are considered: temperature, transistor and passive component variations.

7.8.1 Temperature variations

Industry standard temperatures for consumer products are: -40°C, 27°C (room temperature) and 85°C. First a tuning range has been simulated as illustrated on Figure 7.27.

The tuning range of the oscillator is inversely proportional to the temperature. This
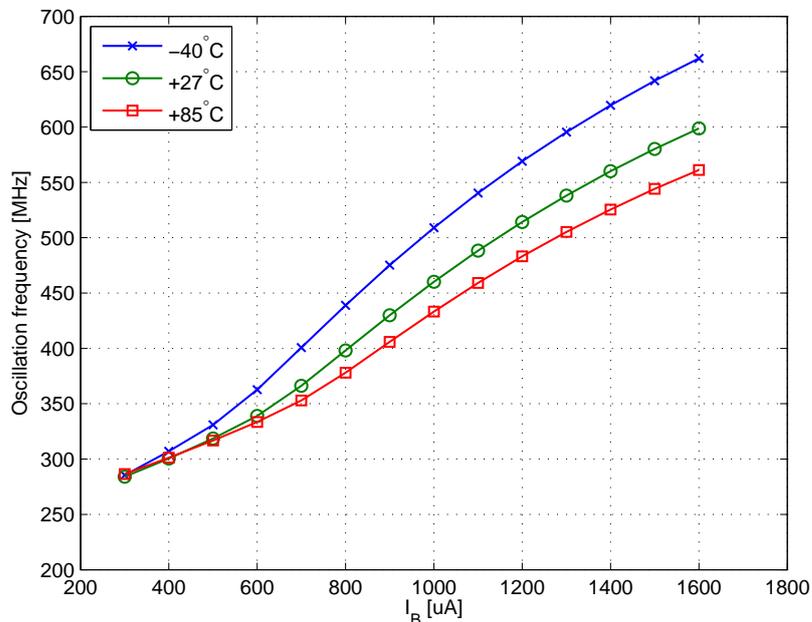
Figure 7.27: Simulated tuning range as a function of temperature.

Table 7.8: Phase noise at 1 MHz offset and output power as functions of temperature.

I_B	-40°		27°		85°	
	PN	P_{RF}	PN	P_{RF}	PN	P_{RF}
µA	dBc/Hz	dBm	dBc/Hz	dBm	dBc/Hz	dBm
400	-94	-6.1	-92.5	-8.4	-90	-11
900	-99	-2.76	-99.5	-2.75	-99.4	-3.23
1600	-97.4	-8.4	-98.4	-7.65	-99	-7.63
f_0 MHz 434	-99	-2.42	-99.6	-2.79	-99.7	-3.38

is a result of the inverse proportionality between the transistor threshold voltage V_{th} and temperature. The bias mirrors force constant current to the oscillator core. When the temperature increases, V_{th} decreases faster than gate to source voltages set by the mutual bias scheme of the gyrator. Thus the overdrive voltage of both transconductors decreases. As a result, gm becomes larger for the fixed value of bias current. Since resonant frequency is inversely proportional to gm, the tuning range must decrease.

The practical implications of temperature variations can be shown by considering circuit sensitivity around the nominal frequency of 434 MHz. For $I_B = 920$ µA, the temperature change from room temperature to -40°C increases the oscillation frequency by 45 MHz. This results in a negative temperature coefficient of 672 kHz/°C. Assuming the tuning sensitivity of the oscillator at 320 kHz/µA, I_B has to be decreased by approximately 140 µA to change the oscillation frequency back to 434 MHz.

Table 7.8 presents how phase noise and signal power change with temperature. Three bias currents are considered, for both ends of the tuning range and the center frequency. Phase noise is measured at 1 MHz offset and RF power is given in dBm. The performance of the oscillator at 434 MHz is presented separately.

It can be seen that phase noise dependence on temperature is complex. For the lower end of the tuning range, phase noise increases with temperature. This is due to a relatively small signal power and harmonic distortion. For $I_B = 900$ µA phase noise and output power do not change significantly. At low temperatures, oscillation frequency increases which, in theory, should result in higher phase noise. At the same time how-

ever, the circuit produces less noise as phase noise is proportional to the temperature. At the high end of the tuning range, the frequency drop due to the temperature changes is the highest however at the same time the output signal has the smallest distortion. In this case, no significant changes of the phase noise levels were observed. Similarly, at the frequency of 434 MHz, phase and noise power are not strongly affected by the temperature.

7.8.2 Resistance and capacitance variations

Finite mask tolerances, doping and oxide thickness variations cause passive components to have different parameter values when manufactured than when designed. For the UMC 180 nm process described here, resistance can vary within $\pm24.5\%$ around nominal values, whereas all MIM capacitances change within $\pm14.5\%$. The most probable scenario assumes R and C change in the same direction i.e. both values are equal to maximum or minimum at the same time.

Figure 7.28 depicts tuning curves of the oscillator with considered RC variations. The behavior of the oscillator corresponds to the small signal AC analysis presented in Section 7.5.2. As resistance R_{out} decreases, the simulated inductance becomes smaller, shifting the resonant frequency upwards. At the same time, the negative conductance decreases, and in extreme situations can become smaller than circuit losses. In the presented case, oscillations do not build up for currents less then 500 µA. When RC components are at a maximum, the tuning curve moves down and the negative conductance becomes larger. Despite this, the circuit still oscillates for all considered bias current values. As previously, it is important to analyse how these process variations affect the oscillator performance. The results of phase noise and output power simulations are presented in Table 7.9. Note, that the lowest bias current (I_B of 500 µA) has been chosen in respect of the lower end of tuning range when RC is minimum as in that case the circuit does not oscillate for smaller currents.

The minimum RC circuit bounds oscillator performance, both in terms of output power and phase noise. Reduced RF signal amplitude is a result of small negative
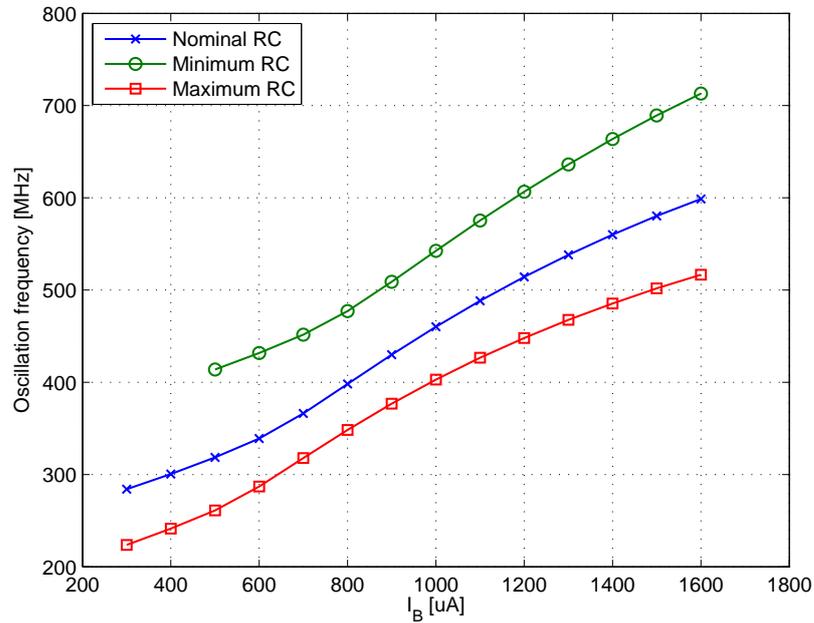
Figure 7.28: Simulated tuning range as a function of RC variations.

Table 7.9: Phase noise at 1 MHz offset and output power as functions of RC variations.

I_B	Minimum RC		Nominal		Maximum RC	
	PN	P_{RF}	PN	P_{RF}	PN	P_{RF}
μA	dBc/Hz	dBm	dBc/Hz	dBm	dBc/Hz	dBm
500	-91.2	-8.6	-94.9	-5.65	-97.6	-4.43
900	-97.3	-3.73	-99.5	-2.75	-100.8	-2.51
1600	-97.7	-7.54	-98.4	-7.65	-98.6	-8.28
f_0						
MHz	-92.3	-6.27	-99.5	-2.75	-100.8	-3.48
434						

conductance generated by the circuit. High phase noise level indicates that the 3 dB frequency of the RC phase shifter moved into higher frequencies and therefore is injecting more thermal noise into the resonator. The opposite applies when RC is large. This behavior can be seen more clearly when the oscillator is tuned to 434 MHz. The maximum RC variation yields smaller signal amplitude than the nominal case, however because the 3 dB corner frequency of the shifter is now moved down, less noise is injected, as predicted in Chapter 4.
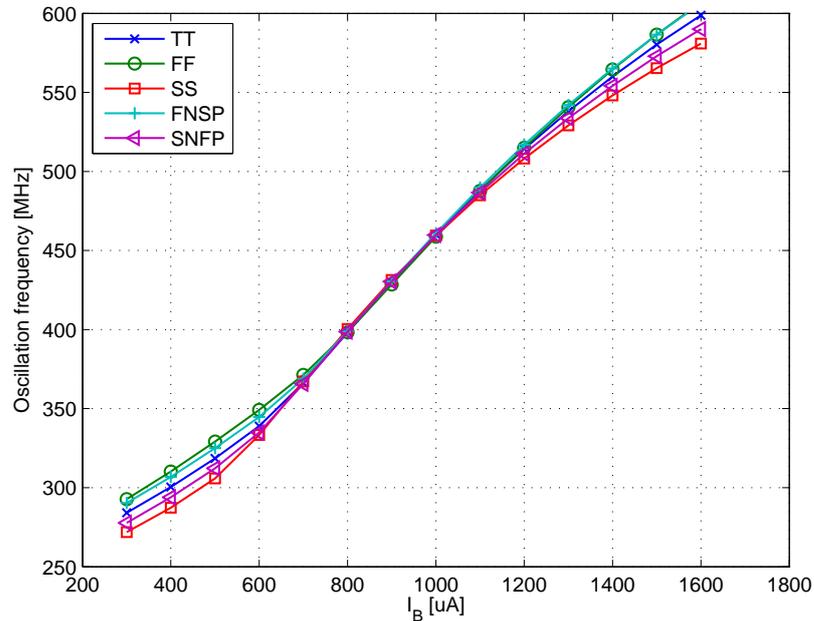
Figure 7.29: Simulated tuning range as a function of process corners.

7.8.3 CMOS process variations

Process corners describe possible deviations of transistor parameters. Four cases are possible: fast-fast (FF), slow-slow (SS), fast-N-slow-P (FNSP) and slow-N-fast-P (SNFP). Fast transistors are characterised by decreased gate oxide thickness and threshold voltage. On the other hand, slow transistors have thicker oxide and larger V_{th}. As NMOS and PMOS transistors are used, this results in the four possible variations.

Figure 7.29 presents tuning curves of the oscillator. Symbol TT represents a typical-typical scenario which sets transistor parameters at its nominal values. The circuit responds relatively well for the different process corners, considering that the oscillator operation depends on active circuits and partially on their parasitic elements. As the circuit has been designed to work around the center frequency of 434 MHz, the simulated process corners do not affect tuning range significantly. Note that at both ends of frequency band, the difference between FF and SS corners averages at 23 MHz which is less than that due to temperature and passive component variations. As before, the

Table 7.10: Phase noise at 1 MHz offset and output power as functions process corners.

I_B	SS		FF		$FNSP$		$SNFP$	
	PN	P_{RF}	PN	P_{RF}	PN	P_{RF}	PN	P_{RF}
µA	dBc/Hz	dBm	dBc/Hz	dBm	dBc/Hz	dBm	dBc/Hz	dBm
400	-93.3	-9.17	-92.3	-7.79	-92.4	-8.2	-92.8	-8.64
900	-99.3	-5.29	-99.9	-1.25	-99.5	-2.04	-99.5	-3.72
1600	-91.6	-17.6	-99.8	-4.18	-99.1	-5.99	-97.1	-10.22

phase noise and output signal power have been analysed. Due to the negligible frequency change around 434 MHz, the data extracted for $I_B = 900$µA are sufficient to describe circuit behavior around the nominal frequency. The results are presented in Table 7.10. Slow transistors cause serious deterioration of output power with increasing bias current, in the extreme case reducing it by 10 dB at high frequencies. The main source of this behavior comes from slow NMOS devices as these are used as transconductors and for the current mirror. It is observed that for the SS corner, the output conductance of each transistor increases by a factor of 1.5 over typical values. This increases resistive losses at both ports of the gyrator, effectively reducing negative conductance and the range of frequencies for which the circuit is compensated. As a result, generated amplitudes are limited. On the other hand, an FF corner improves output power due to the reduced conductance. As long as fast NMOS are considered, slow PMOS transistors do not decrease output power as they are employed in the current mirror only. At the center frequency, phase noise is not affected significantly by the process corners.

7.9   Oscillator performance benchmark

To compare the performance of the proposed oscillator to the existing circuits a normalized figure of merit with tuning range ($FOMT$) is used. This function allows fair benchmark of phase noise of oscillators working at different frequencies and includes additional quantities such as DC power consumption of the core and fractional bandwidth. One generally accepted $FOMT$ has the following form [127, 128]

$$FOMT = L(\omega_m) - 20log\left(\frac{\omega_0}{\omega_m}\frac{FBW}{10}\right) + 10log\left(P_{mWcore}\right) \qquad (7.8)$$

where $\mathcal{L}(\omega_m)$ is phase noise at frequency offset of ω_m, ω_0 is resonant frequency, FBW is a fractional bandwidth and P_{mWcore} is maximum DC power consumption of the core. The main issue related to (7.8) is that it promotes low power consumption oscillators only without taking into account the power efficiency of the overall circuit. In other words, $FOMT$ in the presented form does not convey any information on how much DC energy of the oscillator core is supplied to the load. It is shown that although many authors claim superior phase noise performance and wide tuning ranges the reported output power levels at buffered loads are too small to drive any other circuit. To include RF signal power, the new figure of merit can be given by the following equation

$$FOMTP = \mathcal{L}(\omega_m) - 20log\left(\frac{\omega_0}{\omega_m}\frac{FBW}{10}\right) + 10log\left(P_{mWcore}\right) - P_{RFdBm} \qquad (7.9)$$

where P_{RFdBm} is RF output power value at resonance frequency given in dBm. Function (7.9) corresponds to the previously published FOM equations [128, 129] however, for unknown reasons, the authors did not include the fractional tuning range.

Both (7.8) and (7.9) yield negative values, expressed in dBc/Hz. The smaller the value the better the oscillator circuit i.e. state of the art architectures reach low phase noise, wide tuning ranges with small power consumption and high efficiency. Note that the $FOMT$ functions use phase noise level from the range where it falls by 20 dB/decade or 6 dB/octave (see Chapter 6 for more details). Thus, as authors cite phase noise levels at different offset frequencies, these can be easily recalculated to 1 MHz to normalise the results. Table 7.11 presents a comparison of active inductor oscillators published over the last decade. Phase noise levels are given for the center frequency of each circuit. Note that during thesis preparation, no other active inductor oscillator operating at 434 MHz was found in the available literature. The oscillators chosen for performance comparison are however similar in terms of $FOMT$ due to the fact that the increased power consumption term is compensated by higher frequency of operations and in many cases wide tuning range. In comparison with most of the circuits from Table 7.11, the $FOMT$ of the proposed circuit places it in the bottom of the benchmark list. This is caused by a relatively high phase noise and low frequency of operation. Most oscillators

Table 7.11: Benchmark of CMOS active inductor oscillators.

Publication	Year	Node μm	f_0 MHz	FBW %	P_{core} mW	P_{RF} dBm	PN@1MHz	FOMT dBc/Hz	FOMTP
Thanachayanont et al. [55]	2000	0.8	800	88.2	8.6	-0.5	-85	-152.6	-152.1
Zang et al. [130]	2003	0.35	2400	80	23.75	-20	-99	-170.9	-150.9
Foo et al. [131]	2004	0.18	5000	7	6.87	-3	-95	-157.5	-154.5
Ming et al. [122]	2004	0.25	2000	116	10	-10	-96	-173.3	-163.3
Mukhopadhyay et al. [80]	2005	0.18	1250	120	13.8	-20	-84	-160	-140
Chen et al. [132]	2005	0.18	4000	67.5	18.4	-18	-94	-170	-152
Lu et al. [73]	2006	0.18	1750	143	17	-12.5	-114	-189.7	-177.16
Laskar et al. [123]	2007	0.18	2550	98	5	-12	-94	-175	-163
Fillaud et al. [133]	2008	0.35	915	84	10	-38	-100	-167.7	-129.7
Mehrabian et al. [134]	2008	0.18	5600	64.3	29	–	-92	-168.5	–
Huang et al. [135]	2008	0.18	2750	65.5	21.6	–	-95	-166.8	–
Eun et al. [136]	2009	0.18	24000	11	20	-7	-112	-187.4	-180.4
This work	**2010**	**0.18**	**434**	**69.7**	**5.76**	**-2.75**	**-99.5**	**-161.5**	**-158.8**

however have much larger tuning ranges which translate to better (i.e. smaller) $FOMT$.

In the case of $FOMTP$, the degenerated gyrator achieves much better efficiency than two thirds of the listed circuits. This is due to the relatively large RF power which was extracted with a 3 dB loss in the output buffer. Note, that none of the cited papers revealed information on buffer structures or gains therefore in some cases the actual output power may be obtained by the use of power hungry gain stages. In addition, the authors do not provide any information about temperature and process variations and therefore one can't be sure about the behavior of these circuits under normal manufacturing conditions. Thus, the performance of the proposed circuit may be better since, as shown in this chapter, the process corners and temperature variations are not affecting phase noise, power and tuning range significantly.

7.10   434 MHz 90 nm NMOS OOK transmitter

The effect of negative resistance generation discussed in this thesis is independent of the given CMOS process. At the time of preparation of the thesis, the UMC 90 nm process libraries became available. This allowed us to confirm if the presented circuit can operate for a low supply voltage of 1 V and increased resistive losses of the transistors. This section presents a complete OOK (On-Off Keying) transmitter architecture able to achieve fast switching speeds. The OOK is historically the oldest type of electronic modulation, dating back to the nineteenth century and wire telegraphy. Although simple, OOK allows transmission of digital signals with relative ease thus it has become a popular choice for many applications where reliability and simplicity are required, for example biomedical applications [137–139]. The use of a degenerated active inductor oscillator as the fast OOK transmitter is possible because the parasitic capacitances of transistors are relatively small. As a result, the time necessary to charge these capacitors is relatively short. Thus, if the power supply is switched on the circuit reaches its steady state relatively fast. This in turn allows us to significantly increase the modulation speeds.
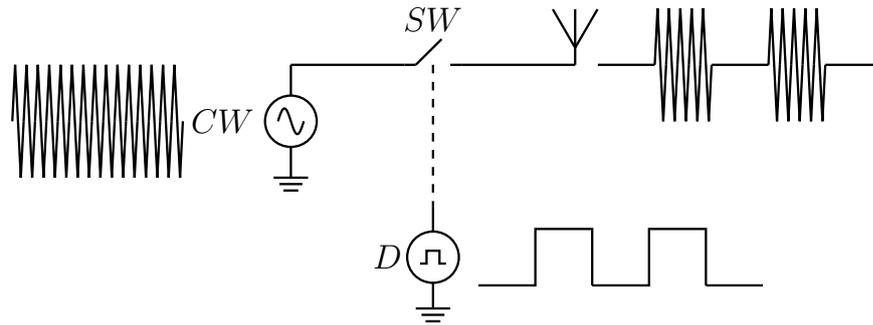
Figure 7.30: Generic architecture of OOK transmitter.

Figure 7.30 presents a generic model of such a transmitter, where the continuous wave from a signal generator is connected to the antenna through a digitally controlled switch. The information is encoded in a form of pulsed version of the oscillator signal at the carrier frequency. To minimise power dissipation, the OOK transmitter should not consume any energy during the off state, which in turn, requires fast transition times to support modulation with high data rates.

7.10.1 Transmitter architecture

Figure 7.31 depicts the proposed concept of the OOK transmitter designed using UMC 90 nm process libraries and the NMOS degenerated gyrator circuit. The circuit consists of three main components: bias network with switches; oscillator core; and a buffer amplifier with 50 Ω load. As previously, most of the transistors used are not minimum size devices due to the relatively poor A_{DC} of 90 nm devices.

7.10.1.1 Switched bias network

The switched bias network allows us to turn on and off the oscillator core and the output buffer. The transmitter is modulated using a binary signal and its inverted version through the inputs D and $\overline{D}$, respectively. A standard 1:1 current mirror topology provides a constant bias current to the oscillator core. Transistors M_8, M_9, M_{11} and M_{12} are used as transmission gates that deliver DC voltage for M_3 and M_6 current sources, respectively. M_7 and M_{10} eliminate charge stored in parasitic capacitances

Figure 7.31: Complete schematics of OOK transmitter.

during the off period. Switches M_{14} and M_{15} act as active loads for the amplifiers, whereas M_{18} and M_{19} form a switchable biasing network.

7.10.1.2   Output buffer

Due to the reduced power supply voltage available, amplitudes are much smaller than in the case of the 180 nm circuit described previously. The oscillator signal therefore has to be amplified. The buffer consists of three, class-A stages for improved linearity. DC blocking capacitors of 1 pF were chosen to minimise time constants during switching, allowing for faster transitions at the cost of a reduced output amplitude. As before, the input amplifier is a common drain voltage follower, providing high impedance load to the oscillator core. Switch M_{14} acts as a linear resistor during the *On* state, while the second stage compensates for losses in the non-ideal source followers. This is a common source amplifier with a switched PMOS linear resistor as a load. Finally, the output stage is a tuned voltage follower with passive LC tank to maximise voltage swing on a load resistor of 50 Ω. To avoid power dissipation due to a lossy inductor, its Q factor should be as large as possible, however its value is not as crucial from the RF signal perspective. The particular values of the LC tank components represent an optimised trade-off between peaking due to a rapid switching, signal distortion and response time. The total voltage gain of the amplifier in this example is set to 0 dB to avoid excessive distortion due to large signal operation of the oscillator.

7.10.2   Simulation results

As previously, the circuit has been simulated in Eldo RF using transient and frequency steady state simulations with noise. The oscillator core has been analysed in terms of typical parameters: carrier frequency, tuning range and phase noise. For the bias currents of 700 µA delivered to each of the transconductors, the core produces sinusoidal oscillations at 433.7 MHz with an amplitude of 200 mV, and an average start-up time of 3 ns. If necessary, the oscillator can be tuned from 382 MHz to 495 MHz. In comparison
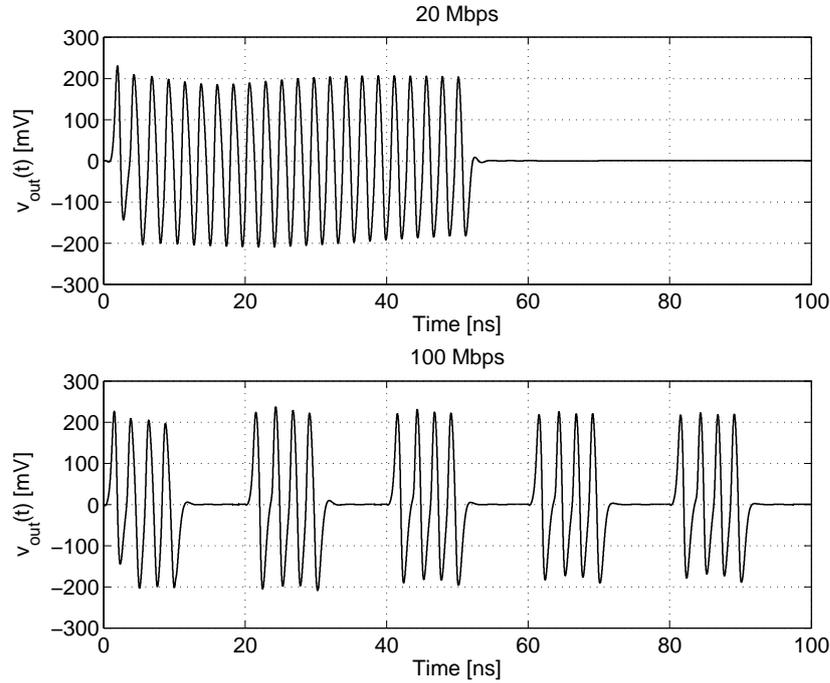
Figure 7.32: Simulated output voltage for 20 Mbps and 100 Mbps modulation speeds.

to the 180 nm circuit, the tuning range is smaller due to the larger mirrors, switching circuitry and the reduced A_{DC} of 90 nm transistors.

The phase noise at 1 MHz offset from 434 MHz signal reaches -96 dBc/Hz. The output amplifier allows delivery of -4 dBm of RF power to a 50 Ω load. Figure 7.32 presents the circuit response for square wave modulation signal with 50% duty cycle. Two modulation speeds were analysed: 20 Mbps and 100 Mbps. Power consumption of the transmitter can be broken down into the following: 7.96 mW for the output, class A amplifier, 1.4 mW for the bias network and 1.4 mW for the oscillator core from a 1 V power supply. Note that power consumption of the core is only 13% of the total DC power necessary to operate the whole transmitter.

7.10.3   Performance comparison

At the time of the thesis preparation no active inductor based OOK transmitter has been found in the available literature. Thus, the circuit performance is compared to the

236

transmitters using passive LC resonators and operating at relatively low RF frequencies. To achieve that, the figure of merit function is used, however now focusing on an average energy per transmitted bit rather than tuning range or phase noise of the oscillator used. This function is given by [140]

$$FOM_{OOK} = \frac{P_{DC}}{D_{rate} \cdot P_{RF}} \tag{7.10}$$

where P_{DC} is the DC power dissipation, D_{rate} is the data rate and P_{RF} is the output power of RF signal from the transmitter. For P_{DC} and P_{RF} expressed in mW, and D_{rate} is given in Mbps, (7.10) has units of nJ/bit/mW. Some authors also present the energy efficiency of the OOK transmitter in pJ/bit without a contribution of the signal power. Table 7.12 presents a comparative study of CMOS OOK transmitters found in recent publications.

It can be seen that, although the presented transmitter circuit consumes more power than the architectures using passive resonators, the obtained energy efficiency of 108 pJ/bit is in the same range. When the signal power is taken into account, the resulting figure of merit of 0.27 nJ/bit/mW makes the presented circuit an attractive alternative to large size area passive implementations.

As an example, consider the two previously published OOK transmitters operating at 434 MHz. The first circuit of Raja et al. [140] utilises an on-chip SAW-based LC tank oscillator and integrated buffer with off-chip resonant network. The authors report active area (without RF pads and routing) of $157.5{\cdot}10^{-3}$ mm^2 (525 µm by 300 µm). The second circuit of Ryu et al. [138] employs an off-chip 40 nH inductor. The reported chip are includes pads and routing; however the provided high quality photography allows us to estimate the active area of the chip as $160{\cdot}10^{-3}$ mm^2 (400 µm by 400 µm). In the case of the proposed degenerated gyrator transmitter, the active area can be estimated from Figure 7.31. To allow us a fair comparison, it is assumed that the wiring between components increases total active area by 50%. A passive LC tank used by the buffer is considered off-chip, as in the aforementioned publications. Thus, the estimated active size of the proposed OOK transmitter is equal to $11.5{\cdot}10^{-3}$ mm^2 (107 µm by 107 µm).

Table 7.12: Benchmark of CMOS OOK transmitters.

Publication	Year	Node	Resonator type	f_0	Data rate	P_{DC}	P_{RF}	FOM_{OOK}	Efficiency	Active area
		µm		MHz	Mbps	mW	mW	nJ/bit/mW	pJ/bit	mm²
Chee et al. [141]	2006	0.13	FBAR*	1900	0.157	1.8	1	11.46	11464	1.78[a]
Chee et al. [142]	2006	0.13	FBAR	1900	0.33	1.32	1.2	3.33	4000	0.98[a]
Daly et al. [143]	2007	0.18	SAW**	916	1	9.1	0.6	15.2	9100	0.27
Ryu et al. [138]	2007	0.18	passive LC	434	40	2.58	0.95	0.07	64	0.16
Raja et al. [140]	2008	0.35	SAW	434	10	0.518	0.054	0.96	52	0.157
Huang et al. [144]	2010	0.09	passive LC	2400	10	2.3	1	0.23	230	0.88[a]
Jung et al. [145]	2010	0.18	passive LC	2400	136	3	0.04	0.55	22	0.7
This work	**2010**	**0.09**	degenerated gyrator	**434**	**100**	**10.8**	**0.4**	**0.27**	**108**	**0.0115**

*- film bulk acoustic resonator, **- surface acoustic wave resonator, [a]- total chip area

It can be seen, that the degenerated gyrator with integrated buffer occupies less than 7.5% of the active area of the alternative transmitters operating at the same frequency, and using passive LC resonators. The additional advantage of the degenerated active inductor OOK transmitter is the fractional tuning bandwidth of 26%, typically larger than that of the most circuits from Table 7.12.

7.11 Chapter summary

This chapter presented a complete design of wideband CMOS degenerated gyrator oscillator. The results allow us to conclude that the proposed circuit architecture behaves as predicted mathematically in Chapters 4- 6. The main contributions of the chapter in relation with the practical oscillator design as follows:

- The complete design methodology of negative resistance oscillator. The design method is presented in a clear, step by step manner and can be applied to any oscillator circuit, not only one utilising an active inductor resonator. The process starts from a small signal characterisation of a resonator. In the case of the degenerated gyrator, the first step is the decision on the DC bias circuit. The proposed oscillator architecture is based on a well known CS-CD gyrator circuit which allows us to utilise a mutual bias of the devices using a feedback loop and current mirrors. After DC simulations, the methodology follows the circuit analysis under small and large signal conditions together with the process and temperature variations.

- The small signal (AC) analysis has been carried out to characterise the active inductor circuit. As predicted in Chapter 4, the use of a single RC phase shifter is sufficient to generate negative resistance high enough to start oscillations. Although the considered circuit had a more complex parasitic structure than initially assumed, the shape of the obtained plots confirms the main mechanisms were captured by the mathematical models. In this section a simple and intuitive method

of determining the resonant frequency of the tank was proposed and applied in practice.

- The large signal (SST) analysis has been used to confirm the non-linear behavior of the circuit. It was shown that harmonic distortion due to a signal build up, limits the oscillation amplitude through the compression of negative conductance. Due to these effects, the simulated inductance is expanded which causes the drop of the resonant frequency from its small signal value. Both effects have been predicted applying the Volterra kernels technique to the simple non-linear mathematical model of the degenerated gyrator from Chapter 5.

- The noise simulation conducted during the SST analysis illustrates that the LTI model proposed in Chapter 6 predicts a correct order of magnitude of phase noise in the degenerated gyrator. Although the linear time invariant approach to phase noise in oscillator circuit has a relatively low accuracy, it allows one to obtain a closed form solution indicating crucial parameters of the circuit and their contribution to the total phase noise of the oscillator.

- The chapter presents an analysis of the influence of process and temperature variations on the performance the proposed oscillator circuit. It was shown that most typical scenarios can be compensated through the bias current flowing to the oscillator core. The proposed circuit responds well to transistor process corners but can be prone to temperature and passive component variations. In the worst case, where RC components have smaller values than the nominal, the circuit can stop oscillating for smaller bias currents. This shows how important the process variations become in relation to the design process and should always be considered. Unfortunately this type of analysis is rarely presented in the literature on active inductor circuits, however this dissertation covers it thoroughly.

- At first, the presented circuit theory was confirmed using 180 nm process libraries. The obtained oscillator achieves a typical phase noise and tuning range perfor-

mance of active inductor VCO which was confirmed by the analysis of figure of merit functions for various state of the art, gyrator-based architectures.

- It was shown that the negative resistance can be generated in the same gyrator circuit designed using 90 nm CMOS process as well. As the presented circuit has small parasitic capacitances, the oscillator signal settles relatively fast after the power supply is switched on. As a result, it was shown that the degenerated oscillator is suitable to operate as an OOK transmitter with a high data rate modulation signal. In comparison to the state of the art CMOS OOK transmitters the proposed circuit is as efficient however consumes 3 to 10 times more DC power. The advantage however is its compact size (more than 90% reduction of active area) in comparison to the oscillators using SAW and FBAR resonators.

Chapter 8

Conclusion and future work

8.0.1 Conclusions

The invention of voltage controlled oscillators made radio transmission possible. Due to the rapid developments of various systems operating at different frequencies, it is important that a single oscillator is able to tune to a wide range of carrier frequencies. At the same time the oscillator has to have low phase noise, small power consumption and allow full on-chip integration, using the minimum area possible. Some of these requirements inherently contradict each other and for this reason it is important to study various solutions leading to the robust and versatile design of harmonic oscillators. One such technique involves the use of active inductors that although have limited performance in comparison to passive LC based VCOs, allow for a high degree of circuit integration.

This thesis presented a new design methodology for a self-oscillating active inductor, that reduces the oscillator circuit to the single resonant tank and does not require any external circuitry to compensate the circuit losses. This was achieved by the use of a simple passive RC network that when connected to the standard gyrator circuit, allows us to generate negative resistance. Although over the years, some active inductors with internally generated negative resistance have been published, little has been done to explore the fundamental properties of these circuits. Before this thesis there were no

known attempts to utilise this technique to obtain a wideband integrated VCO. We also provide the reader with a thorough explanation of the small signal behavior and noise, non-linear properties and phase noise of the circuit. This dissertation addresses these issues as follows:

1. **The minimum number of phase shifters required for oscillations in an active inductor.** It was shown that a single RC phase shifter is sufficient to produce negative resistance, large enough to compensate the circuit losses. It was proven that connecting this network at the input of the feedback transconductor allows us to obtain wide frequency range of operation whilst keeping the self-resonant frequency high.

2. **The sensitivity of the proposed circuit was studied.** In general, this topic is commonly omitted in the literature on any active inductor circuits, hence the conducted sensitivity analysis is a valuable contribution. It was shown that the finite tolerances of integrated RC networks cause the oscillator to operate at a different frequency than designed for however this can be compensated by fine-tuning of transconductances of the gyrator amplifiers.

3. **The effect of transistor losses was discussed.** It was illustrated how the finite output conductances of MOS devices reduce the tuning range of the proposed oscillator. For this reason it is important to use transconductance amplifiers with high gm to g_{out} ratio (DC gain). In the case of single MOS transconductors, devices with the minimum length allowed by the technology have poor DC gain values, resulting in increased losses and therefore are not optimal to use in the proposed oscillator circuit.

4. **The proposed linear model of the oscillator** allows us to confirm the oscillation criteria using a set of simple formulae. The expressions for the negative conductance and the resonant frequency have been found and analysed, showing

243

that the proposed oscillator can achieve very wide fractional bandwidth in the range of 70%.

5. **The noise of an active inductor with a RC shifter has been analysed.** A new set of formulae describing the noise behavior of the circuit confirmed that its noise is inversely proportional to the loaded quality factor of the gyrator based resonator. The presented analysis shows that low-pass characteristics of the RC circuit allows us to decrease the amount of noise it injects into the resonator.

6. **Thesis presented a new non-linear model of the proposed circuit**, derived using the known method of Volterra kernels. It was shown that due to the non-linear character of the transconductance amplifiers, the resulting harmonics are responsible for compression of negative conductance for large signal amplitudes. This conductance compression is the main mechanism of amplitude stabilisation observed in the proposed circuit. The same harmonic products are also responsible for the expansion of the simulated inductance and cause the oscillator to operate at a lower amplitude than expected from the small signal model.

7. **A new linear, time invariant phase noise model of the proposed circuit was derived.** Although simple, the model allows us to obtain a closed form solution, and to study possible ways to improve the phase noise of a practical circuit.

8. **The practical CMOS self-oscillating active inductor was designed and simulated** for different process and temperature variations. All of the theoretical findings presented in this dissertation were confirmed, proving their validity.

9. **A new fully integrated 434 MHz OOK transmitter circuit using the proposed oscillator was designed.** The circuit supports digital modulation speeds up to 100 Mbps with energy efficiency comparable to that of a standard passive LC oscillator circuit, but occupying only a fraction (7.5%) of its passive area, at the expense of a 3-5 more power consumption.

8.0.2 Future work

The future development of the presented technique requires an operating prototype that allows us to obtain empirical measurements. Recently, Medjahdi and Calmon [146] presented a 0.25 μm CMOS development of the self-oscillating circuit of Szczepkowski et al. [125], showing post-layout simulation results, matching the theory presented in this thesis. Authors reported the fractional tuning range of 60%, with core power consumption of 13 mW and phase noise level of -93 dBc/Hz at 1 MHz offset from the carrier. Silicon prototypes are expected for characterisation from this work.

The performance of the proposed oscillator circuit could be further improved if less noise was introduced by the transistors. This in turn implies the use of bipolar transistors. In recent publication of Rohde and Poddar [147] presented an implementation of a 5 GHz standard, two transistor active inductor oscillator using discrete BJT devices. The measured phase noise is better than 105 dBc/Hz at 100 kHz offset from the carrier frequency form from 3 V power supply, thus matching that of fully integrated oscillators with spiral active inductors. This would suggest a profitable avenue for further development for our circuit architecture.

Appendix

88-108 MHz integrated VCO

A.1 Introduction

To show that PMOS transistors can be also employed, a VCO for a 88 MHz-108 MHz radio broadcast system is presented. At these frequencies, a sinusoidal oscillator with passive LC tank is not practical due to its size. Assuming a center frequency of 98 MHz and tank capacitance in the range of 10 pF, inductance in the range of 270 nH is required. This is 20 times more than the largest spiral inductor in 180 nm process can provide. To save space, a passive LC oscillator can be designed at high frequency where LC values can be integrated. The frequency is then decreased using a cascade of power hungry frequency dividers. Designing oscillator at 1 GHz, a division ratio of 10 would be required. The drawback is a significant power dissipation.

The degenerated gyrator presented in this thesis combines a compact size with a relatively small power consumption and its suitable for low voltage design. Figure A.1 depicts complete oscillator circuit that consists of the oscillator core, voltage tuned bias mirrors, output amplifier and integrated tank capacitance. Each block is described in more detail in following subsections. The circuit is another version of the basic oscillator depicted on Figure 7.24. The following modifications were made:

- All transistors were changed to their complementary devices. The same voltage bias scheme (Figure 7.2) is used.

- The reference current I_B is generated by NMOS voltage tuned resistors.

- The oscillator output buffer is now the CS amplifier, providing signal gain to the capacitive load. The buffer is connected to the *gyr_in* node.

A.2 Oscillator core

The core consists of four devices, where M_7 and M_8 are CS and CD transconductors, respectively. Transistors M_9 and M_{10} provide constant bias current. As the bias scheme is the same as from Section 7.3, gate voltages of each device are in the range of 600 mV to 700 mV. As inductance is inversely proportional to gm^2, a the transconductance in the range of 6 mA/V is required. Thus, PMOS transistors are more than two times larger than their NMOS counterparts. Both transconductors consists of 6 devices of 6 fingers each with 6 µm per finger for CS amplifier and 7 µm per finger for CD device. The phase shifter consists of 6.5 kΩ RF resistor and two 0.34 pF MIM capacitors.

A.3 Voltage tuned bias mirrors

To construct the VCO, a tuning voltage has to be converted to a current driving both mirrors. If a single transistor is used, its transconductance is too high for the given overdrive and reference current. As a result, only a fraction of possible tuning voltage range can be utilised, resulting in very large tuning constant.

This problem can be resolved using current bypass devices. Transistors M_3 and M_5 act as resistors sinking current I_C from the mirrors. Transistors M_4 and M_5 act as voltage to current converters, carrying current $I_{tune} < I_C$. As a result, total bias current $I_B = I_C + I_{tune}$, and since I_C is constant, mirrors are tuned only with a fraction of total reference current. The tuning voltage spans now from V_{th} to V_{DD}.

A.4 Output amplifier and tank capacitance

Oscillator is designed to drive a mixer and load is capacitive. As described previously, common source inverting buffer is more suitable to drive such loads, however due to larger input capacitance it has to be connected to the output of CD transconductor. This port produces relatively low amplitude and the output buffer provides gain to boost the signal. The power consumption of buffer is less than 14 mW from 1.8 V supply.

Figure A.2 depicts the circuit. To minimise Miller capacitance, a tuned RF cascode is used where the top transistor acts as common gate amplifier. The top resistor sets the quality factor of the tank. L_s is an off-chip inductor in the range of 1 µH to 10 µH. The exact value depends on the load capacitance and hence, input impedance of mixer has to be characterised *a priori*. Buffer voltage gain is equal to 5. The capacitance of 10 pF is realised of two 70 µm by 70 µm MIM capacitors connected in parallel.

A.5 Simulation results

Figure A.3 shows the tuning curve of the oscillator as a function of tuning voltage V_{Tune}. The tuning range spans between 84 MHz and 116 MHz for V_{Tune} of 0.5 V and 1.8 V, respectively. Non-linear behavior at small tuning voltages is caused by the voltage to current converters (M_4, M_5) reaching their cut-off point. For the centre frequency of 98 MHz, fractional bandwidth of 33% is obtained. Phase noise at 1 MHz offset from the center frequency is equal to 104.8 dBc/Hz and the maximum power consumption of the core is only 1.37 mW. FOMT of -153.6 dBc/Hz is caused by relatively high phase noise level at this low RF frequency. FOMTP can not be calculated as reactive loads do not receive real power. Despite the high phase noise, the circuit produces amplitudes exceeding 620 mV at 1 pF load (Figure A.4) which are sufficient to drive mixer in a large signal regime.
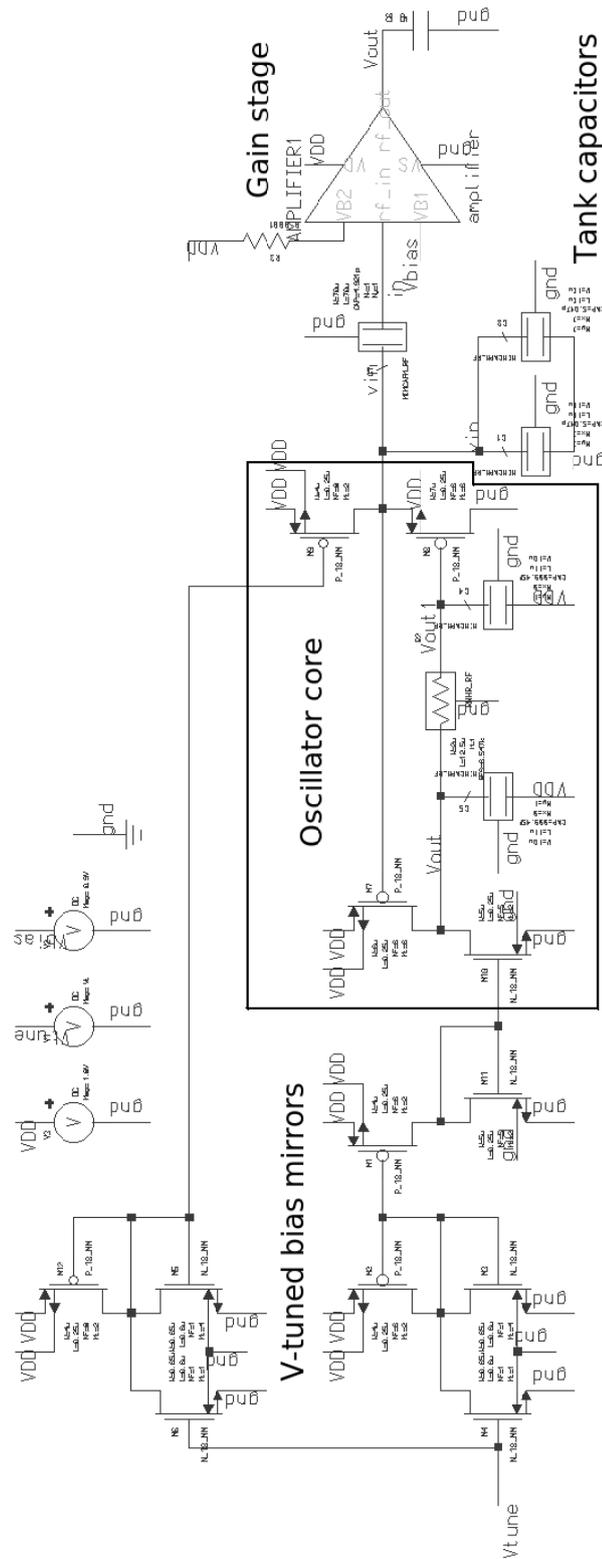
Figure A.1: Complete PMOS oscillator circuit.
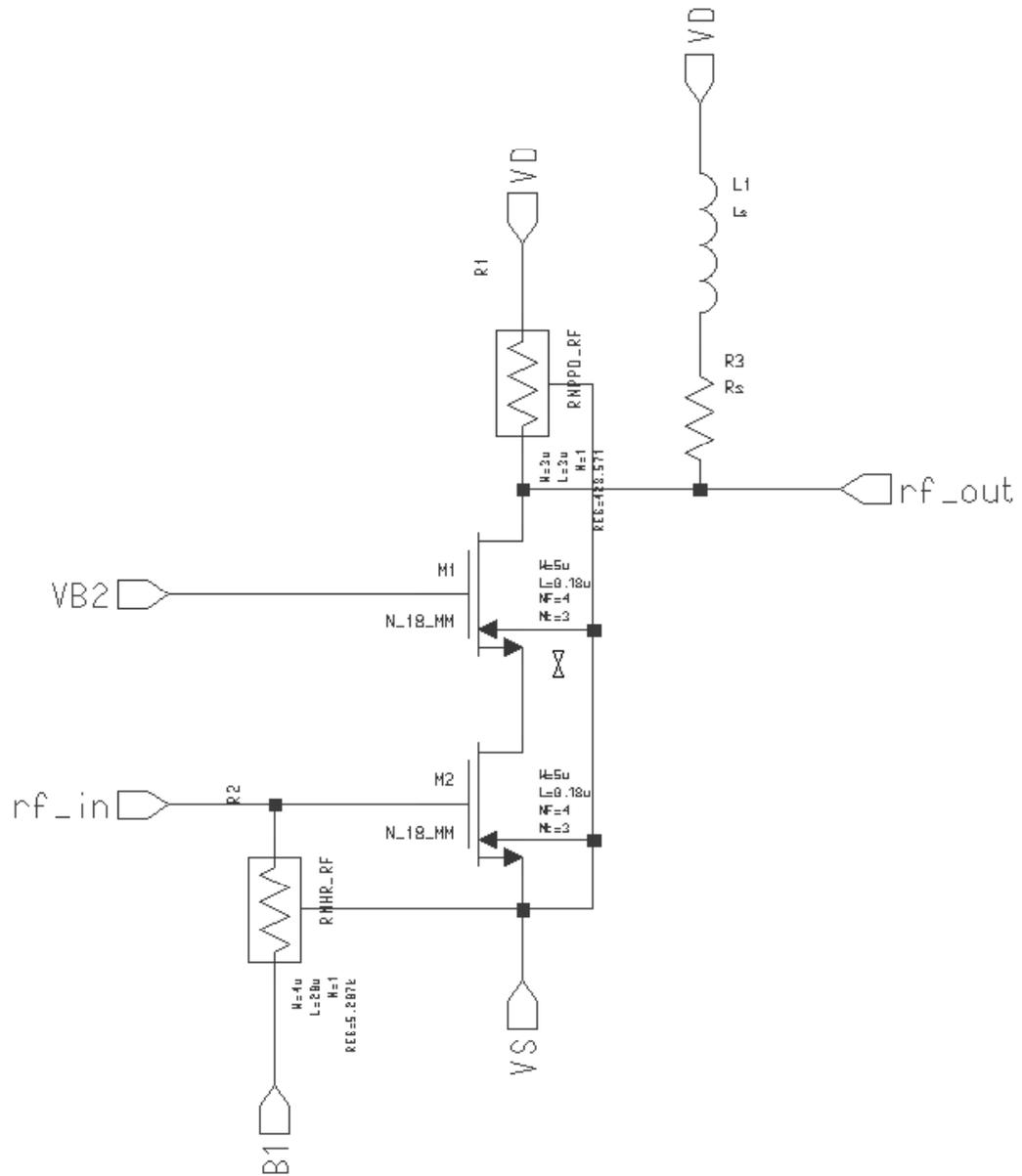
Figure A.2: NMOS tuned cascode output buffer.
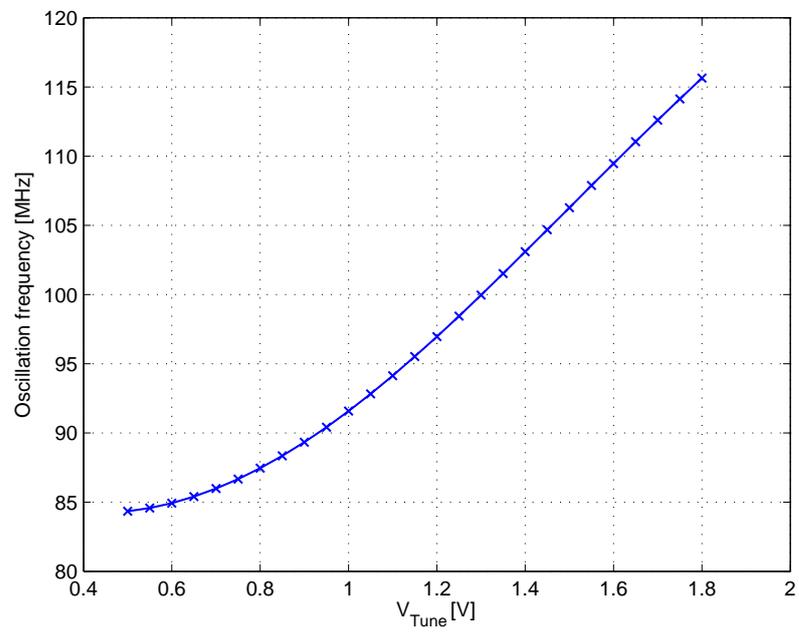
Figure A.3: Simulated tuning curve of PMOS oscillator.
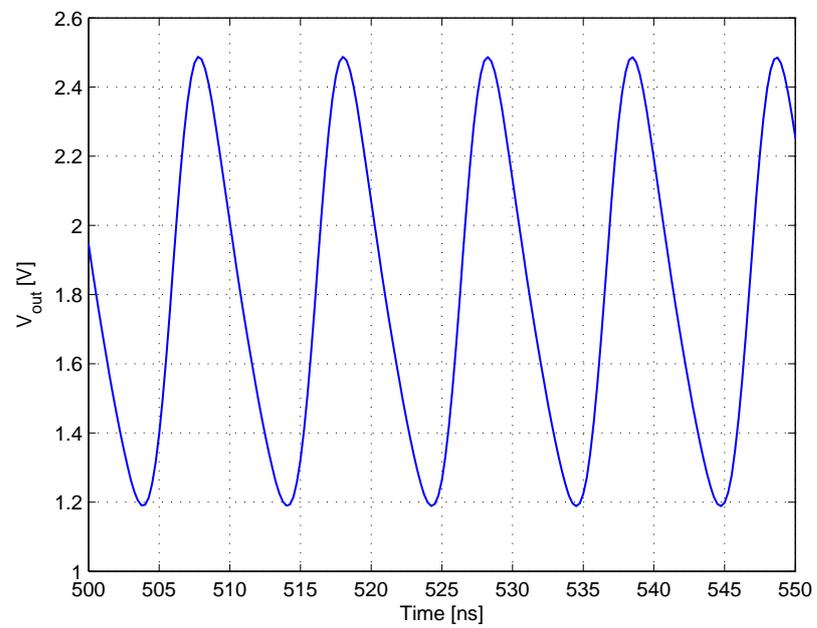
Figure A.4: Simulated output voltage at 98 MHz and 1 pF load.

References

[1] K. H. Lundberg, "Barkhausen stability criterion," http://web.mit.edu/klund/ www/weblatex/node4.html, 2002, Acessed Mar. 2010.

[2] J. C. G. Lesurf, "Oscillators," http://www.st-andrews.ac.uk/~www_pa/Scots_ Guide/RadCom/part4/page1.html, 2006, Acessed Mar. 2010.

[3] E. B. Craft and E. H. Colpitts, "Radio Telephony," *American Institute of Electrical Engineers, Transactions of the*, vol. XXXVIII, no. 1, pp. 305–343, Jan. 1919.

[4] "Gunn diode," http://en.wikipedia.org/wiki/Gunn_diode, 2010, Acessed Jun. 2010.

[5] T. Al-Attar and T. Lee, "Monolithic integrated millimeter-wave IMPATT transmitter in standard CMOS technology," *Microwave Theory and Techniques, IEEE Transactions on*, vol. 53, no. 11, pp. 3557–3561, Nov. 2005.

[6] R. J. Collin, "Hybrid tunnel diodes could leapfrog Moores Law," http://www. eetimes.com/story/OEG20031027S0055, March 2007, Accessed March, 2010.

[7] R. Kaunisto, "Monolithic active resonator fitlers for high frequencies," Ph.D. dissertation, Helsinki Univerity of Technology, Nov. 2000.

[8] D. Ham and A. Hajimiri, "Concepts and methods in optimization of integrated LC VCOs," *Solid-State Circuits, IEEE Journal of*, vol. 36, no. 6, pp. 896–909, Jun. 2001.

[9] M. Tiebout, "Low-power low-phase-noise differentially tuned quadrature VCO design in standard CMOS," *Solid-State Circuits, IEEE Journal of*, vol. 36, no. 7, pp. 1018–1024, Jul. 2001.

[10] F. Herzel, H. Erzgraber, and P. Weger, "Integrated CMOS wideband oscillator for RF applications," *Electronics Letters*, vol. 37, no. 6, pp. 330–331, Mar. 2001.

[11] P. Andreani, A. Bonfanti, L. Romano, and C. Samori, "Analysis and design of a 1.8-GHz CMOS LC quadrature VCO," *Solid-State Circuits, IEEE Journal of*, vol. 37, no. 12, pp. 1737–1747, Dec. 2002.

[12] N. Da Dalt, S. Derksen, P. Greco, C. Sandner, H. Schmid, and K. Strohmayer, "A fully integrated 2.4-GHz LC-VCO frequency synthesizer with 3-ps jitter in 0.18um standard digital CMOS copper technology," *Solid-State Circuits, IEEE Journal of*, vol. 37, no. 7, pp. 959–962, Jul. 2002.

[13] C. De Ranter, G. Van der Plas, M. Steyaert, G. Gielen, and W. Sansen, "CY-CLONE: automated design and layout of RF LC-oscillators," *Computer-Aided Design of Integrated Circuits and Systems, IEEE Transactions on*, vol. 21, no. 10, pp. 1161–1170, Oct. 2002.

[14] N. Fong, J.-O. Plouchart, N. Zamdmer, D. Liu, L. Wagner, C. Plett, and N. Tarr, "A 1-V 3.8 - 5.7-GHz wide-band VCO with differentially tuned accumulation MOS varactors for common-mode noise rejection in CMOS SOI technology," *Microwave Theory and Techniques, IEEE Transactions on*, vol. 51, no. 8, pp. 1952–1959, Aug. 2003.

[15] A. Berny, A. Niknejad, and R. Meyer, "A 1.8-GHz LC VCO with 1.3-GHz tuning range and digital amplitude calibration," *Solid-State Circuits, IEEE Journal of*, vol. 40, no. 4, pp. 909–917, Apr. 2005.

[16] H. Higashi, S. Masaki, M. Kibune, S. Matsubara, T. Chiba, Y. Doi, H. Yamaguchi, H. Takauchi, H. Ishida, K. Gotoh, and H. Tamura, "A 5-6.4-Gb/s 12-channel

transceiver with pre-emphasis and equalization," *Solid-State Circuits, IEEE Journal of*, vol. 40, no. 4, pp. 978–985, Apr. 2005.

[17] D. Hauspie, E.-C. Park, and J. Craninckx, "Wideband VCO with simultaneous switching of frequency band, active core, and varactor size," *Solid-State Circuits, IEEE Journal of*, vol. 42, no. 7, pp. 1472–1480, Jul. 2007.

[18] S. Broussev, T. Lehtonen, and N. Tchamov, "A wideband low phase-noise LC-VCO with programmable KVCO," *Microwave and Wireless Components Letters, IEEE*, vol. 17, no. 4, pp. 274–276, Apr. 2007.

[19] M. Demirkan, S. Bruss, and R. Spencer, "Design of wide tuning-range CMOS VCOs using switched coupled-inductors," *Solid-State Circuits, IEEE Journal of*, vol. 43, no. 5, pp. 1156–1163, May 2008.

[20] J. Gonzalez, F. Badets, B. Martineau, and D. Belot, "A 56-GHz LC-tank VCO with 17% tuning range in 65-nm bulk CMOS for wireless HDMI," *Microwave Theory and Techniques, IEEE Transactions on*, vol. 58, no. 5, pp. 1359–1366, May 2010.

[21] S. Zhang, W. Su, and M. Zaghloul, "Low noise multi-band voltage controlled oscillator using MEMS technology," in *Circuits and Systems, 2007. MWSCAS 2007. 50th Midwest Symposium on*, Aug. 2007, pp. 477–481.

[22] J. Sankaranarayanan and K. Mayaram, "Noise simulation and modeling for MEMS varactor based RF VCOs," in *Circuits and Systems, 2007. ISCAS 2007. IEEE International Symposium on*, May 2007, pp. 2698–2701.

[23] O. Casha, I. Grech, J. Micallef, E. Gatt, D. Morche, B. Viala, J. Michel, P. Vincent, and E. de Foucauld, "Utilization of MEMS tunable inductors in the design of RF voltage-controlled oscillators," in *Electronics, Circuits and Systems, 2008. ICECS 2008. 15th IEEE International Conference on*, Aug. 2008, pp. 718–721.

[24] B. Sreeja and S. Radha, "Design and implementation of MEMS based differential voltage controlled oscillator," in *Electro/Information Technology, 2009. eit '09. IEEE International Conference on*, Jun. 2009, pp. 202–206.

[25] A. M. Semiconductor, "Varactor diode tutorial," http://www.americanmicrosemi. com/information/tutorial/index.php?t_id=15, 2004, Acessed Mar. 2010.

[26] B. Razavi, *RF Microelectronics*. Englewood Cliffs: Prentice Hall, 1998.

[27] R. J. Baker, *CMOS Circuit Design, Layout, and Simulation*. New York: IEEE Press, 1998.

[28] U. Rohde, A. K. Poddar, and G. Boeck, *The Design of Modern Microwave Oscillators for Wireless Applications*. London: J. Wiley, 2005.

[29] A. Bonfanti, S. Levantino, C. Samori, and A. Lacaita, "A varactor configuration minimizing the amplitude-to-phase noise conversion in VCOs," *Circuits and Systems I: Regular Papers, IEEE Transactions on*, vol. 53, no. 3, pp. 481–488, Mar. 2006.

[30] E. Hegazi and A. A. Abidi, "Varactor characteristics, oscillator tuning curves, and AM-FM conversion," *IEEE Journal of Solid-State Circuits*, vol. 38, no. 6, pp. 1033–1039.

[31] M. D. Wei, S. F. Chang, and Y. J. Yang, "A CMOS backgate-coupled QVCO based on back-to-back series varactor configuration for minimal AM-to-PM noise conversion," *Microwave and Wireless Components Letters, IEEE*, vol. 19, no. 5, pp. 320–322, May 2009.

[32] T. Lee, *The Design of CMOS Radio-Frequency Integrated Circuits*. Cambridge: Cambridge University Press, 2004.

[33] C. Yue and S. Wong, "On-chip spiral inductors with patterned ground shields for Si-based RF ICs," *Solid-State Circuits, IEEE Journal of*, vol. 33, no. 5, pp. 743–752, May 1998.

[34] J. Craninckx and M. Steyaert, "A 1.8-GHz CMOS low-phase-noise voltage-controlled oscillator with prescaler," *Solid-State Circuits, IEEE Journal of*, vol. 30, no. 12, pp. 1474–1482, Dec. 1995.

[35] F. Svelto, S. Deantoni, and R. Castello, "A 1 mA, -120.5 dBc/Hz at 600 kHz from 1.9 GHz fully tuneable LC CMOS VCO," in *Custom Integrated Circuits Conference, 2000. CICC. Proceedings of the IEEE 2000*, May 2000, pp. 577–580.

[36] W. De Cock and M. Steyaert, "A CMOS 10GHz voltage controlled LC-oscillator with integrated high-Q inductor," in *Solid-State Circuits Conference, 2001. ESSCIRC 2001. Proceedings of the 27th European*, Sept. 2001, pp. 498–501.

[37] Z. Li and K. O, "A 900-MHz 1.5-V CMOS voltage-controlled oscillator using switched resonators with a wide tuning range," *Microwave and Wireless Components Letters, IEEE*, vol. 13, no. 4, pp. 137–139, Apr. 2003.

[38] H. Kao, D. Yang, Y. Chang, B. Lin, and C. Kao, "Switched resonators using adjustable inductors in 2.4/5 GHz dual-band LC VCO," *Electronics Letters*, vol. 44, no. 4, pp. 299–300, Feb. 2008.

[39] H. Booker, *Energy in Electromagnetism*. Stevenage: Peter Peregrinus on behalf of the Institution of Electrical Engineers, 1982.

[40] Coilcraft Inc., http://www.coilcraft.com/0603ct.cfm?a, 2010, Acessed Sept. 2010.

[41] F. Gardner, *Phaselock Techniques*. New York: Wiley-Interscience, 2005.

[42] M. H. Perrot, "Noise in voltage controlled oscillators (lecture notes)," http://ocw.mit.edu/courses/electrical-engineering-and-computer-science/ 6-776-high-speed-communication-circuits-spring-2005/lecture-notes/lec17.pdf, 2005, Acessed Jun. 2010.

[43] P. Gray, P. Hurst, S. Lewis, and R. Meyer, *Analysis and Design of Analog Integrated Circuits*. New York: Wiley, 2008.

[44] B. Razavi, *Design of Analog CMOS Integrated Circuits.* New York: McGraw-Hill, 2001.

[45] A. Hajimiri and T. Lee, "Phase noise in CMOS differential LC oscillators," in *VLSI Circuits, 1998. Digest of Technical Papers. 1998 Symposium on*, Jun. 1998, pp. 48–51.

[46] A. A. Abidi, "Noise in active resonators and the available dynamic range," *IEEE Transactions on Circuits and Systems I: Fundamental Theory and Applications*, vol. 39, no. 4, pp. 296–299.

[47] J. Craninckx and M. Steyaert, "Low-noise voltage-controlled oscillators using enhanced LC-tanks," *IEEE Transactions on Circuits and Systems II: Analog and Digital Signal Processing*, vol. 42, no. 12, pp. 794–804.

[48] B. D. H. Tellegen, "The gyrator: a new electric network element," *Phillips Research Reports*, no. 3, pp. 81–101, 1948.

[49] J. B. Calvert, "Reciprocity," http://mysite.du.edu/~jcalvert/tech/reciproc.htm, 2003, acessed Jun. 2010.

[50] A. Filipkowski, *Uklady Elektroniczne Analogowe i Cyfrowe.* Warsaw: Wydawnictwa Naukowo-Techniczne, 2006.

[51] F. Yuan, *CMOS Active Inductors and Transformers.* Berlin: Springer, 2008.

[52] M. Ismail, R. Wassenaar, and W. Morrison, "A high-speed continuous-time bandpass VHF filter in MOS technology," in *Circuits and Systems, 1991., IEEE International Sympoisum on*, vol. 3, Jun. 1991, pp. 1761–1764.

[53] Y. Wu, M. Ismail, and H. Olsson, "CMOS VHF/RF CCO based on active inductors," *Electronics Letters*, vol. 37, no. 8, pp. 472–473.

[54] H. Xiao, R. Schaumann, W. R. Daasch, P. K. Wong, and B. Pejcinovic, "A radio-frequency CMOS active inductor and its application in designing high-Q filters,"

in *Circuits and Systems, 2004. ISCAS '04. Proceedings of the 2004 International Symposium on*, vol. 4, pp. 197–200.

[55] A. Thanachayanont and A. Payne, "Cmos floating active inductor and its applications to bandpass filter and oscillator designs," *Circuits, Devices and Systems, IEE Proceedings -*, vol. 147, no. 1, pp. 42–48, Feb. 2000.

[56] T. Y. K. Lin and A. J. Payne, "Design of a low-voltage, low-power, wide-tuning integrated oscillator," in *Circuits and Systems, 2000. Proceedings. ISCAS 2000 Geneva. The 2000 IEEE International Symposium on*, vol. 5, Geneva, pp. 629–632.

[57] E. Sackinger and W. C. Fischer, "A 3-GHz 32-dB CMOS limiting amplifier for SONET OC-48 receivers," in *Solid-State Circuits, IEEE Journal of*, vol. 35, no. 12, San Francisco, CA, pp. 1884–1888.

[58] M. Grozing, A. Pascht, and M. Berroth, "A 2.5 V CMOS differential active inductor with tunable L and Q for frequencies up to 5 GHz," in *Microwave Symposium Digest, 2001 IEEE MTT-S International*, vol. 1, Phoenix, AZ, pp. 575–578.

[59] Y. Wu, X. Ding, M. Ismail, and H. Olsson, "RF bandpass filter design based on CMOS active inductors," *IEEE Transactions on Circuits and Systems II: Analog and Digital Signal Processing*, vol. 50, no. 12, pp. 942–949.

[60] ——, "Inductorless CMOS RF bandpass filter," *Electronics Letters*, vol. 37, no. 16, pp. 1027–1029.

[61] A. Thanachayanont, "Low-voltage low-power high-Q CMOS RF bandpass filter," *Electronics Letters*, vol. 38, no. 13, pp. 615–616.

[62] H. Xiao and R. Schaumann, "Very-high-frequency lowpass filter based on a CMOS active inductor," in *Circuits and Systems, 2002. ISCAS 2002. IEEE International Symposium on*, vol. 2, Phoenix-Scottsdale, AZ, pp. 1–4.

[63] L.-H. Lu, Y.-T. Liao, and C.-R. Wu, "A miniaturized Wilkinson power divider with CMOS active inductors," *IEEE Microwave and Wireless Components Letters*, vol. 15, no. 11, pp. 775–777.

[64] K. H. Liang, C. C. Ho, C. W. Kuo, and Y. J. Chan, "CMOS RF band-pass filter design using the high quality active inductor," *IEICE Transactions on Electronics*, vol. 88, no. 12, pp. 2372–2376, Dec. 2005.

[65] Z. Gao, M. Yu, Y. Ye, and J. Ma, "Wide tuning range of a CMOS RF bandpass filter for wireless applications," in *Electron Devices and Solid-State Circuits, 2005 IEEE Conference on*, 19-21 2005, pp. 53–56.

[66] Z. Gao, J. Ma, M. Yu, and Y. Ye, "A CMOS RF tuning wide-band bandpass filter for wireless applications," in *SOC Conference, 2005. Proceedings. IEEE International*, Herndon, VA, pp. 79–80.

[67] ——, "A CMOS RF bandpass filter based on the active inductor," in *ASIC, 2005. ASICON 2005. 6th International Conference On*, vol. 2, Shanghai, pp. 603–606.

[68] J. Chen, F. Saibi, J. Lin, and K. Azadet, "Electrical backplane equalization using programmable analog zeros and folded active inductors," *IEEE Transactions on Microwave Theory and Techniques*, vol. 55, no. 7, pp. 1459–1466.

[69] L.-H. Lu and Y.-T. Liao, "A 4-GHz phase shifter MMIC in 0.18um CMOS," *IEEE Microwave and Wireless Components Letters*, vol. 15, no. 10, pp. 694–696.

[70] F. Mahmoudi and C. A. T. Salama, "8 GHz tunable CMOS quadrature generator using differential active inductors," in *Circuits and Systems, 2005. ISCAS 2005. IEEE International Symposium on*, pp. 2112–2115.

[71] J. Jiang and F. Yuan, "A new CMOS current-mode multiplexer for 10GB/s serial links," in *Electrical and Computer Engineering, 2004. Canadian Conference on*, vol. 3, pp. 1665–1668.

[72] F. Yuan, "A modified Park-Kim voltage-controlled ring oscillator for multi-Gbps serial links," *Analog Integr. Circuits Signal Process.*, vol. 47, no. 3, pp. 345–353, May 2006.

[73] L.-H. Lu, H.-H. Hsieh, and Y.-T. Liao, "A wide tuning-range CMOS VCO with a differential tunable active inductor," *IEEE Transactions on Microwave Theory and Techniques*, vol. 54, no. 9, pp. 3462–3468.

[74] H. Xiao and R. Schaumann, "A 5.4-GHz high-Q tunable active-inductor bandpass filter in standard digital CMOS technology," *Analog Integrated Circuits and Signal Processing*, vol. 51, pp. 1–9, Apr. 2007, 10.1007/s10470-007-9040-1.

[75] R. M. Weng and R. C. Kuo, "An Q tunable CMOS active inductor for RF bandpass filters," in *Signals, Systems and Electronics, 2007. ISSSE '07. International Symposium on*, Montreal, QC, pp. 571–574.

[76] A. Tang, F. Yuan, and E. Law, "A new CMOS active transformer QPSK modulator with optimal bandwidth control," *IEEE Transactions on Circuits and Systems II: Express Briefs*, vol. 55, no. 1, pp. 11–15.

[77] ——, "Class AB CMOS active transformer voltage-controlled oscillators," in *Signals, Systems and Electronics, 2007. ISSSE '07. International Symposium on*, Montreal, Que., pp. 501–504.

[78] Y. T. Wang and A. A. Abidi, "CMOS active filter design at very high frequencies," *IEEE Journal of Solid-State Circuits*, vol. 25, no. 6, pp. 1562–1574.

[79] L.-H. Lu, H.-H. Hsieh, and Y.-T. Liao, "A wide tuning-range CMOS VCO with a differential tunable active inductor," *IEEE Transactions on Microwave Theory and Techniques*, vol. 54, no. 9, pp. 3462–3468.

[80] R. Mukhopadhyay, Y. Park, P. Sen, N. Srirattana, J. Lee, C. H. Lee, S. Nuttinck, A. Joseph, J. Cressler, and J. Laskar, "Reconfigurable RFICs in Si-based technolo-

gies for a compact intelligent RF front-end," *Microwave Theory and Techniques, IEEE Transactions on*, vol. 53, no. 1, pp. 81–93, Jan. 2005.

[81] H. Xiao and R. Schaumann, "A low-voltage low-power CMOS 5-GHz oscillator based on active inductors," in *Electronics, Circuits and Systems, 2002. 9th International Conference on*, vol. 1, pp. 231–234.

[82] A. Tang, F. Yuan, and E. Law, "Low-noise CMOS active transformer voltage-controlled oscillators," in *Circuits and Systems, 2007. MWSCAS 2007. 50th Midwest Symposium on*, Montreal, Que., pp. 1441–1444.

[83] K. Moulding, "Fully integrated selectivity at high frequency using gyrators," *Broadcast and Television Receivers, IEEE Transactions on*, vol. BTR-19, no. 3, pp. 176–180, Aug. 1973.

[84] K. W. Moulding and G. A. Wilson, "A fully integrated 5 gyrator filter at video frequencies," in *Solid State Circuits Conference ESSCIRC '77. 3rd European*, Ulm, F.R. Germany, 1977, pp. 148–151.

[85] S. Hara, T. Tokumitsu, T. Tanaka, and M. Aikawa, "Broad-band monolithic microwave active inductor and its application to miniaturized wide-band amplifiers," *IEEE Transactions on Microwave Theory and Techniques*, vol. 36, no. 12, pp. 1920–1924.

[86] S. Hara, T. Tokumitsu, and M. Aikawa, "Lossless broad-band monolithic microwave active inductors," *IEEE Transactions on Microwave Theory and Techniques*, vol. 37, no. 12, pp. 1979–1984.

[87] S. Lucyszyn and I. D. Robertson, "Monolithic narrow-band filter using ultrahigh-Q tunable active inductors," *IEEE Transactions on Microwave Theory and Techniques*, vol. 42, no. 12, pp. 2617–2622.

[88] R. Kaunisto, P. Alinikula, K. Stadius, and V. Porra, "A low-power HBT MMIC filter based on tunable active inductors," *IEEE Microwave and Guided Wave Letters*, vol. 7, no. 8, pp. 209–211.

[89] H. Hayashi, M. Muraguchi, Y. Umeda, and T. Enoki, "A novel loss compensation technique for high-Q broad-band active inductors," in *Microwave and Millimeter-Wave Monolithic Circuits Symposium, 1996. Digest of Papers., IEEE 1996*, San Francisco, CA, pp. 103–106.

[90] ——, "A high-Q broad-band active inductor and its application to a low-loss analog phase shifter," *Microwave Theory and Techniques, IEEE Transactions on*, vol. 44, no. 12, pp. 2369–2374, Dec. 1996.

[91] W. Li, B. L. Ooi, Q. J. Xu, and P. S. Kooi, "High Q active inductor with loss compensation by feedback network," *Electronics Letters*, vol. 35, no. 16, pp. 1328–1329.

[92] M. U. Nair, Y. J. Zheng, and Y. Lian, "1 V, 0.18um area and power efficient UWB LNA utilising active inductors," *Electronics Letters*, vol. 44, no. 19, pp. 1127–1129.

[93] R. Kaunisto, K. Stadius, and V. Porra, "A 3 GHz silicon-BJT active resonator and filter," in *Electronics, Circuits and Systems, 1998 IEEE International Conference on*, vol. 3, Lisboa, pp. 197–200.

[94] U. Yodprasit and J. Ngarmnil, "Q-enhancing technique for RF CMOS active inductor," in *Circuits and Systems, 2000. Proceedings. ISCAS 2000 Geneva. The 2000 IEEE International Symposium on*, vol. 5, Geneva, pp. 589–592.

[95] A. A. Abidi, "Noise in active resonators and the available dynamic range," *IEEE Transactions on Circuits and Systems I: Fundamental Theory and Applications*, vol. 39, no. 4, pp. 296–299, Apr. 1992.

[96] MathWorks, "Matlab documentation centre," http://www.mathworks.com/help/techdoc, 2010, acessed Mar. 2010.

[97] A. Sedra and K. C. Smith, *Microelectronic Circuits*. Oxford, Oxfordshire: Oxford University Press, 1998.

[98] K. Manetakis, S.-M. Park, A. Payne, S. Setty, A. Thanachayanont, and C. Toumazou, "Wideband CMOS analog cells for video and wireless communications," in *Wideband Circuits, Modelling and Techniques, IEE Colloquium on*, May 1996, pp. 6/1–6/10.

[99] C.-C. Hsiao, C.-W. Kuo, C.-C. Ho, and Y.-J. Chan, "Improved quality-factor of 0.18um CMOS active inductor by a feedback resistance design," *Microwave and Wireless Components Letters, IEEE*, vol. 12, no. 12, pp. 467–469, Dec. 2002.

[100] A. Ilker Karsilayan and R. Schaumann, "A high-frequency high-Q CMOS active inductor with DC bias control ," in *Circuits and Systems, 2000. Proceedings of the 43rd IEEE Midwest Symposium on*, vol. 1, Aug. 2000, pp. 486–489.

[101] H. Uyanik and N. Tarim, "Compact low voltage high-Q CMOS active inductor suitable for RF applications," *Analog Integrated Circuits and Signal Processing*, vol. 51, pp. 191–194, 2007.

[102] G. Szczepkowski and R. Farrell, "Noise and dynamic range of CMOS degenerated active inductor resonators," in *Circuit Theory and Design, 2009. ECCTD 2009. European Conference on*, Antalya, 2009, pp. 595–598.

[103] P. Wambacq and W. Sansen, *Distortion Analysis of Analog Integrated Circuits*. Boston: Kluwer Academic, 1998.

[104] H. Jardón-Aguilar, G. M. Galván-Tejada, and J. A. Tirado-Méndez, "Amplitude estimation for near-sinusoidal oscillators by using a modified Barkhausen criterion: Research Articles," *Int. J. RF Microw. Comput.-Aided Eng.*, vol. 15, no. 6, pp. 536–543, 2005.

[105] V. Volterra, *Theory of Functionals and of Integral and Integrodifferential Equations*, Reprint of 1930 edition ed. New York: Dover Publications, 2005.

[106] N. Wiener, *Nonlinear Problems in Random Theory*. Cambridge: The MIT Press, 1966.

[107] J. Bussgang, L. Ehrman, and J. Graham, "Analysis of nonlinear systems with multiple inputs," *Proceedings of the IEEE*, vol. 62, no. 8, pp. 1088–1119, Aug. 1974.

[108] J. Nilsson, *Electric Circuits*. Upper Saddle River: Pearson/Prentice Hall, 2008.

[109] Cherry, J. A., "Distortion analysis of weakly nonlinear filters using Volterra series," Master's thesis, Carleton University, Canada, Dec. 1994.

[110] F. Giannini, *Nonlinear Microwave Circuit Design*. New York: Wiley, 2004.

[111] S. Boyd, Y. S. Tang, and L. Chua, "Measuring Volterra kernels," *IEEE Transactions on Circuits and Systems*, vol. 30, pp. 571–577, 1983.

[112] L. Chua and C.-Y. Ng, "Frequency domain analysis of nonlinear systems: general theory," *Electronic Circuits and Systems, IEE Journal on*, vol. 3, no. 4, pp. 165 –185, Jul. 1979.

[113] S. Maas, *Nonlinear Microwave and RF Circuits*. Boston: Artech House, 2003.

[114] D. Leeson, "A simple model of feedback oscillator noise spectrum," *Proceedings of the IEEE*, vol. 54, no. 2, pp. 329–330, Feb. 1966.

[115] G. Sauvage, "Phase noise in oscillators: a mathematical analysis of Leeson's model," *Instrumentation and Measurement, IEEE Transactions on*, vol. 26, no. 4, pp. 408–410, Dec. 1977.

[116] A. Hajimiri and T. Lee, "A general theory of phase noise in electrical oscillators," *Solid-State Circuits, IEEE Journal of*, vol. 33, no. 2, pp. 179–194, feb 1998.

[117] A. Hajimiri, S. Limotyrakis, and T. Lee, "Jitter and phase noise in ring oscillators," *Solid-State Circuits, IEEE Journal of*, vol. 34, no. 6, pp. 790–804, Jun. 1999.

[118] T. Lee and A. Hajimiri, "Oscillator phase noise: a tutorial," *Solid-State Circuits, IEEE Journal of*, vol. 35, no. 3, pp. 326–336, Mar. 2000.

[119] B. Razavi, *Monolithic Phase-Locked Loops and Clock Recovery Circuits.* New York: IEEE Press, 1996.

[120] Mentor Graphics Corporation, *Eldo RF User's Manual*, 3rd ed., 2003.

[121] B. Razavi, "A study of phase noise in CMOS oscillators," *Solid-State Circuits, IEEE Journal of*, vol. 31, no. 3, pp. 331–343, Mar. 1996.

[122] M. J. Wu, J. N. Yang, and C. Y. Lee, "A constant power consumption CMOS LC oscillator using improved high-Q active inductor with wide tuning-range," in *Circuits and Systems, 2004. MWSCAS '04. The 2004 47th Midwest Symposium on*, vol. 3, Jul. 2004, pp. 347–350.

[123] J. Laskar, R. Mukhopadhyay, and C.-H. Lee, "Active inductor-based oscillator: A promising candidate for low-cost low-power multi-standard signal generation," in *Radio and Wireless Symposium, 2007 IEEE*, Jan. 2007, pp. 31–34.

[124] C. Saint and J. Saint, *IC Layout Basics.* New York: McGraw-Hill, 2002.

[125] G. Szczepkowski, G. Baldwin, and R. Farrell, "Wideband 0.18 um CMOS VCO using active inductor with negative resistance," in *Circuit Theory and Design, 2007. ECCTD 2007. 18th European Conference on*, Aug. 2007, pp. 990–993.

[126] R. Gilmore, *Practical Rf Circuit Design for Modern Wireless Systems Vol. 2.* Norwood: Artech House Publishers, 2003.

[127] J. Kim, J.-O. Plouchart, N. Zamdmer, M. Sherony, Y. Tan, M. Yoon, R. Trzcinski, M. Talbi, J. Safran, A. Ray, and L. Wagner, "A power-optimized widely-tunable 5-GHz monolithic VCO in a digital SOI CMOS technology on high resistivity

substrate," in *Low Power Electronics and Design, 2003. ISLPED '03. Proceedings of the 2003 International Symposium on*, Aug. 2003, pp. 434–439.

[128] H.-Y. Chang, Y.-S. Wu, and Y.-C. Wang, "A 38% tuning bandwidth low phase noise differential voltage controlled oscillator using a 0.5um E/D-PHEMT process," *Microwave and Wireless Components Letters, IEEE*, vol. 19, no. 7, pp. 467–469, Jul. 2009.

[129] K. W. Tang, S. Leung, N. Tieu, P. Schvan, and S. P. Voinigescu, "Frequency scaling and topology comparison of millimeter-wave CMOS VCOs," in *Compound Semiconductor Integrated Circuit Symposium, 2006. CSIC 2006. IEEE*, Nov. 2006, pp. 55–58.

[130] X. Zhang, P. Mok, M. Chan, and P. Ko, "Large-signal and phase noise performance analysis of active inductor tunable oscillators," in *Circuits and Systems, 2003. ISCAS '03. Proceedings of the 2003 International Symposium on*, vol. 1, May 2003, pp. 705–708.

[131] J. Y. Foo and R. Weber, "Low power 5GHz quadrature phase CMOS LC oscillator with active inductor," in *Communications and Information Technology, 2004. ISCIT 2004. IEEE International Symposium on*, vol. 2, Oct. 2004, pp. 1084–1089.

[132] C. C. Wei, H. C. Chiu, and W. S. Feng, "An ultra-wideband cmos vco with 3-5 ghz tuning range," in *Radio-Frequency Integration Technology: Integrated Circuits for Wideband Communication and Wireless Sensor Networks, 2005. Proceedings. 2005 IEEE International Workshop on*, Dec. 2005, pp. 87–90.

[133] M. Fillaud and H. Barthelemy, "Design of a wide tuning range VCO using an active inductor," in *Circuits and Systems and TAISA Conference, 2008. NEWCAS-TAISA 2008. 2008 Joint 6th International IEEE Northeast Workshop on*, June 2008, pp. 13–16.

[134] M. Mehrabian, A. Nabavi, and N. Rashidi, "A 4-7ghz ultra wideband VCO with tunable active inductor," in *Ultra-Wideband, 2008. ICUWB 2008. IEEE International Conference on*, vol. 2, Sept. 2008, pp. 21–24.

[135] G. Huang and B.-S. Kim, "Programmable active inductor-based wideband VCO/QVCO design," *Microwaves, Antennas Propagation, IET*, vol. 2, no. 8, pp. 830–838, Dec. 2008.

[136] S. K. Eun, C. S. Cho, J. Lee, and J. Kim, "A low power VCO using active inductor for low phase noise and wide tuning range," in *Microwave Conference, 2009. EuMC 2009. European*, Sept. 2009, pp. 1255–1258.

[137] P. Quinlan, P. Crowley, M. Chanca, S. Hudson, B. Hunt, K. Mulvaney, G. Retz, C. E. O'Sullivan, and P. Walsh, "A multimode 0.3-200-kb/s transceiver for the 433/868/915-MHz bands in 0.25-um CMOS," *IEEE Journal of Solid-State Circuits*, vol. 39, no. 12, pp. 2297–2310, 2004.

[138] J. Ryu, M. Kim, J. Lee, B.-S. Kim, M.-Q. Lee, and S. Nam, "Low power OOK transmitter for wireless capsule endoscope," in *Microwave Symposium, 2007. IEEE/MTT-S International*, Honolulu, HI, 2007, pp. 855–858.

[139] F. Zhao, X. Gao, H. Zhang, K. Hu, and Z. Hong, "A CMOS 434/868 MHz FSK/OOK transmitter with integrated fractional-n PLL," in *Wireless and Microwave Technology Conference, 2009. WAMICON '09. IEEE 10th Annual*, Clearwater, FL, 2009, pp. 1–4.

[140] M. Raja and Y. P. Xu, "A 52 pJ/bit OOK transmitter with adaptable data rate," in *Solid-State Circuits Conference, 2008. A-SSCC '08. IEEE Asian*, Nov. 2008, pp. 341–344.

[141] Y. Chee, A. Niknejad, and J. Rabaey, "An ultra-low-power injection locked transmitter for wireless sensor networks," *Solid-State Circuits, IEEE Journal of*, vol. 41, no. 8, pp. 1740–1748, Aug. 2006.

[142] ——, "A 46% efficient 0.8 dBm transmitter for wireless sensor networks," 2006, pp. 43–44.

[143] D. Daly and A. Chandrakasan, "An energy-efficient OOK transceiver for wireless sensor networks," *Solid-State Circuits, IEEE Journal of*, vol. 42, no. 5, pp. 1003–1011, May 2007.

[144] X. Huang, P. Harpe, X. Wang, G. Dolmans, and H. de Groot, "A 0dBm 10Mbps 2.4 GHz ultra-low power ASK/OOK transmitter with digital pulse-shaping," in *Radio Frequency Integrated Circuits Symposium (RFIC), 2010 IEEE*, May 2010, pp. 263–266.

[145] J. Jung, S. Zhu, P. Liu, L. Wang, T.-N. Luo, Y.-J. Chen, and D. Heo, "Energy efficient 136 Mb/s OOK implantable transmitter for wireless brain computer interface," in *Microwave Symposium Digest (MTT), 2010 IEEE MTT-S International*, May. 2010, pp. 1604–1607.

[146] A. Medjahdi and F. Calmon, "Wideband 2.5 GHz VCO with active inductance in a 0.25 um CMOS technology," in *Electronics, Circuits, and Systems, 2009. ICECS 2009. 16th IEEE International Conference on*, Dec. 2009, pp. 735–738.

[147] U. Rohde and A. Poddar, "Tunable active inductor offers integrable and cost-effective alternatives of varactor tuned VCOs," in *Frequency Control Symposium, 2009 Joint with the 22nd European Frequency and Time forum. IEEE International*, Apr. 2009, pp. 962–967.